

Dissertation  
submitted to the  
Combined Faculties for the Natural Sciences and for Mathematics  
of the Ruperto-Carola University of Heidelberg  
for the degree of  
Doctor of Natural Sciences

Put forward by  
Dipl.-Phys. Johannes Thomas Lux  
Born in Zittau

Oral examination:  
20<sup>th</sup> June 2018



Dissertation

**A new target preparation facility for high  
precision AMS measurements and  
strategies for efficient  $^{14}\text{CO}_2$  sampling**

Johannes T. Lux

Referees:

Dr. Ingeborg Levin  
Prof. Dr. Bernd Jähne



## **Eine neue Targetpräparationsanlage für hochpräzise AMS-Messungen und Strategien zur effizienten $^{14}\text{CO}_2$ -Probenahme**

Ziel dieser Arbeit war es, die Prozessierung von in großem Umfang genommenen atmosphärischen  $^{14}\text{CO}_2$ -Proben zu Graphittargets für die hochpräzise Analyse an einem Beschleuniger-Massenspektrometer (AMS) zu ermöglichen und die Probennahme selber, die in ganz Europa im Rahmen des Netzwerks Integrated Carbon Observation System (ICOS) stattfindet, weiterzuentwickeln. Für den ersten Teil wurde im Zentralen Radiokohlenstofflabor (CRL) von ICOS eine zum größten Teil automatisierte Extraktions- und Graphitisierungsanlage (EGL) entwickelt, die Konstruktion in der Institutswerkstatt angeleitet und das Prozessverhalten sowie die Targetgüte optimiert und charakterisiert. Die Prozessfraktionierung in  $\delta^{13}\text{C}$  von der Luftprobenflasche bis zum Graphittarget ist mit  $(0.04 \pm 0.09) \text{‰}$  nicht unterscheidbar von Null. Die Abweichung zur absoluten, kanonischen  $\Delta^{14}\text{C}$ -Skala wurde bestimmt als  $(0.7 \pm 0.5) \text{‰}$ . Es wurde gezeigt, dass die Reproduzierbarkeit der  $\Delta^{14}\text{C}$ -Ergebnisse von prozessierten Luftproben für die finalen Graphitisierungsparameter bei  $\pm 1.9 \text{‰}$  oder darunter liegt. Kompatibilitätstests lieferten eine Abweichung der Ergebnisse der mit der EGL prozessierten und am AMS des Curt-Engelhorn-Zentrum Archäometrie (CEZ) analysierten Proben von den Resultaten des CRL Low-Level-Zählungslabors (LLC) von  $(2.2 \pm 0.9) \text{‰}$ , wobei der Grund noch unbekannt ist. Für die Weiterentwicklung der  $^{14}\text{CO}_2$ -Probennahme wurde eine neue trajektoriengetriggerte Strategie in einem atmosphärischem Vorwärtsmodellsystem simuliert. Es wurde gezeigt, dass hiermit schwache fossile  $\text{CO}_2$ -Signale von Emissionshotspots bei vier deutschen ICOS-Stationen um einen Faktor von bis zu 7 verstärkt werden können, während der Signalhintergrund mit parallel genommenen Proben abgeschätzt wird.

## **A new target preparation facility for high precision AMS measurements and strategies for efficient $^{14}\text{CO}_2$ sampling**

The aim of this thesis was to allow for the processing of large-scale atmospheric  $^{14}\text{CO}_2$  samples into graphite targets for high-precision analysis on an accelerator mass spectrometer (AMS) and to further develop the sampling itself, which takes place throughout Europe within the Integrated Carbon Observation System (ICOS) network. For the first part, a largely automated Extraction and Graphitisation Line (EGL) was developed at the ICOS Central Radiocarbon Laboratory (CRL); the construction at the institute workshop was guided and process behaviour and target quality was characterised. Process fractionation in  $\delta^{13}\text{C}$  from the whole-air sample flask to the graphite target cannot be distinguished from zero with  $(0.04 \pm 0.09) \text{‰}$ . The deviation from the absolute canonical  $\Delta^{14}\text{C}$  scale was determined to  $(0.7 \pm 0.5) \text{‰}$ . It was shown that the reproducibility of  $\Delta^{14}\text{C}$  results from processed air samples is at  $\pm 1.9 \text{‰}$  or below for the final graphitisation parameters. Compatibility tests provided a deviation of the results of samples processed with EGL and analysed by the AMS at the Curt-Engelhorn-Centre Archaeometry (CEZ) from the results of the CRL Low-Level Counting (LLC) laboratory of  $(2.2 \pm 0.9) \text{‰}$ . The reason for the deviation is currently unknown. For the further development of  $^{14}\text{CO}_2$  sampling, a new trajectory-triggered strategy was simulated in an atmospheric forward modelling system. It was shown that weak fossil  $\text{CO}_2$  signals from emission hotspots at four German ICOS stations can be amplified by a factor of up to 7, while the signal background is estimated with parallelly taken samples.



# Contents

<b>Introduction</b>	<b>9</b>
<b>1. Basics</b>	<b>15</b>
1.1. The Central Radiocarbon Laboratory in the ICOS network . . . . .	15
1.1.1. $^{14}\text{CO}_2$ sampling in the ICOS network . . . . .	16
1.1.2. Role of the ICOS Central Radiocarbon Laboratory . . . . .	17
1.2. Radiocarbon formalism . . . . .	17
1.2.1. Specific activity . . . . .	18
1.2.2. Handling isotope fractionation . . . . .	18
1.2.3. Notation and standards . . . . .	22
1.3. Estimates of regional FFCO <sub>2</sub> . . . . .	23
1.3.1. Effect of the biogenic $^{14}\text{C}$ signature . . . . .	25
1.3.2. Applications of $^{14}\text{CO}_2$ measurements for FFCO <sub>2</sub> estimation . . . . .	25
1.4. $^{14}\text{CO}_2$ analysis by accelerator mass spectrometry . . . . .	26
1.4.1. Performing measurements with MICADAS . . . . .	26
1.4.2. Measurement evaluation . . . . .	28
1.4.3. The graphitisation reaction . . . . .	30
1.5. Modelling principles & methods . . . . .	34
1.5.1. Mixing processes in the planetary boundary layer . . . . .	34
1.5.2. Theoretical background of inverse modelling . . . . .	36
1.5.3. Model systems . . . . .	38
1.5.4. Emission inventories for FFCO <sub>2</sub> . . . . .	41
<b>2. AMS sample preparation in the IUP <math>^{14}\text{C}</math> -laboratory</b>	<b>43</b>
2.1. Graphitisation . . . . .	43
2.1.1. Fractionation effects in the graphitisation line . . . . .	43
2.2. Quality control . . . . .	45
2.2.1. Target gases . . . . .	45
2.2.2. LLC aliquots . . . . .	48
2.3. Storage test of graphitised samples and blank contamination . . . . .	51
2.4. Test of the target press . . . . .	53
2.5. Consequences of the preparatory phase . . . . .	54
2.5.1. Magazine composition . . . . .	54
<b>3. Set-up of the AMS target Extraction and Graphitisation Line</b>	<b>57</b>
3.1. Processing chain . . . . .	57

## Contents

3.2.	Construction of the EGL . . . . .	59
3.2.1.	Sample inlets and outlets . . . . .	59
3.2.2.	CO <sub>2</sub> extraction . . . . .	61
3.2.3.	CO <sub>2</sub> transfer inside EGL . . . . .	65
3.2.4.	Quantification . . . . .	65
3.2.5.	Aliqotation and $\delta^{13}\text{C}$ analysis . . . . .	68
3.2.6.	Graphitisation . . . . .	70
3.2.7.	Properties of the whole system . . . . .	75
3.3.	Regulation electronics and user interface . . . . .	82
3.4.	Development of the EGL control software . . . . .	82
3.4.1.	User Interface . . . . .	85
3.4.2.	Pipelining of the tasks . . . . .	87
3.5.	Optimisation of the graphitisation parameters . . . . .	91
3.5.1.	Overview of performance indicator choice . . . . .	92
3.5.2.	Test of iron type . . . . .	100
3.5.3.	Test of graphitisation duration . . . . .	102
3.5.4.	Test of catalyst pretreatment . . . . .	103
3.5.5.	Test of temperature and hydrogen amount variations . . . . .	106
3.5.6.	Test of catalyst amount . . . . .	110
3.5.7.	Overview of the parameter test results . . . . .	113
3.6.	Fractionation during preprocessing . . . . .	114
3.6.1.	Extraction . . . . .	114
3.6.2.	Transfer to reactors . . . . .	114
3.6.3.	Sampling of standard gases . . . . .	115
3.6.4.	Graphitisation . . . . .	117
3.7.	Establishing EGL quality control . . . . .	119
3.7.1.	Target gases . . . . .	119
3.7.2.	LLC compatibility . . . . .	122
3.7.3.	Oxalic Acid I as primary QC . . . . .	122
3.7.4.	Overview of the first results of the EGL QC test series . . . . .	125
<b>4.</b>	<b>Development of new <sup>14</sup>CO<sub>2</sub> sampling strategies</b>	<b>127</b>
4.1.	Set-up of time-triggered integrated <sup>14</sup> CO <sub>2</sub> sampling in Heidelberg . . . . .	127
4.1.1.	Objectives . . . . .	127
4.1.2.	Catchment area . . . . .	128
4.1.3.	Sampling set-up . . . . .	130
4.1.4.	Trace gases . . . . .	131
4.1.5.	<sup>14</sup> CO <sub>2</sub> results . . . . .	133
4.1.6.	Nighttime FFCO <sub>2</sub> offset in Heidelberg . . . . .	135
4.2.	Modelling of trajectory-triggered integrated sampling . . . . .	138
4.2.1.	Model environment . . . . .	139
4.2.2.	Virtual FFCO <sub>2</sub> sampling at German ICOS stations . . . . .	143
4.2.3.	Emission inventory error reduction potential . . . . .	153

<b>Summary &amp; outlook</b>	<b>157</b>
<b>Annex</b>	<b>161</b>
<b>A. Detailed explanations</b>	<b>163</b>
A.1. Description of regulation electronic and hardware control . . . . .	163
A.1.1. Control of heating elements . . . . .	163
A.1.2. Control of extraction pumps, elevators and reactor cooling .	164
A.1.3. Pressure sensors . . . . .	165
A.1.4. Pneumatic valve control . . . . .	169
A.1.5. Air flow control . . . . .	169
A.1.6. Controlling PC . . . . .	171
<b>B. Additional figures</b>	<b>173</b>
<b>C. Material lists</b>	<b>183</b>
C.1. Software . . . . .	183
C.2. EGL parts . . . . .	183
<b>List of Figures</b>	<b>185</b>
<b>List of Tables</b>	<b>189</b>
<b>List of abbreviations</b>	<b>191</b>
<b>Bibliography</b>	<b>193</b>
<b>Credits</b>	<b>203</b>



## Introduction

In December 2015, 195 member countries of the United Nations signed a declaration of intent that was called an historical event in the public. And – in fact for the first time – all of the world’s governments except Syria and Nicaragua stated that they are

[...] recognizing the need for an effective and progressive response to the urgent threat of climate change on the basis of the best available scientific knowledge.

Consequently, these nations agreed on adopting measures to achieve a limitation of the current temperature increase at “well below 2°C” above the pre-industrial level. The agreement encourages all parties to strengthen their efforts in scientific and technological progress to fulfil this goal (UNFCCC, 2015). This goal, however, seems to be very ambitious as a later start in reducing the global greenhouse gas (GHG) emissions means that the rate of reductions, which have to be undertaken, will be more demanding. Figure 1 shows modelled surface temperature changes for different carbon dioxide (CO<sub>2</sub>) emission scenarios, which range from a net negative emission in the middle of the century (blue lines) to the worst-case scenario with emissions increasing to more than 100 Pg CO<sub>2</sub> a<sup>-1</sup> and a corresponding temperature increase of 3.2°C to 5.4°C (red lines). The black line in Figure 2 gives an impression of the rate of reduction of CO<sub>2</sub> equivalent GHGs the global community has to accomplish to not exceed the 2-degree goal at a 66% likelihood. The emission pathways for individual nations or confederations following the intended nationally determined contributions (INDC) of the Paris agreement are shown in different colours. The emission pledges of the top-4 emitters leave no room for the rest of the world. This highlights once again how demanding the required GHG emission reductions are to stay below 2°C temperature increase.

As shown by Le Quéré et al. (2016), the ten most populous nations span a wide range of emissions per capita. Beginning with the USA with 17 tons CO<sub>2</sub> equivalent per capita and year, EU and China with about 7 and India with 2 tons CO<sub>2</sub> equivalent per capita and year. The world average amounts to 5 tons CO<sub>2</sub> per capita and year. Considering the 2°C goal and a growing world population this world average soon has to be reduced, since the remaining quota of CO<sub>2</sub> emissions after 2016 amounts to 816 Pg CO<sub>2</sub> and would be consumed within 25 years at a current emission rate of 35 Pg a<sup>-1</sup>. Therefore, we have to find a compromise between equity in the “right” to emit GHGs and making it possible for less wealthy countries to develop on a lower level of GHG emissions.

## Introduction

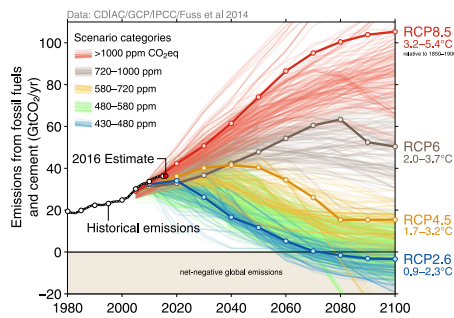


**Figure 1.:** Emission scenarios and associated surface temperature models. Thick lines represent four representative concentration pathways and related temperature increase (Le Quéré et al., 2016).

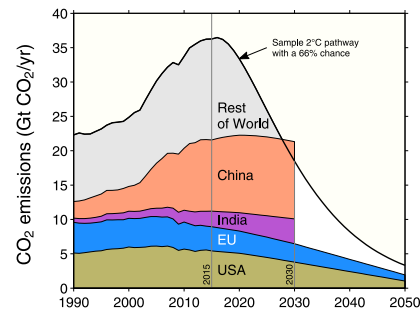


**Figure 2.:** Required emission progress to accomplish 2-degree target with 66% likelihood and INDCs of the top-4 emitters in different colours (Le Quéré et al., 2016).

Europe's role in this situation could be not only to reduce its own emission amount below these 5 tons CO<sub>2</sub> per capita and year but also to act as a model for emerging countries how to handle the will for prosperity of the population and the need to deal with climate change. In this setting there is a need to have tools to check the impact of the taken measures for reducing GHG emission independently. A need, for which in 2008 the Integrated Carbon Observation System Research Infrastructure (ICOS RI) was realised in Europe.

The mission of ICOS RI is to enable research to understand GHG budgets and perturbations. ICOS provides a framework to perform and maintain long-term observations in order to understand the present state and predict future behaviour of the global carbon cycle and GHG emissions. In short it can be summarised in two objectives (ICOS RI, 2014):

**The 1st objective** is to give access to a single and coherent data set to enable a multi-scale analysis of GHG emissions, sinks and underlying processes that determine them. ICOS aims to be a template for future similar integrated GHG observation networks

**The 2nd objective** is to provide reliable information for research and understanding of regional budgets of GHG sources and sinks, their drivers and their control mechanisms. The network shall give early warnings of negative changes and responses of natural fluxes to changes in climatic circumstances. Furthermore, it permits to reduce uncertainties in earth system models.

The present thesis is dedicated to bring progress in fulfilling both objectives in the framework of ICOS. To improve our understanding of the impact of anthropogenic emissions to the climate system, we need to be able to measure the corresponding quantities in the atmosphere with sufficient precision. The arrows in Figure 3 show the current yearly CO<sub>2</sub> net fluxes between the three main carbon

storage compartments on earth. The perturbation by human activities, mainly combustion of fossil fuels and change in land usage (e.g. deforestation), represents only a small portion of the total fluxes between atmosphere and biosphere respectively ocean. It leads, however, to a steady increase of most recently – in 2016 –  $(22.4 \pm 0.7) \text{ Pg a}^{-1}$  of carbon dioxide in the atmospheric reservoir of about  $2900 \text{ Pg CO}_2$  (Le Quéré et al., 2017). This increase in atmospheric  $\text{CO}_2$  acts as the main driver of global warming (see e.g. Ciais et al., 2013), even though only 54% of the anthropologically released  $\text{CO}_2$  remained in the atmosphere in 2016. Averaged over the last 10 years, 44% of the anthropogenic emission led to an increase in atmospheric  $\text{CO}_2$  concentration, 28% was absorbed by the biosphere and 22% by the ocean.

The numbers above are determined by using national emission budgets based on energy statistics and cement production data (Le Quéré et al., 2017). That means the global anthropogenic emissions are calculated bottom-up, by multiplying a so called “emission factor” to given statistical activity data. Thus, they are sensitive to systematic errors and – in worst case – to manipulation. In order to be able to validate emission reporting independently, it is inevitable to precisely measure suitable tracers for fossil fuel  $\text{CO}_2$  ( $\text{FFCO}_2$ ) in the atmosphere.

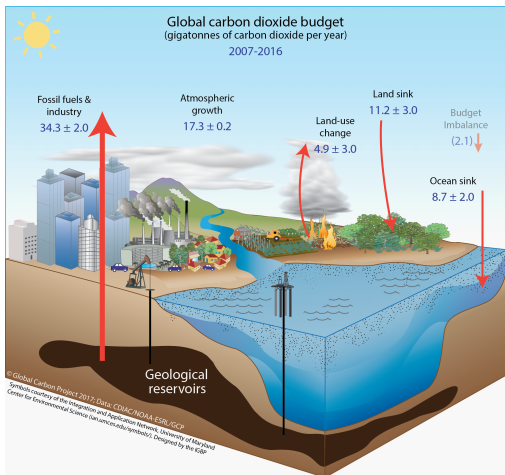


Figure 3.: Schematic representation of the global carbon budget 2007-2016. The numbers on the arrows indicate  $\text{CO}_2$  fluxes into and out of reservoirs. Picture taken from Le Quéré et al. (2017).

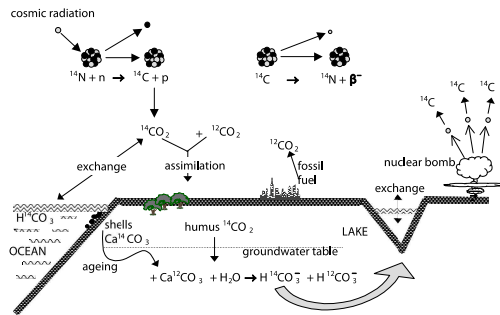
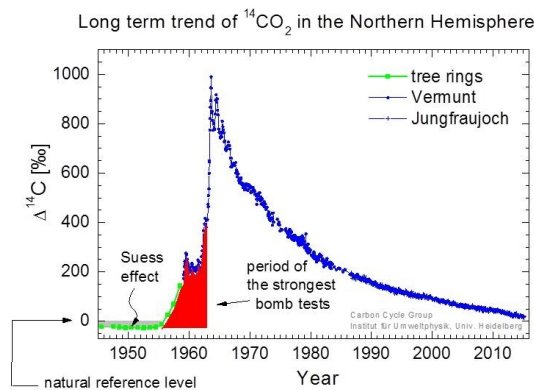


Figure 4.: Origin and reservoirs of  $^{14}\text{C}$ . Natural equilibrium between production and decay has been disturbed by the release of  $\text{FFCO}_2$  and  $^{14}\text{C}$  production in nuclear reactors and nuclear weapon tests. Picture taken from Mook (2000).

Atmospheric  $^{14}\text{CO}_2$  has proven to be an efficient tracer to separate fossil fuel induced from ecosystem fluxes (see e.g. Levin et al., 1989; Levin and Hesshaimer, 2000; Levin and Rödenbeck, 2008; Levin et al., 2003, 2008, 2011; Graven, 2015; Turnbull et al., 2015a). Radiocarbon is naturally formed in the transitional zone

between the lower stratosphere and the upper troposphere (see Libby, 1946; Mook, 2000).  $^{14}\text{C}$  is produced by a nuclear reaction of atmospheric nitrogen with thermal neutrons (Figure 4). Thermal neutrons are produced by reactions of high-energetic cosmic ray protons and molecules of the atmosphere. The formed  $^{14}\text{C}$  is rapidly oxidised to  $^{14}\text{CO}$  and  $^{14}\text{CO}_2$ , which mixes with atmospheric  $\text{CO}_2$  and takes part at all  $\text{CO}_2$  exchange processes.

In the undisturbed carbon cycle, balance is reached between cosmic ray induced production and radioactive decay of  $^{14}\text{C}$ . With start of the industrialisation the first major anthropogenic disturbance of the natural  $^{14}\text{C}/\text{C}$  ratio began. Fossil energy carrier are free from radioactive carbon since their genesis time was millions of years ago, i.e. very long compared to the 5700 years half life of  $^{14}\text{C}$ . Hence, with the invention of the steam machine and the combustion of fossil coal, humanity begun to dilute the  $^{14}\text{C}/\text{C}$  ratio in the more rapidly exchanged carbon reservoirs on earth, namely biosphere, the top of the oceans and especially the atmosphere. This effect was measured in 1955 by Hans Suess and is therefore called Suess effect (Suess, 1955).



**Figure 5.:** Development of tropospheric  $\Delta^{14}\text{C}$  of the Northern Hemisphere during the last 70 years. Data until 1959 derived from tree rings (Stuiver and Quay, 1981); later from measurements at alpine sites (Levin et al., 2010).

in ‰, in the northern hemisphere.

As mentioned above, radiocarbon observations are – due to the properties of  $^{14}\text{CO}_2$  – essential to separate the fossil part of regionally emitted atmospheric  $\text{CO}_2$ . This can be done by measuring a regional  $\Delta^{14}\text{C}$  offset from a background value. But, since only one in  $10^{12}$  atmospheric carbon atoms is a  $^{14}\text{C}$  atom and disturbances due to anthropogenic activities are small, it is challenging to measure  $\Delta^{14}\text{C}$  sufficiently precise in a reproducible way.

The WMO (World Meteorological Organisation) recommends to achieve a reproducibility of 30 % to 50 % for individual measurements of the regional  $\Delta^{14}\text{C}$

The second major disturbance was caused by extensive testing of nuclear weapons from 1956 until the inception of the Nuclear Test Ban Treaty by the Soviet Union and the USA in 1963, which has for the most part put an end to these tests. Production of  $^{14}\text{C}$  by reaction with thermal neutrons from the atmospheric tests doubled the  $^{14}\text{C}/\text{C}$  ratio in the troposphere. The uptake of this  $^{14}\text{CO}_2$  into fast exchanging reservoirs superposed the decline caused by the Suess effect for several decades. Recently the larger perturbation is once again the emission of  $\text{FFCO}_2$  (Levin et al., 2008, 2010). Figure 5 shows the long term trend in tropospheric  $\Delta^{14}\text{C}$ , which reports the normalised  $^{14}\text{C}$  activity relative to a standard

offset (GAW, 2015). This goal is not demanding for urban stations like Heidelberg, which show yearly mean FFCO<sub>2</sub> surpluses of typically about 10 ppm (e.g. Levin et al., 2008). Rural stations, on the other hand, typically show mean offsets of 1 ppm to 3 ppm, corresponding to a required  $\Delta^{14}\text{C}$  reproducibility of about 0.5 ‰ to 2.4 ‰.

Therefore, coming now back to the first of the ICOS objectives, the main part of my thesis was the set-up of a new extraction and graphitisation line (EGL) at the ICOS Central Radiocarbon Laboratory (CRL) in Heidelberg. The CRL offers its expertise built upon decades of high-precision <sup>14</sup>C analytics and monitoring <sup>14</sup>CO<sub>2</sub> in Heidelberg and worldwide. In this framework, the EGL provides an additional preprocessing capacity of 1500 atmospheric <sup>14</sup>CO<sub>2</sub> samples for accelerator mass spectrometry (AMS) analysis per year.

The EGL combines three preprocessing steps, which had to be performed separately until now, namely, extraction of CO<sub>2</sub> from whole air samples, determination of  $\delta^{13}\text{C}$  and graphitisation. A flexible and disturbance-tolerant control software has been developed to provide a high degree of automation and standardisation. Test series on atmospheric target gases were used to demonstrate precision and accuracy of analysis. Furthermore, determination of the sample's  $\delta^{13}\text{C}$  inside the EGL facilitates not only immediate monitoring of process fractionation and contaminations, but also fractionation correction to its true value and avoidance of the  $\delta^{13}\text{C}$ -Suess effect, which causes a slight  $\Delta^{14}\text{C}$  offset, and allows the calculation of a  $\delta^{14}\text{C}$  value (Stuiver and Polach, 1977). Extensive tests of measurement stability and reaction parameters have been conducted to ensure a process fractionation of less than 0.1 ‰ in  $\delta^{13}\text{C}$ . I give a detailed description of the technical realisation of the construction, the electronic and sensor systems and the software architecture of the EGL.

Finally, I address the understanding of regional FFCO<sub>2</sub> sources and budgets and, hence, the second of the two objectives of ICOS. Even though we are now able to measure 1500 whole-air samples for  $\Delta^{14}\text{C}$  per year, this number of analyses is far from being able to perform continuous  $\Delta^{14}\text{C}$  measurements in the ICOS network. Moreover, most observational stations are located far from FFCO<sub>2</sub> emission hotspots, therefore providing only weak  $\Delta^{14}\text{C}$  signals. Thus, new sampling strategies for atmospheric <sup>14</sup>CO<sub>2</sub> have been virtually tested in this work on a model basis, that address the problem to resolve weak signals in few samples by triggering sampling by anticipating air mass trajectories passing emission hotspots. On the basis of atmospheric transport model data for different ICOS stations, the increase of surface-to-atmosphere emission sensitivity of the FFCO<sub>2</sub> signal for a defined target region has been examined. This includes estimates of large-scale station-specific FFCO<sub>2</sub> background, which needs to be subtracted from the total signal. This means that a new, regional application of the proven approach of evaluating FFCO<sub>2</sub> against a continental background signal is presented.



# 1. Basics

## 1.1. The Central Radiocarbon Laboratory in the ICOS network

In the introduction, I gave a short overview about objectives and aims of ICOS RI. Here we will have a closer look at the structure of the network as well as the integration of the CRL in this structure and especially its tasks. ICOS-RI aims to integrate the results of its widespread measurement networks (see Figure 1.1) to coherent data sets. Therefore all components bundle their activities in the respective thematic centres, which, in turn, pass the data to the ICOS Carbon Portal, which provides data and elaborated data products to the public as well as to the scientific community as presented by Hellström et al. (2016) and shown in Figure B.1.

The ecosystem stations measure heat fluxes and especially  $\text{CO}_2$ ,  $\text{CH}_4$  and  $\text{H}_2\text{O}$  together with environmental variables to improve the understanding of ecosystem-atmosphere exchange and the underlying processes. The stations are located at different typical ecosystem sites (e.g. cropland, forests, grassland, marshes) to enable up-scaling of the results to areas without measurements (ICOS RI, 2017b).

The ocean network consists of a combination of measurements on land-based stations as well as sampling on research vessels or commercial liners. Currently carbon uptake and parameters like acidification, surface temperature and salinity are monitored on 21 stations in the north Atlantic, the Baltic and the Mediterranean sea (ICOS RI, 2017b).

The CRL mainly provides services for the atmospheric network, which focusses on measurements of trace gas con-

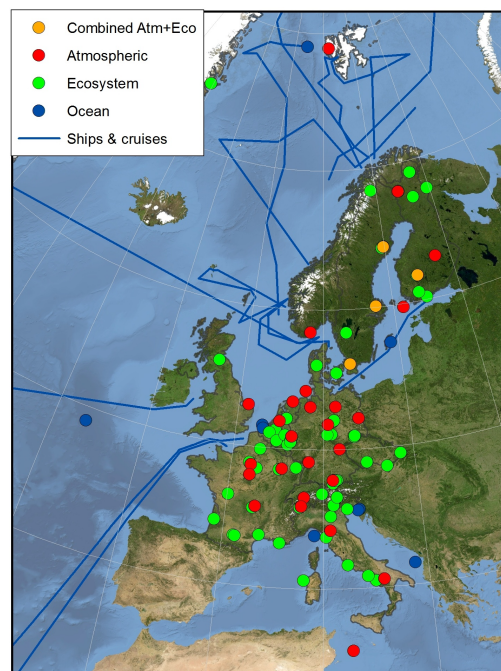


Figure 1.1.: Current station network of ICOS RI for atmospheric, ecosystem and ocean measurements (ICOS RI, 2017b).

## 1. Basics

centrations of CO<sub>2</sub>, CH<sub>4</sub>, CO and N<sub>2</sub>O as well as on stable isotopes in these gases and <sup>14</sup>CO<sub>2</sub>, which is the focus of this work. Criteria for the locations of the atmospheric stations were determined by a network design task force during ICOS preparatory phase: In multi-transport model footprint simulations for hypothetical networks, a number of recommendations have been elaborated to achieve the highest possible reduction in uncertainties in surface-atmosphere fluxes. In short, the benchmark for the distance between stations should be about 300 km, but not less than 50 km. Furthermore station placement should avoid short distance from strong anthropogenic sources like cities (Laurent, 2016). The last point is especially important for measurement of atmospheric <sup>14</sup>CO<sub>2</sub>, since the FFCO<sub>2</sub>-related gradients strongly drop with distance from large emitters (see sections below). This leads to the high demands in measurement precision in  $\Delta^{14}\text{C}$  of 2 ‰ to resolve FFCO<sub>2</sub> signals of less than 1 ppm.

An important goal of ICOS-RI is to enable quantitative analysis of global or continental scale atmospheric data from different stations and networks. Therefore, the instrumentation of the atmospheric stations has been chosen to be in compliance with the compatibility goals, which the WMO published in GAW (2015); the compatibility goal for  $\Delta^{14}\text{C}$  – the CRL commits to – is better than 0.5 ‰.

### 1.1.1. <sup>14</sup>CO<sub>2</sub> sampling in the ICOS network

The <sup>14</sup>CO<sub>2</sub> sampling in ICOS RI aims to provide a measure to separate FFCO<sub>2</sub> from biospheric fluxes. Hence, the sampling method is adapted to the constraints and requirements of current atmospheric modelling as the tool to realise this separation, as presented e.g. by Trusilova et al. (2010):

- Night-time concentrations near the surface are too much influenced by small scale circulation patterns, which are not resolved in global or regional models.
- Day-time measurements at tall towers in a well mixed planetary boundary layer are well represented in current atmospheric models.



Figure 1.2.: 3 L flask for whole air <sup>14</sup>CO<sub>2</sub> sampling (ICOS RI, 2017b)

Heidelberg.

Therefore, day-time <sup>14</sup>CO<sub>2</sub> sampling at 100 m in 3 litre glass flasks (see Figure 1.2) is recommended for class 1 stations (Laurent, 2016). In my thesis, new sampling strategies for whole air <sup>14</sup>CO<sub>2</sub> sampling at ICOS stations have been examined. Also, in the framework of RINGO (Readiness of ICOS for Necessities of integrated Global Observations) new approaches in this direction are currently investigated at the CRL in

Diurnal cycle and event-based sampling will be made with the standard ICOS flask sampler; supplied by the FCL (Flask and Calibration Laboratory ICOS RI, 2017a). In the CRL, the sample flasks will be completely tracked in all their accumulating measurement metadata and important preprocessing parameters, so that we can deliver complete and comprehensive datasets in the end after final  $^{14}\text{C}$  analysis. In addition to the flask sampling, integrated samples are taken at ICOS Class-1 stations in the traditional way by absorbing  $\text{CO}_2$  in basic NaOH solution (Levin et al., 1980).

### 1.1.2. Role of the ICOS Central Radiocarbon Laboratory

In short, the tasks of the CRL can be summarised in four points, that all have been subject of this work (ICOS RI, 2017a):

**High precision AMS analysis** of  $^{14}\text{CO}_2$  from atmospheric whole air samples. This service includes  $\text{CO}_2$  extraction, in-line  $\delta^{13}\text{C}$  analysis, graphitisation and target preparation for up to 1500 AMS samples per year. Furthermore, internal and inter-laboratory compatibility and processing quality assessment is provided.

**Pilot station operation** in the urban Heidelberg area. Here, all important long-lived GHGs are routinely measured as well as integrated  $^{14}\text{CO}_2$  and  $^{222}\text{Rn}$  progenies. Additionally new methods for  $\text{FFCO}_2$  quantification and sample-taking and new atmospheric tracers are examined before implementing them into the ICOS atmospheric station network.

**Low Level Counting (LLC)  $^{14}\text{C}$  analysis** of 500 high-volume pure- $\text{CO}_2$  samples per year in an underground laboratory and prior  $\text{CO}_2$  extraction from the basic solution. This includes compatibility studies with other labs, especially the AMS analysis.

**Network services** for the ICOS atmospheric stations. This includes supply of integrating high-volume  $^{14}\text{CO}_2$  samplers and the corresponding  $\text{CO}_2$  free NaOH solutions. In combination with the sampling methods examination at the pilot station, the CRL develops new sampling equipment.

Together with the Flask and Calibration Laboratory (FCL) in Jena the CRL forms the Central Analytical Laboratories, which aim to assure the accuracy of ICOS atmospheric measurement data.

## 1.2. Radiocarbon formalism

In 1949 the first radiocarbon dating was performed by Libby et al. (1949) and since then the corresponding formalism has developed based on measuring the radioactive decay of  $^{14}\text{C}$ . In later years, AMS analysis made it possible to directly

## 1. Basics

measure isotope ratios in solid carbon samples (Currie, 1978), but the corresponding units and normalisation procedures are still based on a specific activity  $A_s$  of the sample. Here I introduce the units and calculation regarding radiocarbon measurement used in this work. Stenström et al. (2011) give a comprehensive derivation of these calculations.

### 1.2.1. Specific activity

The net specific activity  $A$  of an examined sample ( $A_s$ ) or standard ( $A_{stand}$ ) is in first order provided by subtraction of a measured background activity  $\tilde{A}_b$  from the measured target activity  $\tilde{A}$ :

$$A = \tilde{A} - \tilde{A}_b. \quad (1.1)$$

In AMS analysis no specific activity is measured. Instead, carbon isotope nuclides are counted yielding the numbers of nuclides  $N(^{12}\text{C})$ ,  $N(^{13}\text{C})$  and  $N(^{14}\text{C})$ . The specific activity in the sample is proportional to the ratio of  $^{14}\text{C}$  atoms to the total number of carbon atoms. Hence following approximation can be made

$$A \propto R = \frac{N(^{14}\text{C})}{N(^{12}\text{C}) + N(^{13}\text{C}) + N(^{14}\text{C})} \approx \frac{N(^{14}\text{C})}{N(^{12}\text{C}) + N(^{13}\text{C})} \approx \frac{N(^{14}\text{C})}{N(^{12}\text{C})} := \frac{^{14}\text{C}}{^{12}\text{C}} \quad (1.2)$$

with the isotope ratio  $R$ , that is for the AMS results presented in this work derived from the measured ratio  $\tilde{R}$  and the background ratio  $\tilde{R}_b$  analogous to (1.1) (Wacker et al., 2010b):

$$R = \tilde{R} - \tilde{R}_b \quad (1.3)$$

The last approximation in (1.2) means, that all ratios of specific activities can be also performed for ratios of isotope ratios  $\frac{N(^{14}\text{C})}{N(^{12}\text{C})}$ . All AMS results presented in this work have been calculated using (1.2). Donahue et al. (1990) specified the error introduced by this approximation to 0.1 ‰ on the calibrated result. For simplicity reasons, I will display isotope counts of carbon isotopes with mass  $x$  as  $^x\text{C}$  instead of  $N(^x\text{C})$  in this work.

### 1.2.2. Handling isotope fractionation

All chemical processes lead to a fractionation between different isotopologues of the same substance. In general this is described by an isotope fractionation factor  $\alpha_{B/A}$  for a transition  $A \rightleftharpoons B$  or  $A \rightarrow B$  for irreversible processes

$$\alpha_{B/A} = \frac{R_B}{R_A} \neq 1 \quad (1.4)$$

for the isotope ratios  $R$  before and after reaction. In principle one can differentiate between three effects responsible for isotopic fractionation (see Mook, 2000):

**Kinetic fractionation** results from irreversible physical or chemical processes, e.g. the evaporation of water from the ocean with immediate removal by wind. The effect depends on the binding energy of the compounds in the way that isotopically lighter particles have generally smaller binding energies and higher velocities than heavier. Chemical reactions occur faster for lighter particles as well.

**Inverse kinetic fractionation** takes place for reactions that behave opposite from the rules for kinetic fractionation, that means the heavier isotope having a lower binding energy. This effect commonly occurs for reactions involving hydrogen, e.g.  $^{13}\text{CO}_2$  has a lower solubility in water than  $^{12}\text{CO}_2$

**Equilibrium fractionation** is the effect involved in an equilibrium reaction. The fractionation factor equals the equilibrium constant between the phases containing the different isotopes. The fractionation factor depends approximately exponentially on the inverse temperature:  $\alpha \approx Ae^{B/T}$ , with  $A$  and  $B$  containing the temperature independent reaction parameters. In general equilibrium fractionation effects are smaller than kinetic fractionations.

These fractionation effects can be calculated, if all corresponding binding energies are known. However, this is often not the case in practise; furthermore, almost no reactions are occurring purely irreversible or reversible (Mook, 2000). Following this, the isotopic fractionation has to be most often determined experimentally, what, in this thesis, has been done for most of the relevant processes.

### 1.2.2.1. $\delta$ -notation

Fractionation of carbon in carbon cycle exchange processes or in the laboratory lead to an enrichment or depletion of  $^{13}\text{C}$  in the measured sample. The resulting  $^{13}\text{C}/^{12}\text{C}$  ratio is canonically expressed relative to the Vienna Pee Dee Belemnite (VPDB) standard:

$$\delta^{13}\text{C} = \left( \frac{\left(\frac{^{13}\text{C}}{^{12}\text{C}}\right)_S - \left(\frac{^{13}\text{C}}{^{12}\text{C}}\right)_{VPDB}}{\left(\frac{^{13}\text{C}}{^{12}\text{C}}\right)_{VPDB}} \right) \cdot 1000 \text{ ‰} \quad (1.5)$$

This defines the  $\delta$ -notation for  $^{13}\text{C}/^{12}\text{C}$  ratios for a sample  $S$  in per mille.

### 1.2.2.2. $\delta^{13}\text{C}$ Normalisation

Normalisation of the  $^{14}\text{C}$  results based on their  $^{13}\text{C}$  isotope ratio becomes mandatory when comparing  $^{14}\text{C}/\text{C}$  ratios of samples from different natural reservoirs, which underwent different chemical production processes, e.g. in archaeometry bone samples ( $\delta^{13}\text{C} \approx -20 \text{ ‰}$ ) and charcoal ( $\delta^{13}\text{C} \approx -25 \text{ ‰}$ ). The processes leading to the mass-dependent fractionation in  $^{13}\text{C}$  lead to a higher effect in  $^{14}\text{C}/\text{C}$  ratios,

## 1. Basics

since the mass difference to the abundant isotope  $^{12}\text{C}$  is doubled. Furthermore and more importantly for this work, different laboratories processing and measuring similar samples can apply different grades of fractionation by deviations in the sampling or measurement technique. Not correcting for fractionation would render the results of these laboratories as not compatible.

To quantify this and allow to correct  $^{14}\text{C}$  fractionation, Stuiver and Robinson (1974) introduced a  $^{13}\text{C}$  fractionation factor  $f_{13}$

$$f_{13} = \frac{\left(\frac{^{13}\text{C}}{^{12}\text{C}}\right)_{[-25]}}{\left(\frac{^{13}\text{C}}{^{12}\text{C}}\right)_S}, \quad (1.6)$$

which is the ratio of the  $^{13}\text{C}/\text{C}$  ratio of a sample with  $\delta^{13}\text{C} = -25 \text{‰}$  with the  $^{13}\text{C}/\text{C}$  ratio of a sample. This can be expressed using the  $\delta$ -notation (1.5)

$$f_{13} = \frac{0.975}{\left(1 + \frac{\delta^{13}\text{C}_S}{1000}\right)} \quad (1.7)$$

with the  $\delta^{13}\text{C}$  value of the sample  $S$ . Stuiver and Robinson (1974) approximated the  $^{14}\text{C}$  fractionation factor  $f_{14}$  to

$$f_{14} \approx f_{13}^b \approx f_{13}^2 \quad (1.8)$$

In radiocarbon reporting the exponent  $b$  has been set to  $b := 2$  and hence  $f_{14} := f_{13}^2$ , despite Stuiver and Robinson (1974) already supposed  $b = 1.9$  to be more correct; the impacts of this definition will be discussed later.

Using this formalism, any specific activity  $A$  of a sample with known  $\delta^{13}\text{C}_S$  can now be normalised to  $\delta^{13}\text{C} = -25 \text{‰}$  by

$$A_N = A \cdot f_{14} = A \cdot f_{13}^2 = A \cdot \left(\frac{0.975}{\left(1 + \frac{\delta^{13}\text{C}_S}{1000}\right)}\right)^2. \quad (1.9)$$

In the following we discuss two effects, that have to be kept in mind when examining normalised (atmospheric)  $^{14}\text{CO}_2$  samples.

### 1.2.2.3. Suess effect in $^{13}\text{C}$ and $^{14}\text{C}$

As explained in the introduction, we can use  $^{14}\text{CO}_2$  as quantitative tracer for fossil fuel combustion due to the large difference in  $^{14}\text{C}$  activity in modern air and fossil fuels. The dilution of the atmosphere in specific radiocarbon activity by FFCO<sub>2</sub> emissions is called the Suess effect (Suess, 1955). However, a similar, but smaller effect is also observed in atmospheric  $\delta^{13}\text{C}$ , which could be used to differentiate

carbon dioxide emitters (e.g. Vardag et al., 2016). Figure 1.3 shows the relations regarding  $^{14}\text{C}$  and  $^{13}\text{C}$  in different natural reservoirs.

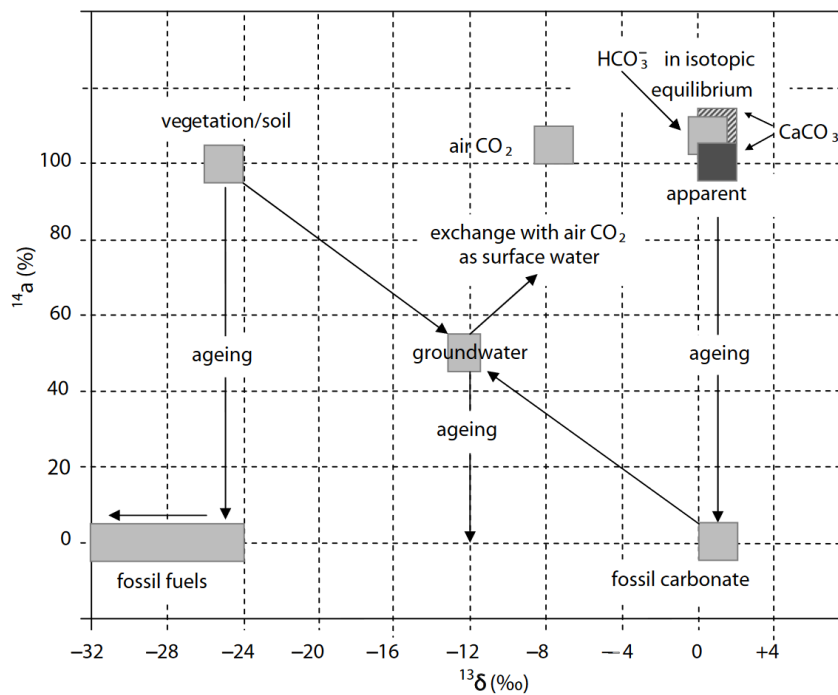


Figure 1.3.: Relation between variations in  $^{13}\text{C}$  and  $^{14}\text{C}$  in nature.  $^{14}a$  is the  $^{14}\text{C}$  activity ratio. Picture taken from Mook (2000).

Ongoing dilution of atmospheric background  $^{13}\text{CO}_2/^{12}\text{CO}_2$  by  $\text{FFCO}_2$  hence leads to an increase in the fractionation factors  $f_{13}$  (see (1.7)), which is not induced by fractionation effects. With  $f_{14} = f_{13}^2$  this process changes the normalised  $^{14}\text{C}$  activity  $A_N$  of an atmospheric sample independent from its actual activity  $A$ . Correction of the specific activity  $A$  of a sample for measurement and processing induced fractionation to its atmospheric  $\delta^{13}\text{C}$  value would be a measure to avoid this influence on  $^{14}\text{CO}_2$  results. Analogously to (1.5), this would lead to a fractionation corrected  $\delta^{14}\text{C}$  value.

#### 1.2.2.4. Deviations from the normalisation by different fractionation processes

As mentioned above Stuiver and Robinson (1974) worked out, that in normalisation of radiocarbon activities an exponent  $b = 1.9$ , rather than 2.0, would lead to more accurate results. Recently, Fahrni et al. (2017) determined an experimental value of  $b = 1.882 \pm 0.019$  for fractionation occurring during graphitisation of Oxalic Acid I or II samples. Photosynthesis induced fractionation led to  $b = 1.953 \pm 0.025$  for C3 and C4 plants growing in synthetic air mixed with  $\text{CO}_2$  from Oxalic Acid I. The fractionation exponents for equilibrium ( $b = 1.857$ ) and

## 1. Basics

kinetic fractionation ( $1.89 \leq b \leq 2$ , depending on the molecular mass of contributing particles) have been estimated using different approximations. Hence, the exponent for the graphitisation reaction as measured by Fahrni et al. (2017) can be interpreted as a large contribution of equilibrium fractionation or kinetic fractionation involving low-mass particles. In this work, similar studies have been performed, leading to comparable results (see Section 3.5.1).

Since it is in practise never known, which fractionation processes take part in the sample preparation and measurement processes, this leads to the conclusion, that process fractionation should be minimised, where possible. Following the considerations above, an equilibrium reaction induced fractionation of  $\Delta\delta^{13}\text{C} = -5\text{‰}$  causes an deviation of  $1.4\text{‰}$  in  $f_{14}$  compared to an evaluation with the canonical value of  $b = 2$  for a sample with a true value of  $\delta^{13}\text{C} = -10\text{‰}$ . Such large fractionation effects can occur during AMS measurements (see Section 1.4) and potential biases in  $\Delta^{14}\text{C}$  results should be kept in mind.

### 1.2.3. Notation and standards

By definition, radiocarbon is reported relative to a standard with a specific activity of (e.g. Mook and van der Plicht, 1999)

$$A_{abs} = 226 \text{ Bq kg}^{-1}. \quad (1.10)$$

As standard material NIST Oxalic Acid I has been chosen. The normalised (to  $\delta^{13}\text{C} = -19\text{‰}$ ) standard activity  $A_{ON}$  is defined as

$$A_{ON} = 0.95 A_{OxI} \left( \frac{1 - \frac{19}{1000}}{1 + \frac{\delta^{13}\text{C}}{1000\text{‰}}} \right)^2 \quad (1.11)$$

with the activity of Oxalic Acid I  $A_{OxI}$ .  $A_{ON}$  is decaying with time and can be converted back to  $A_{abs}$  using the law of radioactive decay

$$A_{abs} = A_{ON} e^{\lambda_C(y-1950)} \quad (1.12)$$

with the decay constant of radiocarbon  $\lambda_C = 1/8267 \text{ a}^{-1}$  and  $y$  as the year of measurement.

When the stock of OxI started to dwindle, new standard materials were produced. In the present thesis, most samples were measured relative to the Oxalic Acid II standard, which is defined as

$$A_{ON} = 0.759 A_{OxII} \left( \frac{1 - \frac{25}{1000}}{1 + \frac{\delta^{13}\text{C}}{1000\text{‰}}} \right)^2 \quad (1.13)$$

normalised to  $\delta^{13}\text{C} = -25\text{‰}$ .

In this work, as used to be done in reporting of atmospheric <sup>14</sup>C, an age-corrected  $\Delta$  notation (Stuiver and Polach, 1977) is used for reporting sample results:

$$\Delta^{14}\text{C} = \left( \frac{A_{SN} e^{\lambda_C(y-x)}}{A_{abs}} - 1 \right) \cdot 1000 \text{‰} = \left( \frac{A_{SN} e^{\lambda_C(1950-x)}}{A_{ON}} - 1 \right) \cdot 1000 \text{‰} \quad (1.14)$$

with  $x$  as the year of sampling and  $A_{SN}$  as the normalised sample activity, corresponding to the unit  $\Delta$  in Stuiver and Polach (1977). This value is independent of the time of measurement and reports <sup>14</sup>C data in numerical values appropriate to the expected signals.

### 1.2.3.1. <sup>14</sup>C age

The classical motivation for performing <sup>14</sup>C measurements is radiocarbon dating in the age range of  $1 \times 10^2$  a to  $1 \times 10^5$  a. By convention in radiocarbon dating, the year 1950 is set to  $t = 0$  and the Libby decay constant is set to  $\lambda_L = 1/8033 \text{ a}^{-1}$ . With these definitions, the conventional radiocarbon age  $T_{14\text{C}}$  can be expressed as

$$T_{14\text{C}} = -\frac{1}{\lambda_L} \ln \left( \frac{A_{SN}}{A_{ON}} \right) = -\frac{1}{\lambda_L} \ln \left( \left( \frac{\Delta^{14}\text{C}}{1000 \text{‰}} + 1 \right) e^{\lambda_C(x-1950)} \right) \quad (1.15)$$

where  $\lambda_C$  is the decay constant of radiocarbon as used in the  $\Delta^{14}\text{C}$  notation, i.e.  $1/8267 \text{ a}^{-1}$ , and  $x$  the year of sampling.

In this thesis, the <sup>14</sup>C age is used to present low sample or standard activities (esp. of blanks) and their uncertainties in an appropriate format, i.e. comparable with the values from literature.

## 1.3. Estimates of regional FFCO<sub>2</sub>

Suess (1955) detected the dilution in atmospheric <sup>14</sup>CO<sub>2</sub> by FFCO<sub>2</sub> emissions in tree ring measurements. On a global scale, e.g. Stuiver and Quay (1981) found good agreement between tree-ring derived  $\Delta^{14}\text{CO}_2$  data between 1820 and 1954 and predictions by a global box-diffusion model – taking into account natural variations in radiocarbon production and estimated FFCO<sub>2</sub> release in this time. They found industrial FFCO<sub>2</sub> emissions to be responsible for 85 % of the observed decrease in  $\Delta^{14}\text{CO}_2$ . Levin et al. (1989) developed a method to resolve regional FFCO<sub>2</sub> offsets relative to a continental background site. They found the FFCO<sub>2</sub> concentrations at the rural Schauinsland station and the urban station in Heidelberg comparing well in the yearly mean to the expected concentrations derived from emission inventories, but showing a more distinct seasonality.

## 1. Basics

In principle, the concentration of the regional FFCO<sub>2</sub> component is calculated by combining two balance equations for the CO<sub>2</sub> concentration  $c$  and the corresponding  $\Delta^{14}\text{C}$  values:

$$c_{meas} = c_{bg} + c_{bio} + c_{foss} \quad (1.16)$$

$$\begin{aligned} c_{meas}(\Delta^{14}\text{C}_{meas} + 1000 \text{‰}) &= c_{bg}(\Delta^{14}\text{C}_{bg} + 1000 \text{‰}) \\ &+ c_{bio}(\Delta^{14}\text{C}_{bio} + 1000 \text{‰}) \\ &+ c_{foss}(\Delta^{14}\text{C}_{foss} + 1000 \text{‰}), \end{aligned} \quad (1.17)$$

where *meas* indicates the measured quantities at the station and *bg* the corresponding background measurements e.g. at a continental background station. Various approaches have been made or are in preparation to yield the appropriate background for a station; this will be discussed below. *bio* marks the regional biogenic CO<sub>2</sub> and *foss* the FFCO<sub>2</sub> component.

Following Levin et al. (2003), we set  $\Delta^{14}\text{C}_{foss} = -1000 \text{‰}$ , since the FFCO<sub>2</sub> component is free of <sup>14</sup>C. Furthermore, the <sup>14</sup>C signature of the biosphere is assumed to be close to the background:

$$\Delta^{14}\text{C}_{bio} = \Delta^{14}\text{C}_{bg} \quad (1.18)$$

I will address the implications of this approximation later in this section. With these assumptions we can solve equations (1.16) and (1.17) to

$$c_{foss} = c_{meas} \frac{\Delta^{14}\text{C}_{bg} - \Delta^{14}\text{C}_{meas}}{\Delta^{14}\text{C}_{bg} + 1000 \text{‰}}. \quad (1.19)$$

The corresponding measurement induced variance  $\sigma(c_{foss})^2$  in the calculation is described by

$$\begin{aligned} \sigma(c_{foss})^2 &= \left( \sigma(c_{meas}) \left( 1 - \frac{\Delta^{14}\text{C}_{meas} + 1000 \text{‰}}{\Delta^{14}\text{C}_{bg} + 1000 \text{‰}} \right) \right)^2 + \left( c_{meas} \left( \frac{\sigma(\Delta^{14}\text{C}_{meas})}{\Delta^{14}\text{C}_{bg} + 1000 \text{‰}} \right) \right)^2 \\ &+ \left( c_{meas} \left( \frac{(\Delta^{14}\text{C}_{meas} + 1000 \text{‰}) \cdot \sigma(\Delta^{14}\text{C}_{bg})}{(\Delta^{14}\text{C}_{bg} + 1000 \text{‰})^2} \right) \right)^2 \end{aligned} \quad (1.20)$$

assuming Gaussian uncertainty. When we assume the measurement uncertainty for radiocarbon ratios to be the same for background and station samples

$$\sigma(\Delta^{14}\text{C}_{meas}) = \sigma(\Delta^{14}\text{C}_{bg}) = \sigma(\Delta^{14}\text{C})$$

and the relative error of the concentration measurement much smaller than the uncertainty in radiocarbon measurements

$$\frac{\sigma(c)}{c} \ll \frac{\sigma(\Delta^{14}\text{C})}{\Delta^{14}\text{C} + 1000 \text{‰}},$$

we can simplify (1.20) to the measurement uncertainty for the FFCO<sub>2</sub> component

$$\sigma(c_{foss}) = \frac{c_{meas}\sigma(\Delta^{14}C)}{(\Delta^{14}C_{bg} + 1000 \text{‰})^2} \sqrt{(\Delta^{14}C_{bg} + 1000 \text{‰})^2 + (\Delta^{14}C_{meas} + 1000 \text{‰})^2}. \quad (1.21)$$

For recent atmospheric radiocarbon ratios and CO<sub>2</sub> concentrations (1.21) leads to  $\approx 0.6 \text{ ppm } \text{‰}^{-1}$  uncertainty on the calculated concentration of FFCO<sub>2</sub> due to  $\Delta^{14}C$  measurement uncertainty. This highlights the necessity for precise radiocarbon measurements with precisions  $< 2 \text{‰}$  for the ICOS network, since rural stations show typical FFCO<sub>2</sub> surpluses of 1 ppm to 2 ppm; e.g. Levin et al. (2008) presented a long term FFCO<sub>2</sub> excess of  $(1.31 \pm 0.09) \text{ ppm}$  for the Schauinsland station in the black forest region.

### 1.3.1. Effect of the biogenic <sup>14</sup>C signature

For (1.19)  $\Delta^{14}C_{bio}$  has been set equal to  $\Delta^{14}C_{bg}$ . Without using approximation (1.18) equation (1.19) becomes

$$c_{foss} = \frac{c_{bg}(\Delta^{14}C_{bg} - \Delta^{14}C_{bio}) - c_{meas}(\Delta^{14}C_{meas} - \Delta^{14}C_{bio})}{\Delta^{14}C_{bio} + 1000 \text{‰}} \quad (1.22)$$

$\Delta^{14}C_{bio}$  has been estimated using model calculations by Naegler (2005) of biogenic heterotrophic respiration in the mid latitudes of the northern hemisphere. In Heidelberg heterotrophic respiration accounts only for one half of the biogenic CO<sub>2</sub> component, the other half is caused by autotrophic respiration, whose radiocarbon signature can be approximated by  $\Delta^{14}C_{bg}$ . For Heidelberg, these calculations lead to the result that equation (1.19) underestimates the FFCO<sub>2</sub> component on average by 0.17 ppm in the period from 1996-2006 (Levin et al., 2008).

### 1.3.2. Applications of <sup>14</sup>CO<sub>2</sub> measurements for FFCO<sub>2</sub> estimation

Levin et al. (2011) presented an application of (1.19) on the long time measurement series of  $\Delta^{14}C$  in the catchment area of Heidelberg and the high-alpine station Jungfraujoch in the Alps, that has been used as background in this comparison. Using the differences of the monthly means of the biweekly sampled integrated night-time  $\Delta^{14}C$  from the Heidelberg station and smoothed background  $\Delta^{14}C$  values leads to an monthly averaged FFCO<sub>2</sub> offset. This method allows to estimate long term changes in the averaged FFCO<sub>2</sub> offset (see Levin and Rödenbeck, 2008).

There are a number of other applications of this top-down method for quantifying FFCO<sub>2</sub> offsets on different locations. Turnbull et al. (2015a) used 12 tower locations inside and outside the urban area of Indianapolis, USA, to collect samples of air parcels before and after passing the urban area and therefore to directly measure the FFCO<sub>2</sub> enhancement by the city. They compared these results to those derived by using a continental background station for supplying  $\Delta^{14}C_{bg}$ .

## 1. Basics

A similar approach is currently under development in the RINGO project, I mentioned in Section 1.1.1, for investigating the Rhein-Neckar metropolitan area and especially the city of Mannheim, using two stations in upwind and downwind direction of the main emitters.

Graven et al. (2009) investigated the use of  $\Delta^{14}\text{C}$  for the estimation of FFCO<sub>2</sub> in airborne measurements. They could resolve patterns of CO<sub>2</sub> source components in the planetary boundary layer and showed that campaigns of this type could be used to enhance the knowledge of vertical mixing of surface fluxes, that is used in atmospheric modelling.

### 1.4. <sup>14</sup>CO<sub>2</sub> analysis by accelerator mass spectrometry

As mentioned in Section 1.2, the traditional method of radiocarbon dating is LLC analysis of the decay products. Since the ratio  $\frac{^{14}\text{C}}{\text{C}}$  lies for modern atmospheric samples in the order of  $10^{-12}$ , large sample amounts are needed to provide sufficient counting statistic in a time-frame of days. E.g. the integrated samples at the Heidelberg station consist typically of  $\approx 16$  g CO<sub>2</sub> and are measured for 3 d to 4 d to achieve a Poisson uncertainty of about 2 ‰.

In AMS analysis, in contrast, isotope counts and consequently  $\frac{^{14}\text{C}}{^{12}\text{C}}$  ratios are measured directly, which causes a massive reduction of the required sample amount to typically 0.5 mg to 2 mg of carbon corresponding to 1.8 mg to 7.3 mg of CO<sub>2</sub>. The measurement time to achieve less than 2 ‰ uncertainty is reduced as well to less than 2 h from several days counting time in LLC analysis.

#### 1.4.1. Performing measurements with MICADAS

All AMS targets in this work have been analysed using the Mini-Radiocarbon Dating System (MICADAS) at the Curt-Engelhorn-Centre for Archaeometry (Curt-Engelhorn-Zentrum für Archäometrie – CEZ) in Mannheim (see Kromer et al., 2013). The concept of this low-energy accelerator dating system has been described by Synal et al. (2004); Synal et al. (2007) give a comprehensive description of the technical details of the system, while Wacker et al. (2010a) give an overview over the machine performance. Here we focus on outlining the essential technical aspects of the used AMS.

With the progress in AMS measurement techniques it became possible to lower the AMS operation voltage from 500 kV to less than 200 kV. The lower beam energy allowed the construction of more compact tabletop systems like MICADAS. Figure 1.4 shows the accelerator layout with the essential functional components. Following procedure steps are taken between target insertion and <sup>14</sup>C detection:

**Target insertion** into the ion source is done automatically. A linear magazine – holding up to 39 graphite targets – is located outside the ion source box in an evacuated chamber, from where a mechanism transfers single target cathodes into the sputtering position in the ion source.

## 1.4. $^{14}\text{CO}_2$ analysis by accelerator mass spectrometry

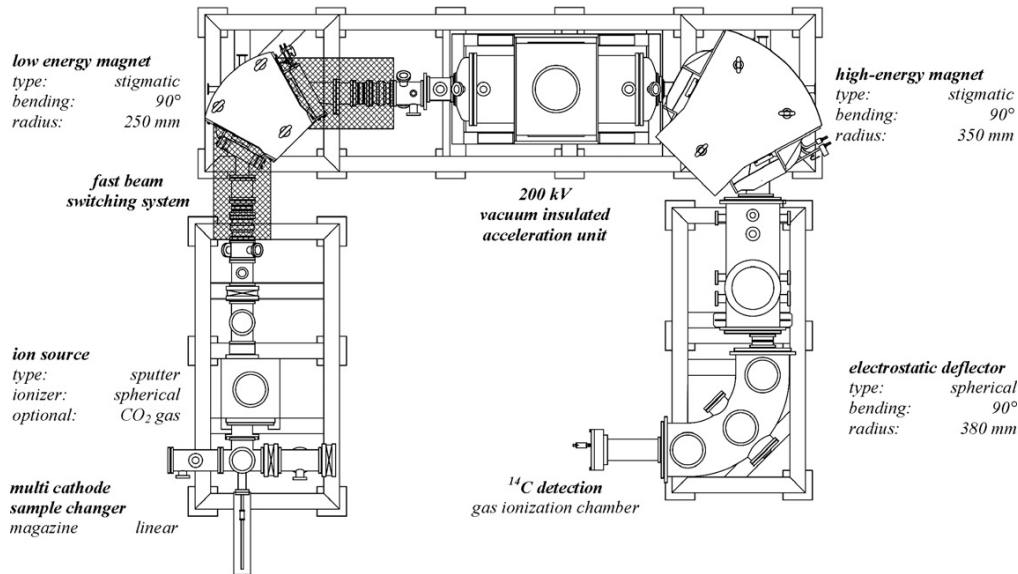


Figure 1.4.: Schematic picture of the Mini-Radiocarbon Dating System (MICADAS). The linear target magazine (current size: 39) is inserted at the bottom left side. Picture taken from Synal et al. (2007)

**Target sputtering** is performed by a 5 keV to 12 keV  $\text{Cs}^+$  beam. A spherical ionizer and two lenses are used to focus the sputtering stream onto the target. Sputtered ions from the target (e.g.  $\text{C}^-$ ) are extracted and accelerated to up to 40 keV, leading to typical negative ion currents of 30  $\mu\text{A}$  to 50  $\mu\text{A}$ .

**Low energy mass spectrometry** is implemented using a dipole magnet on the low energy side for mass separation. An off-set Faraday cup is placed in the image plane of the magnet to measure the negative ion current from the source. The abundant isotope  $^{12}\text{C}$  is not measured here, but detected at the high-energy mass spectrometer, since this has been proven before to be advantageous for measurement precision (e.g. Suter et al., 1984). A fast beam pulsing system injects short isotope beams of  $^{12}\text{C}$  (50  $\mu\text{s}$ ),  $^{13}\text{C}$  (500  $\mu\text{s}$ ) and  $^{14}\text{C}$  (40 ms) using electrostatic lenses.

**Ion acceleration and molecule destruction** is performed in the acceleration unit. The ions are accelerated by a terminal voltage of 200 kV. Within the acceleration unit a permanent stripper gas pressure of  $1 \times 10^{-5}$  mbar is maintained to change the injected negative ions into positive ions. Furthermore, molecules are destroyed, that passed through the low energy mass spectrometer; e.g.  $^{13}\text{CH}^-$  molecules are injected together with  $^{14}\text{C}$ . Currently,  $\text{N}_2$  is used as stripper gas, but there are plans to implement a He stripping system at the CEZ-AMS, which would probably increase the ion transmission rate and reduce scattering losses.

## 1. Basics

**High energy mass spectrometry** follows the acceleration. A stigmatic magnet performs separation regarding particle charge and impulse ( $p/q$  separation); Faraday cups on the focal plane of this magnet are measuring currents of the stable carbon isotopes  $^{12}\text{C}$  and  $^{13}\text{C}$  as well as the fragments of  $^{13}\text{CH}^-$  molecules, destroyed by collisions with the stripper gas. “Molecule currents” presented in this work have been measured here.

**$^{14}\text{C}$  detection** is the final step in the isotope ratio determination.  $^{14}\text{C}$  ions are identified in a gas ionisation chamber using isobutane as detector gas. An  $^{14}\text{C}$  ion deposits a total energy of 428 keV in the detector, which is used for particle identification.

### 1.4.2. Measurement evaluation

The evaluation of the measured AMS targets and the reduction of the data produced during analysis has been performed using the software BATS, that has been described in detail by Wacker et al. (2010b). The principles of  $\Delta^{14}\text{C}$  calculation are described in Section 1.2; here I give an overview about the formalisms, that are used by BATS to utilise the MICADAS measurement data.

Initially, the raw isotope ratios  $R = \frac{^{14}\text{C}}{^{12}\text{C}}$  and  $\frac{^{13}\text{C}}{^{12}\text{C}}$  are calculated. As described above, the stable isotopes are measured quasi-simultaneously with  $^{14}\text{C}$  as ion currents  $I_x$  in Faraday cups. Stable isotope counts are therefore calculated using

$${}^x\text{C} = I_x \cdot T_{14}/e \quad (1.23)$$

with the measurement time  $T_{14}$  for  $^{14}\text{C}$  and the elementary charge  $e$ .

#### 1.4.2.1. Correction of systematic effects

Three types of systematic effects can be manually addressed on single measurement level in BATS before calculating sample and standard means:

- Influence of beam current variations on measured isotopic ratios.
- Drifts in measured isotopic ratios depending on time.
- Disturbances in the background measurement (by blank samples) due to misidentified events, that can result e.g. by break-up of molecules.

All AMS measurements carried out for this work were systematically evaluated at the CEZ regarding to the first point in the list above. For every magazine a linear function has been set up to correct the raw isotopic ratio of each measurement:

$$\left(\frac{^{14}\text{C}}{^{12}\text{C}}\right)_{\text{curr. corr.}} = \left(\frac{^{14}\text{C}}{^{12}\text{C}}\right) (1 - c_I \cdot (I - I_0)) \quad (1.24)$$

#### 1.4. $^{14}\text{CO}_2$ analysis by accelerator mass spectrometry

with the high energy  $^{12}\text{C}$  current  $I$ , a current offset  $I_0$  (set to  $5\ \mu\text{A}$ ) and the correction factor  $c_I$ .  $c_I$  is determined by minimising the slope of standard target measurements'  $\left(\frac{^{14}\text{C}}{^{12}\text{C}}\right)_{\text{std},\text{curr},\text{corr}}$  depending on  $I$ . Following this,  $c_I$  is applied on all measurements of the same magazine. Typically  $c_I$  is  $1\ \text{‰}\ \mu\text{A}^{-1}$ .

##### 1.4.2.2. Background correction

An empirical molecule correction is applied to all measured ratios  $R$ , since background count rates show a linear relationship to measured molecule counts  $^{13}\text{C}_{\text{mol}}$ :

$$R_{\text{mol}} = \frac{^{14}\text{C} - k_{\text{mol}}^{13}\text{C}_{\text{mol}}}{^{12}\text{C}} \quad (1.25)$$

with  $k_{\text{mol}}$  as a constant experimentally determined factor. This correction is typically small. The molecule current correction is then complemented by a blank target correction following (1.3); subtracting the mean blank target ratio from all other targets:  $R_{\text{mol},\text{bl}} = R_{\text{mol}} - \langle R_{\text{mol}}(\text{bl}) \rangle$ .

##### 1.4.2.3. Fractionation correction

Every single background corrected measurement is then analysed for  $\delta^{13}\text{C}$  using the mean ratio  $\left\langle \frac{^{13}\text{C}}{^{12}\text{C}}(\text{std}) \right\rangle$  of the standard targets as  $\delta^{13}\text{C}$  standard. With the  $\delta^{13}\text{C}$  of every single measurement a normalisation to  $-25\ \text{‰}$  is carried out, correcting  $R_{\text{mol},\text{bl}}$  for fractionation processes occurring with an exponent of  $b = 2$  on the  $^{13}\text{C}$  fractionation factor (see Section 1.2.2.2) and thus leading to a normalised ratio  $R_{\text{mol},\text{bl},\text{norm}}$ .

##### 1.4.2.4. Calibration

For calibration, the weighted mean of all normalised and corrected standard measurements is calculated:  $\langle R_{\text{mol},\text{bl},\text{norm}}(\text{std}) \rangle$ . Following this, all sample ratios can be calibrated for the nominal value of the standard targets ( $R_{\text{nom}}(\text{std})$ ):

$$R_{\text{mol},\text{bl},\text{norm},\text{std}} = \frac{R_{\text{nom}}(\text{std})}{\langle R_{\text{mol},\text{bl},\text{norm}}(\text{std}) \rangle} R_{\text{mol},\text{bl},\text{norm}} \quad (1.26)$$

As final step, the weighted mean of the single measurements of every target is calculated:  $\langle R_{\text{mol},\text{bl},\text{norm},\text{std}} \rangle$ . This value can then be utilised to express the measurement results in  $\Delta$ -notation, following (1.14).

##### 1.4.2.5. Determination of the uncertainties

To every result  $R_{\text{mol},\text{bl},\text{norm},\text{std}}$  a measurement uncertainty  $\sigma(R_{\text{mol},\text{bl},\text{norm},\text{std}})$  is assigned. In summary, BATS accounts for uncertainties in

## 1. Basics

**Counting statistics:** In most cases the Poisson uncertainty of the counting statistics ( $\sigma_{poiss} = \sqrt{^{14}\text{C}}$ ) is the dominant part in the resulting uncertainty of the radiocarbon ratio measurement  $\sigma(R_{mol,bl,norm,std})$ .

**Standard mean:**  $\sigma(\langle R_{mol,bl,norm}(std) \rangle)$  is the statistical uncertainty in the mean value of the standard targets. In general, a higher standard target count  $n$  leads to a more precise determination of  $\langle R_{mol,bl,norm}(std) \rangle$ , since the mean error decreases with  $1/\sqrt{n}$ .

**Molecule current correction:** This accounts for errors in the molecule current correction factor  $k_{mol}$ , that propagates with  $\sigma(k_{mol}) \cdot ^{13}\text{C}$

**Blank measurements:** This error contribution is calculated as the scatter of blank targets:  $\sigma(R_{mol}(bl))$ . It accounts for the variability in blank contamination of the samples; more than one blank target has to be measured in the magazine to consider for this error.

**Nominal standard value:**  $\sigma(R_{nom})$  is the uncertainty of the nominal standard value  $R_{nom}$ .

**External interference:** This contribution covers additional errors  $\sigma_{ex}$  (e.g. machine instabilities or differences in target preparation). Per default, it is estimated from the scatter of individual standard target ratios  $R_{mol,bl,norm,std}(std)$  around their common mean. More standard targets in a magazine lead to a better estimation of  $\sigma_{ex}$ .

In BATS Gaussian error propagation is assumed; the related formulas can be reviewed in Wacker et al. (2010b). For the total error  $\sigma(R_{mol,bl,norm,std})$  therefore the contributions are added quadratically; that leads to

$$\sigma(R_{mol,bl,norm,std}) = \langle R_{mol,bl,norm,std} \rangle \cdot \sqrt{\left(\frac{\sigma_{poiss,bl,mol,ex}}{\langle R_{mol,bl,norm} \rangle}\right)^2 + \left(\frac{\sigma(\langle R_{mol,bl,norm}(std) \rangle)}{\langle R_{mol,bl,norm}(std) \rangle}\right)^2 + \left(\frac{\sigma(R_{nom})}{R_{nom}}\right)^2}, \quad (1.27)$$

where  $\sigma_{poiss,bl,mol,ex}$  contains the errors for counting statistics, molecule current correction, blank variability and external interference.

### 1.4.3. The graphitisation reaction

The design of the MICADAS as well as the majority of current AMS devices for radiocarbon analysis require solid carbon in graphite form for high-precision measurements. The process to reduce  $\text{CO}_2$  to graphite can be simplified described by a Bosch reaction



which can be catalysed by e.g. iron or cobalt. This balanced equation is, however, the product of a large number of different reactions occurring simultaneously in the graphitisation reactor. In the following, I will give an overview about the chemical details of the graphitisation.

A number of publications cover this topic with different intentions: McNichol et al. (1992) studied the composition of the gas phases during graphitisation using an in-line gas chromatograph. They examined changes in catalyst, hydrogen amount and reaction temperature. Němec et al. (2010) focus on optimising the graphitisation parameters for the recently developed Automated Graphitisation Equipment (AGE) system (Wacker et al., 2010c) in consideration of the theoretically expected chemical reactions. Gudenau et al. (2005) approach the topic from the other side, that means in research of efficient ways to reduce iron oxides to pure iron using carbon as reduction agent; the chemical processes, however, are the same as for the graphitisation process in AMS target preparation.

Here I focus on reactions involving iron as catalyst at temperatures between  $400\text{ }^\circ\text{C}$  to  $650\text{ }^\circ\text{C}$ , since most labs operate in this range (Turnbull et al., 2010b). The following reactions take place in a  $\text{H}_2/\text{H}_2\text{O}$  atmosphere between the gases and iron and its oxides hematite ( $\text{Fe}_2\text{O}_3$ ), magnetite ( $\text{Fe}_3\text{O}_4$ ) and wustite ( $\text{FeO}$ ):



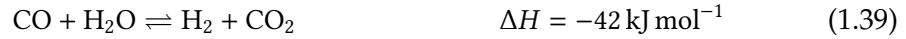
Reaction (1.32) only takes place below  $570\text{ }^\circ\text{C}$ , since the wustite phase does not occur there. Equivalently to (1.29-1.32) the following reactions occur in a  $\text{CO}/\text{CO}_2$  atmosphere:



The reaction enthalpies  $\Delta H$  indicate, if the reaction is occurring exothermically ( $\Delta H < 0$ ) or endothermically ( $\Delta H > 0$ ) and, thus, the temperature dependency of these reactions. Figure 1.5 shows a combination of the Baur-Glaessner diagrams for the reactions (1.29-1.36). It shows the fractions of  $\text{CO}/\text{CO}_2$  resp.  $\text{H}_2/\text{H}_2\text{O}$  in the gas phase over iron and its oxides depending on the temperature.

## 1. Basics

The activities of  $H_2$ ,  $CO$  and  $CO_2$  are coupled according to the water gas reduction, which can take place in different forms:



The reactions (1.37) and (1.39) slide to the side of  $CO$  for higher temperatures.

Between graphite,  $CO$  and  $CO_2$  the Boudouard-reaction takes place, that is endothermic and also highly dependent on temperature:



Simultaneously, methane production is occurring, which is generally unwanted in graphitisation and taking place exothermically and therefore decreasing with temperature:



Figure 1.6 shows the temperature dependency of the water gas, Boudouard and methanisation reactions. Generally, we see an increase in  $CO$  and an decrease in

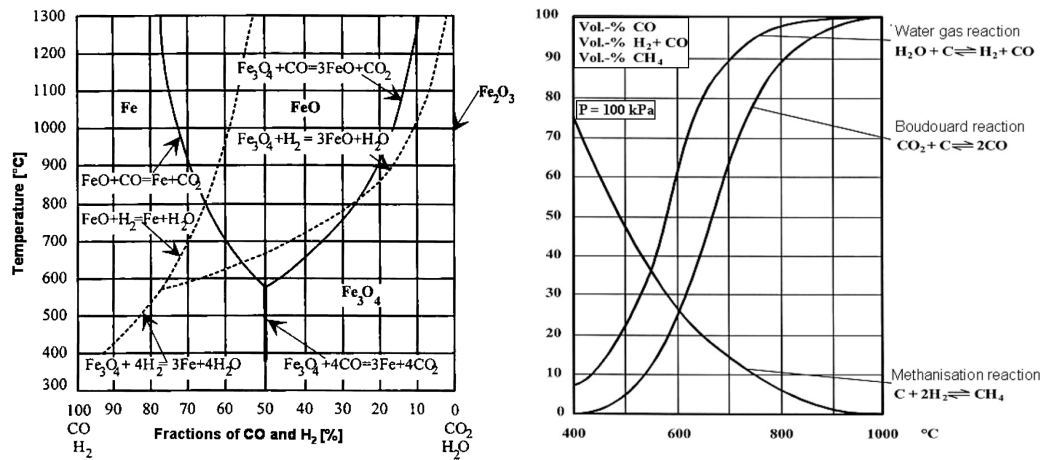


Figure 1.5.: Baur-Glaessner diagrams for the reactions between iron, carbon and hydrogen compounds. Picture from Gudenau et al. (2005).

Figure 1.6.: Equilibria and temperature dependency of the water gas reaction. Picture from Gudenau et al. (2005).

$CH_4$  production with temperature. The first attempt in optimising the reaction temperature would be, to choose the temperature on the intercept point of the

boudouard and the methanisation curve, to minimise CO as well as  $\text{CH}_4$  end products, i.e. at  $\approx 600^\circ\text{C}$ .

Furthermore, considering the reactions containing  $\text{H}_2$  and  $\text{H}_2\text{O}$ , the reaction products can be pushed in direction of reduced carbon compounds by removing the water from the reactor and adding more  $\text{H}_2$ . The drawback in addition of too much hydrogen, however, is the enforcing of additional methane production, following the reactions (1.41) and (1.42).

In real reactors the desired reaction conditions (e.g. homogeneous temperature) can hardly be achieved. For every graphitisation line therefore an optimised set of parameters has to be figured out. McNichol et al. (1992) performed an in-line measurement of reaction gas components during graphitisation for different temperatures, shown in Figure 1.7. Here we see in the first place the order of product

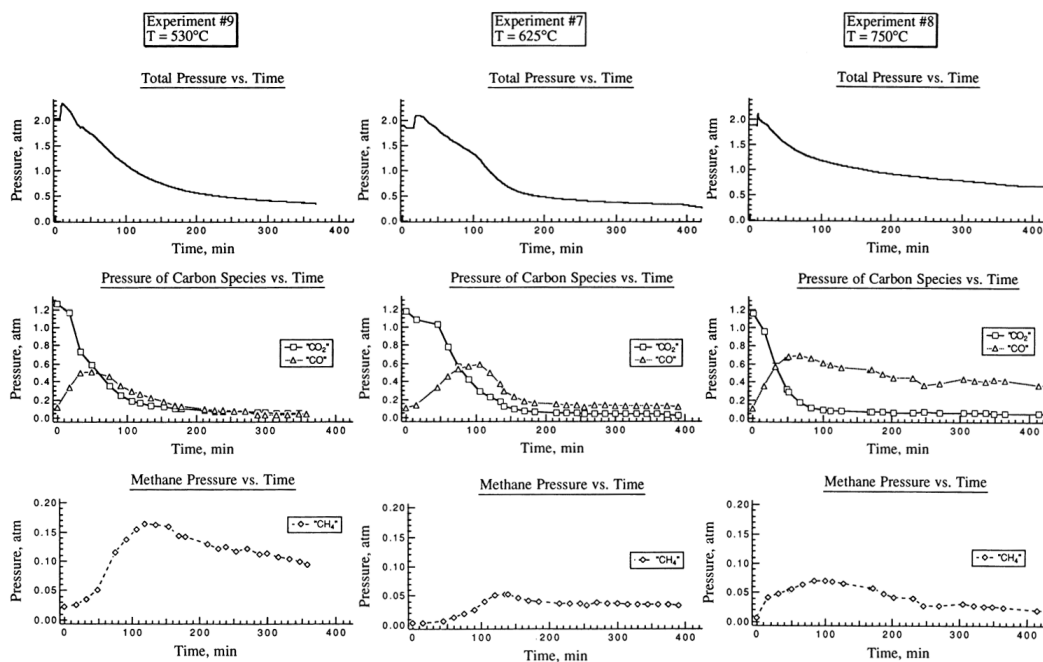


Figure 1.7.: Changes in total,  $\text{CO}_2$ ,  $\text{CO}$  and  $\text{CH}_4$  pressure during graphitisation using different reaction temperatures; measured utilising an in-line gas chromatograph. Experiments performed by McNichol et al. (1992).

genesis, that means first  $\text{CO}_2$  is reduced to  $\text{CO}$ , which then is further processed until a temperature dependent end pressure is reached. As expected from the theoretical considerations above, the  $\text{CO}$  end pressure increases with temperature and  $\text{CH}_4$  production decreases between temperatures of  $530^\circ\text{C}$  to  $625^\circ\text{C}$ , but show no further decrease at higher temperatures.

## 1. Basics

### 1.4.3.1. Catalyst pretreatment

Typically iron is used as catalyst for graphitisation (Turnbull et al., 2010b), but the type of iron as well as the pretreatment methods differ widely. Most labs are using elementary iron that is reduced in a hydrogen atmosphere according to the reactions (1.29-1.32). Some labs oxidise the iron surface prior to hydrogen induced reduction, in order to oxidise and therefore remove contaminations with organic carbon, though this approach can lead to sintering of the iron. E.g. Turnbull et al. (2015b) starts with magnetite powder, that is reduced afterwards.

Similar to the situation for the graphitisation parameters, there exist no canonical pretreatment “recepte”. Therefore, in this work a large number of tests to work out the optimal parameters for the graphitisation in the EGL have been performed.

## 1.5. Modelling principles & methods

As explained before, understanding of the sources and sinks of radiatively active trace gases in the atmosphere is essential for quantifying the human impact on the climate (e.g. Mooney et al., 1987). Observational networks like ICOS provide data on atmospheric concentrations with high temporal and increasingly dense spatial resolution (ICOS RI, 2017b).  $\Delta^{14}\text{C}$  measurements, however, are still limited in their ability to cover high temporal resolutions, due to the high effort, that has to be made to achieve atmospheric  $\Delta^{14}\text{C}$  values with a precision of  $\approx 2\text{‰}$ . Therefore, I examined a new sampling method, set-up in a model framework, that specifically targets regions with high FFCO<sub>2</sub> emissions and parallel corresponding background regions, to enhance the resulting  $\Delta^{14}\text{C}$  difference and hence the amount of information on the target region’s FFCO<sub>2</sub> emissions retrieved from a small number of measurements by enhancing the signal to noise ratio (section 4.2).

CO<sub>2</sub> concentrations in the Planetary Boundary Layer (PBL), where most of our measurements take place, are sensitive to surface fluxes. Nevertheless, the impact of these fluxes is heavily influenced by atmospheric transport. Since the globally averaged ventilation time for the PBL is about four days, one can estimate the length scale for the relevant transport processes and hence the size of the area influencing the observations to 100 km to 1000 km. Thus, in order to resolve FFCO<sub>2</sub> sources in this area, one has to model atmospheric transport as accurately as possible (Lin et al., 2003). This section addresses the basics of atmospheric modelling and introduces the model systems used in the present thesis.

### 1.5.1. Mixing processes in the planetary boundary layer

Near field atmospheric transport models need to account for mixing and transport processes in the PBL. Stull (2012) defines these lowest 100 m to 3000 m of the atmosphere as follows:

We can define the boundary layer as that part of the troposphere that is directly influenced by the presence of the earth's surface, and responds to surface forcings with a timescale of about an hour or less.

These forcings include for example frictional drag, evaporation, transpiration, heat transfer, terrain induced flow modification and emission of pollutants.

In principle, air flow can be divided into three categories: mean wind, turbulence and waves. Each of these exists in the boundary layer. Mean wind is responsible for horizontal transport or advection; the wind speed usually slows down heavily near the ground towards the surface layer. Waves usually transport not much heat, humidity or particles, but are effective in transporting momentum and energy. The main source of vertical transport are turbulent processes. Turbulence can be visualised as irregular swirls of motion, which are called eddies. Usually the turbulence builds up from many differently scaled eddies, superimposed on each other. The largest eddies in the PBL can scale up to the height of the PBL. To adequately represent this turbulent vertical transport is one of the major challenges of current highly resolving atmospheric models.

Since in the PBL the main interference of surface and atmosphere takes place, its structure and depth is highly dependent on surface properties and varies in a wide range. Over land surfaces in high pressure regions the PBL has a defined structure, which evolves with the diurnal cycle (see Figure 1.8). The surface layer

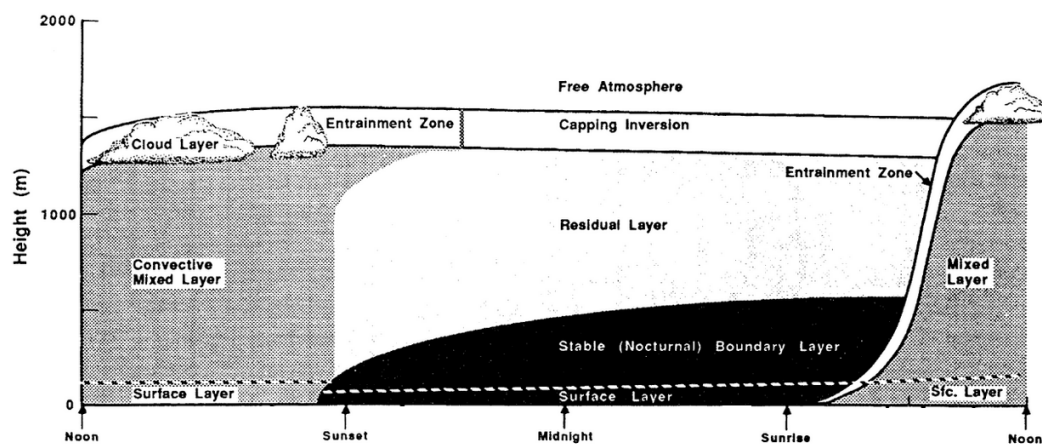


**Figure 1.8.:** The PBL in high pressure regions. One can differentiate three main parts: A turbulent mixed layer at day-time, a less turbulent residual layer that contains the air from the former mixed layer and a stable boundary layer at night. Picture from Stull (2012).

represents the region on the bottom of the PBL, where turbulent fluxes and stress vary by less than 10 % of their magnitude. The mixed layer builds up on day-time; it's turbulence is usually convectively driven. Current atmospheric models are able to represent this well mixed layer well (Trusilova et al., 2010), which leads

## 1. Basics

to favouring of day-time over night-time sampling serving for inverse modelling (see Section 1.5.2). When approaching sunset, thermal convection starts to diminish and turbulences decay. This leads in first place to a layer of air, containing the properties and concentrations of the formerly mixed layer, which is therefore called residual layer. During the night, a stable boundary layer forms from the ground upwards. Other than the diurnal mixed layer, the stable boundary layer has no clearly defined top and transitions smoothly into the residual layer on top (Stull, 2012). Especially important for atmospheric trace gas measurements is the fact, that any surface emissions at day-time are mixed into a larger volume than at night-time, what leads to an higher sensitivity for regional surface fluxes at night.

### 1.5.2. Theoretical background of inverse modelling

The general problem is to estimate surface fluxes from ambient measurements of GHG concentrations. This means, in principle, to go back from the effect to the cause; an approach known as *Inverse Problem*. The general inverse problem can be addressed by setting up and solving a set of equations (linear or non-linear) while considering uncertainties in some of the parameters (e.g. measurement errors). The considerations outlined in this section can be studied in more detail in Rodgers (2000).

#### 1.5.2.1. Formulation of the problem

We start with the most general expression of the problem:

$$\vec{y} = \vec{F}(\vec{x}) + \vec{\epsilon} \quad (1.43)$$

The finite number ( $m$ ) of quantities that are measured ( $y_1, y_2, \dots, y_m$ ) can be represented by the measurement vector  $\vec{y}$ , whilst the related errors form the vector of errors  $\vec{\epsilon}$ .  $\vec{F}$  is called the *forward model*, which maps the state of the system to the measurement space. The state of the system – the element aimed to be retrieved – is represented by a *state vector*  $\vec{x}$ . In general the dimension  $n$  of  $\vec{x}$ , that means the number of states needed to describe the system ( $x_1, x_2, \dots, x_n$ ), is infinite, since nature is not discretised.

#### 1.5.2.2. Linear problem with Gaussian uncertainties

To handle this problem, several assumptions have to be made. First, it is considered a linear problem, in order that we can write

$$\vec{y} = \vec{F}(\vec{x}) + \vec{\epsilon} = \mathbf{F}\vec{x} + \vec{\epsilon} \quad (1.44)$$

with  $\mathbf{F}$  being a  $m \times n$ -matrix performing the linear mapping. Secondly we assume all uncertainties to be Gaussian. This assumption is suitable for measurement uncertainties but is maybe not suitable for other types of errors.

**Describing errors with probability density functions** The probability density function (pdf)  $P(y)$  of a measurement with a value  $\bar{y}$  and Gaussian error  $\sigma$  can be written as

$$P(y) = \frac{1}{(2\pi)^{1/2}\sigma} \exp\left(-\frac{(y - \bar{y})^2}{2\sigma^2}\right). \quad (1.45)$$

When the measured quantity is a vector, the pdf in equation (1.45) takes the form

$$P(\vec{y}) = \frac{1}{(2\pi)^{n/2}|\mathbf{S}_y|^{1/2}} \exp\left(-\frac{1}{2}(\vec{y} - \vec{\bar{y}})^T \mathbf{S}_y^{-1}(\vec{y} - \vec{\bar{y}})\right), \quad (1.46)$$

where  $\mathbf{S}_y$  is the error covariance matrix of  $\vec{y}$ . The diagonal elements of  $\mathbf{S}_y$  are the variances of the  $y_i$ .

**Applying Bayes' theorem** After introducing the formalism of pdfs let's now define several more special pdfs suitable for the given problem:

$P(\vec{x})$  is the prior pdf of  $\vec{x}$ . This term expresses the knowledge about  $\vec{x}$  before the measurement.

$P(\vec{y})$  is the pdf of the measurement vector  $\vec{y}$ , before it is made. Since it is not dependent on  $\vec{x}$ , it stays constant during parameter estimation.

$P(\vec{y}|\vec{x})$  is the conditional pdf of  $\vec{y}$  under the condition that  $\vec{x}$  happened; that means with a given state  $\vec{x}$

$P(\vec{x}|\vec{y})$  is the quantity of interest when solving the inverse problem. It is the pdf of  $\vec{x}$  under the condition of the pdf of the measurement – a given  $\vec{y}$ .

*Bayes' Theorem* expresses the general relationship between two conditional pdfs:

$$P(\vec{x}|\vec{y}) = \frac{P(\vec{y}|\vec{x})P(\vec{x})}{P(\vec{y})} \quad (1.47)$$

This term gives us a formalism for calculating the posterior pdf of  $\vec{x}$  by using a measurement pdf.

**Retrieving of the state vector** Assuming Gaussian errors we can express  $P(\vec{y}|\vec{x})$  with (1.44) and (1.46) as

$$-2 \ln P(\vec{y}|\vec{x}) = (\vec{y} - \mathbf{F}\vec{x})^T \mathbf{S}_e^{-1}(\vec{y} - \mathbf{F}\vec{x}) + c_1 \quad (1.48)$$

and, analogously,  $P(\vec{x})$  as

$$-2 \ln P(\vec{x}) = (\vec{x} - \vec{x}_a)^T \mathbf{S}_a^{-1}(\vec{x} - \vec{x}_a) + c_2. \quad (1.49)$$

## 1. Basics

$c_1$  and  $c_2$  are constants,  $S_\epsilon$  and  $S_a$  are the error covariance matrices of the measurement  $\vec{y}$  resp. the a priori state  $\vec{x}_a$ . Substituting the equations above in (1.47) and doing some algebra gives us the best estimate of  $\vec{x}$  – the expected value  $\hat{\vec{x}}$ :

$$\hat{\vec{x}} = \vec{x}_a + S_a \mathbf{F}^T (\mathbf{F} S_a \mathbf{F}^T + S_\epsilon)^{-1} (\vec{y} - \mathbf{F} \vec{x}_a) \quad (1.50)$$

The corresponding error covariance matrix can be described as follows (Thompson et al., 2011; Tarantola, 2005):

$$\hat{S} = S_a - S_a \mathbf{F}^T (\mathbf{F} S_a \mathbf{F}^T + S_\epsilon)^{-1} \mathbf{F} S_a \quad (1.51)$$

The equations (1.50) and (1.51) are used as computational backbone in Section 4.2 to estimate the impact of the proposed new sampling system on future inverse modelling attempts made with real world measurement data. The effect of different sampling approaches on sampled FFCO<sub>2</sub> concentration is estimated using equation 1.44 with a linear mapping function  $\mathbf{F}$  (see Section 1.5.3.2) and different emission inventories  $\vec{x}$  (section 1.5.4).

### 1.5.3. Model systems

In this section, I will give an short overview of the model systems used. Since this work focuses not on model development, but on the usage of model results for sampling methods development, I refer to the cited publications for detailed derivations of the related mathematics.

#### 1.5.3.1. Modelling particle trajectories with HYSPLIT\_4

The HYSPLIT\_4 (HYbrid Single-Particle Lagrangian Integrated Trajectory) model was used in this study to calculate particle trajectory forecasts. Draxler and Hess (1998) describe the model in detail and give an overview about the underlying equations. HYSPLIT\_4 is – beside particle trajectory calculation – capable of calculating air concentrations for analytical studies and supporting atmospheric emergency response applications. In the following we focus on the usage of HYSPLIT\_4 for trajectory calculation.

In principle, atmospheric dispersion modelling is divided into two categories: Eulerian models, that calculate the advection-diffusion equation on a fixed grid and Lagrangian models, in which advection and diffusion equations are solved independently. Eulerian models are typically favoured when handling complex emission scenarios, while Lagrangian frameworks are chosen, when point-source emissions only require a few grid-points. The method HYSPLIT is utilising is a hybrid between Lagrangian and Eulerian approach; the trajectory calculations, however, are made in a Lagrangian framework:

**Trajectory calculation** A strength of the HYSPLIT\_4 model is, that it can process a variety of different meteorological data as input. Internally this data is linearly interpolated to a terrain following coordinate system  $\sigma$ :

$$\sigma = 1 - z/Z_{top} \quad (1.52)$$

where  $z$  is the height and  $Z_{top}$  the height of the HYSPLIT coordinate system. Horizontally, the grid system is identical to that of the used meteorological input data.

After the minimal required meteorological parameters  $U, V$  (horizontal wind components),  $T$  (temperature),  $z$  (height) and  $p$  (pressure) have been scaled and interpolated to the model grid, the particle advection in a 3-dimensional velocity grid  $\mathbf{V} = (U, V, W)$  can be calculated: Given an initial particle position  $P(t)$  and the mean velocity in space and time  $\overline{\mathbf{V}(P, t)}$  a first guess position  $P'(t + \Delta t)$  is calculated

$$P'(t + \Delta t) = P(t) + \overline{\mathbf{V}(P, t)}\Delta t \quad (1.53)$$

and on this basis the final particle position after the time step  $\Delta t$ :

$$P(t + \Delta t) = P(t) + 0.5(\overline{\mathbf{V}(P, t)} + \overline{\mathbf{V}(P', t + \Delta t)})\Delta t \quad (1.54)$$

$\Delta t$  is computed following the requirement that the advection distance per  $\Delta t$  has to be smaller than 0.75 of the meteorological grid spacing. For trajectory forecasts, Draxler (1991) found an spatial accuracy of 20 % to 30 % of the travelled distance.

In the framework of ICOS, Kuderer (2016) and Kneuer (2017) already used HYSPLIT\_4 to trigger sampling in a first trajectory-triggered sampling prototype device; furthermore the influence of nuclear power plants on the integrated radiocarbon sampling has been quantified (Kuderer et al., 2018).

### 1.5.3.2. STILT

The Stochastic Time-Inverted Lagrangian Transport (STILT) model has been designed to determine surface-to-atmosphere fluxes. In this work, however, I utilised this system to set-up a simulated atmosphere at different ICOS stations and at the station of Heidelberg. Here, I will give a short overview about the principles of this model, which is covered in more detail in Lin et al. (2003).

Lagrangian particle dispersion models – like STILT – are able to address the challenge to represent the near-field influences of atmospheric transport in the PBL by simulating turbulence and capturing subgrid scale transport (advection as well as dispersion). Particle locations are calculated without restriction of grid cells, that means small-scale effects or fine structures can be resolved. The straightforward way to determine the effect of an emission source on the concentration at the measurement site (the receptor) is to transport a number of tracer particles from the source forward in time through the modelled atmosphere. The number

## 1. Basics

of particles arriving at the receptor divided by the released particles corresponds to the emitter's influence on the receptor's concentration.

If the transport processes are time-reversible, the backward run of the model – starting from the receptor – results in the same fraction of molecules at the receptor. The resulting spatial particle density provides an *influence density*, which is defined as “the change in tracer concentration at the receptor in response to fluxes at the locations and times where the particles are found in the time-reversed model” (Zannetti, 1990). Figure 1.9 illustrates the difference between forward and backward time simulations. STILT makes use of this method and embodies a

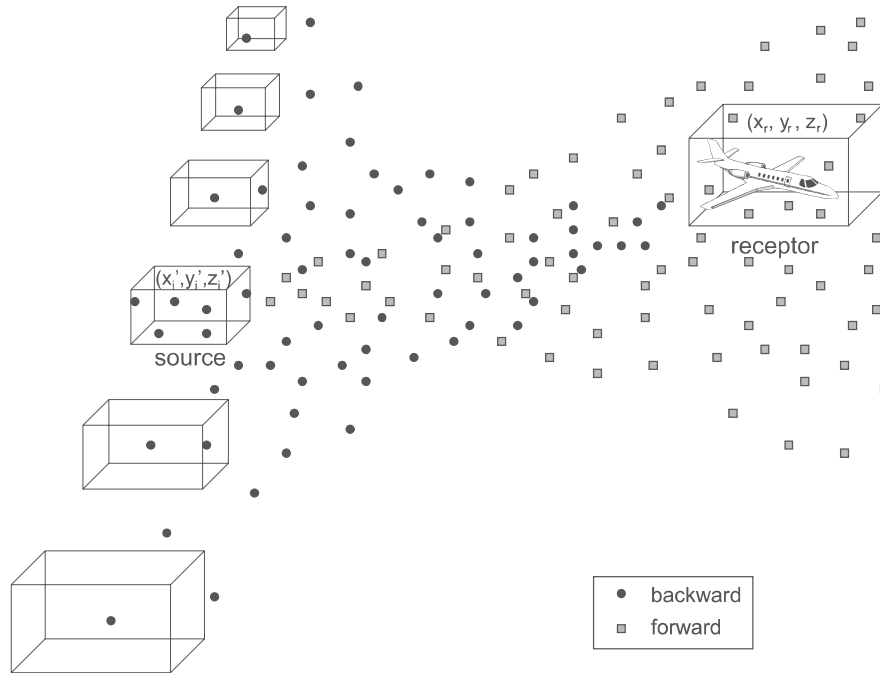


**Figure 1.9.:** Comparison between forward and backward time simulations. A backward time release of particles provides an influence map of the particle count at the receptor depending on particle releases in all source areas and times. Picture from Lin et al. (2003).

powerful tool to create highly-resolved emission influence maps (*footprints*) for atmospheric measurement stations, which are, however, dependent on the resolution and accuracy of the underlying meteorological data.

The footprints, provided by STILT model runs, can be seen as linear models  $\mathbf{F}$  to map emission inventories  $\vec{x}$  in space and time onto time series  $\vec{y}$  of concentrations at the receptor location. The derivation of the related matrix equations has been shown in Section 1.5.2. The principles of emission inventory composition will be presented in Section 1.5.4.

#### 1.5.4. Emission inventories for FFCO<sub>2</sub>

Reliable emission inventories for FFCO<sub>2</sub> are of great importance for the present study as well as for current inverse atmospheric measurement applications. Typically, FFCO<sub>2</sub> emissions are designated as background flux; this means these emissions are inserted into the models with a small error, relative to other sources and sinks (e.g. biological fluxes), leading to only minor adjustments on the a priori values (Gurney et al., 2005). FFCO<sub>2</sub> estimation by  $\Delta^{14}\text{C}$  analysis, on the other hand, targets the fossil component and aims to improve our knowledge about FFCO<sub>2</sub> emissions.

The first step in emission inventory composition is the creation of national emission inventories, which are usually provided by the appropriate government agencies (e.g. for Germany (1990-2015): Strogies and Gniffke, 2017). In the case of FFCO<sub>2</sub>, so called emission factors are applied to usually known fossil fuel imports and statistics (e.g. the official German emission factors are published by Juhrich, 2016), specified for fuel and combustion types.

##### 1.5.4.1. Inventory decomposition

These national inventories then have to undergo a spatial and temporal disaggregation, down to the required resolution. E.g. Pregger et al. (2007) give an extensive description of the methods used to compose an high resolution inventory for Europe (spatial grid size 5', *IER-5*) and Germany (spatial grid size 1', *IER-1*). They further resolved national emission data with statistical data for administrative units (e.g. population density) and geographic information like point source coordinates, land use maps and road and railway maps. Sources have been differentiated into point, line and area sources. For emission variations in time, the total emissions have been assigned to seven major emission sources: Power plants, industrial combustion plants, small combustion plants, refineries, industrial processes, road transport and air transport. The temporal course of the assigned emissions has been scaled down to hourly resolution by usage of socio-economic data (e.g. working times for industrial processes).

##### 1.5.4.2. Uncertainties

Even though large effort is made to decompose national data to regional scale, differences in the used decomposition methods and also in inter-national differences in the generation of the national inventories lead to large discrepancies between existing inventories. Pregger et al. (2007) estimate the errors on the underlying national inventories for CO<sub>2</sub> for *IER-1* and *IER-5* to 10 % to 30 %. Peylin et al. (2011) found that the annual totals of four European countries differ by 10 % in average and up to 40 %. Gurney et al. (2005) performed model experiments using different seasonal variations in the fluxes and found the potential biases introduced by the lack of seasonality to be up to 50 % of the residual flux. Wang et al. (2013) reported

## 1. Basics

the relative errors for the  $0.1^\circ \times 0.1^\circ$  CO<sub>2</sub> emission maps PKU-FUEL and PKU-CO<sub>2</sub> to be 63 %.

In summary, therefore, it can be said that there is still need to further develop reliable regionally scaled emission inventories for FFCO<sub>2</sub> and independent measurements to validate them.

## 2. AMS sample preparation in the IUP $^{14}\text{C}$ -laboratory

From 2008 to 2016 the ICOS project was situated in the so called preparatory phase. In this time more than 1200 targets for AMS analysis have been prepared at the Institute of Environmental Physics (Institut für Umweltphysik)  $^{14}\text{C}$  laboratory to introduce new methods in sample handling, preprocessing, and quality control (QC) for the AMS target preparation. This section presents the results of the present thesis in this phase and their consequences for the development of the final CRL set-up.

### 2.1. Graphitisation

The samples presented in the following subsections have been extracted and graphitised at existing processing systems at the IUP. The IUP graphitisation line (see Figure 2.1) has been in operation since 2006 (Unkel, 2006). The graphitisation parameters, which led to the best results in repeatability and precision for the IUP line have been determined in the beginning of this work by Roos (2013) and are listed in Table 2.1.

Table 2.1.: Applied parameters for graphitisation reaction at IUP (see Roos, 2013)

Parameter	Values
Iron oxidation	1000 mbar laboratory air for 5 min at 400 °C
Iron reduction	2× 400 mbar H <sub>2</sub> for 10 min at 400 °C
$m_{\text{Fe}} : m_{\text{C}}$	3 : 1
$n(\text{H}_2) : n(\text{CO}_2)$	2.2
Temperature	575 °C
Reactor length	12 cm
Graphitisation end	2× no change in pressure sensor value for 3 min

#### 2.1.1. Fractionation effects in the graphitisation line

To assess the fractionation induced by the sample processing at the IUP graphitisation line, a measurement series was started by transferring Oxalic acid II CO<sub>2</sub> samples the whole way through the graphitisation line similar to normal samples. Instead of graphitisation after transfer to the reactor, this CO<sub>2</sub> was trapped

## 2. AMS sample preparation in the IUP $^{14}\text{C}$ -laboratory



Figure 2.1.: Graphitisation line at IUP  $^{14}\text{C}$  laboratory Photo Florian Freundt.

inside a glass break-seal, followed by 2 to 4  $\delta^{13}\text{C}$  analyses using mass spectrometry (MSP – Thermo Fisher Scientific, *Finnigan MAT 252*). In a second series the gas was graphitised applying the standard parameters (Table 2.1) and the resulting graphite/iron powder mixture was combusted in an elemental analyser (EA – Elementar Inc, *Vario MicroCube*) at CEZ. The thereby formed  $\text{CO}_2$  was then again analysed for  $\delta^{13}\text{C}$  by mass spectrometry. The results of both experiments are shown in Table 2.2.

**Table 2.2.:**  $\delta^{13}\text{C}$  fractionation at the IUP graphitisation line before and after graphitisation. Tests have been performed by using Oxalic Acid II  $\text{CO}_2$  as examination agent ( $\delta^{13}\text{C} = -17.8\text{‰}$ ). Mean fractionation is the mean of differences between the test result and the nominal value ( $\delta^{13}\text{C}_{\text{test}} - \delta^{13}\text{C}_{\text{nom}}$ ). The error is calculated as the error of the mean values of the measurement results.

Tested fractionation	N	Mean fractionation
After transfer to reactor	6	$(-0.004 \pm 0.002)\text{‰}$
After graphitisation	5	$(0.007 \pm 0.060)\text{‰}$

The fractionation of  $-0.004\text{‰}$  in the process of freezing-over the sample to the reactor is not significant considering the measurement variation. Though, the results indicate, that the IUP graphitisation line does not introduce an additional fractionation bias prior to graphitisation.

The processing to graphite and combustion leads to a larger scatter ( $\pm 0.06\text{‰}$ ), but inside its uncertainty it doesn't show a bias from the nominal value. The variation is small compared to the typically observed spread of standard targets in  $\delta^{13}\text{C}$  during AMS analysis of  $\approx 2\text{‰}$ .

## 2.2. Quality control

To monitor precision in the whole range of measurement, long term stability, influence of the sampling method and inter-laboratory compatibility we specified and tested two different quality control methods at the IUP  $^{13}\text{C}$  laboratory, presented in the following two subsections.

### 2.2.1. Target gases

Whole air target gas cylinders were started to be analysed in 2013. Beside keeping an eye on long term stability of the AMS measurements, these are serving as QC for the range of expected  $\Delta^{14}\text{C}$  results. For that purpose we filled two aluminium tanks (Luxfer) with dry ambient air from Heidelberg. One in winter for low  $\Delta^{14}\text{C}$ , one in summer for heavier isotope. In the following these are referred to as *Target gas low* respectively *Target gas high*. Furthermore, these measurements allow us to separate the error introduced by sampling and storing samples in glass flasks (like Figure 1.2) from other measurement and preprocessing related errors:  $\text{CO}_2$  from Target gas high was extracted directly from the storage cylinder, whereas Target gases low was filled and stored in conditioned flasks before extracting its  $\text{CO}_2$ . Figure 2.2 shows the AMS results of 4 years target gas QC in preparation for the EGL in the final operational CRL.

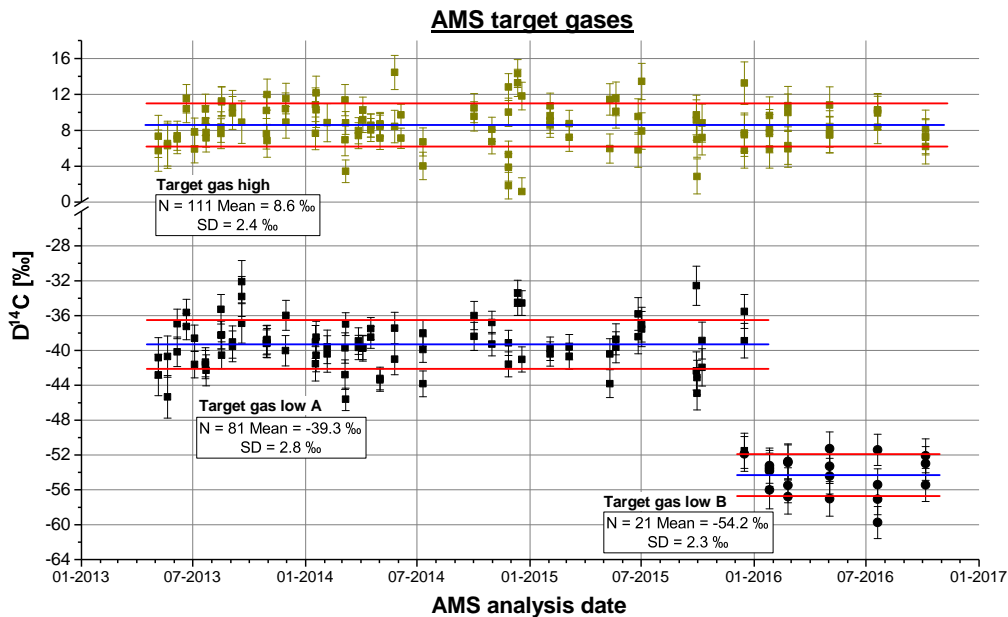


**Figure 2.2.:** AMS target gases during preparatory phase.  $\text{CO}_2$  from Target gas high was extracted directly from the storage cylinder; Target gases low were filled and stored in conditioned flasks before extracting  $\text{CO}_2$ . Error bars indicate the error  $\sigma_{\text{AMS}m}$  in the AMS measurement.

## 2. AMS sample preparation in the IUP $^{14}\text{C}$ -laboratory

### 2.2.1.1. Error decomposition

With that longterm dataset of samples not only an empirical standard deviation ( $\sigma_{emp}$ ) from the common mean value ( $\overline{\Delta^{14}\text{C}}$ ) of each QC type could be calculated, but also separation of errors in the AMS measurement ( $\sigma_{AMS_m}$ ), short-term uncertainties and long-term deviations from the mean was performed. This has been conducted by Turnbull et al. (2015b) before; similar calculation methods are used here. The applied relationship for the errors is shown in equation 2.1:

$$\sigma_{emp}^2 \approx \sigma^2 = \sigma_{AMS_m}^2 + \sigma_{wm}^2 + \sigma_{am}^2. \quad (2.1)$$

The unknown width of the assumed gaussian distribution of measurement results ( $\sigma$ ) is estimated by  $\sigma_{emp}$ .  $\sigma_{AMS_m}$  – the measurement error given by BATS – is dominated by the poisson uncertainty ( $1/\sqrt{N}$ ) of counting the  $^{14}\text{C}$  atoms of an individual sample in the accelerator. A typical sample reaches 500000 counts, contributing a Poisson uncertainty of 1.4 ‰.  $\sigma_{wm}$  is the within-magazine repeatability, consisting of deviations from the target mean in the same AMS magazine and therefore short-term uncertainties in the measurement, that are not covered by  $\sigma_{AMS_m}$  as well as errors in sampling, sample handling and graphitisation, which exist from sample to sample.  $\sigma_{am}$ , on the other hand, is the across-magazine uncertainty, made-up by long-term changes in the parameters mentioned above; for example graphitisation parameter changes or changes in the tuning of the AMS.

We can now calculate the within-magazine standardised residual  $r_{wmi}$  for every QC sample:

$$r_{wmi} = \frac{\Delta^{14}\text{C}_i - \overline{\Delta^{14}\text{C}_{wm}}}{\sigma_{AMS_{mi}}}. \quad (2.2)$$

These residuals should uniformly scatter around 0 in case of normal distribution. Same calculation can be done for the across-wheel standardised residual  $r_{ami}$ :

$$r_{ami} = \frac{\Delta^{14}\text{C}_i - \overline{\Delta^{14}\text{C}}}{\sigma_{AMS_{mi}}}, \quad (2.3)$$

representing the scattering around the common mean of all results of the same QC type. Figures 2.3 and 2.4 show the residuals of the AMS results of the 3 used QC target gases from the total mean respectively from the mean of each single magazine.

To quantify the visual finding of a greater scatter in the across-wheel residuals a  $\chi^2$  evaluation was performed, such that

$$\chi_Y^2 = \frac{\sum_i r_i^2}{Y}, \quad (2.4)$$

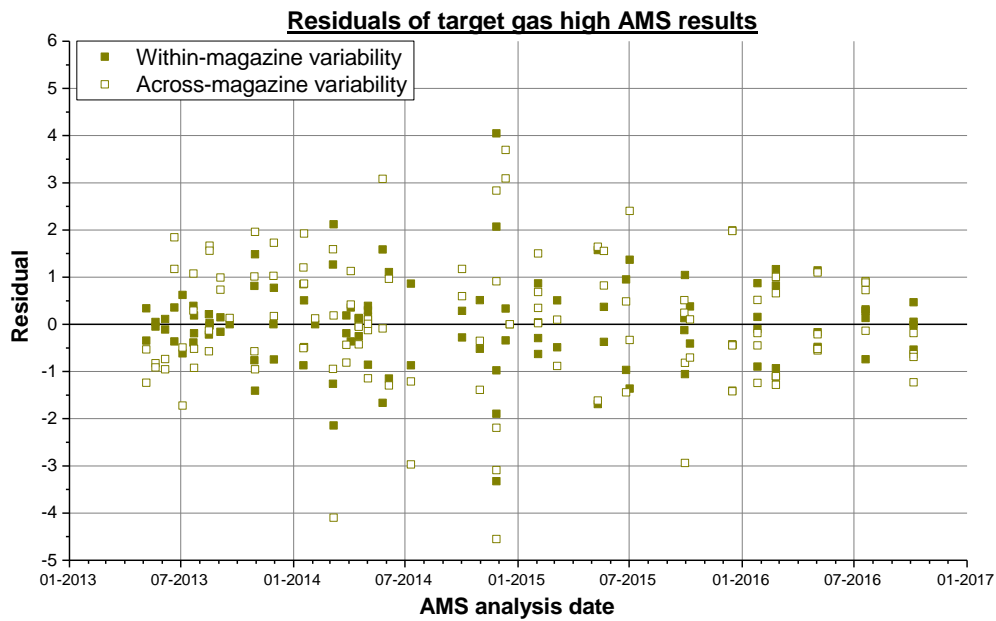


Figure 2.3.: Target gas high AMS result residuals within every magazine ( $r_{wm}$ , closed symbols) and across all samples ( $r_{am}$ , open symbols).

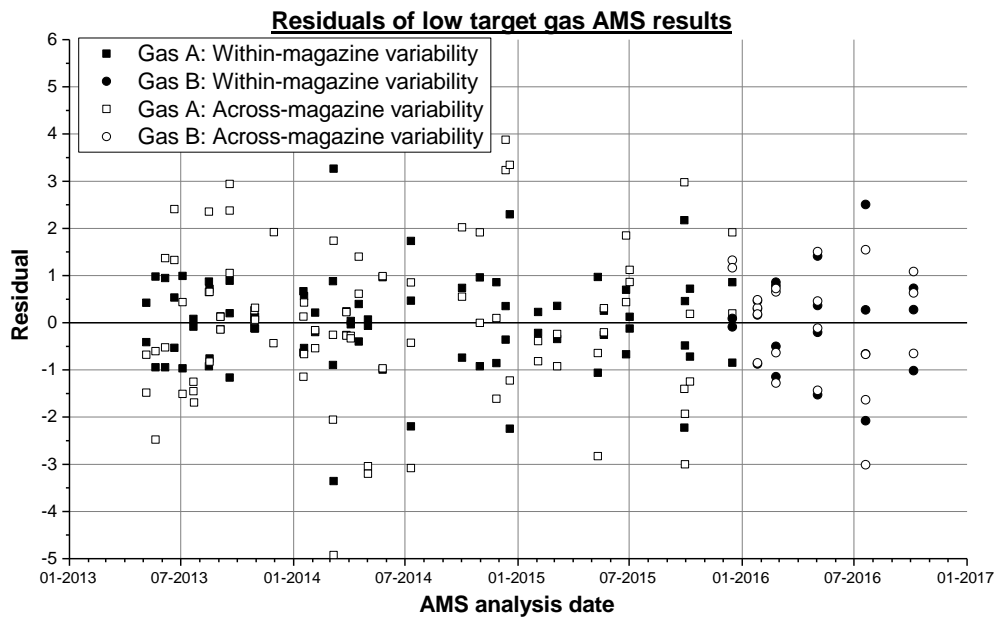


Figure 2.4.: Target gas low AMS result residuals within every magazine ( $r_{wm}$ , closed symbols) and across all samples ( $r_{am}$ , open symbols).

## 2. AMS sample preparation in the IUP $^{14}\text{C}$ -laboratory

where  $r$  is  $r_{wm}$  respective  $r_{am}$  and  $\gamma$  the degree of freedom, here the sample count of each type minus 1. A  $\chi^2$  of about 1 means, that the assumed error (here the AMS error) describes the uncertainties well. A  $\chi^2$  far from 1 indicates additional errors. These additional errors can be calculated as follows for  $\sigma_{wm}$

$$\sigma_{wm} = \overline{\sigma_{AMS m}} \cdot \sqrt{\chi_{wm}^2 - 1} \quad (2.5)$$

with the mean given AMS uncertainty  $\overline{\sigma_{AMS m}}$  as estimated underlying error. And same for  $\sigma_{am}$ :

$$\sigma_{am} = \sqrt{\overline{\sigma_{AMS m}}^2 + \sigma_{wm}^2} \cdot \sqrt{\chi_{am}^2 - 1}. \quad (2.6)$$

Table 2.3 shows the results of the statistical analysis. Apparently the additional within-magazine variability is very small ( $<0.5\text{‰}$ ) with a  $\chi^2$  around 1. This means,

**Table 2.3.:** Results of the error analysis of target gas measurement series (see Fig. 2.2) for within-magazine (wm) and across-magazine (am) repeatability. The  $\chi^2$  hypothesis test was conducted by assuming the AMS error  $\sigma_{AMS m}$  as error for the distribution

Sample	Mean	STD	Typ. error	Distrib. test		Addit. errors	
	$\overline{\Delta^{14}\text{C}}$	$\sigma_{emp}$	$\overline{\sigma_{AMS m}}$	$\chi_{wm}^2$	$\chi_{am}^2$	$\sigma_{wm}$	$\sigma_{am}$
Target high	8.58 ‰	2.42 ‰	1.76 ‰	0.96	1.90	-	1.67 ‰
Target low A	-39.27 ‰	2.80 ‰	1.72 ‰	1.01	2.70	0.19 ‰	2.26 ‰
Target low B	-54.19 ‰	2.27 ‰	1.97 ‰	1.06	1.42	0.49 ‰	1.31 ‰

the deviation of the observed  $\sigma_{emp}$  from the expected variability of  $\overline{\sigma_{AMS}}$  is almost exclusively caused by long term changes in the accelerator accuracy, e.g. exchange of the ion source, or the target preparation, e.g. usage of a new standard gas. Responsible for parts of the across-magazine variability might be drifts in the isotopy of the target cylinders: Target gas low A was monitored throughout its lifetime (until exchange of the cylinder filling) down to a cylinder pressure of about 50 bar, showing with 2.3 ‰ a larger additional long-term variability than Target gas low B with 1.3 ‰.

In summary, this QC method provides valuable information about the contribution of measurement errors from different sources. In particular, it could be shown here that the short-term uncertainty, the repeatability, corresponds to the uncertainties, which are given by BATS after evaluation of the AMS analysis.

### 2.2.2. LLC aliquots

As mentioned in the introduction, the WMO recommends an inter laboratory compatibility of  $\Delta^{14}\text{C} < 0.5\text{‰}$ . The CRL will operate resp. is operating two different labs to determine atmospheric  $\Delta^{14}\text{C}$  values: LLC analysis for large samples and AMS analysis for small flask samples; that means two methods that are fundamentally different in sample taking, handling and analysis. In this thesis a long

term effort has been undertaken to determine the inter laboratory compatibility over four years from 2013 to 2016. In 2017 and the beginning of 2018, the CRL target preparation facility EGL was under construction and testing. First compatibility tests between LLC and AMS analysis for the CRL are presented in Section 3.7.2.

The samples, which have been investigated, are in sodium hydroxide absorbed ambient CO<sub>2</sub> taken at the Heidelberg pilot station at the IUP (see Section 1.3.2). Graphitising-aliquots of these high-volume specimen have been taken at the conventional <sup>14</sup>C laboratory by freezing ≈100 μmol CO<sub>2</sub> into duran glass break-seals. The aliquots have been graphitised and AMS analysed alongside with other samples over the whole investigation period in the framework of this work. The examination of the mother samples has been undertaken by the LLC lab (Kromer and Münnich, 1992).

Figure 2.5 shows the deviations of the AMS aliquots from the LLC results over the 4 years. An error was assigned to each point according to

$$\sigma_{LLC-AMS_i} = \sqrt{\sigma_{AMS_i}^2 + \sigma_{LLC}^2}. \quad (2.7)$$

Here  $\sigma_{AMS_i}$  is assigned to each AMS result equivalent to Section 2.2.1. There we could see that  $\sigma_{AMS_{mi}}$  covers well the short term uncertainties in graphitising, preprocessing and AMS analysis. The long-term reproducibility of graphite target preparation and AMS analysis is estimated using  $\sigma_{am}$  of Target gas high – its examination period covers the same time like this AMS-LLC comparison – so that

$$\sigma_{AMS_i} = \sqrt{\sigma_{AMS_{mi}}^2 + \sigma_{am}(\text{Target gas high})^2} \quad (2.8)$$

is true with  $\sigma_{AMS_{mi}}$  as the individually assigned machine uncertainty. For  $\sigma_{LLC}$  a flat value of 2.1 ‰ is chosen, which is derived from the standard deviation of LLC QC results<sup>1</sup>, because the individually assigned error  $\sigma_{LLC_i}$  would only consist of the Poisson uncertainty, which has been proven as too low by replicate LLC-QC measurements.

Corresponding to (2.3), a residual for every point has been calculated as well as a  $\chi_{LLC-AMS}^2$  (2.4). In Table 2.4 the related values are summarised. We see that the assigned errors describe the empirical standard deviation of 3.7 ‰ for the most part. The additional errors – corresponding to a  $\chi_{LLC-AMS}^2$  of 1.3 – add up to 1.7 ‰. The most probable source for that uncertainty are problems in the aliquotation of the small AMS from the voluminous LLC sample. These could be leakages in the aliquotation facility as well as fractionation during freezing-over of the CO<sub>2</sub>.

The main result, however, represents the mean deviation of the two measurement and processing techniques of  $(0.1 \pm 0.3)$  ‰. That means that the two labs match their compatibility inside the 0.5 ‰ goal of the WMO within  $1\sigma$  probability. Hammer et al. (2017) showed a similar agreement of the Heidelberg LLC lab with

<sup>1</sup>Personal communication: Samuel Hammer, 2017

## 2. AMS sample preparation in the IUP $^{14}\text{C}$ -laboratory

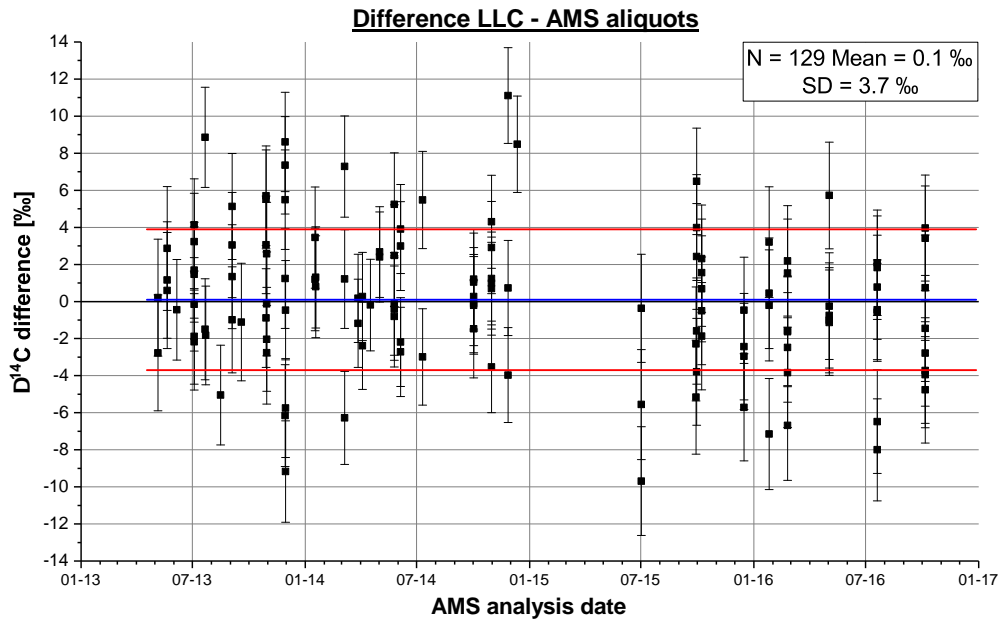


Figure 2.5.: Compatibility between CRL low-level counting and CRL AMS analysis from 2013-2016. Compared samples are high-volume pure  $\text{CO}_2$  sampled in Heidelberg (see Section 1.3.2) and its aliquots processed and graphitised at the IUP. The error bars correspond to  $\sqrt{\sigma_{AMS_i}^2 + \sigma_{LLC}^2}$

Table 2.4.: Characteristics of the measurements results of the AMS-LLC compatibility study. Measurement errors are  $\overline{\sigma_{AMS_i}}$  resp.  $\sigma_{LLC}$ . Mean deviation is the averaged difference between the LLC result and each of its AMS aliquots. The error of mean deviation is calculated as the error of the mean

Analysis method	Meas. error	Sample count	Mean deviation	STD of dev.	Distrib. test $\chi^2_{LLC-AMS}$	Unacc. uncert.
AMS	2.5 ‰	129	$(0.1 \pm 0.3) \text{ ‰}$	3.7 ‰	1.3	1.7 ‰
LLC	2.1 ‰	70				

### 2.3. Storage test of graphitised samples and blank contamination

a consensus value of different AMS laboratories all over the world in different samples. But due to lack of pure sample count no  $1\sigma$  probability accordance to the goal could be achieved before for the CRL labs.

### 2.3. Storage test of graphitised samples and blank contamination

Usually graphitised samples are analysed by AMS within one to four weeks after their reaction from  $\text{CO}_2$  in air or from a pure  $\text{CO}_2$  sample to graphite. However, there could be situations, when the AMS is under repair and not usable or when more urgent samples are demanding the measurement time, so that already preprocessed graphite needs to be stored. To examine the influence of prolonged storage time on the  $\Delta^{14}\text{C}$  results a storage test with samples of known  $\Delta^{14}\text{C}$  was started. These are graphite from blank  $\text{CO}_2$  from combusted natural gas that should not contain any  $^{14}\text{C}$  and Oxalic Acid I standard. After standard graphitisation procedure these specimen have been stored in the standard glass vials (see Section *EGL parts* in the annex) for different periods of time between one month and 2.5 years.

Figure 2.6 shows the AMS results in  $\Delta^{14}\text{C}$  of the analysed samples in comparison to their respective target values. Linear fits have been plotted to the data to quantify the storage effect.

Oxalic Acid I has a  $\Delta^{14}\text{C}$  reference value of 39.8 ‰ when measured as “unknown” sample in the AMS (see Section 1.2). The mean  $\Delta^{14}\text{C}$  of the storage test results fits to this value with  $(38.9 \pm 1.1)$  ‰ (error of mean). The slope of the fit over all points gives no evidence of any storage effect to the activity ratio of graphite from samples with near atmospheric  $\Delta^{14}\text{C}$ .

The nominal value of the blanks has been determined by two samples measured immediately after graphitisation. The found starting  $\Delta^{14}\text{C}$  is  $(-998.84 \pm 0.02)$  ‰. We see an increase in this  $\Delta^{14}\text{C}$  of  $(0.24 \pm 0.05)$  ‰  $\text{a}^{-1}$ . Taking into account the small absolute errors of the blanks we observe a small, but significant increase in blank sample activities over longer periods of time. Expressed in  $^{14}\text{C}$  age, this slope corresponds to an decrease of  $(-1500 \pm 300)$   $\text{a a}^{-1}$ .

An explanation for this behaviour could be a slowly but steadily happening exchange of carbon atoms in the graphite surface with those in the ambient laboratory air. Brown (1952) showed that for example the reaction



could take place, so that atmospheric  $^{14}\text{C}$  switches places with  $^{12}\text{C}$  in the blanks. That reaction would have a much smaller effect on the OxI samples, because the difference in the  $^{14}\text{C}$  ratio is – compared to the blanks – very small, namely  $\approx 50$  ‰ instead of  $\approx 1000$  ‰. In summary, these test suggests to avoid extremely long storage of blank graphite, but don't show an effect on other samples.

## 2. AMS sample preparation in the IUP $^{14}\text{C}$ -laboratory

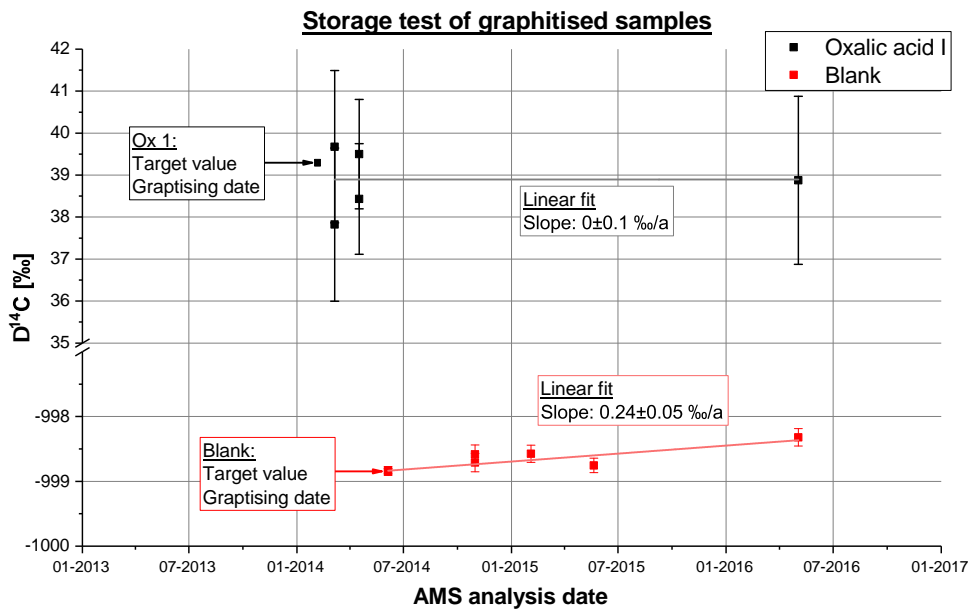


**Figure 2.6.:** Chronological sequence of AMS measurements in different times after one common graphitising date for every sample type (Blank samples and Oxalic Acid I). The samples have been stored in graphite powder form. Small squares pointed on by the arrows mark the target value and graphitising date.

Similar reactions might happen, when transferring the graphitised and pressed targets to the AMS, in our case from Heidelberg to the CEZ in Mannheim. Figure 2.7 shows the course of measurement of two blank targets in the AMS. In both cases we see a higher  $\Delta^{14}\text{C}$  in the beginning of the measurement, reaching a lower saturation value after several runs, when the caesium stream burnt deeper into the target surface and went through the potentially contaminated layer. Since the graphite is mixed homogeneously before the target pressing and a much shorter running-in effect is observed in blanks, which have been transported sheltered in a nitrogen 5.0 atmosphere (red points in Figure 2.7) as well as in those produced in Mannheim near the accelerator, that points onto some surface interaction happening with the air during transport. The black coloured sample, shown in Figure 2.7, was transferred on open-air, sheltered only by aluminium foil. To reliably quantify this effect, however, a systematic test series would be necessary, but nevertheless, the findings here suggest to use a tight transport container, preferably filled with non-reacting,  $\text{CO}_2$ -free gas to avoid contamination of samples with ambient  $\text{CO}_2$ .

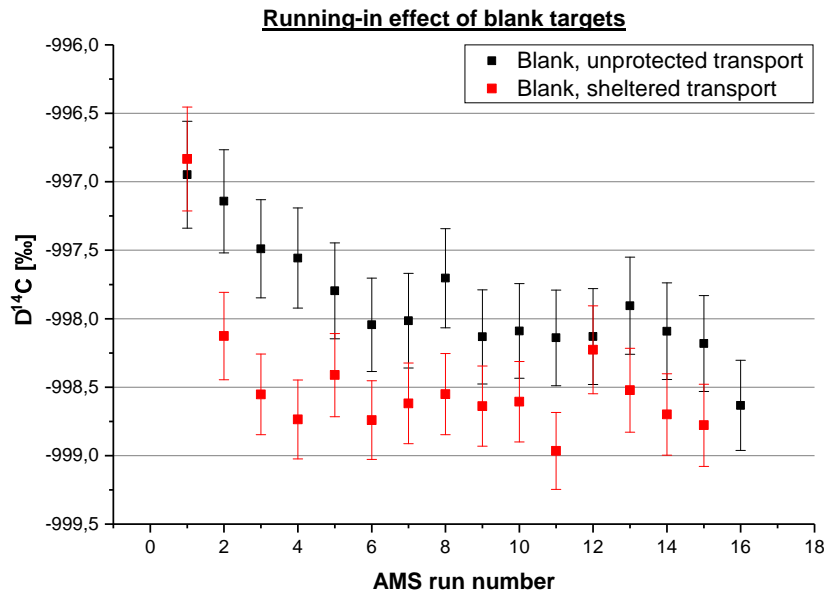


**Figure 2.7.:** Typical running-in effects of two blank measurements in the AMS. Every point represents the result of one run. The black points correspond to a target, that was transported in the open air; the red target was transported in an air-tight bag, filled with nitrogen 5.0.

## 2.4. Test of the target press

The last step in preparing  $^{14}\text{C}$  samples for AMS analysis is to press graphitised samples into aluminium target holder in a specialised target press. During the course of this work a new target press has been constructed by the IUP workshop and tested for the implementation in the CRL lab. The graphite, inserted into the target, is fixed under the press by a specialised target holder. The pressing stamp presses the graphite/iron powder over a small aluminium ball onto a clean ceramic sphere, driven by 3.2 bar of pressurised air. So the resulting target graphite gets a smooth, slightly concave surface for the following AMS measurement.

To quantify potential effects of the target press on the  $\Delta^{14}\text{C}$  results, two experiments have been performed:  $\text{CO}_2$  from combusted Oxalic Acid I has been graphitised under the same standard procedure and was afterwards pressed with the target press either in Mannheim at the CEZ (Ionplus, *PSP - Pneumatic Sample Press*) or with the newly built CRL press, which works according to a similar principle. Table 2.5 shows the AMS results of both batches.

Within the errors, the samples pressed by both target presses don't differ. The nominal value of  $-39,8\text{‰}$  lies barely out of the error range of the CRL target press results, while the CEZ press target's mean is  $0,7\text{‰}$  heavier. Sample scattering is larger in the CRL case, but still about  $0,5\text{‰}$  lower than the expected value due to pure measurement uncertainty. In summary, we see no significant difference

## 2. AMS sample preparation in the IUP $^{14}\text{C}$ -laboratory

**Table 2.5.:** Target press comparison of the CEZ press or the CRL press:  $\Delta^{14}\text{C}$  results. The error of mean  $\Delta^{14}\text{C}$  is  $2.4 \text{ ‰}/\sqrt{N}$ . Sample SD is the scatter of AMS results.

Used target press	N	Mean $\Delta^{14}\text{C}$	Sample SD
CEZ press	6	$(41.8 \pm 1.0) \text{ ‰}$	0.4 ‰
CRL press	4	$(41.1 \pm 1.2) \text{ ‰}$	1.5 ‰

between CRL and CEZ press and the nominal value of the targets lies in the  $2\sigma$  range of both measurement batches.

## 2.5. Consequences of the preparatory phase

Even though the build-up of the AMS sample preparation lab was not finished before early 2017 and most targets during this work have been processed at the corresponding devices at the IUP, the results presented above in this section provided valuable knowledge for the further development of the CRL and especially the EGL as part of it, as well as a foundation for choosing efficient and meaningful quality control methods for future sample processing at the CRL.

### 2.5.1. Magazine composition

During most time of the preparatory phase, AMS measurements at the MICADAS in Mannheim were performed using AMS magazines holding 22 targets. Target gases, which spanned the expected atmospheric  $\Delta^{14}\text{C}$  range from low (2 targets) to high (2 targets) values were introduced to monitor the analysis quality (section 2.2.1). In that case, the low target gas served as well as monitoring agent for potential effects of flask conditioning, filling and storage. Every magazine contained at least two blanks to make variations in sample contamination during preparation, storage and measurement visible. For assessment of the inter-laboratory compatibility between AMS and LLC on average about 3 aliquots of high-volume Raschig tube samples per magazine have been processed. Magazines were calibrated by 6 Oxalic Acid II standard samples per magazine.

Recent and future specimen are analysed in a larger, 39 target holder, magazine. In Section 1.4.2.5 an overview is given about the uncertainties considered by the AMS evaluation software BATS (Wacker et al., 2010b). A substantial error component, which can be directly addressed by the magazine composition, is the statistical uncertainty of the mean value of the standard targets  $\sigma(\langle R_{mol,bl,norm}(std) \rangle)$ . A higher count of standard samples  $N_{std}$  per magazine allows a more precise determination of the standard's  $\frac{^{14}\text{C}}{^{12}\text{C}}$ . Figure 2.8 shows the dependency of the total AMS measurement uncertainty for non-standard samples depending on the number of standards in the magazine and the AMS  $^{14}\text{C}$  counts of the targets. Typical  $^{14}\text{C}$  counts range from 300 000 to 555 000 during 2 d to 3 d magazine analysis. For 5 standards per magazine, the uncertainty for the lower threshold 300 000 falls below

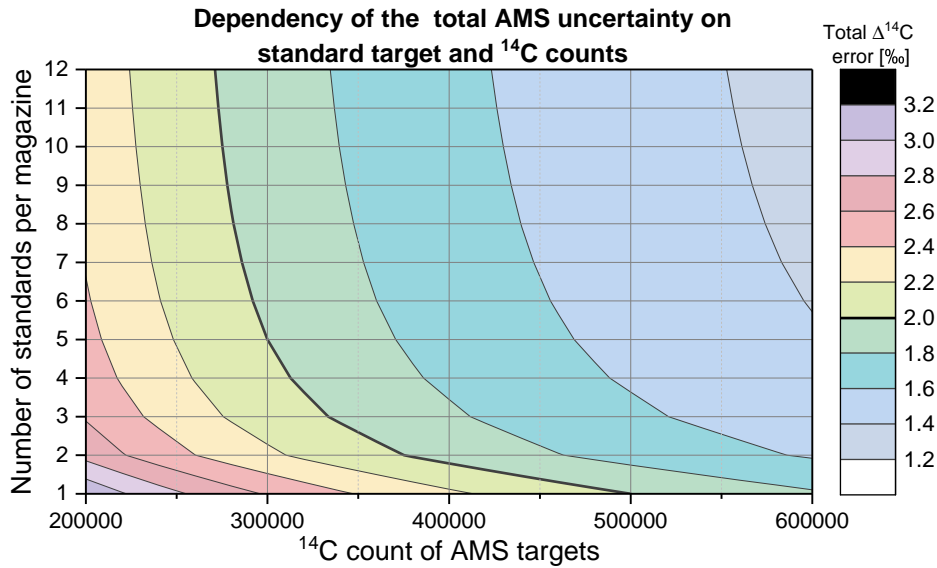


**Figure 2.8.:** Dependency of the AMS measurement uncertainty increase on the number of standard targets in the same magazine and the AMS <sup>14</sup>C counts of the targets. For this plot, the total error has been estimated to consist of Poisson uncertainty  $\sigma_{poiss}$  and the statistical uncertainty of the mean value of the standard targets  $\sigma(\langle R_{mol,bl,norm}(std) \rangle)$ . Bold black line indicates a total error of 2 %.

2 %. In order to maintain a reserve standard target and considering that Figure 2.8 neglect errors beside Poisson and standard target uncertainty, a number of 6 standards per magazine holding 39 targets is recommended.

Furthermore, two blanks are required to allow BATS to estimate the blank scatter uncertainty  $\sigma(R_{mol}(bl))$ . The count of LLC aliquot targets for QC is determined by the large-volume sampling at the pilot station Heidelberg. Since samples are taken integrated over two weeks and at least 2 aliquots of each sample should be analysed, this leads to 1 to 2 LLC aliquot per magazine for 1000 to 1500 scientific samples and 40 to 60 analysed magazines per year. A pure CO<sub>2</sub> QC measurement series, which was started in this work (section 3.7.3) using Oxalic Acid I for absolute scale determination, is designed for long term QC and hence should be measured at most once per magazine.

Finally, the target gas analyses are intended to place the within-magazine and across-magazine error analysis on a broad statistical base as demonstrated in Section 2.2.1. It is recommended here, to continue the parallel preparation of QC target flask targets (up to now: *target gas low*) and targets, which are obtained by directly connected air gas cylinders (up to now: *target gas high*). To be able to perform continuous within and across magazine analysis for both sample types, 2 of each should be included in each magazine. Table 2.6 gives an overview of the amount of set target places in every magazine.

## 2. AMS sample preparation in the IUP $^{14}\text{C}$ -laboratory

**Table 2.6.:** Planned composition of future magazines for the CEZ AMS. Magazine size amounts to 39.

<b>Sampletype</b>	<b>Target count</b>
Standards	6
Blanks	2
Target gas High	2
Target gas Low	2
Pure CO <sub>2</sub> QC	1
LLC aliquots	1 to 2
Scientific samples	24 to 25

In summary, about 1/3 of the magazine is reserved for calibration and QC targets, which means, that analysis of 1000 to 1500 scientific samples per year requires preparation of 1400 to 2000 targets in total. E.g. Graven et al. (2007) use 12 to 14 standard and QC targets in a 24 target holder magazine for high-precision AMS measurements; Turnbull et al. (2015b) include 2 tuning targets, 8 standard targets, 3 whole-air QC targets and 1 process blank in a 40 target AMS wheel.

### 3. Set-up of the AMS target Extraction and Graphitisation Line

In the Sections 2.2, 2.3 and 2.4 we discussed sources of uncertainties for the  $^{14}\text{C}$  measurement results and how these can be assessed during routine operation. The finding was that long-term repeatability and inter-laboratory compatibility as well as blank contamination can be reliably determined, but for the cost of additional samples in every magazine. In Section 2.5.1 a magazine composition for the future CRL operation was recommended. Following this, about 60 % of the number of scientific samples have to be prepared as additional targets for calibration, blank correction and quality control. This emphasises once again not only the need for precision but also for labour and resource efficient preprocessing.

Consequently, this chapter targets the development of the new Extraction and Graphitisation Line (EGL) at the Central Radiocarbon Laboratory (CRL) in the framework of the Integrated Carbon Observation System (ICOS) as a tool to manage the given tasks. First, Section 3.1 gives an overview about the processing steps of a  $^{14}\text{C}$  sample before AMS analysis. In Section 3.2, 3.3 and 3.4 an in-detail-description of the soft- and hardware developed to manage the samples arriving at the CRL for AMS analysis is given. Section 3.5 shows the results of comprehensive tests, we performed to examine the best process parameters for the EGL operation. Finally, Section 3.7 presents the first results of continuously performed quality control measurements to assess the EGL performance in comparison to primary scales and compatibility to the IUP  $^{14}\text{C}$  laboratory and the CRL LLC-lab.

#### 3.1. Processing chain

Table 3.1 lists the steps an incoming sample has to pass until AMS analysis at the CEZ. The listed estimated expenditures of time for each preprocessing step until *magazine preparation* assume flawless sample handling and sample processing one by one. The most time-consuming steps conducted at the CRL are the evacuations of the tubing (10 min to 30 min), the iron pretreatment (1 h to 2 h),  $\text{CO}_2$  extraction from flasks or aluminium containers (5 min to 20 min) and graphitisation (2.5 h to 5 h). In the following Section 3.2 we will follow this step list for the different container types to explain what measures have been taken to parallelise and pipeline especially these tasks until the target is readily prepared for the AMS as far as possible.

### 3. Set-up of the AMS target Extraction and Graphitisation Line

**Table 3.1.:** Steps of procedure for AMS sample preparation and measurement at the CRL. From “Magazine preparation” on, the prepared magazine of 39 samples is handled as one. The column “Sample container type” lists the points, where samples in different form can be inserted in (←) or taken out of (→) the processing chain. Duration is estimated and summed up for successive execution of the steps. Automatic processing means here processing steps that don’t need permanent attendance: Evacuation, conditioning, graphitisation and AMS counting

↓ Processing step	Duration per sample	Sample container type
Preparing graphitisation	≈5 min	
Iron conditioning	1 h to 2 h	
Evacuate processing line	10 min to 30 min	
Extraction of CO <sub>2</sub>	5 min to 20 min	← Whole air sample container
Evacuating residual gas	1 min	
Expanding CO <sub>2</sub>	1 min to 3 min	→ Pure CO <sub>2</sub> break-seal
Transferring to quantific. vol.	2 min to 3 min	← Pure CO <sub>2</sub> break-seal or mini flask
Flushing evacuated tubing	2 min to 5 min	
Expanding CO <sub>2</sub>	2 min to 4 min	
Quantify CO <sub>2</sub> amount	1 min	
Taking aliq. for δ <sup>13</sup> C analysis	30 s	
Transfer to reactor	2 min to 5 min	
Adding H <sub>2</sub> into reactor	2 min	
Expanding CO <sub>2</sub>	2 min to 4 min	
Graphitisation	2.5 h to 5 h	
Weighting and containerising	5 min to 10 min	
Pressing into target	2 min	← Graphite sample
Magazine preparation	30 min/39 samp.	
Magazine transport to CEZ	2 h/39 samp.	
AMS analysis	1 d/39 to 3 d/39 samp.	
Result evaluation	1 h/39 to 3 h/39 samp.	
<b>Sum person minutes</b>	<b>37 min to 75 min</b>	
<b>Sum automatic processing</b>	<b>262 min to 565 min</b>	

The sums of required processing times listed in the two lines at bottom of Table 3.1 shows the need to reduce the required working time for every sample between arrival at the CRL and writing the final  $\Delta^{14}\text{C}$  result into the database. In Section 3.4, it will be shown to what extent software automatization and parallelisation of the processes affect these numbers.

During this work, the CRL database was adapted in cooperation with the CRL database administration team to map the physical processing steps into the database and enable tracking of the current processing step for each sample during the AMS preprocessing.

## 3.2. Construction of the EGL

In this section the technical build-up and construction of the Extraction and Graphitisation Line (EGL) is described. Tests to assess the performance and influences of the different components (e.g. fractionation) to the sample result will be presented in Section 3.6. Figure 3.1 shows the principal scheme of the EGL with all technical components, which will be addressed from left to right. In the Section *EGL parts* in the annex, the built-in commercial components are listed.

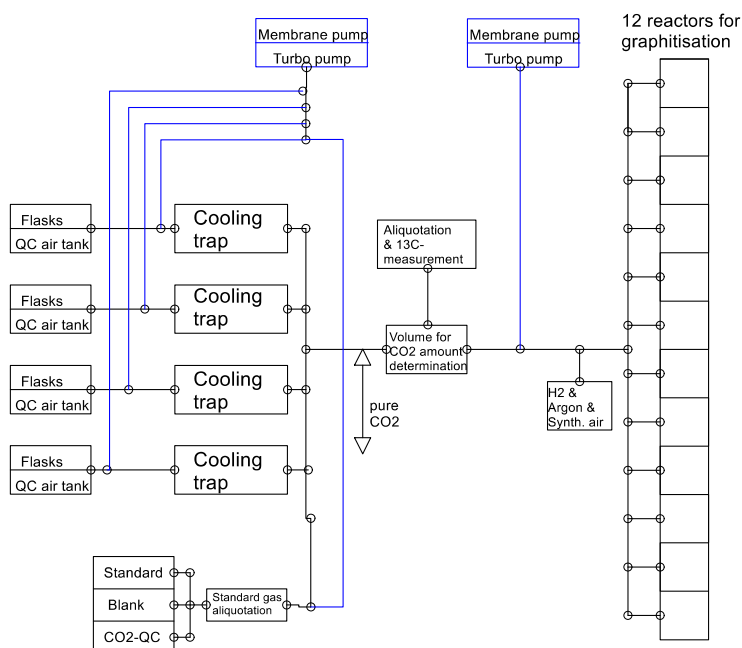


Figure 3.1.: Basic scheme of the main technical components of the EGL and allocated features. A detailed scheme is given in Figure 3.8

### 3.2.1. Sample inlets and outlets

Here I present, how to insert whole air sampling containers, QC air, pure CO<sub>2</sub> samples and <sup>14</sup>CO<sub>2</sub> standards into the EGL.

#### 3.2.1.1. Whole-air insertion

The majority of samples processed by the EGL will be whole-air filled 31 glass flasks (see Figure 1.2 and a technical drawing in the annex in Figure B.4). These samples enter the processing chain for extraction of CO<sub>2</sub>, the same does the quality control target gas. As seen in Table 3.1, the required time for this working step until CO<sub>2</sub> expansion sums up to – depending on the extraction speed – 7 min to 24 min. To enable parallel CO<sub>2</sub> extraction to improve this time, we added four

### 3. Set-up of the AMS target Extraction and Graphitisation Line

vacuum screw connections (1/2") to attach the flasks. Directly on the base of each of these connections a 1/8" tubing has been welded on to provide direct and leak free access to a target gas tank for quality control. The fourfold implementation of that element enables parallelisation of that time consuming step as well as simple insertion of the quality control gas, which follows then the exact same pathway through the EGL as flask samples – a necessary part of complete assessment of the device's reliability.

#### 3.2.1.2. Pure CO<sub>2</sub> insertion and draw-off

Beside these whole-air samples, a smaller number will have to enter the processing as pure CO<sub>2</sub>, primarily for QC and inter-laboratory compatibility (see 2.2.2).

On the other hand the capability is needed to store extracted CO<sub>2</sub> encapsulated in glass containers; that may be desired due to limited AMS measurement capacity, so that incoming flasks have to be processed but can't be analysed and have to be stored for longer periods of time. Production of inter-comparison samples may be another reason.

In summary, due to the limited number of samples, that follow this path, and the short time, that is needed to transfer the CO<sub>2</sub> to the quantification volume (Table 3.1), only one pure CO<sub>2</sub> insertion and extraction component has been built in the EGL. This is a 1/2" vacuum screw connection; here an element consisting of a 1/2" convoluted metal tubing, that is filler plugged at one side, can be inserted to crack break-seal CO<sub>2</sub> samples. The same socket can be used in combination with an adapter to a 3/8" vacuum screw connection, in order to plug in 8 mm glass break-seal tubes for flaming-off previously extracted CO<sub>2</sub>.

#### 3.2.1.3. Standard gases and pure-CO<sub>2</sub>-QC supply

The EGL includes an internal supply of standard gases and pure CO<sub>2</sub> quality control gas. This leads – in comparison to manual insertion of the standard gas over one of the sample insertions described above – to an higher degree of standardisation in standard target production and the possibility to fully automate the standard gas aliquotation in the EGL. The graphitisation of a pure CO<sub>2</sub> quality control gas allows to systematically monitor the quality of standard gas processing in the EGL. Figure 3.2 shows a schematic picture of the EGL standard gases and pure-CO<sub>2</sub>-QC supply part.

The 6 l or 10 l glass containers can be closed by attached hand valves for transport to refilling. In standard operation the hand valves are opened and the pressure in the subsequent capillaries ( $L = 1 \text{ m}$ ,  $\varnothing = 0.4 \text{ mm}$ ) equilibrates with the pressure of the respective glass container. For standard gas processing, the corresponding valve to the evacuated measuring volume  $V$  opens and slowly increases the pressure in  $V$  ( $\approx 10 \text{ mbar s}^{-1}$ ) until a defined target pressure is reached and the valves are closed. The sampled CO<sub>2</sub> is then further processed like other targets and cryogenically transferred to the quantification volume.

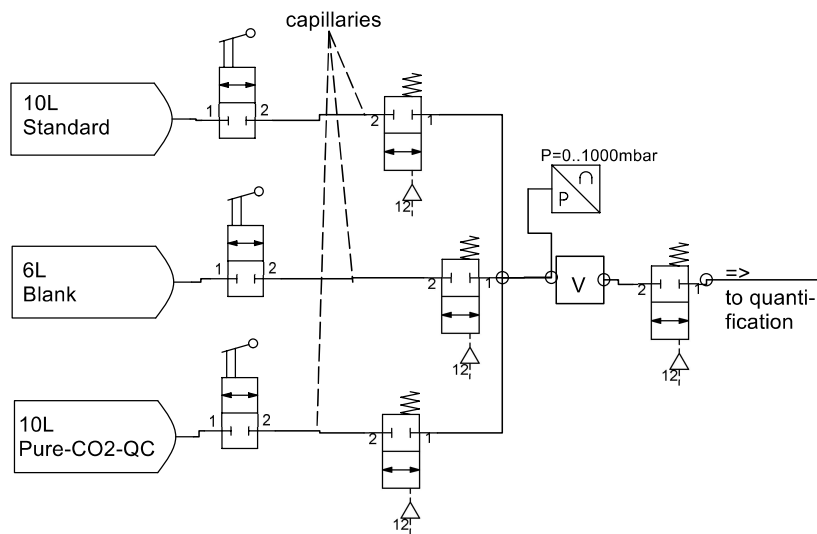


**Figure 3.2.:** Schematic figure of the EGL standard gases and pure-CO<sub>2</sub>-QC supply part. The glass tanks containing the gases can be closed by hand valves; the connection to the measuring volume V is made through pneumatic valves and capillaries inside the 1/8" tubing ( $L = 1\text{ m}$ ,  $\varnothing = 0.4\text{ mm}$ ). Further CO<sub>2</sub> transfer and evacuation is performed through the pneumatic valve on the right side.

The volume V amounts ( $5.5 \pm 0.4$ ) ml and is mainly defined by the internal volume of the four pneumatic valves. That means that for a standard target of  $100\ \mu\text{mol CO}_2$  a pressure of 490 mbar in V has to be measured. Therefore, a glass tank reaching this pressure has to be refilled. The current primary standard for EGL targets is Oxalic Acid II CO<sub>2</sub>, the blank is CO<sub>2</sub> produced by combustion of natural gas and as gas for standard gas quality control Oxalic Acid I CO<sub>2</sub> is used.

### 3.2.2. CO<sub>2</sub> extraction

The EGL operates four parallel CO<sub>2</sub> extraction lines, one for each whole-air sample inlet, whose components will be described in the following.

#### 3.2.2.1. Cooling trap

A common way of extracting CO<sub>2</sub> out of air samples is cryogenical extraction. Other labs (e.g. Turnbull et al., 2007) use cryogenically performed CO<sub>2</sub> separation with an air flow of 200 ml through a liquid nitrogen cooled double glass trap. The formerly used CO<sub>2</sub> extraction facility at the IUP <sup>14</sup>C lab followed a similar approach before comparative CO<sub>2</sub> extraction tests in this thesis yielded a higher freezing-out efficiency for multiply coiled stainless steel tubing in liquid nitrogen. Basically, the outflow concentration of these stainless steel cooling traps turned

### 3. Set-up of the AMS target Extraction and Graphitisation Line

out to be below the detection limit of the Licor NDIR (Non Dispersive Infrared) analyser (Licor, LI-820); therefore we chose to build the cryogenical extraction line around that component.

Figure 3.3 shows technical drawings of the deployment of the EGL cooling traps. The fourfold winding of the EGL traps results from structural properties of solid

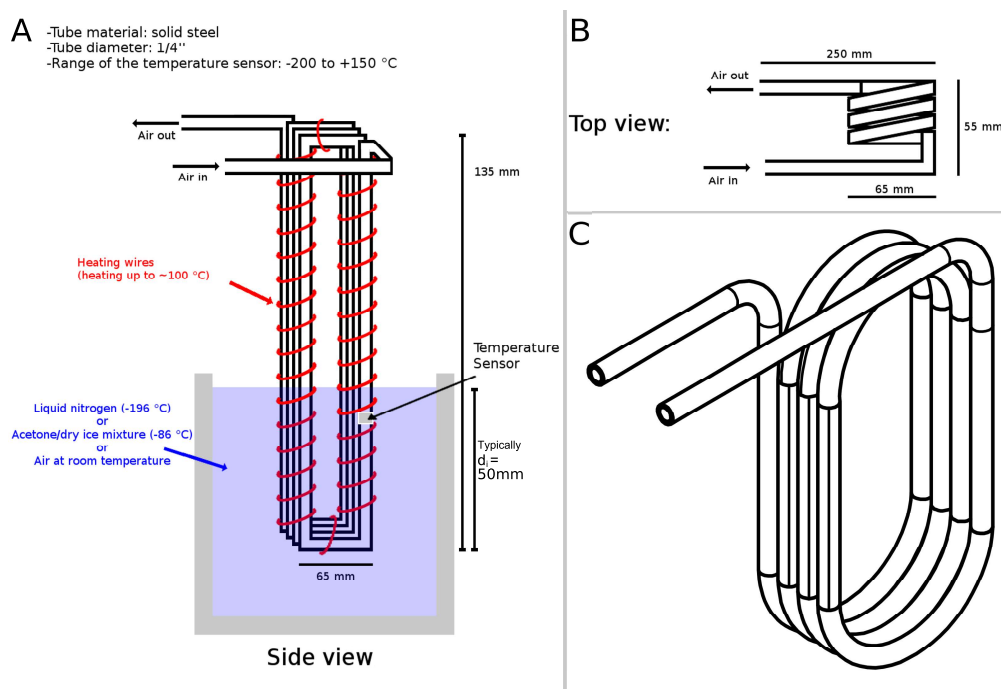


**Figure 3.3:** EGL cooling trap. **A:** Side view, schematic, with heights and width, on freezing-out immersion depth  $d_i$ ; in red electric heating wires to thaw up frozen  $\text{CO}_2$  and to reach a defined temperature level in the trap (regulated by a NiCr-Ni thermal element). **B:** Top view, schematic, of the trap with dimensions. **C:** Technical 3D drawing of the bend 1/4" stainless steel tube (see Figure B.5).

$\text{CO}_2$ : Out of the gas phase resublimating  $\text{CO}_2$  tends to immediately freeze on surfaces whose temperature falls below  $-80^\circ\text{C}$ . This leads to a thick layer of inhomogeneously oriented  $\text{CO}_2$  crystals within the first few mm of the cooling trap. That can lead to choking of tight tubing or, especially in high-flow environments, to a breaking off of  $\text{CO}_2$  flakes, which can then migrate with the cooled air flow out of the trap. Glass traps usually counter that effect by using a frit on the trap exit to filter out  $\text{CO}_2$  crystals before leaving the cooled section. The design of the EGL trap aims to force arising  $\text{CO}_2$  flakes to traverse tubing parts that exceed sublimation temperature to change them back into gas phase in order to resublimate the resulting  $\text{CO}_2$  again at the next cold coil. For this reason, the upper part of the EGL trap remains outside of liquid nitrogen during extraction. In Section 3.6.1,

the results of a test to specifically target the influence of the immersion depth  $d_i$  on sample fractionation are presented.

#### 3.2.2.2. Flow regulation

The air flow through the extraction line is driven by a drawing membrane pump (KNF, PM28170-938.50, EPDM membrane) at the end of each line, which has been tested for CO<sub>2</sub> back-flush from the ambient laboratory air back into the trap (see Section 3.6.1). Flow regulation is performed by a Low  $\Delta p$  mass flow controller (MFC – Bronkhorst, F-201DV-ABD-88-V), regulating the flow before entering the cooling coil. These MFCs are capable of maintaining the set flow, even when the pressure difference is smaller than 1 mbar before and after the steering valve. That property shows its importance, when the attached sample flask runs empty and the pressure difference between drawing pump and flask approaches zero. It enables freezing out onto a lower flask pressure in a reasonable timeframe: The EGL CO<sub>2</sub> extraction process is ended at a flow of 20 ml<sub>n</sub>/min. The cooling trap pressure is monitored during extraction, stopping the flow in case of more than 150 mbar gas pressure, to prevent potentially dangerous condensation of O<sub>2</sub> in the tubing.

#### 3.2.2.3. Cooling and elevators

The cooling agent N<sub>2</sub>(l) is held by a stainless steel dewar (KGW-Isotherm) on freezing-out height. It is fixed to a threaded rod, which again is driven by an electromotor to enable the nitrogen dewar to automatically move up- and downward. Three positions are defined by applied electric switches, which signal the controlling PC about the current position of the dewar elevator:

**Elevator on top position:** This means, the elevator holds the topmost position and most part of the cooling trap is immersed into N<sub>2</sub>(l). This position is used for residual gas evacuation after freezing-out, in other words removal of nitrogen and oxygen within the trap tubing and ensuring to keep as much CO<sub>2</sub> in solid form as possible.

**Elevator on freezing-out position:** On this height CO<sub>2</sub> extraction is performed (Figure 3.3A); the steel coil immerses into N<sub>2</sub>(l) to a depth of 50 mm above the bottom wind (see Section 3.6.1 for corresponding fractionation tests).

**Elevator at bottom:** After extraction and residual gas removal the elevator moves down to this position for heating-up and CO<sub>2</sub> expansion.

#### 3.2.2.4. Heating

For thawing of the extracted CO<sub>2</sub> 3 m stainless steel heating wire (Thermocoax, SEA15/300, 60 V, 200 W, up to 600 °C) are blazed on each trap tubing; these are insulated by compressed magnesium oxide ad coated by a stainless steel layer and

### 3. Set-up of the AMS target Extraction and Graphitisation Line

resistant to extreme temperature changes. The heating is driven by 200 W, which leads to a quick heating up to laboratory temperature from  $-195.8\text{ }^{\circ}\text{C}$  temperature of the  $\text{N}_2(\text{l})$  in less than 2 min and therefore rapid  $\text{CO}_2$  expansion. A NiCr-Ni thermoelement for temperature regulation and monitoring is fixed 40 mm above the bottom of the cooling trap coils. The thermovoltage for this type is defined from  $-270\text{ }^{\circ}\text{C}$  to  $1300\text{ }^{\circ}\text{C}$ ; due to that wide range, they are used here to signal the heater temperature as well as a feedback for the trap's immersion into liquid nitrogen. Regulation of the heating wire is described in Section A.1.1; it is performed automatically by an autonomous device to a settable value by the technician. However, the temperature should never be regulated above  $\approx 100\text{ }^{\circ}\text{C}$ , since the blazing starts to soften at the contacts with the hot wire, when about this temperature is reached at the sensor's location.

#### 3.2.2.5. Extract properties

Other  $\text{CO}_2$  extraction lines (e.g. Turnbull et al. (2007) or the  $\text{CO}_2$  extraction at the IUP  $^{14}\text{C}$  laboratory) operate a water trap upstream of the  $\text{CO}_2$  trap or after the  $\text{CO}_2$  extraction. Cooling agents like ethanol or dry ice/acetone mixture are used to lower the moisture content to a dew point of  $-60\text{ }^{\circ}\text{C}$  to  $-90\text{ }^{\circ}\text{C}$ . The EGL  $\text{CO}_2$  extraction line doesn't separate water from  $\text{CO}_2$  for three main reasons:

- The current ICOS Atmospheric Station Specifications (Laurent, 2016) recommend drying of  $^{14}\text{C}$  samples collected in flasks; so we expect to face a low water content in processed flasks.
- Moisture is removed separately at the graphitisation reactors, this also addresses residual water from the air sample.
- Cooling agents can potentially cause harmful health issues, when degasing in proximity to the technician (e.g. acetone).

Not only water is extracted alongside  $\text{CO}_2$  but also  $\text{N}_2\text{O}$  condensates at temperatures below  $-88.8\text{ }^{\circ}\text{C}$ . No attempt is made to remove that share from the  $\text{CO}_2$  extract; since no interference with the graphitisation process has been observed before (Smith et al., 2007).

It must be kept in mind, that the partial pressure of these gases add to all pressures, that are measured in the further processing. When we assume an air sample with  $400\text{ }\mu\text{mol mol}^{-1}$   $\text{CO}_2$  concentration and  $0.330\text{ }\mu\text{mol mol}^{-1}$   $\text{N}_2\text{O}$  concentration, that was dried to a dewpoint of  $-40\text{ }^{\circ}\text{C}$  ( $\approx 0.13\text{ mbar} \approx 130\text{ }\mu\text{mol mol}^{-1}$   $\text{H}_2\text{O}$ ), we would get a bias in all  $\text{CO}_2$  pressure measurements in the EGL of

$$\left( \frac{400 + 0.33 + 130}{400} - 1 \right) \cdot 100\% = 32.6\%$$

if all water is in its gaseous phase. Since the vapour pressure of water at a laboratory temperature of  $20\text{ }^{\circ}\text{C}$  to  $30\text{ }^{\circ}\text{C}$  ranges from 23 mbar to 42 mbar and the  $\text{N}_2\text{O}$

influence is small, water vapour in non-heated sections of the EGL would condensate at – depending on temperature –  $p_{H_2O}^{max}$  (23 mbar to 42 mbar) for total pressures greater than  $530.43/130 \times p_{H_2O}^{max}$ , which would be 94 mbar to 171 mbar. Below this threshold pressure the percentage dependency is valid. This means, measured pressure values of CO<sub>2</sub> of moist samples have to be corrected for their water vapour contribution.

#### 3.2.3. CO<sub>2</sub> transfer inside EGL

Post- extraction CO<sub>2</sub> transfers inside the EGL are performed by desublimating it into the respective volumes using cooling fingers in N<sub>2</sub>(l). Similar handling was conducted at the graphitisation line at the IUP <sup>14</sup>C laboratory, but other methods to transfer CO<sub>2</sub> inside a processing line are also used. E.g. Wacker et al. (2010c) use Zeolith to trap CO<sub>2</sub> in the reaction section. But because of easy, clean and fast regeneration by simply heating up the cooling finger and evacuating the residuals as well as successful experience at the IUP <sup>14</sup>C laboratory line, we decided to use cryogenical transfer at the EGL. Transfer of gaseous CO<sub>2</sub> is performed in three parts of the extraction and graphitisation process:

- In case of taking out extracted CO<sub>2</sub> of the EGL, the target is transferred to a break-seal glass tube, which is flamed off after transfer.
- From the EGL CO<sub>2</sub> extraction line or pure CO<sub>2</sub> insertion ports the gas is transferred to a stainless steel quantification volume (see Section 3.2.4).
- After target amount quantification the CO<sub>2</sub> is transferred into a graphitisation reactor (see Section 3.2.6). Here the sample is frozen into a Duran glass tube ( $\varnothing = 6$  mm, wall thickness 2 mm).

#### 3.2.4. Quantification

All targets processed by the EGL undergo a step to quantify the amount of target, which has been extracted – or inserted as pure CO<sub>2</sub> – and therefore are transferred to a quantification volume. Figure 3.4 shows a schematic image of the quantification finger.

The quantification element consist of a stainless steel CO<sub>2</sub> freezing finger ( $\varnothing 1/4''$ ), that is over-wrapped by 0.75 m blazed-on heating wire (compare Section 3.2.2.4), driven by 100 W (Thermocoax, SEA10/75, 30 V, 100 W, up to 600 °C). The finger is placed above a similar elevator construction as described in Section 3.2.2.3. Here we define two possible positions of the elevator, which can be read out and targeted by the controlling PC:

**Elevator on bottom:** On that position the dewar on the elevator can be filled with N<sub>2</sub>(l) by the technician. Automatic heating and expanding of the CO<sub>2</sub> sample takes place here.

### 3. Set-up of the AMS target Extraction and Graphitisation Line

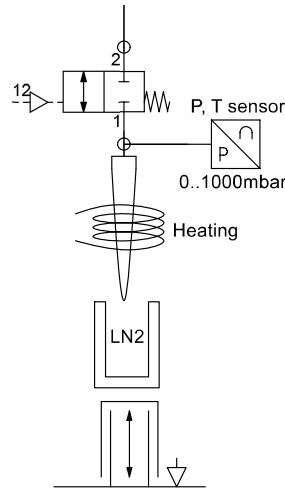


Figure 3.4.: Scheme of the EGL CO<sub>2</sub> quantification finger.

**Elevator on top:** Here the quantification finger almost completely immerses into the N<sub>2</sub>(l) in the dewar below. Whenever reaching this elevator position one should keep in mind, that it takes 60 s to 70 s to equilibrate in temperature with the N<sub>2</sub>(l); so when manually transferring a sample into the quantification element one should wait this amount of time before starting the transfer.

#### 3.2.4.1. Calculation of CO<sub>2</sub> amount and uncertainties

In principle the sample amount is calculated by measuring the CO<sub>2</sub> pressure in a known volume with known temperature using the state equation for ideal gases

$$n = \frac{p_q \cdot V_q}{R \cdot T_q} \quad (3.1)$$

with quantification pressure  $p_q$  and the ideal gas constant  $R = 8.3 \text{ J mol}^{-1} \text{ K}^{-1}$ . The determination of the finger's volume  $V_q = (2.69 \pm 0.20) \text{ ml}$  is shown in Section 3.2.7.1; the temperature  $T_q$  is determined on the outer surface of the steel finger by a NiCr-Ni thermocouple. The ideal gas equation is used here in favour over the Van-der-Waals equation for real gases, since the differences in the calculated amount of substance for real and ideal gases at room temperature are way smaller than the error induced by pressure or temperature measurement uncertainty.

The volume is chosen in a way, that regular samples of about 55  $\mu\text{mol}$  to 110  $\mu\text{mol}$  CO<sub>2</sub> span a pressure range of 500 mbar to 1000 mbar at the sensor for  $p_q$ , so that absolute sensor errors are small in comparison to the measurement value. The sensor's uncertainty after calibration is smaller than 0.15 % of the full-scale of here

1000 mbar:  $\Delta p_q^{meas} = 1.5$  mbar. As deduced in Section 3.2.2.5, is the pressure deviation within that pressure range set by  $p_{\text{H}_2\text{O}}^{max}$ , defined by the vapour pressure at  $T_q$ . It has been observed, however, that the water needs much ( $>10$  min) longer to reach equilibrium pressure within the quantification volume. Since the quantification pressure measurement is performed one minute after  $\text{CO}_2$  expansion, we set an empirically determined  $p_q^{\text{H}_2\text{O}} = (18 \pm 5)$  mbar for gases containing  $\text{H}_2\text{O}$  and  $p_q^{\text{H}_2\text{O}} = 0$  for moisture free samples. By default, the heating target temperature is set to  $30^\circ\text{C}$ , but since not the whole quantification volume is wrapped-in by heating wires, we set the resulting effective quantification temperature to  $T_q = (25 \pm 5)^\circ\text{C}$ . For the quantification result we now change equation 3.1 for moist samples to

$$n_{\text{CO}_2} = \frac{(p_q - p_q^{\text{H}_2\text{O}}) \cdot V_q}{R \cdot T_q} = (p_q - 18 \text{ mbar}) \cdot 0.109 \mu\text{mol mbar}^{-1} \quad (3.2)$$

with an error of

$$\begin{aligned} \sigma(n_{\text{CO}_2}) &= \frac{1}{RT_q} \sqrt{(p_q - p_q^{\text{H}_2\text{O}})^2 \left( \left( \frac{\sigma(T_q)}{T_q} \right)^2 + \left( \frac{\sigma(V_q)}{V_q} \right)^2 \right) + \sigma(p_q^{\text{H}_2\text{O}})^2} \\ &= \sqrt{(p_q - 18 \text{ mbar})^2 + 4.3 \times 10^3 \text{ mbar}^2} \cdot 8.3 \times 10^{-3} \mu\text{mol mbar}^{-1} \end{aligned} \quad (3.3)$$

for a negligible error of the pressure measurement  $\sigma(p_q)$ . For the amount of  $\text{CO}_2$  for water-free samples we get

$$n_{\text{CO}_2} = \frac{p_q \cdot V_q}{R \cdot T_q} = p_q \cdot 0.109 \mu\text{mol mbar}^{-1} \quad (3.4)$$

with

$$\Delta n_{\text{CO}_2} = \frac{p_q \cdot V_q}{R \cdot T_q} \sqrt{\left( \frac{\sigma(V_q)}{V_q} \right)^2 + \left( \frac{\sigma(T_q)}{T_q} \right)^2} = p_q \cdot 8.3 \times 10^{-3} \mu\text{mol mbar}^{-1} \quad (3.5)$$

These equations allow the calculation of the extracted or inserted  $\text{CO}_2$  amount with its errors for on-line comparison between actual sample size and the expected sample size, derived from database information, to evaluate the extraction and transfer efficiency. It is suggested here to use equations 3.2 and 3.3 for all processed flask samples and equations 3.4 and 3.5 for processed pure  $\text{CO}_2$  and high-pressure air (i.e. from pressurised cylinders).

The other main purpose for this quantification effort is to calculate the amount of hydrogen in the graphitisation reactor, that is needed for the size of the current sample, this will be described in Section 3.2.6.

### 3. Set-up of the AMS target Extraction and Graphitisation Line

#### 3.2.5. Aliquotation and $\delta^{13}\text{C}$ analysis

As explained in Section 1.2 it is necessary to determine a sample's  $\delta^{13}\text{C}$  during the AMS measurement to correct for fractionation in the accelerator and normalising the results to  $\delta^{13}\text{C} = -25\text{‰}$ . However, there may be the need to provide precise  $\delta^{13}\text{C}$  for samples that have not undergone the regular analysis chain within the CALs; i.e. they have not been analysed for  $\delta^{13}\text{C}$  at the FCL in Jena. Furthermore and more importantly, a regular precise determination ( $\sigma < 0.1\text{‰}$ ) of the  $\text{CO}_2$ 's  $\delta^{13}\text{C}$  before graphitisation provides an important quality control measure for targets with known  $\delta^{13}\text{C}$ : Fractionation resulting from  $\text{CO}_2$  extraction and transfer inside the EGL can be routinely quantified that way. Therefore we connected the EGL to an additional on-line  $\delta^{13}\text{C}$  measurement device, which determines each sample's  $\delta^{13}\text{C}$  post-quantification and pre-graphitisation.

The instrument chosen for these tasks is a Delta Ray Infrared Isotope Spectrometry (IRIS) instrument, that has been characterised in detail by Zipf (2017). Figure 3.5 illustrates the connection of the two devices schematically. 3.5A shows the parts of the EGL taking part in aliquotation: After quantification and 60 s mixing time the sample gas in section [1] is expanded into [2] and [3]; the aliquot for  $\delta^{13}\text{C}$  is then closed into [3]. After this the aliquot is transferred into a stainless steel tubing sample storage loop, utilising liquid nitrogen induced freezing over through the multiport valves V1 and V2 (Figure 3.5B, see also Zipf (2017)). At the end of the working day, when no more aliquots are expected to be stored in the loops, the Delta Ray IRIS control software starts to flush the stored aliquots with a carrier gas ( $<0.2\text{ ppm CO}_2$ ) through V1, V2 and V3 into the analyser for  $\delta^{13}\text{C}$  analysis.

In principle, repeatabilities of  $0.02\text{‰}$  and long-term reproducibilities of  $0.04\text{‰}$  in  $\delta^{13}\text{C}$  can be reached, when following the optimal calibration and measurement procedure with this instrument. Tests with mini-flasks and a  $\text{CO}_2$  concentration of 1000 ppm in the Delta Ray IRIS lead to a reproducibility of  $0.05\text{‰}$  and a accuracy of  $0.05\text{‰}$  (Zipf, 2017). The amount of  $\text{CO}_2$  taken as aliquot was adjusted in a way to enable the Delta Ray IRIS to reach these 1000 ppm when diluting the pure  $\text{CO}_2$  for measurement. Hence, volume [3] was set to 1.2 ml corresponding to an aliquot of 6.5% of the total sample amount (Table 3.2). A regular sample amounts  $\approx 100\text{ }\mu\text{mol}$  of  $\text{CO}_2$  and is split into  $93.5\text{ }\mu\text{mol}$  for graphitisation and  $^{14}\text{C}$  analysis and  $6.5\text{ }\mu\text{mol}$  for  $\delta^{13}\text{C}$  analysis.

**Table 3.2.:** Fractions of the total  $\text{CO}_2$  amount for  $\Delta^{14}\text{C}$  and  $\delta^{13}\text{C}$  analysis. Uncertainties originate from pressure measurement errors in the volume ratio determination (Table 3.5).

Quota of sample/standard $\text{CO}_2$ for	
$\Delta^{14}\text{C}$ meas.: $Q_{14}$	$\delta^{13}\text{C}$ meas.: $Q_{13}$
$(93.574 \pm 0.003)\%$	$(6.426 \pm 0.003)\%$

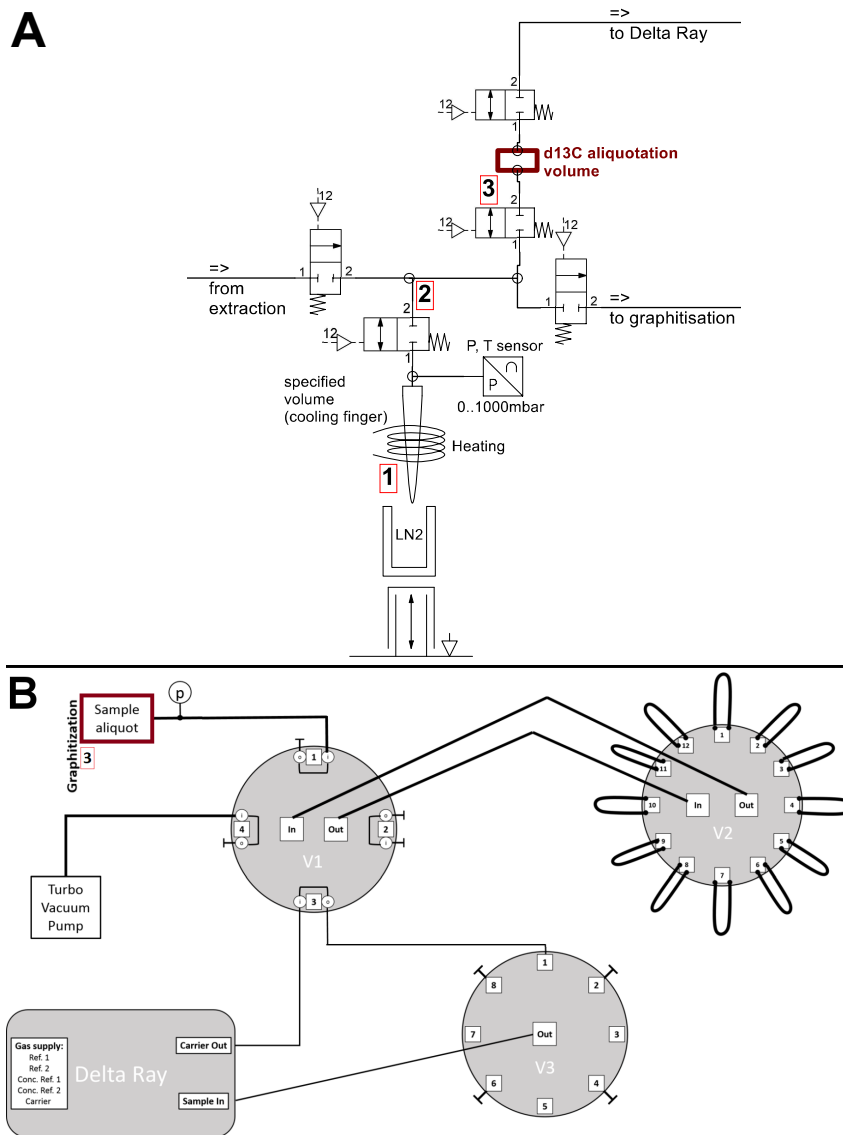


**Figure 3.5:** **A:** Functional scheme of the sections taking part in  $\delta^{13}\text{C}$  aliquotation in the EGL. **1:** Quantification volume. **2:** Tubing between quantification and aliquotation volume. **3:** Aliquot volume; quantified samples are expanded into this volume. **B:** Overview sketch of the planned valve setup for EGL aliquot measurement in the Delta Ray, modified from Zipf (2017). "Sample aliquot" corresponds to section 3 in **A**. p marks a pirani pressure sensor; V1, V2 and V3 are Vici Valco multiport selector valves: V2 is connected to stainless steel tubing loops for temporary aliquot storage; V1 selects between aliquot storing and transfer to Delta Ray; V3 chooses between different sample inputs for the Delta Ray.

### 3. Set-up of the AMS target Extraction and Graphitisation Line

The valve and tubing set-up shown in Figure 3.5B is under construction at the moment, so no further testing of the quality of the EGL aliquotation could be performed, but will be done after finalisation of the set-up.

#### 3.2.6. Graphitisation

The central parts of the EGL are its graphitisation reactors. As described in Section 1.4.3 the reduction of CO<sub>2</sub> to graphite requires to provide optimal conditions for the corresponding reactions and, at the same time, to minimise production of methane and residual amounts of carbon monoxide. On the other hand, the reactors ought to provide the possibility for uncomplicated and fast catalyst and sample handling by the technician. Figure 3.6 shows the final design of the EGL graphitisation reactor, its parts are described below.

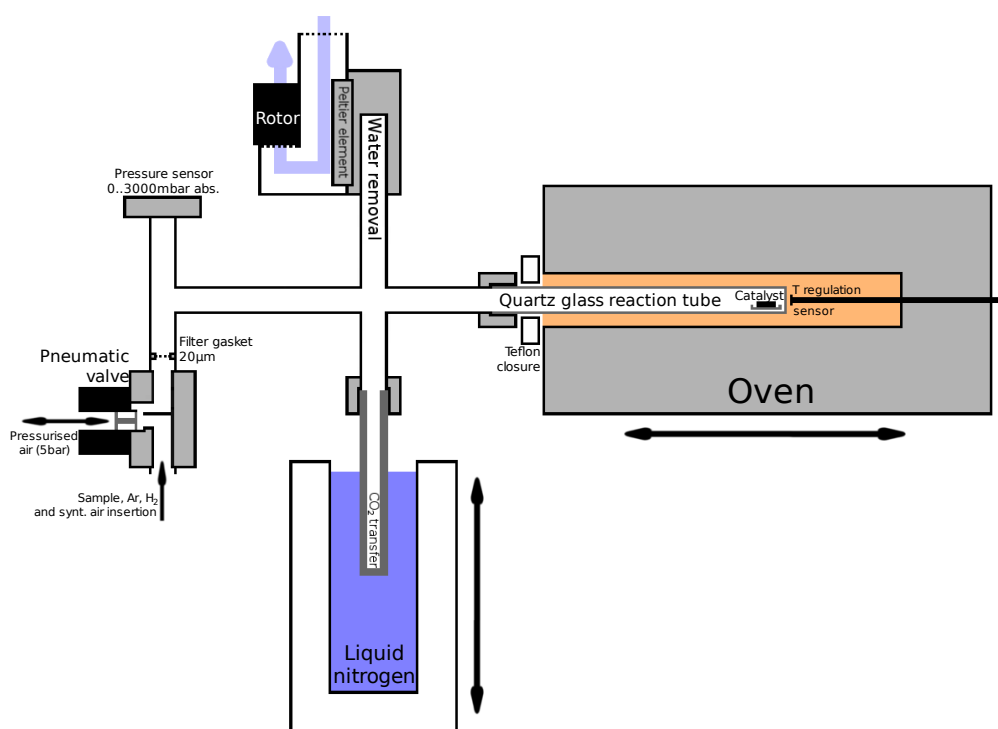


Figure 3.6.: Schematic representation of the EGL graphitisation reactor.

Twelve reactors have been installed on the EGL, as the graphitisation is with 2.5 h to 5 h duration by far the most time-consuming step in the target preparation process; so I introduced here the largest degree of parallelisation in the EGL.

Every reactor is equipped with a linear pressure sensor (Keller AG, PAA-9 LD, 0 mbar to 3000 mbar abs., TEB<sup>1</sup> = 0.5 % FS) to control working gas insertion and to monitor graphitisation pressure. In an EGL prototype system we faced issues with

<sup>1</sup>Total Error Band: Maximum deviation inside the specified pressure and temperature range

internally leaking pneumatic valves. Apparently, graphite or iron dust migrated onto the valve membrane and hindered complete closure; therefore I installed silver-plated filter gaskets with a mesh size of 20  $\mu\text{m}$  (Swagelok, SS-4-VCR-2-20M) at the end of each reactor, to protect the other parts of the EGL from graphite contamination.

#### 3.2.6.1. CO<sub>2</sub> transfer/storage tube and liquid nitrogen elevator

CO<sub>2</sub> transfer into the reactor is performed cryogenically into a liquid nitrogen cooled Duran glass tube ( $L = 6 \text{ cm}$ ,  $\varnothing = 6 \text{ mm}$ , WT= 2 mm). The wall thickness of 2 mm was chosen to reduce the volume in the reactor not providing reaction space due to low temperature.

Liquid nitrogen cooling is provided by an automatic dewar elevator, constructed at the IUP workshop. This elevator is able to move in two dimensions: Horizontal movement to head for the reactor that needs nitrogen cooling and vertical movement to immerse or emerge the CO<sub>2</sub> transfer and storage tube. Due to location determination by position sensors the liquid nitrogen cooling can be initiated fully automatically. The filling of the dewar through a funnel on top of each reactor has to be done manually.

#### 3.2.6.2. H<sub>2</sub>, Ar and synthetic air supply

The EGL provides built in supply of three types of working gases:

**Hydrogen** serves in the first place as reducing agent for CO<sub>2</sub>. It's second purpose is again to reduce iron oxides on the surface of the catalyst during pretreatment.

**Argon** is inserted to the reactor after finalisation of the graphitising reaction. It works as protective gas for the newly produced graphite and shields from possible contamination due to interaction with the laboratory air.

**Synthetic air** resp. its containing oxygen functions as oxidising agent in catalyst pretreatment. Pure O<sub>2</sub> tended to sinter the catalyst powder during pretreatment and was therefore excluded as oxidising agent

The tanks containing these gases are connected to the EGL via  $\approx 8 \text{ m}$  of stainless steel tubes. The possibility to achieve fine dosing of the inserted gas amount is achieved by stainless steel capillaries inside these tubes. The need for finer (hydrogen) or faster (Argon, synt. air) dosing defined the respective capillary diameter. Automatic gas dosing into the EGL is steered by pneumatic valves. Table 3.3 lists the used gases and capillary types.

### 3. Set-up of the AMS target Extraction and Graphitisation Line

Table 3.3.: Working gas and connection properties.

Gas	Purity	Pressure regulator	Admiss. pressure	Capillary
H <sub>2</sub>	<0.1 ppm CO <sub>2</sub>	Druva, <i>FMD50016</i>	1.6 bar	$L = 1 \text{ m}, \varnothing = 0.4 \text{ mm}$
Ar	<0.2 ppm CO <sub>2</sub>	Druva, <i>FMD50016</i>	3.5 bar	$L = 1 \text{ m}, \varnothing = 0.5 \text{ mm}$
Synt. air	<1 ppm CO <sub>2</sub>	Druva, <i>FMD30018</i>	3 bar	$L = 1 \text{ m}, \varnothing = 0.5 \text{ mm}$

#### 3.2.6.3. Water removal system

Other graphitisation lines use acetone dry ice mixtures with  $\approx -75^\circ\text{C}$  (e.g. the line at the IUP <sup>14</sup>C-laboratory (see Section 2.1)) or magnesium perchlorate (Graven et al., 2007) to fulfil the necessary removal of water, forming during graphitisation reaction. A less labour intensive and automatable method is water removal by thermo electric cooling (e.g. Wacker et al., 2010c). Roos (2013) showed in preparation of the EGL design, that the acetone dry ice method could be replaced by thermo-electric cooling by an air-cooled peltier element (reaching  $\approx -30^\circ\text{C}$  under load) for the cost of 0.5 h longer reaction time due to a higher H<sub>2</sub>O partial pressure in the reactor. Since an important goal of the EGL is to automatise the target preparation process as far as possible, we equipped the EGL reactors with such a cooling system.

This system consists of a 1/4'' stainless steel pipe stub positioned on top of the CO<sub>2</sub> transfer and storage tube. The stub is enclosed into an aluminium block providing the contact to a multi-level peltier element (TRU components, *TEC2-127-63-04*,  $V = 14.6 \text{ V}$ ,  $I_{max} = 4.2 \text{ A}$ ,  $\Delta T_{max} = 88 \text{ K}$ ). Heat dissipation is carried out by a radial fan driven air-flow cooled aluminium fin block.

#### 3.2.6.4. Oven

Heating of the catalyst and the reacting gases to their reaction temperatures is performed by ceramic fiber tubular furnaces (Watlow, *VC400J06A-0000R*, inner- $\varnothing = 13 \text{ mm}$ ,  $L = 152 \text{ mm}$ ,  $175 \text{ W}$ ,  $60 \text{ V}$ ). The fibre material has been coated into a stainless steel hull, so that only the opening for insertion of the reaction tube remains open. The ovens are moved over the reaction glass tubes mounted on rails.

Temperature regulation is conducted by an autonomous temperature regulation system (shown in Section A.1.1). The corresponding regulation sensor (thermal element, type K, Ni–NiCr) is placed next to the reaction catalyst, this means the end of the glass tube, to ensure as precise temperature regulation at the catalyst surface – where the graphitisation takes place – as possible.

Figure 3.7 shows the temperature dependency – measured by a Ni–NiCr thermal element inside the reaction glass tube – from the depth the reactor is moved inside the oven. That experiment has been performed for differently set temperatures, that are regulated outside the reactor by the regulation sensor, that was fixed

in position inside the oven. We see a strong decrease from the target temperature towards oven opening and furthermore an offset of 5 K to 10 K towards lower temperatures inside the reactor for the measurements taken at the same depth like the regulation sensor is placed. The measurement sensor has been 1-point calibrated to the value of the regulation sensor at 600 °C.

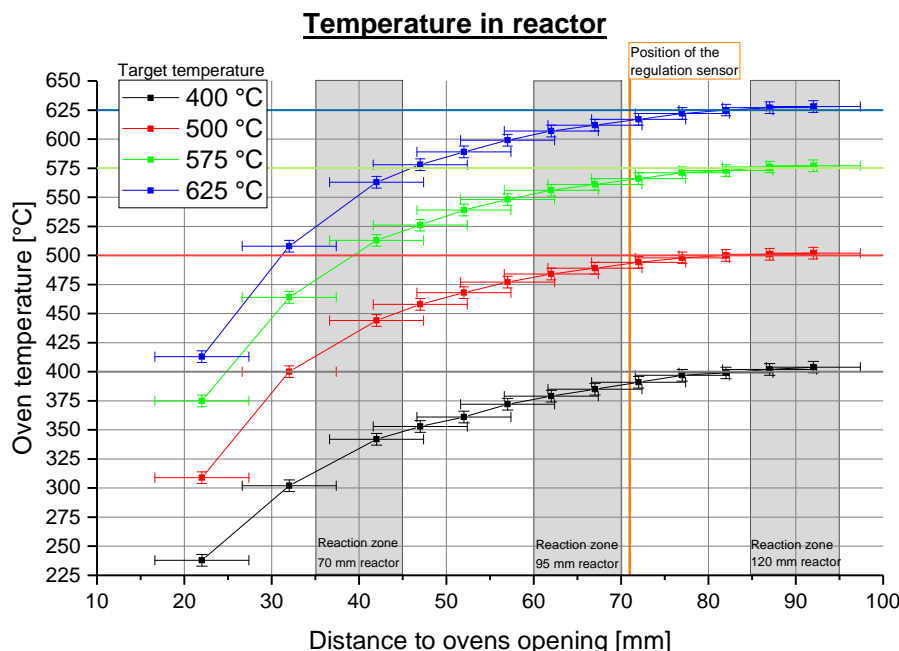


**Figure 3.7.:** Temperature profiles in the reaction zone of the graphitisation reactor in dependency of the distance to the oven's opening. Temperature measurements taken with a Ni-NiCr thermocouple, 1-point calibrated to the regulation sensor at 600 °C. For all points, the measurement probe was placed at the end inside a quartz glass reaction tube ( $L = 12$  cm,  $\varnothing = 6$  mm, WT= 0.5 mm). Grey zones mark the position of the graphitisation catalyst inside the oven for different reaction tube lengths.

To lower the temperature slope towards the opening we fabricated a teflon closure ring with an inner diameter of  $\approx 6$  mm, that fits over the reaction glass tube and covers the oven opening. The temperature tests in Figure 3.7 are done with that closure ring.

### 3.2.6.5. Reaction space

The graphitisation reactions are conducted inside quartz glass tubes (proQuarz,  $L = 95$  mm,  $\varnothing = 6$  mm, WT= 0.5 mm). Other labs use borosilicate glass like Pyrex (Turnbull et al., 2010b) or Duran (Wacker et al., 2010c), that has a melting point of about 600 °C, what leads to an upper threshold for the reaction temperature. Like other labs (e.g. the IUP  $^{14}\text{C}$  laboratory) we chose quartz consisting of pure

### 3. Set-up of the AMS target Extraction and Graphitisation Line

silicium dioxide and a transition point of  $\approx 1200^\circ\text{C}$  (see proQuarz, 2017). However, this material has the drawback of being brittle compared to other glass types and therefore requires careful handling.

The iron catalyst is placed upon a sample scoop (quartz glass,  $L = 10\text{ mm}$  to  $20\text{ mm}$ ,  $\varnothing = 4\text{ mm}$ ), that is pushed to the end of the reaction tube after dosing the  $2\text{ mg}$  to  $5\text{ mg}$  iron catalyst amount on it.

It turned out, that the length of the reaction tube has a significant impact on the graphitisation result. I conducted a number of graphitisations under the same graphitisation parameters comparing different sets of quartz glass reaction tube lengths. Table 3.4 lists the results of these tests.

**Table 3.4.:** Comparison of the influence of different reaction tube dimensions (length  $L$  and wall thickness  $WT$ ) to the duration of the graphitisation and the sample yield. Sample yield has been calculated as percentage of the weight gain during graphitisation from the expected gain calculated by the known amount of  $\text{CO}_2$ . The error of duration is the standard deviation of each sample set; the error of the yield is the sample amount error ( $\pm 0.1\text{ mg}$ ) combined with the SD of the graphite masses;  $N$  is the sample count. All tests were performed with following parameters:  $T_{graph,set} = 575^\circ\text{C}$ ,  $n(\text{H}_2)/n(\text{CO}_2) = 2.2 - 2.4$ ,  $\varnothing_{tube} = 6\text{ mm}$ . Graphitisations were ended, when the pressure slope  $\dot{p}_{graph} > -0.18\text{ mbar min}^{-1}$ . Tests with  $WT = 1\text{ mm}$  were performed at an EGL prototype line, which was manually controlled.

<b>L</b> [mm]	<b>WT</b> [mm]	<b>N</b>	<b>Duration</b> [h]	<b>Yield</b> [%]	<b>Commentary</b>
95	0.5	8	$3.5 \pm 0.2$	$78 \pm 15$	Final choice for EGL
120	0.5	6	$3.9 \pm 0.3$	$77 \pm 10$	
70	0.5	8	$3.9 \pm 0.2$	$36 \pm 39$	Low and variable graphitisation temperature on catalyst (see fig. 3.7)
120, 70	1	25	Not comparable		Difficult handling due to narrow sample scoop

The short (70 mm) tubes showed a very low and at the same time variable sample yield. As seen in Figure 3.7, the catalyst scoops in these tubes are placed in a variable temperature regime  $50^\circ\text{C}$  to  $100^\circ\text{C}$  below the oven's set point. This could lead to an incomplete graphitisation reaction, e.g. by increased methane production.

The 120 mm tubes on the other hand, even though enabling a reaction in a constant and well-set temperature zone, are showing a longer graphitisation duration (0.4 h) than 95 mm tubes. The sample yield for both lengths is indistinguishable inside the error margins. The faster graphitisation time points to more favourable reaction conditions in the 95 mm tubes, which therefore have been chosen for the equipment of the EGL. A possible reason for the difference in durations could be a decreased convection over the catalyst surface for longer reactors and a less efficient water removal. In an EGL prototype system also reaction tubes with only 4 mm inner diameter ( $WT = 1\text{ mm}$ ) have been tested, but have shown an impracticable handling of iron dosing onto the narrower sample scoops.

### 3.2.7. Properties of the whole system

The functional parts of the EGL described above have been assembled at the workshop at the IUP. Figure 3.8 shows a technical scheme of the whole EGL and allocates the respective indices of vacuum sections (green), heating elements (red), pressure sensors (blue) and pneumatic valves (grey), that are used in the following sections as well as in the EGL control software.

Connective tubing consists especially of 1/4" stainless steel tubing (Dockweiler, TCC LZ1.4404/316L (S)) or 1/2" tubing directly on the vacuum pumps (see Section 3.2.7.2). Following connection types are used:

**Tube welding** is used wherever possible for connections, that are not needed to be detachable (e.g. for expendable parts.). All weld seams are helium leak-tested.

**Face-Seal Fittings** (Fitok, 1/4") are used for connection of all pneumatic valves to the tubing system. Seal rings are silver coated stainless steel rings. Face-Seal is equivalent to VCR (Swagelok); statements of both companies about combinability of both systems are contradictory. Leak rate per connection  $<4 \times 10^{-9} \text{ cm}_n^3 \text{ s}^{-1}$  (manufacturer's specifications)<sup>2</sup>.

**Small flanges** (Ger.: Kleinflansch, Pfeiffer Vakuum, ISO-KF, sizes: 16, 25, 40) are used on vacuum valves in the vacuum area and for connection of pirani and cold cathode pressure sensors. Leak rates per connection:  $<9.9 \times 10^{-10} \text{ cm}_n^3 \text{ s}^{-1}$  (manufacturer's specifications).

**Swagelok Tube Fittings** connect working gas tanks and internal CO<sub>2</sub> supply (standard, blank, pure CO<sub>2</sub> QC) to the EGL. Leak rates are not provided, but are said to be lower than Face-Seal Fitting leak rates<sup>3</sup>:  $<4 \times 10^{-9} \text{ cm}_n^3 \text{ s}^{-1}$

All software controlled valves in the EGL are Low Pressure Pneumatic Diaphragm Valve (PDVN – Plastic Diaphragm Valve Nest) (TK-FUJIKIN, S4PDVN-VM-C) with a Ni-Co alloy membrane over a PCTFE (Polychlorotrifluoroethylene) seat. PCTFE is chemically similar to PTFE (Polytetrafluoroethylene), that has proved to be a suitable membrane and sealing material in trace gas handling in the carbon cycle group at the IUP due to its chemical stability. The valves are normally closed, opening is controlled by pressurised air (4 bar to 6 bar), which is controlled by a set of magnetic valves, which are described in Section A.1.4.

#### 3.2.7.1. Section volumes

After assembly of the EGL the volumes of most vacuum sections have been quantified. This has been performed in two steps:

<sup>2</sup>standard cubic centimetre per second

<sup>3</sup>Personal communication: Patrick Düppuis, Swagelok employee

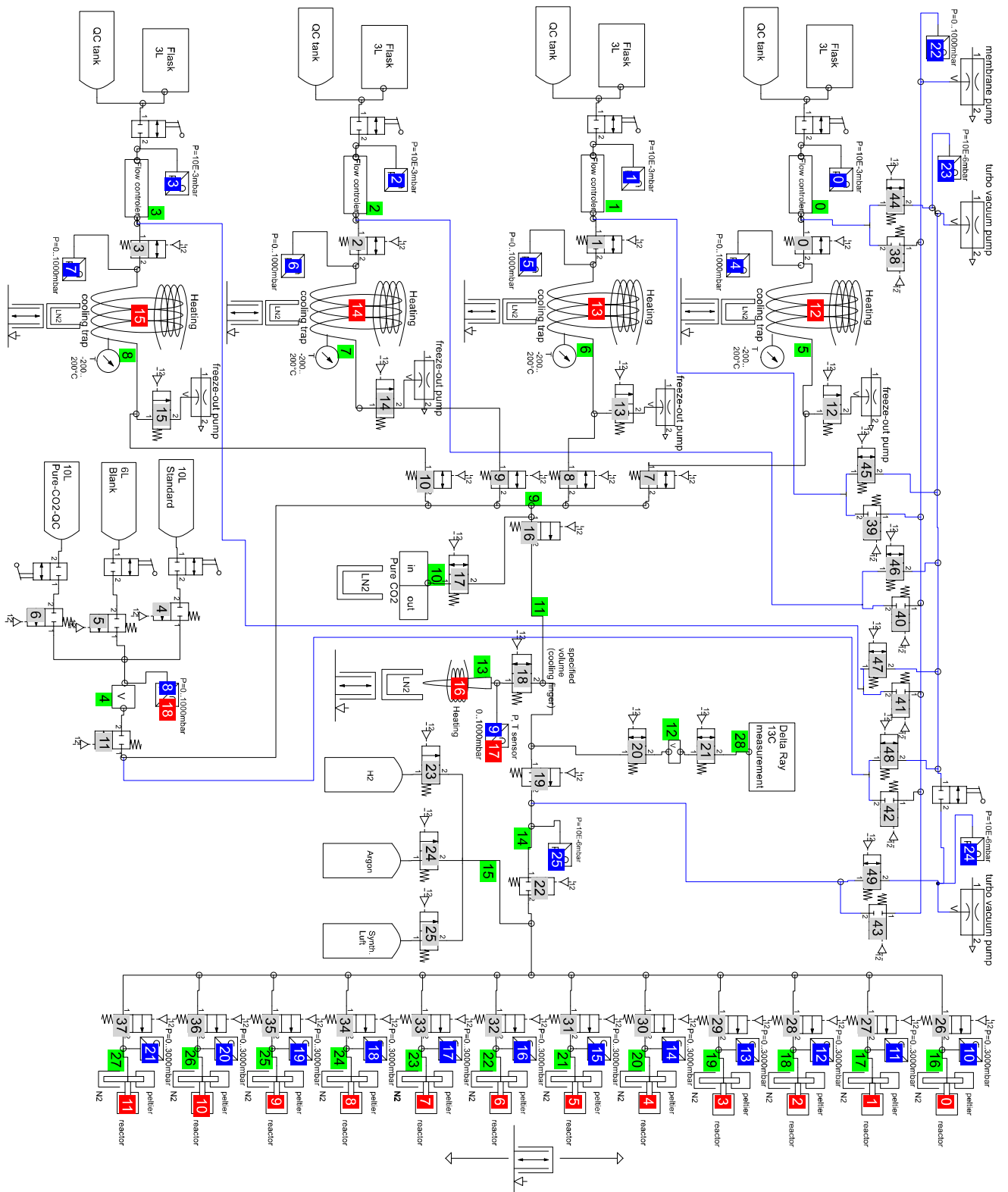


Figure 3.8.: Complete scheme of mechanical and electrical parts of the EGL interacting with the samples. Blue numbers represent pressure sensor indices, red temperature and oven sensor indices, grey valve indices and green vacuum section indices.

**Determination of volume ratios** After evacuation of the whole line the vacuum sections 5, 9, 11, 14 and 15 (green numbers in Figure 3.8) have been filled with  $\approx 900$  mbar Argon, leading to a pressure at sensor  $P_0$  of  $p_{5,9,11,14,15}$ . While keeping the connecting valves between these vacuum sections open, the valve to the respective measured volume  $V_i$  was opened, enabling pressure equalisation. After closure of the valve to the test volume the pressure at  $P_0$  ( $p_{5,9,11,14,15,i}$ ) can be used to calculate a volume ratio  $\frac{V_i}{V_{5,9,11,14,15}}$  with  $V_{5,9,11,14,15} = V_5 + V_9 + V_{11} + V_{14} + V_{15}$ :

$$\frac{p_{5,9,11,14,15}}{p_{5,9,11,14,15,i}} = \frac{V_{5,9,11,14,15} + V_i}{V_{5,9,11,14,15}} = \frac{V_i}{V_{5,9,11,14,15}} + 1 \quad (3.6)$$

These volume ratios were then used to express every  $V_i$  in units of the quantification volume  $V_{13}$ :

$$\frac{V_i}{V_{5,9,11,14,15}} / \frac{V_{13}}{V_{5,9,11,14,15}} = \frac{V_i}{V_{13}} \quad (3.7)$$

Volume ratios  $\frac{V_i}{V_{13}}$  for the sections  $i = 4, 6, 7, 8, 12, 16, 17, 18$  could be directly determined by two pressure measurements as described above. The volume ratios of the sections  $j = 0, 1, 2, 3, 5, 9, 11, 14, 15$  to the quantification volume were calculated indirectly by determining pressure ratios between known sections  $i$  and unknown sections  $j$ . The additional introduced measurement uncertainty due to more required pressure measurements leads to an increased relative volume uncertainty (see Table 3.5).

The main application for this ratio is the  $H_2$  dosing into the reactor. Since a certain  $H_2/CO_2$  ratio is given by the process parameters, the correct  $H_2$  pressure in the reactor can be calculated without thawing and metering the  $CO_2$  there, leading to a  $\approx 3$  min to 5 min shorter preparation time per target.

**Volume measurement of the quantification volume** To calculate absolute volume values for those sections, I transferred a known amount of  $CO_2$  into the quantification volume and determined its pressure and hence its volume  $V_{13}$  and – using the  $\frac{V_i}{V_{13}}$  – the other volumes  $V_i$ . The amount of substance  $n$  was measured by extracting  $CO_2$  from a volume  $V_{air,n}$  (measured by the built-in MFC) of a gas with known  $CO_2$  concentration  $c$ . The extract consisted mainly of  $CO_2$  and  $H_2O$ . Cooling the extract to  $\approx -75^\circ C$  with an Aceton/dry ice mixture lead to separation of water and purification of  $CO_2$ , which has been transferred to the quantification volume and heated to a temperature  $T$ , leading to a pressure  $p_{13}$  in  $V_{13}$ .  $V_{13}$  can be calculated by

$$V_{13} = \frac{nRT}{p_{13}} = \frac{\epsilon c V_{air,n} RT}{p_{13} V_m} \quad (3.8)$$

using the ideal gas equation with ideal gas constant  $R$ , molar volume  $V_m$  and a  $CO_2$  extraction and transfer efficiency  $\epsilon$ , which we assume as 1 since all exhaust

### 3. Set-up of the AMS target Extraction and Graphitisation Line

gas measurements with a Licor analyser showed a concentration below the instrument's detection limit.

**Volume errors** All measured quantities used for the calculations above are error-prone. It is, however, difficult to assign a reliable error value for the effective temperature  $T$  in the quantification volume after thawing the  $\text{CO}_2$ : The part of the quantification volume  $V_{13}$  containing the solid  $\text{CO}_2$  after transfer is heated to  $30^\circ\text{C}$ , while the residual tubing of that part and the internal volume remains at temperatures near laboratory temperature ( $20^\circ\text{C}$ ). Similar to Section 3.2.2.5, I therefore estimated  $(25 \pm 5)^\circ\text{C}$  as effective temperature in  $V_{13}$  during quantification.

Also not known is the uncertainty of the extraction and transfer efficiency  $\sigma(\epsilon)$ . The value of this uncertainty together with variations in the experimental procedure were estimated by double measurements of the volumes and volume ratios.

Table 3.5 shows the volumes and volume to quantification volume ratios for the examined vacuum sections. Knowing the volumes enables tracking of the

**Table 3.5.:** Volumes and volume to quantification volume ratios for different EGL vacuum sections. Errors in absolute volume  $\sigma V_i$  are estimated from double measurements (result differences); the errors for  $V_i/V_{13}$  are derived from deviations in the pressure measurements. The errors in mean reactor and mean cooling trap values includes margins in tubing and reaction glass volumes.

Section index $i$	Volume $V_i$ [ml]	Rel. vol. $V_i/V_{13}$	Description
0	$13.53 \pm 1.01$	$5.030 \pm 0.004$	Sample insertion and FC at port 1
1	$13.54 \pm 1.01$	$5.033 \pm 0.004$	Sample insertion and FC at port 2
2	$13.28 \pm 0.99$	$4.938 \pm 0.003$	Sample insertion and FC at port 3
3	$13.23 \pm 0.99$	$4.920 \pm 0.003$	Sample insertion and FC at port 4
4	$5.50 \pm 0.41$	$2.043 \pm 0.001$	Standard gas volume
5	$29.64 \pm 2.21$	$11.019 \pm 0.008$	Cooling trap port 1
6	$29.11 \pm 2.17$	$10.822 \pm 0.005$	Cooling trap port 2
7	$28.98 \pm 2.16$	$10.773 \pm 0.005$	Cooling trap port 3
8	$29.04 \pm 2.17$	$10.794 \pm 0.005$	Cooling trap port 4
9	$41.12 \pm 3.07$	$15.286 \pm 0.011$	Tubing after $\text{CO}_2$ traps and std. gas vol.
11	$14.84 \pm 1.11$	$5.582 \pm 0.004$	Tubing betw. $\delta^{13}\text{C}$ aliq. and quantific.
12	$1.22 \pm 0.09$	$0.4520 \pm 0.0002$	$\delta^{13}\text{C}$ aliquotation volume
13	$2.69 \pm 0.20$	1	Quantification volume
14	$23.58 \pm 1.76$	$8.765 \pm 0.006$	Tubing after quantification
15	$43.93 \pm 3.28$	$16.333 \pm 0.012$	Tubing to reactors
16	$7.64 \pm 0.57$	$2.842 \pm 0.001$	Reactor 1, $L = 95$ mm
17	$7.64 \pm 0.57$	$2.841 \pm 0.001$	Reactor 2, $L = 95$ mm
18	$7.70 \pm 0.57$	$2.862 \pm 0.001$	Reactor 3, $L = 95$ mm
16, 17, 18	$7.66 \pm 0.57$	$2.85 \pm 0.01$	Mean reactor
6, 7, 8	$29.04 \pm 2.17$	$10.80 \pm 0.02$	Mean cooling trap

sample amount for quality control during routine operation, by measuring the CO<sub>2</sub> pressure in the respective volumes. The errors in the volume ratios are small ( $\leq 0.012$ ) due to low relative errors in the pressure measurements. The error in the absolute volumes originates in the error in volume determination of  $V_{13}$ , here dominates the experimental error in transfer efficiency  $\sigma(\epsilon)$ , estimated by double measurements.

It would be beneficial, to execute more measurements for the absolute value of  $V_{13}$  in the future to decrease the error of currently 7% on the volumes.

#### 3.2.7.2. Evacuation

The EGL evacuation system (blue lines in Figure 3.8) is structured on two levels: The first step is always to evacuate the bulk of gas amounts with an high throughput membrane pump (vacuubrand, *MD 1*) to a pressure  $<5$  mbar. Then the evacuation switches to one of two turbo molecular vacuum pumps (Pfeiffer Vacuum, *HiCube*) to finish evacuation until medium to high vacuum, depending on pumping time. This approach has three main advantages over using the turbo pump in the first place:

- When facing large amounts of medium, exceeding an internal threshold, the turbo vacuum pump performs an emergency shut-off. The two-level approach eliminates this issue and possible sample loss due to evacuation breakdown and contamination with laboratory air.
- The operating life of the turbo pumps is prolonged, since the stress on the blades of the turbo pump is reduced, due to lower molecule counts to be evacuated.
- The pumping performance of the whole system is increased, as the turbo pump can constantly operate on maximum rotational speed and maintains high vacuum ( $10^{-6}$  mbar) in the volume before the pump.

The evacuation system reaches pressures of about  $7 \times 10^{-7}$  mbar near the turbo pump and  $8 \times 10^{-5}$  mbar at sensor  $P_{25}$  at a central position in the EGL.

**Leakage evaluation** To examine leakage rates and their influence on the  $\Delta^{14}\text{C}$  results, a comprehensive pressure test of the vacuum sections of the EGL has been performed. Figure 3.9 shows the pressure increase in closed sections or sets of sections after more than 4 d of precursory evacuation.<sup>4</sup> The pressure increase of the graphitising reactors has not been measured directly this way, since it is highly variable and dependent on wear parts like o-rings and quartz glass reaction tubes. Instead, process data of 475 EGL graphitisations has been used: Preceding every catalyst pretreatment, a 5 min pressure test after evacuation to  $2.2 \times 10^{-3}$  mbar for

<sup>4</sup>This test has been executed after preliminary pressure tests lead to identification and removal of severe post-assembly leakages.

### 3. Set-up of the AMS target Extraction and Graphitisation Line

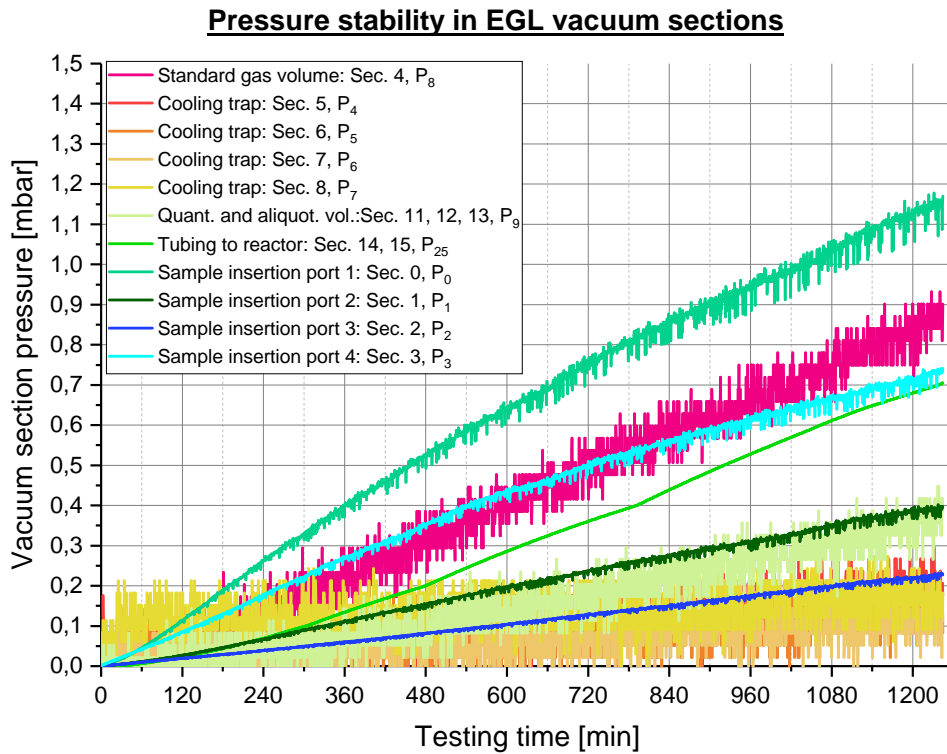


Figure 3.9.: Pressure increase during 1 d in EGL vacuum sections after >4 d evacuation and closing of the listed sections or sets of sections. The measurement values scatter differently, because of different types of used pressure sensors:  $P_0 - P_3$ : pirani pressure sensors,  $P_4 - P_9$ : linear sensors,  $P_{25}$ : cold cathode sensor.

each reactor is performed by default; the pressure increase is saved to the CRL database. Using this quality control data I estimated a mean reactor pressure increase rate.

For sections with known volume  $V$  the pressure increase rate  $\dot{p}$  can be utilised to calculate a standardised leaking rate  $R_L$

$$R_L = \frac{V \cdot \dot{p}}{p_n} \quad (3.9)$$

with the standard pressure  $p_n = 1013.3$  mbar. This rate can be caused by external leakage, e.g. through vacuum screw connections or imperfect welding seams, hence leading to a contamination with laboratory air. Alternatively, not properly closing pneumatic valves could cause internal leakage. This is especially important for the standard gas volume (vacuum section 4), where internal leaking could cause a contamination of the standard, blank or pure  $\text{CO}_2$  quality control target with  $\text{CO}_2$  holding a very different  $\Delta^{14}\text{C}$  value (e.g.  $-1000$  ‰ blank with  $341$  ‰ Oxalic Acid II).

To judge the influence of these leakages, I estimated a possible CO<sub>2</sub> contamination  $\mu$  using

$$\mu = \frac{R_L t_{typ} c}{n_{typ} V_m} \quad (3.10)$$

where  $t_{typ}$  indicates a typical time of residency for the processed gas in the respective volume,  $n_{typ} = 100 \mu\text{mol}$  is the typical CO<sub>2</sub> amount of a sample and  $c$  is the concentration of CO<sub>2</sub> in the contaminating gas:  $c = 1$  for pure CO<sub>2</sub> and estimated as  $c = 500 \mu\text{mol mol}^{-1}$  for laboratory air.

Table 3.6 lists the results of these calculations, showing  $\dot{p}$ ,  $R_L$  and  $\mu$  for all tested sections. Evidently,  $\mu$  is most important in the standard gas volume, since a contamination with pure CO<sub>2</sub> from other tanks can't be excluded. The contamination

**Table 3.6:** Pressure increase after evacuation, leakage rates and CO<sub>2</sub> contaminations in different EGL sections. Errors in  $\dot{p}$  are derived from the uncertainty in pressure measurement. Errors in  $R_L$  and  $\mu$  additionally include errors in the volume determination (see Table 3.5).

Tested section	Mean press. slope $\dot{p}$ [mbar min <sup>-1</sup> ]	Leak rate $R_L$ [cm <sup>3</sup> s <sup>-1</sup> ]	Possible CO <sub>2</sub> contam. $\mu$ [%]
Mean reactor	$(1.7 \pm 3.0) \times 10^{-2}$	$(2.1 \pm 3.8) \times 10^{-6}$	$(6.8 \pm 12.2) \times 10^{-4}$
Standard gas volume	$(7.2 \pm 1.2) \times 10^{-4}$	$(6.6 \pm 1.2) \times 10^{-8}$	$(2.6 \pm 0.5) \times 10^{-3}$
Cooling trap port 1	$(1.5 \pm 1.2) \times 10^{-4}$	$(6.9 \pm 5.8) \times 10^{-8}$	$(2.8 \pm 2.3) \times 10^{-6}$
Cooling trap port 2	$(0.6 \pm 1.2) \times 10^{-4}$	$(3.1 \pm 5.8) \times 10^{-8}$	$(1.2 \pm 2.3) \times 10^{-6}$
Cooling trap port 3	$(0.9 \pm 1.2) \times 10^{-4}$	$(4.2 \pm 5.8) \times 10^{-8}$	$(1.7 \pm 2.3) \times 10^{-6}$
Cooling trap port 4	$(1.5 \pm 1.2) \times 10^{-4}$	$(6.9 \pm 5.8) \times 10^{-8}$	$(2.8 \pm 2.3) \times 10^{-6}$
Quantific. and aliquot.	$(3.1 \pm 1.2) \times 10^{-4}$	$(9.7 \pm 3.8) \times 10^{-8}$	$(3.9 \pm 1.5) \times 10^{-6}$
CO <sub>2</sub> transfer to reactor	$(9.4 \pm 0.6) \times 10^{-4}$	$(1.0 \pm 0.1) \times 10^{-6}$	$(5.6 \pm 0.4) \times 10^{-5}$
Sample insertion port 1	$(9.4 \pm 0.9) \times 10^{-4}$	$(2.1 \pm 0.2) \times 10^{-7}$	$(1.1 \pm 0.1) \times 10^{-5}$
Sample insertion port 2	$(3.2 \pm 0.3) \times 10^{-4}$	$(7.1 \pm 0.7) \times 10^{-8}$	$(3.8 \pm 0.4) \times 10^{-6}$
Sample insertion port 3	$(1.9 \pm 0.2) \times 10^{-4}$	$(4.2 \pm 0.4) \times 10^{-8}$	$(2.2 \pm 0.2) \times 10^{-6}$
Sample insertion port 4	$(6.0 \pm 0.6) \times 10^{-4}$	$(1.3 \pm 0.1) \times 10^{-7}$	$(7.0 \pm 0.7) \times 10^{-6}$

in the reactor during graphitisation is also relevant, due to long residency time and a relatively high leaking rate there. On the other hand, contamination during extraction or quantification and aliquotation is as negligible as the one during sample transfer inside the EGL.

Assuming now the most considerable contamination  $\mu = (2.6 \pm 0.5) \times 10^{-3} \%$  with the – at the moment – largest possible  $\Delta^{14}\text{C}$  difference in the EGL ( $\Delta(\Delta^{14}\text{C}) = 1334 \text{‰}$ ), we can determine the additional error on the  $\Delta^{14}\text{C}$  analysis due to EGL leakages  $\sigma_\mu$  as  $\sigma_\mu = \Delta(\Delta^{14}\text{C}) \cdot \mu = (0.030 \pm 0.007) \text{‰}$ . This value is negligible (two orders of magnitude smaller) compared to the uncertainties in AMS analysis, that means we don't expect any influence on the target quality due to EGL leakage at

### 3. Set-up of the AMS target Extraction and Graphitisation Line

the current state, following the pressure test protocols at the beginning of each preprocessing.

#### 3.3. Regulation electronics and user interface

In this section the principal electrical interconnection of the EGL is shown. A detailed list and description of the individual components and useful information for the hardware control is given in the annex in Section A.1. Figure 3.10 gives a schematic overview of the electric interconnection of the EGL. The type of interconnection is represented by the line colour.

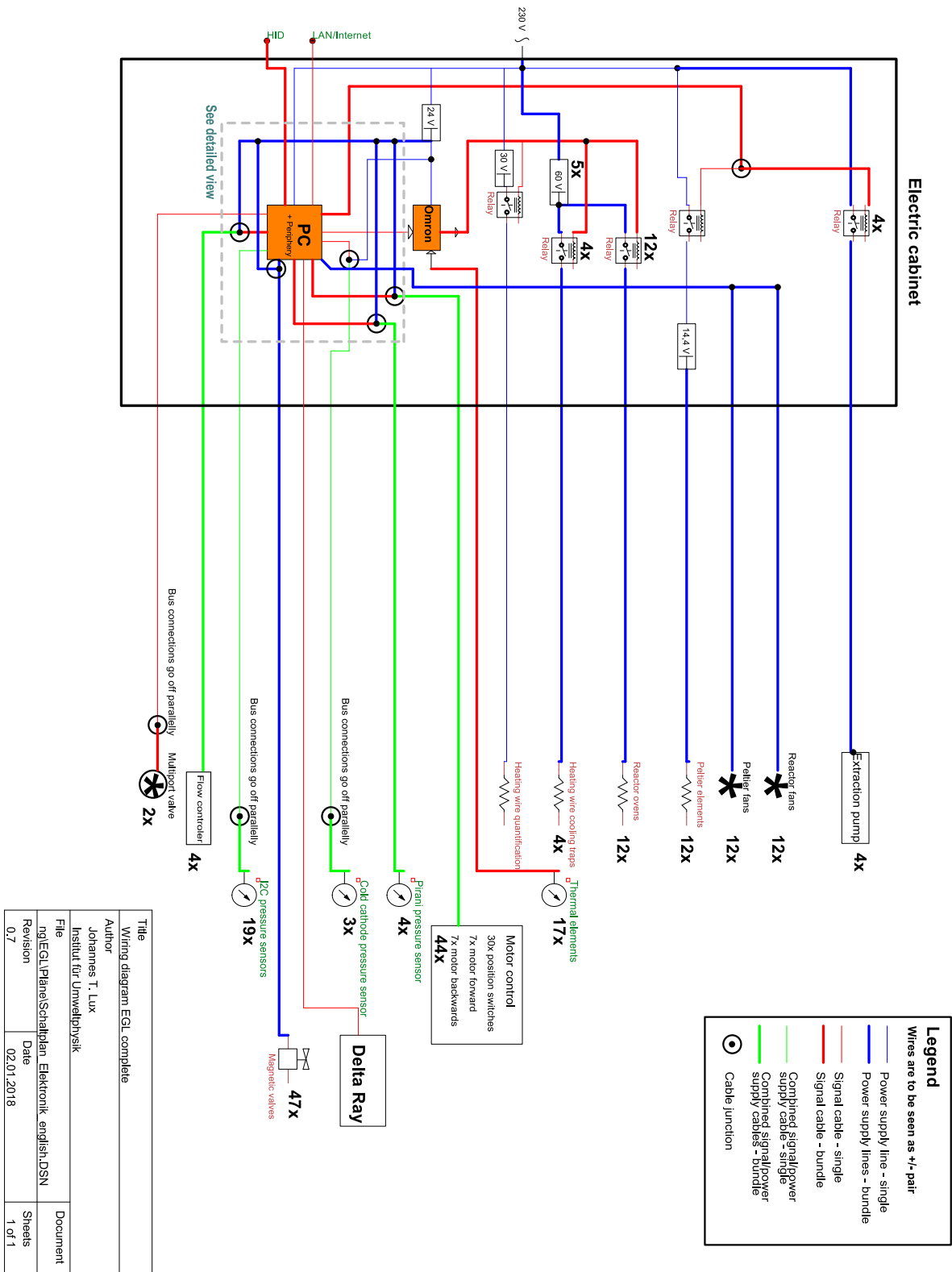
All power supply units except the 5 V power supply for the I<sup>2</sup>C sensors, current switching semiconductor relays, almost all communication and steering electronic as well as the controlling PC are built into an 1798 mm × 800 mm × 600 mm electric cabinet (Pentair Technical Solutions, *Eurorack*). The connection between the sample processing part and the electric cabinet is provided by a set of bundled cable equipped with standardised plugs for connection. This separation between sample processing and electronic was introduced for four main reasons:

- Providing accessibility of the electronics in case of malfunction and debugging, as well as giving enough space in the cabinet to allow for adapting wiring of the components if necessary.
- Open electric contacts above the legal contact voltage threshold of AC 25 V<sub>eff</sub> and DC 60 V are separated from the laboratory environment to avoid harmful electrical contacts.
- During target preprocessing liquid nitrogen is used, furthermore on cold surfaces on the EGL air moisture condenses in considerable amounts. This approach prevents damage on the electric components by contact with liquids.
- Splitting of the EGL into two parts allowed transport of the system from the construction to the laboratory area and facilitates the transport in case of future design changes, when necessary.

Figure 3.11 illustrates the part of the electronics marked by the dashed grey box in Figure 3.10, which is the controlling PC with periphery, i.e. digital or analogous input/output (I/O) devices. All components have been chosen regarding to functionality and the existence of LabVIEW drivers or the possibility to write new drivers in the framework of this thesis.

#### 3.4. Development of the EGL control software

A control software has been developed in the framework of this work, which parallelises, standardises and automatises the target preparation processes as well as



Title	Writing diagram EGL complete	
Author	Johannes T. Lux	
File	ngEGL/Platne/Schaltplan_Elektronik_english.DSN	
Revision	Date	Sheets
0.7	02.01.2018	1 of 1

Figure 3.10.: Schematic view of the interconnection regarding signalling and power supply of the electrical components of the EGL. A detailed view of the PC, its periphery and directly connected devices (grey, dashed box) is given in 3.11.

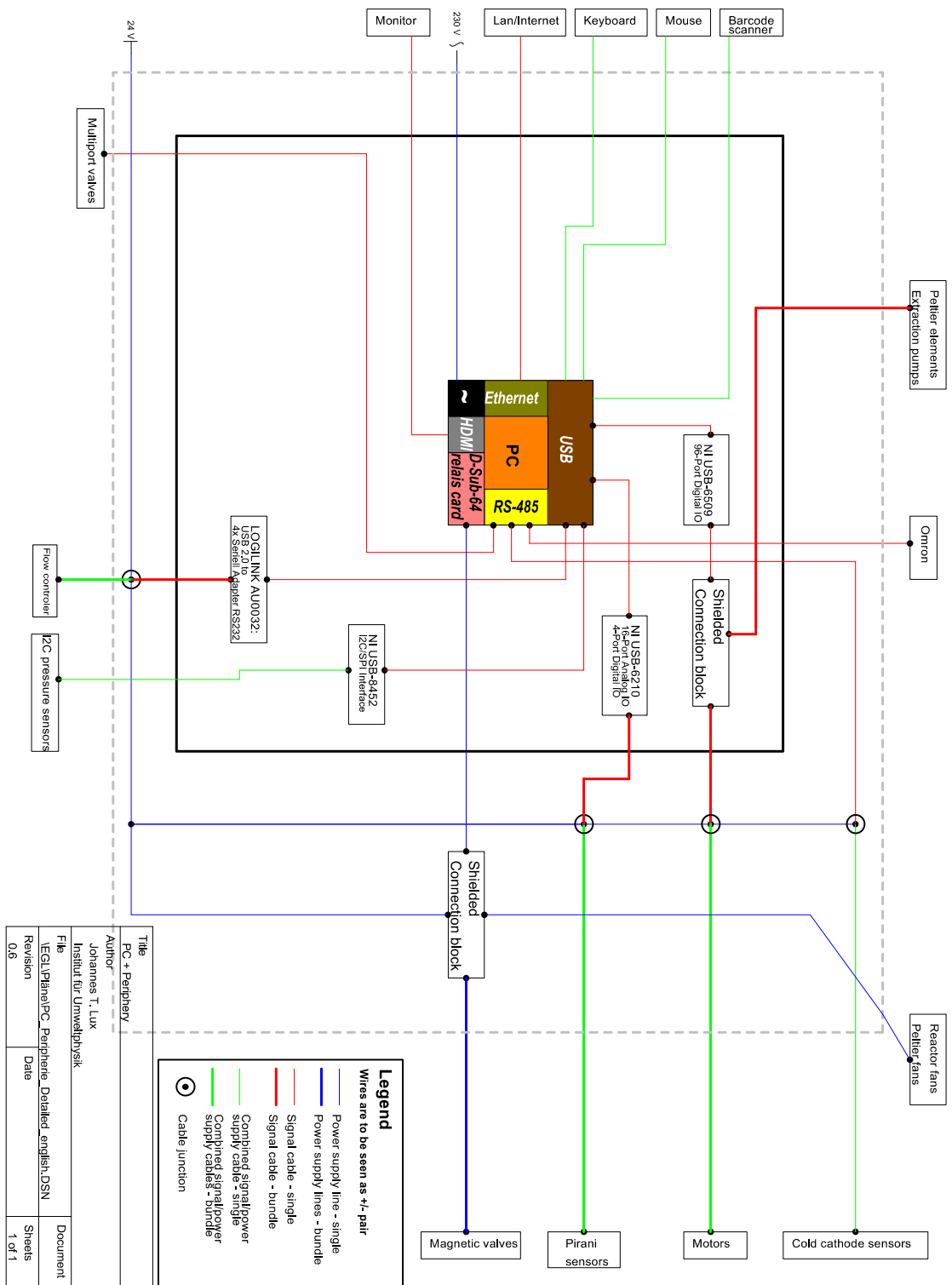


Figure 3.11.: Detailed view of the controlling PC, its periphery and directly connected devices. The used communication interfaces are shown in different coloured boxes.

guides the technician through the steps of procedure, which have to be done manually. All regulation electronics, presented in Sections 3.3 and A.1, are controlled by this software. The software has been developed in the LabVIEW environment, since it features the intrinsic possibility to parallelise sub-processes and, foremost, is supported by driver software by a large part of the suppliers of the electronic components of the EGL.

#### 3.4.1. User Interface

The software presents its functionality in high clarity. Interactive elements, which are needed in routine operation, are displayed prominently. Settings for process parameters and software properties, which need to be altered only occasionally, can be directly changed in an annotated configuration file. This design choice has the purpose to clarify at all times during routine operation, which steps have to be performed to ensure an as efficient operation as possible.

During routine operation one of the EGL screens displays an interactive graphical representation of the EGL, shown in Figure 3.12. It shows the evacuation state of the different vacuum sections of the EGL (e.g. “evac finished” or “section blocked for evacuation”) as well as the opening states of all pneumatic valves, the position of the multiport valves going to  $\delta^{13}\text{C}$  measurement, working state of the extraction pumps and the outputs of all sensors built in the EGL. Therefore, this overview provides the user comprehensive information about the current state of the system and enables intuitive control of the EGL by manually switching valves and pumps directly in the scheme.

The second screen is showing the control surface, usually the graphitisation surface guiding through the sample processing (see Figure 3.13). The properties of the different control panels are explained in the following.

##### 3.4.1.1. Target compilation

The User Interface (UI) at the “Prepare Graphitisation” tab (see Figure B.8) provides the main linkage of the EGL control software to the CRL database. A list of samples present at the CRL is displayed, showing the estimated sample size based on  $\text{CO}_2$  concentration and sample volume. These samples can be selected for graphitisation here as well as predetermined for sample splitting. This means, that large samples can be split off here in several new samples in the database. A split air sample is not completely extracted in automatic processing, but regarding to its expected size and the amount of splits ought to be produced from it. New targets for the database can be created here as well; this is required for targets produced at the EGL, i.e. QC targets and standards.

In this UI, the targets for the respective next graphitisation procedure can be compiled manually or chosen automatically: Originating from a predefined magazine composition (e.g. Table 2.6), the software scans the database for targets,

### 3. Set-up of the AMS target Extraction and Graphitisation Line

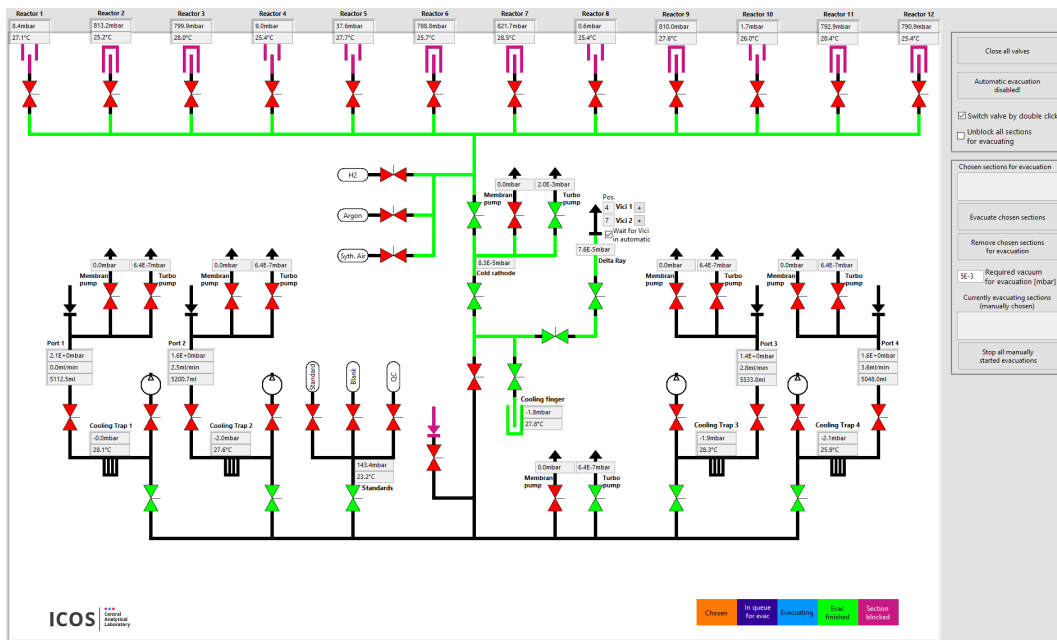


Figure 3.12.: Graphical representation of tubing, reactors, measurement devices, evacuation and valve control in EGL control software. The evacuation status of the EGL parts is displayed in different colours.

Prepare Graphitisation Control Graphitisation Diagrams Simulation Debugging Load Backup Exit

General Broadcasts Scanned ID  
 test at Port 1 done in 192 seconds. \*\*\* Sample container HD005a for reactor 7 ready to be scanned! \*\*\* Sample container HC

General Tasks Done! Alarm!

Reactors	Conditioning States	Preproc. ID	Preprocessing States	Port	Graph. ID	Graphitising States	Current tasks	Done!
1	Not conditioning	11980	Start processing	Port 2	69325	Graphitising	Please close last flask, close QC-direct valve, insert new sample and open the hand valve to Port 2.	Done!
2	Not conditioning	69328	Pressure Test	Port 1		Not graphitising		Done!
3	Not conditioning	69327	Start processing	Port 3		Not graphitising		Done!
4	Not conditioning	69324	Expanding	Standard		Not graphitising		Done!
5	Not conditioning	69326	Start processing	Standard		Not graphitising		Done!
6	Not conditioning	11983	Start processing	Port 4		Not graphitising	Please close last flask, close QC-direct valve, insert new sample and open the hand valve to Port 4.	Done!
7	Not conditioning	11975	Start processing	No Port Assigned		Not graphitising		Done!
8	Not conditioning	11981	Start processing	No Port Assigned		Not graphitising		Done!
9	Not conditioning	11982	Start processing	No Port Assigned		Not graphitising		Done!
10	Not conditioning	11976	Start processing	No Port Assigned		Not graphitising	Do you want to start the processing of the sample HEI_1_140519_070000.split1 now?	Done!
11	Not conditioning	11979	Start processing	No Port Assigned		Not graphitising	Do you want to start the processing of the sample HEI_1_140602_070000.split1 now?	Done!
12	Not conditioning	11978	Start processing	No Port Assigned		Not graphitising	Do you want to start the processing of the sample HEI_2_140526_131400.split1 now?	Done!

Figure 3.13.: User interface of the EGL control software for automatic sample processing.

already assigned to the current magazine, and adds or creates targets for the next graphitisation, which are missing to accomplish this composition.

#### 3.4.1.2. Catalyst pretreatment and graphitisation

The “Graphitisation” section (see Figure 3.13) represents the main control interface during routine operation of the EGL. It displays for every graphitisation reactor the current state of the respective catalyst conditioning (e.g. “1st conditioning with H<sub>2</sub>”), target preprocessing (e.g. “Quantification”) and graphitising. Furthermore, corresponding manual tasks to every target are displayed, in particular regarding sample insertion and keeping the N<sub>2</sub>(l) dewars filled, which can be confirmed by the technician after completion. On this surface, also the sample registration (pure CO<sub>2</sub> or flasks) by container ID scanning takes place.

#### 3.4.1.3. Process monitoring, direct control and process simulation

All pressure values in the parts of the EGL containing processed CO<sub>2</sub> are continuously monitored during automatic processing. The UI section “Diagrams” (Figure B.9) shows the courses of pressures and flow rates for CO<sub>2</sub> extraction, transfer, quantification and graphitisation.

The tab control “Control” provides direct manual access to the control parameters, which are utilised by the automatic processing. This means, sample processing is possible manually without software guidance as well.

Finally, a process simulation has been implemented: To every valve a flow resistance and to every EGL vacuum section a volume value has been assigned. After simulated sample insertion, a pressure exchange defined by these parameters is calculated on every valve, effectively enabling simulation of evacuation and sample transfer in the EGL. This feature facilitates testing of newly developed software components, without potentially erroneously addressing the hardware components of the EGL.

#### 3.4.2. Pipelining of the tasks

As described in Section 3.1 and Table 3.1, a serial conduct of the required processing steps would not be possible in CRL routine operation, since the amount of working minutes required per target sums up to 30.5 min to 78.5 min between finishing of catalyst pretreatment and start of graphitisation. When introducing the choices for construction components for the EGL in Section 3.2, I motivated the different levels of parallelisation: 4× CO<sub>2</sub> extraction, 1× CO<sub>2</sub> quantification, pure CO<sub>2</sub> insertion and standard gas sampling as well as 12 graphitisation reactors and 2 independent evacuation lines. Here, I explain principally how the potential for parallelisation in the different compartments of the EGL has been realised programmatically by the EGL control software.

### 3. Set-up of the AMS target Extraction and Graphitisation Line

During routine operation, unforeseeable incidents can delay further processing of a sample (e.g. leakages at flask connection or prolonged CO<sub>2</sub> transfer time due to unexpected high humidity in the sample). A predefined process sequence would be delayed by the same amount of time even if set up in a parallel matter. For this reason, I developed a system of 25 parallel running finite state machines<sup>5</sup>, which can flexibly make use of opening time windows, while following a set of rules to prohibit unwanted interaction of the processes. Figure 3.14 gives a simplified overview about the set-up system of state machines, which interact with the other essential program components, namely UI, hardware control, database communication and backup system. In the following, these components will be explained in short.

**Hardware control & sensing:** A common principle in component development of the EGL control software is the centralisation of hardware interaction. This means, every hardware control, presented in Section 3.3, is implemented once in the software and being conducted regularly (every 100 ms to 1000 ms). Every request for hardware actions (e.g. setting of the reactor oven temperature) or sensing data (e.g. pressure values) by other program components is performed via internal variables. This approach prevents access violation on the respective communication buses and unexpected hardware behaviour by simultaneous access by different processes.

**Conditioning state machine:** This state machine waits until the technician confirms catalyst insertion into the chosen reactors and conducts the defined pretreatment routine (see Section 1.4.3.1) for all catalysts, supposing the respective reactors are not occupied by the graphitising state machines. Vice versa, successful completion of the conditioning is a prerequisite for transferring a target into the reactor for the other state machines. At all times, the state is published to the other program components.

**Preprocessing state machines:** This part is the core component of the software, since it covers all steps from sample registration at the EGL until start of the graphitisation process. The software runs one preprocessing state machine for every graphitisation reactor and potential target in preprocessing. At all times, the state is published to the other program components. In case of a delay of one of the machines, the other 11 can freely pass by, if the delayed process is not blocking a singular physical EGL component (e.g. quantification volume). After transfer to the reactor, expansion of the condensed CO<sub>2</sub> and start of the chemical reaction, the respective target is handed over to one of the graphitising state machines, freeing the preprocessing for a new target, which can in principle be started to process during graphitisation in

---

<sup>5</sup>According to Kent and Williams (1991), a finite state machine is a mechanism for defining algorithms in terms of memory (state variable), which can take a defined, finite number of values (its states). A set of processing rules defines for a particular input, what state changes (transitions) and actions (outputs) are performed.

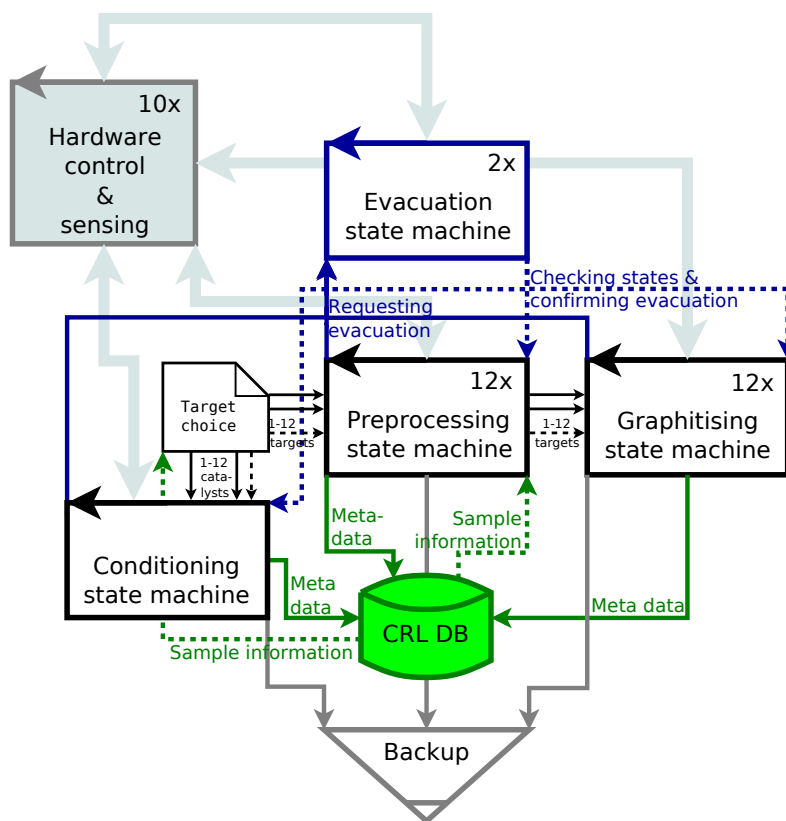


**Figure 3.14.:** Simplified overview chart about the data flow and process arrangement in the EGL control software. Target preparation usually starts at the left side with “Target choice”. The numbers  $Nx$  on the top right of the process loops indicate the number of parallel processes of the respective type. Small arrows show the main data flow pathways in the program. Broad grey arrows indicate communication with the EGL hardware.

the allocated reactor. This facilitates high-throughput processing in case of important or numerous pending samples.

**Graphitising state machines:** Analogous to preprocessing, these machines monitor the graphitisation processes and initiate the reaction end by reactor evacuation and subsequent filling of the reactor with insulation gas (Ar).

**Evacuation state machines:** The two evacuation state machines are responsible for the evacuation of the sampling and extraction region, respectively the quantification and reactors region of the EGL. They serve as “doormen” to prevent evacuation or mixture of targets in commonly used EGL components: The conditioning, preprocessing and graphitising processes enqueue their evacuation requests, assigned with priority values. The requesting state

### 3. Set-up of the AMS target Extraction and Graphitisation Line

machine has to wait with proceeding to the status, where the evacuation is needed, until the evacuation is confirmed by the evacuation state machine. The evacuation state machines handle these requests beginning with the first entry with the highest priority. Simultaneously, all public states of the other state machines are checked for states, which block evacuation of certain EGL sections (e.g. the state "Fillig reactor with H<sub>2</sub>" blocks the evacuation of the respective reactor and the tubing to the H<sub>2</sub> tank). Blocked evacuations are skipped, leading to a flexible adaptation to the current overall status of the EGL and immediate evacuation of the most important free sections. Furthermore, an automatic evacuation is conducted for free sections, when no other evacuation request is pending, to keep the EGL in an evacuated state at all times.

**Database communication:** The EGL control software is inextricably linked to the CRL database (CRL DB). Metadata occurring during conditioning, preprocessing and graphitising are routinely stored into the DB, linked to the respective sample ID of the processing target. The user interface is fed by sample information from the DB to provide support to the technician. During preprocessing, potential handling mistakes or sample defects ought to be revealed by comparison of process data with known sample properties from the DB (e.g. actual extraction volume vs. container volume and sample pressure from DB).

**User interface:** The UI is updated every 500 ms with the current states of all running state machines. If a state transition requires an action of the technician, the machine sends the corresponding task to the task interface in the graphitisation UI and waits for task confirmation by operation of the "Done!" button. All measurement values are updated regularly in the UI as well.

**State backup:** Since many tasks and operations are performed parallelly at the EGL, it would be difficult for the user to remember the states of every target after a computer crash or blackout. To prevent sample loss in these cases, a backup process is running, which regularly (by default every 20 s) saves all software states at the hard drive of the computer. These can be loaded into the program after restart.

#### 3.4.2.1. Optimised processing chain

The self-organised process organisation, outlined above, works well in current routine operation. After catalyst pretreatment, we reach a target transfer rate into the reactors of up to 1/15 min, which is more than a factor of two faster than the fastest estimated subsequent processing time of 30.5 min, derived from Table 3.1. The largest delay in time is observed, when processing humid flask samples, whose CO<sub>2</sub> transfer times inside the EGL differ by a factor 2 to 4 compared to dry CO<sub>2</sub> targets.

### 3.5. Optimisation of the graphitisation parameters

As outlined in Section 1.4.3, a wide variety of chemical reactions takes place in the graphitisation reactor, depending on the reaction conditions. Incomplete graphitisation can lead to kinetic or equilibrium fractionation (see Section 1.2.2). In this section, I present test series, that have been conducted to adjust the preprocessing parameters to optimise AMS target quality.

The graphitisation parameter test series have been designed considering the estimated strength of the influence of the varied parameters and the number of tests that had to be performed to achieve a comprehensive set of graphitisation parameters. Figure 3.15 gives a schematic overview of the experiment planning and the available parameters to judge the graphitisation performance.

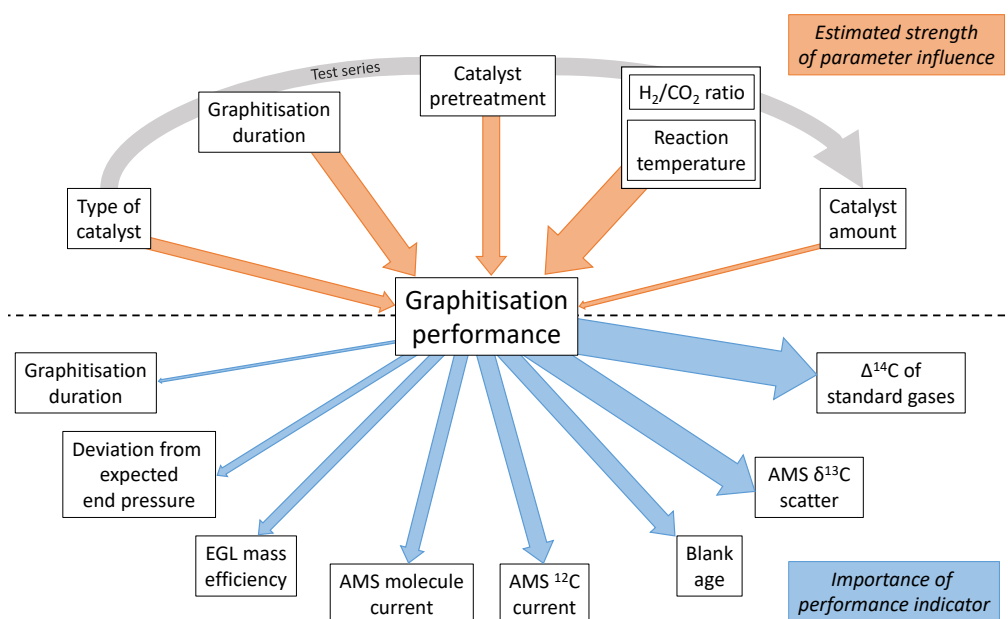


Figure 3.15.: Scheme of the adjustable (orange) and measurable (blue) parameters for the EGL parameter test. Width of arrows indicates the estimated strength of the corresponding signal for test series order (top) and parameter selection (bottom).

In this test series a total of 168 graphite targets has been prepared using gases with known nominal  $\delta^{13}\text{C}$  and  $\Delta^{14}\text{C}$  values. These were sampled from Oxalic Acid II and  $^{14}\text{C}$  free blank gas containers, which have been permanently installed at the EGL (see 3.2.1.3).

108 targets have been analysed by AMS; 68 of these are Oxalic Acid II targets and 40 blanks. Standardisation of the AMS results according to the scheme shown in Section 1.4.2.4 has been performed by concurrently measured Oxalic Acid II targets prepared at the target preparation line at the CEZ  $^{14}\text{C}$  laboratory in Mannheim. In the course of the test series, a number of graphitisation parameter sets

### 3. Set-up of the AMS target Extraction and Graphitisation Line

$P$  have been developed, starting from the parameter set of the IUP  $^{14}\text{C}$  laboratory  $P_{iup}$  (see Table 2.1).

#### 3.5.1. Overview of performance indicator choice

On the basis of long-term experiences at the IUP graphitisation line (see Section 2.1) and preparatory tests on the EGL, as well as results of other labs (e.g. Němec et al., 2010), I chose the performance indicators, presented in the following subsections, for examination of the test series, ordered by the assigned importance.

##### 3.5.1.1. $\Delta^{14}\text{C}$ of standard gas

The variability and the absolute value of the  $\Delta^{14}\text{C}$  analysis is the most important indicator, since the EGL performance is crucially dependent on the stability of  $\Delta^{14}\text{C}$  results. It has been evaluated as the AMS  $\Delta^{14}\text{C}$  of the Oxalic Acid II samples. Comparisons with the nominal value of  $\Delta^{14}\text{C} = 340.07 \text{ ‰}$  should be made with regard to the fact, that the samples have been standardised using CEZ targets, which were prepared under different but constant graphitisation parameters. Therefore, main focus is the scatter of the samples under certain conditions.

##### 3.5.1.2. AMS $\delta^{13}\text{C}$ scatter

I evaluated the deviations of the samples from their nominal  $\delta^{13}\text{C}$  value, which is  $-19.3 \text{ ‰}$  for Oxalic Acid II and  $-37.4 \text{ ‰}$  for the blank  $\text{CO}_2$  used in this study.  $\delta^{13}\text{C}$  is an essential parameter to optimise, since it directly yields a measure to quantify the fractionation during preprocessing, graphitisation and AMS analysis, while the  $\Delta^{14}\text{C}$  value only shows fractionation effects, that are not corrected by the normalisation to  $\delta^{13}\text{C} = -25 \text{ ‰}$  (see (1.9)). In general, we aim to uphold a high level of reproducibility in all measurements, this includes the  $\delta^{13}\text{C}$ , which directly influences the  $\Delta^{14}\text{C}$  results by the normalisation procedure.

Furthermore, as explained in Section 1.2.2.4, deviations from a fractionation exponent  $b = 2$  lead to a systematic error in the  $\Delta^{14}\text{C}$  results. In order to illustrate this effect, Figure 3.16 shows the deviation of the target gas results, prepared at the graphitisation line of the IUP  $^{14}\text{C}$  laboratory, depending on its  $\delta^{13}\text{C}$ .

The linear fit, applied to these results, indicates a mean  $\Delta^{14}\text{C}$  deviation of the normalised values of  $(0.17 \pm 0.08) \text{ ‰}$  per  $\text{‰}$  deviation in  $\delta^{13}\text{C}$ . Even though the majority of the scatter originates from other sources (discussed in Section 2.2), which the linear model can not represent, a part of the  $\Delta^{14}\text{C}$  deviation is significantly linearly correlated to the AMS  $\delta^{13}\text{C}$ .

To gain further insight in the responsible effects, I re-evaluated the normalisation of the points given in Figure 3.16: A fractionation factor of  $b = 1.85 \pm 0.06$  would cancel out the linear dependency of  $\Delta^{14}\text{C}$  on  $\delta^{13}\text{C}$ . This factor compares well to  $b = 1.882 \pm 0.019$ , found by Fahrni et al. (2017) for graphitisation of Oxalic

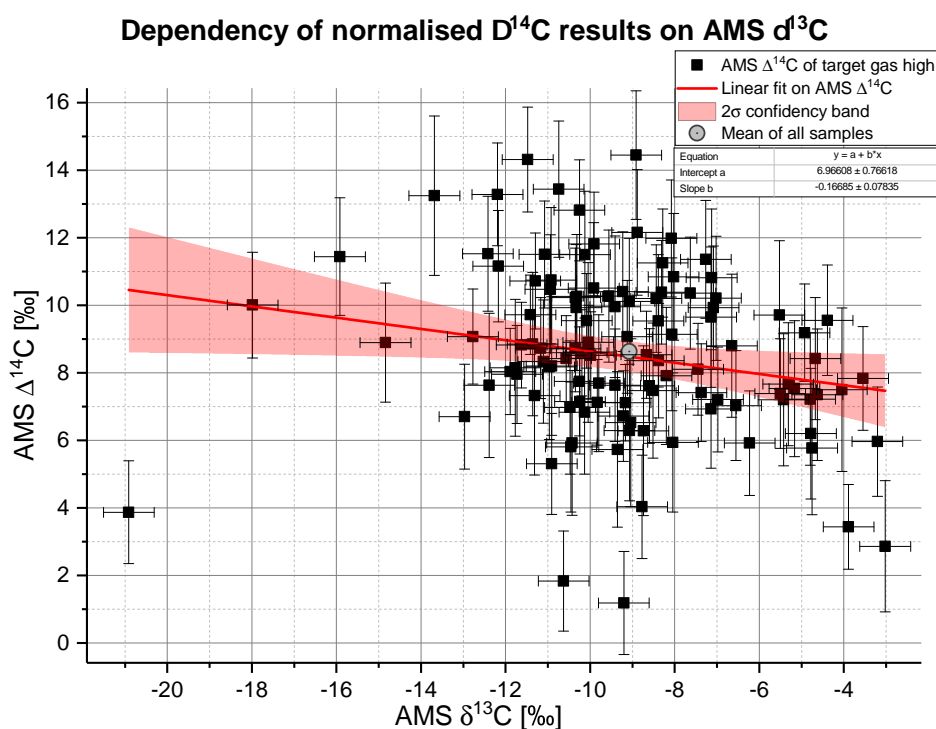


Figure 3.16.: Dependency of  $\Delta^{14}\text{C}$  results of target gas targets prepared at the IUP 14C laboratory on AMS  $\delta^{13}\text{C}$  results. Data points for the linear fit are weighted inversely to the square of AMS  $\Delta^{14}\text{C}$  uncertainties. The dot inside the grey circle shows the mean of all 111 measurements in  $\delta^{13}\text{C}$  and  $\Delta^{14}\text{C}$ . The grey circle indicates the error of the means of approximately 0.2 ‰.

Acid samples. However, evaluation of the  $\Delta^{14}\text{C}$  with new normalisation parameters would put the CRL  $\Delta^{14}\text{C}$  results on a new scale and render them incompatible with measurements by other labs, using the standard normalisation. This further emphasises, that fractionation should be avoided in graphite samples as well as standards to minimise this effect.

Similar to the evaluation in  $\Delta^{14}\text{C}$  the AMS  $\delta^{13}\text{C}$  results are standardised according to the CEZ standard targets' ( $\frac{^{13}\text{C}}{^{12}\text{C}}$ ), graphitised using the CEZ parameters. Therefore, the scatter of the  $\delta^{13}\text{C}$  results is a more meaningful indicator for process quality than the absolute values. The uncertainty  $\sigma(\delta^{13}\text{C})$  is not dominated by the measurement error in the AMS, since the  $^{13}\text{C}$  currents are high. Main contribution is the error in  $\delta^{13}\text{C}$  calibration, introduced by the  $\delta^{13}\text{C}$  scatter of the standard targets. Therefore,  $\sigma(\delta^{13}\text{C})$  was estimated by the mean scatter of Oxalic Acid II standard targets, analysed in 2016, divided by  $\sqrt{6}$ , for 6 standard targets per magazine.

### 3. Set-up of the AMS target Extraction and Graphitisation Line

#### 3.5.1.3. AMS $^{12}\text{C}$ current

This indicator is the positive  $^{12}\text{C}$  current measured by Faraday cups at the high energy mass spectrometry site of the AMS (see Section 1.4.1). The  $^{12}\text{C}$  current is dependent on and a signal for the density of carbon atoms in the target material. In this regard, a more complete graphitisation reaction leads to an higher carbon content in the target, yielding an higher  $^{12}\text{C}$  current.

In terms of measurement technique, for the carbon isotope currents  $I(^x\text{C})$  of a sample the relationship  $I(^{12}\text{C}) \propto I(^x\text{C})$  is valid. Therefore, an increased  $^{12}\text{C}$  current points to an increased  $^{14}\text{C}$  counting rate, thus a better counting statistic and lower measurement uncertainty (see Section 1.4.2.5). In addition, targets with low carbon content and  $^{12}\text{C}$  current tend to burn through in the course of AMS measurement, which leads to a drastic decrease in the current and the  $\delta^{13}\text{C}$  isotopy.

Considering the AMS evaluation, an important part of the measurement value generation is the  $\frac{^{14}\text{C}}{^{12}\text{C}}$  correction depending on AMS  $^{12}\text{C}$  current (see Section 1.4.2.1). Errors in the determination of the linear correction function lead to substantial deviations in  $\Delta^{14}\text{C}$  for targets showing much higher or lower AMS  $^{12}\text{C}$  currents than the magazine standard targets. This points out the need to keep the target scatter low in the  $^{12}\text{C}$  current over all targets in a magazine. In summary, I aimed to set the parameters in order to maximise the  $^{12}\text{C}$  current, while minimising the scatter between the single targets.

#### 3.5.1.4. Blank age

The blank age is a measure for the contamination of the samples, introduced by catalyst and EGL processing. Here, it is calculated using the  $\left(\frac{^{14}\text{C}}{^{12}\text{C}}\right)$  of blank targets, according to Section 1.2.3. In preparation of the parameter test series, this indicator has been introduced to quantify the cleanliness of the target preprocessing and especially the catalyst pretreatment (section 1.4.3.1).

However, in the course of the test series, I observed a high variability in blank ages even in between targets prepared under same parameters. I determined a correlation between low blank ages, i.e. high levels of contamination of the target, and processing of Oxalic Acid II targets before the respective blank in the EGL.

The reason behind this effect might be adsorption of previously processed  $\text{CO}_2$  standard gas molecules on stainless steel surfaces in the EGL (e.g. Langenfelds et al., 2005). A part of these bonded molecules cannot be removed from the surface by diffusive transport during 3 min evacuation in standard operation of the EGL. Equilibration of the adsorbed  $\text{CO}_2$  with an isotopic signature of  $\gg -1000$  ‰ with the blank  $\text{CO}_2$  then leads to a contamination in  $^{14}\text{C}$  of the blank target.

I addressed this effect by implementing a “flushing stage” into the processing routine of the EGL and its software. Before evacuating and filling with a new sample or standard gas, the EGL tubing is 2× filled with 100 mbar Argon and afterwards evacuated again. This procedure facilitates evacuation of small  $\text{CO}_2$  partial pressures and subsequent relief of the  $\text{CO}_2$  molecules bonded onto the surface. Si-

### 3.5. Optimisation of the graphitisation parameters

milarly, the standard gas volume (vacuum section index 4) is  $3\times$  filled with  $\approx 20\%$  (100 mbar) of the amount of the gas planned to be sampled afterwards. This is followed by an equilibration time of 1 min to allow exchange of the molecules adsorbed at the surface and evacuation of the flushing  $\text{CO}_2$ . Figure 3.17 shows the effect of this approach in blank ages typically achieved by EGL blanks. I managed to increase the mean blank age by about 1700 a to a mean of 51 000 a and to decrease the scatter from 2000 a to 1300 a.

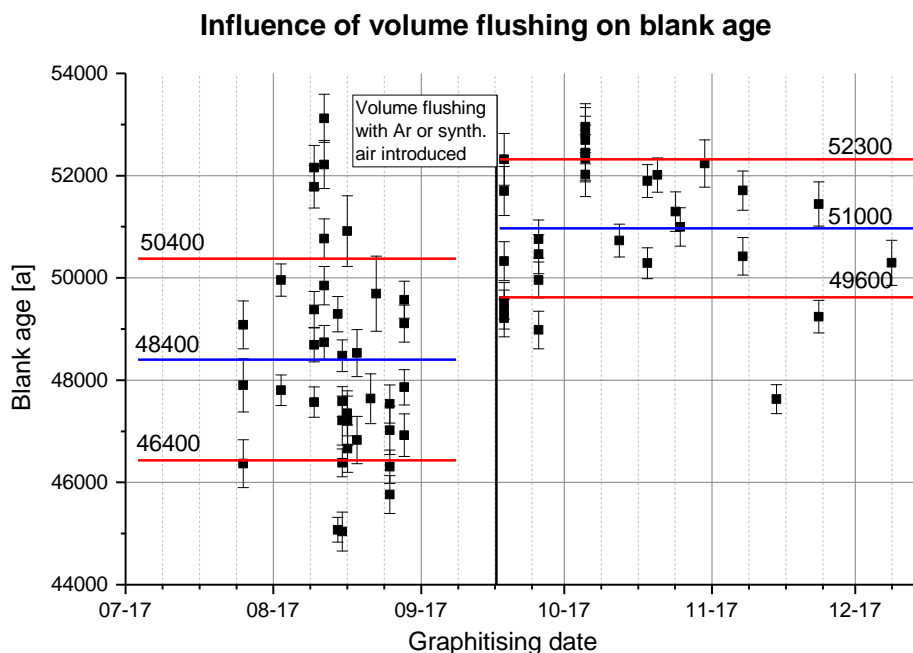


**Figure 3.17.:**  $^{14}\text{C}$  age of blank targets during the course of parameter test series. The vertical black line indicates the date, when EGL volume flushing with first synthetic air and then argon gas was introduced. Horizontal blue lines show the mean age of the respective periods with red lines enclosing the  $1\sigma$  range of the corresponding standard deviations.

The consequence for the parameter test series is, that in particular blank targets should be compared, which are either prepared after introduction of the flushing routine or whose processing predecessor was another blank target. Potentially contaminated blank results by the effect described here are in the following marked by an exclamation mark. The given uncertainties of the blank ages are mainly determined by the Poisson uncertainties in the AMS.

#### 3.5.1.5. AMS molecule current

The AMS molecule current (see Section 1.4.1) is a measure for the amount of hydrocarbon molecules in the graphite target. Hydrocarbon molecules on the target

### 3. Set-up of the AMS target Extraction and Graphitisation Line

surface can originate in sample contamination after graphitisation, e.g. during transport to the AMS. Though, here we focus on the hydrocarbons molecules forming during graphitisation: Incomplete graphitisation, e.g. by low temperatures, leads to enhanced methane production (section 1.4.3); further unknown but generally unfavourable chemical reactions might also lead to an increased molecule counting rate in the AMS.

There is, however, a linear dependency of molecule current  $I_{mol}$  on AMS  $^{12}\text{C}$  current  $I_{^{12}\text{C}}$ : A higher density of carbon atoms in the target, usually indicates a higher absolute hydrocarbon count, produced in graphitisation. To correct for this effect I present molecule current results in this section as relative molecule current  $I_{mol}/I_{^{12}\text{C}}$  with the unit  $\text{pA } \mu\text{A}^{-1}$ .

The attempt in this test series was minimising the molecule current as well as the current differences between samples to increase compatibility of sample and standard measurements.

#### 3.5.1.6. EGL mass efficiency

In routine operation of the EGL, every sample and standard is quantified regarding its amount of substance  $n_{\text{CO}_2}$ , following equation 3.4 in Section 3.2.4.1. Furthermore the weight of the graphitisation catalyst  $m_{\text{Fe}}$  and the resulting iron-graphite mixture  $m_{\text{target}}$  is determined by default, using a  $\mu\text{g}$  scale. These values can be utilised to calculate an EGL mass efficiency, that indicates how complete the sample processing after quantification was performed, esp. the graphitisation.

In order to assess the reliability of the mass measurements, I performed a test series to determine the mass loss in certain steps of catalyst handling. The test samples (4 mg Fe powder) have been weighted, filled into the reactor, undergone the standard catalyst pretreatment and weighted again in a similar way as a graphitised sample. Table 3.7 lists the resulting losses. We see, that the mean sample

**Table 3.7.:** Catalyst mass loss during different processing steps. Mass changes are derived from weight measurements of the catalyst powder resp. the whole reactor glass tube before and after catalyst pretreatment. Uncertainties are the standard deviation of  $N = 8$  catalyst samples with the error of the respective mean in brackets. Respectively 4 samples were prepared with 3.8 mg to 4.2 mg iron catalyst of grain size  $<74 \mu\text{m}$  and  $<44 \mu\text{m}$ .

Catalyst mass loss [mg] during			Total
Reactor filling	Pretreatment	Harvesting	loss [mg]
$0.23 \pm 0.24(\pm 0.09)$	$0.09 \pm 0.07(\pm 0.03)$	$-0.05 \pm 0.11(\pm 0.04)$	$0.27 \pm 0.28(\pm 0.10)$

loss of  $(0.27 \pm 0.28)$  mg mainly originates from handling losses in filling the catalyst into the reactor. A smaller, but significant mean weight loss occurs during pretreatment. Presumably this is caused by reduction of present iron oxides and, though, loss of the oxygen mass.

### 3.5. Optimisation of the graphitisation parameters

An important point here is, that the measured mass loss takes place before graphitisation and is therefore affecting solely pure catalyst. That means, for calculating the produced carbon mass  $m_C$  we can add the total loss  $m_{loss}$  to the difference of the graphitisation product mass  $m_{target}$  and the catalyst mass  $m_{Fe}$ :

$$m_C = m_{target} - m_{Fe} + m_{loss} \quad (3.11)$$

With this value we can define a graphitisation efficiency  $\epsilon_{graph}$ , which gives the fraction of produced graphite over the expected carbon mass from the gas amount measurement:

$$\epsilon_{graph} = m_C / (n_{CO_2} Q_{14} M_C) \quad (3.12)$$

with the mole mass of carbon  $M_C$ . The related uncertainties are

$$\sigma(m_C) = \sqrt{\sigma(m_{target})^2 + \sigma(m_{Fe})^2 + \sigma(m_{loss})^2} \quad (3.13)$$

$$\sigma(\epsilon_{graph}) = \epsilon_{graph} \sqrt{\left(\frac{\sigma(m_C)}{m_C}\right)^2 + \left(\frac{\sigma(n_{CO_2})}{n_{CO_2}}\right)^2 + \left(\frac{\sigma(Q_{14})}{Q_{14}}\right)^2} \quad (3.14)$$

with  $\sigma(m_{target})$  and  $\sigma(m_{Fe})$  as the weighting uncertainty of 0.1 mg and  $\sigma(m_{loss})$  as the standard deviation of the total loss in Table 3.7, containing measurement errors and deviations in the loss.  $Q_{14}$  is the quota of the total sample for  $\Delta^{14}C$  analysis, given in Table 3.2.

Since in preparatory graphitisation tests low mass efficiencies coincided with incomplete highly fractionating graphitisation reactions, I aimed in this test series to maximise the efficiency. The uncertainty of this indicator is in the order of 20 % to 30 %, which is large relative to the performance indicators originating from AMS measurements.

#### 3.5.1.7. Deviation from expected end pressure

This indicator is the deviation of the reactor pressure at the end of graphitisation from the expected pressure assuming complete reaction of the  $CO_2$  following the Bosch reaction (1.28). This value gives insight in the type of reactions occurring in the reactor (see Section 1.4.3). In particular, we expect lower end pressures than expected, when large amounts of methane are produced. On the other side, an excess of carbon monoxide production leads to an offset of CO as well as  $H_2$  in the reactor and therefore to high end pressures.

The measured  $CO_2$  pressure  $p_q$  in the quantification processing step determines the target pressure  $p_{H_2}$  of  $H_2$  inserted into the graphitisation reactor by means of the mean relative reactor volume  $\frac{V_R}{V_{13}}$  (see Table 3.5):

$$p_{H_2} = p_q F_C Q_{14} \frac{n_{H_2}}{n_{CO_2}} \frac{V_R}{V_{13}} \quad (3.15)$$

### 3. Set-up of the AMS target Extraction and Graphitisation Line

Here  $F_C$  is a reactor specific cooling factor, that gives the relative pressure change of a gas in the reactor when applying cooling on parts of the reactor (by liquid nitrogen and peltier elements) during H<sub>2</sub> filling. For switched on peltier elements, 9.5 cm reactor length and 6 cm long N<sub>2</sub>(l) cooling fingers, I found  $F_C = 0.904 \pm 0.005$ .

The hydrogen to carbon dioxide ratio  $\frac{n_{H_2}}{n_{CO_2}}$  is defined by the user of the graphitisation. In Section 3.5.5 the test results of a variation of this parameter from 2 to 2.8 are presented.  $Q_{14}$  is the fraction of the sample's total CO<sub>2</sub> in the reactor (Table 3.2).

We can now express an expected end pressure for 1000 mbar reaction start pressure as function of the set-up hydrogen to carbon dioxide ratio, when we assume to use two H<sub>2</sub> per CO<sub>2</sub> molecule:

$$p_{end,exp}^{1000\text{ mbar}} \left( \frac{n_{H_2}}{n_{CO_2}} \right) = \frac{\left( \frac{n_{H_2}}{n_{CO_2}} \right) - 2}{\left( \frac{n_{H_2}}{n_{CO_2}} \right) + 1} \cdot F_H \cdot 1000\text{ mbar} \quad (3.16)$$

Analogous to the cooling factor in (3.15),  $F_H$  is a heating factor, which represents the gas expansion in the reactor by heating of the reaction tube. For switched on peltier elements, 9.5 cm reactor length and 575 °C reaction temperature it was determined as  $F_H = 1.106 \pm 0.008$ .

The measured end pressure  $p_{end,meas}$  can now be normalised to a reaction start pressure  $p_{start,meas}$  of 1000 mbar

$$p_{end,meas}^{1000\text{ mbar}} = p_{end,meas} \cdot \frac{1000\text{ mbar}}{p_{start,meas}} \quad (3.17)$$

to eliminate variations induced solely by differences in sample size and hence reaction start pressure. The difference  $p_{end,meas}^{1000\text{ mbar}} - p_{end,exp}^{1000\text{ mbar}}$  is used as the performance indicator "deviation from expected end pressure" in the following sections.

In the time of the parameter test series the  $\frac{n_{H_2}}{n_{CO_2}}$  ratio inserted into the EGL reactors was accomplished with a mean offset of  $-0.006 \pm 0.051$  in 389 graphitisations. The targets, analysed for errors in  $\frac{n_{H_2}}{n_{CO_2}}$ , include standards, pure CO<sub>2</sub> samples, target gas and flask samples. The standard deviation of  $\approx 2.5\%$  of the  $\frac{n_{H_2}}{n_{CO_2}}$  is the dominant uncertainty in this indicator.

#### 3.5.1.8. Graphitisation duration

The EGL control software automatically recognises start and end of the graphitisation reaction by monitoring the reaction pressure in the reactor. Figure 3.18 shows the typical course of reactor pressure at the end of the graphitisation and a corresponding pressure slope calculated from the difference of the respective pressure sensor's measurement value with the value 5 min before. This slope value is used by the EGL software to trigger stopping of the graphitisation by reactor evacuation, when it exceeds a settable threshold (e.g.  $-0.2\text{ mbar min}^{-1}$ ) for longer

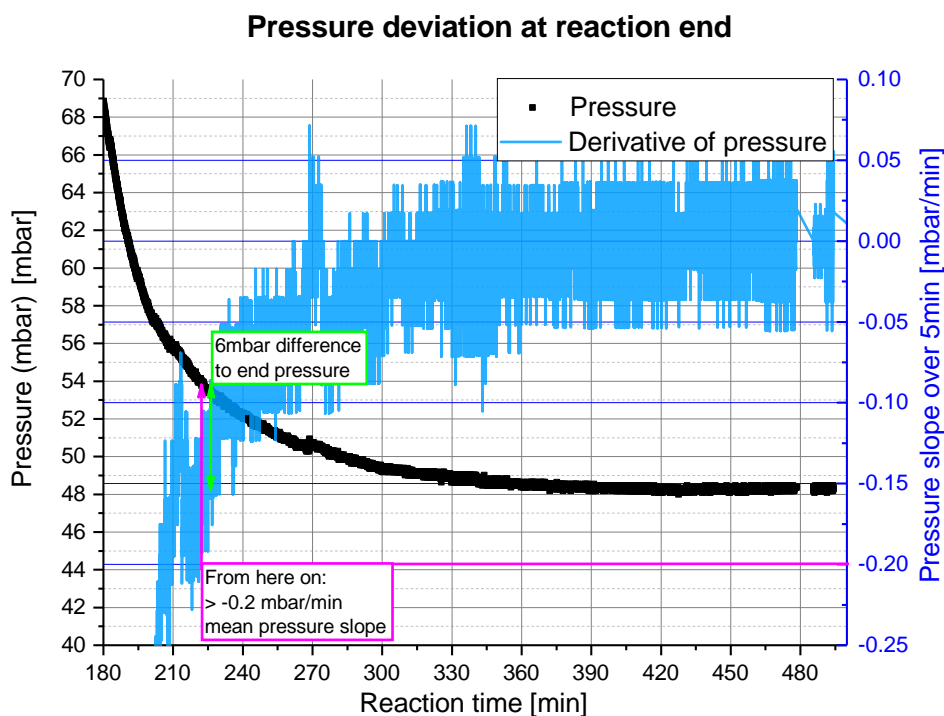


Figure 3.18.: Reaction pressure (black) and corresponding pressure slope (light blue) at the end of the graphitisation. The pink line indicates the time, when the noise of the slope (calculated over 5 min) lies sustainably above the threshold value. The green arrow indicates the pressure difference between shut-off pressure and reaction end pressure.

than 1 min to 2 min. This threshold value is given in the respective figures of the test series results, since it directly influences the duration measured.

The duration acts as adjustable reaction parameter as well as performance indicator for these. It can be seen as qualitative indicator for favourable reaction conditions. I assessed, however, the importance of this indicator as low relatively to the others. In preparatory tests, I observed short reaction times at graphitisation temperatures  $< 530^{\circ}\text{C}$  in conjunction with low graphite production rate and therefore low  $^{12}\text{C}$  currents in AMS measurements, which indicates an increased methane production rate. Furthermore, graphitisation in routine operation is performed automatically by the EGL after end of the working day, therefore a reduction in reaction time would not lead to an immediate improvement in operational efficiency.

I don't provide uncertainties for the data points regarding graphitisation duration, since the error in time measurements of the EGL software and the amount of time passing during the defined graphitisation end and the actual evacuation of the reactor is very short compared to the graphitisation duration.

### 3. Set-up of the AMS target Extraction and Graphitisation Line

#### 3.5.2. Test of iron type

As sketched in Section 1.4.3.1, there are many different preferences of AMS laboratories regarding their catalyst choice. Santos et al. (2007) give an overview about 11 commonly used catalysts and their performance in AMS analysis. In the parameter test series, I examined four different types of iron catalyst for graphitisation at the EGL. Table 3.8 lists these iron powders and the respective abbreviations, which are used below.

Table 3.8.: Iron catalyst powders, that have been tested in this series.

	Trade name	Size	Comment
A	Alfa Aesar -325 mesh, >99 % purity	<44 $\mu\text{m}$	Used in IUP $^{14}\text{C}$ laboratory
C			Iron A, preheated 3 h, 200 $^{\circ}\text{C}$
B	Alfa Aesar -200 mesh, >99 % purity	<74 $\mu\text{m}$	
E	Alfa Aesar -200 mesh, >99 % purity	<74 $\mu\text{m}$	Used in graphitisation at CEZ

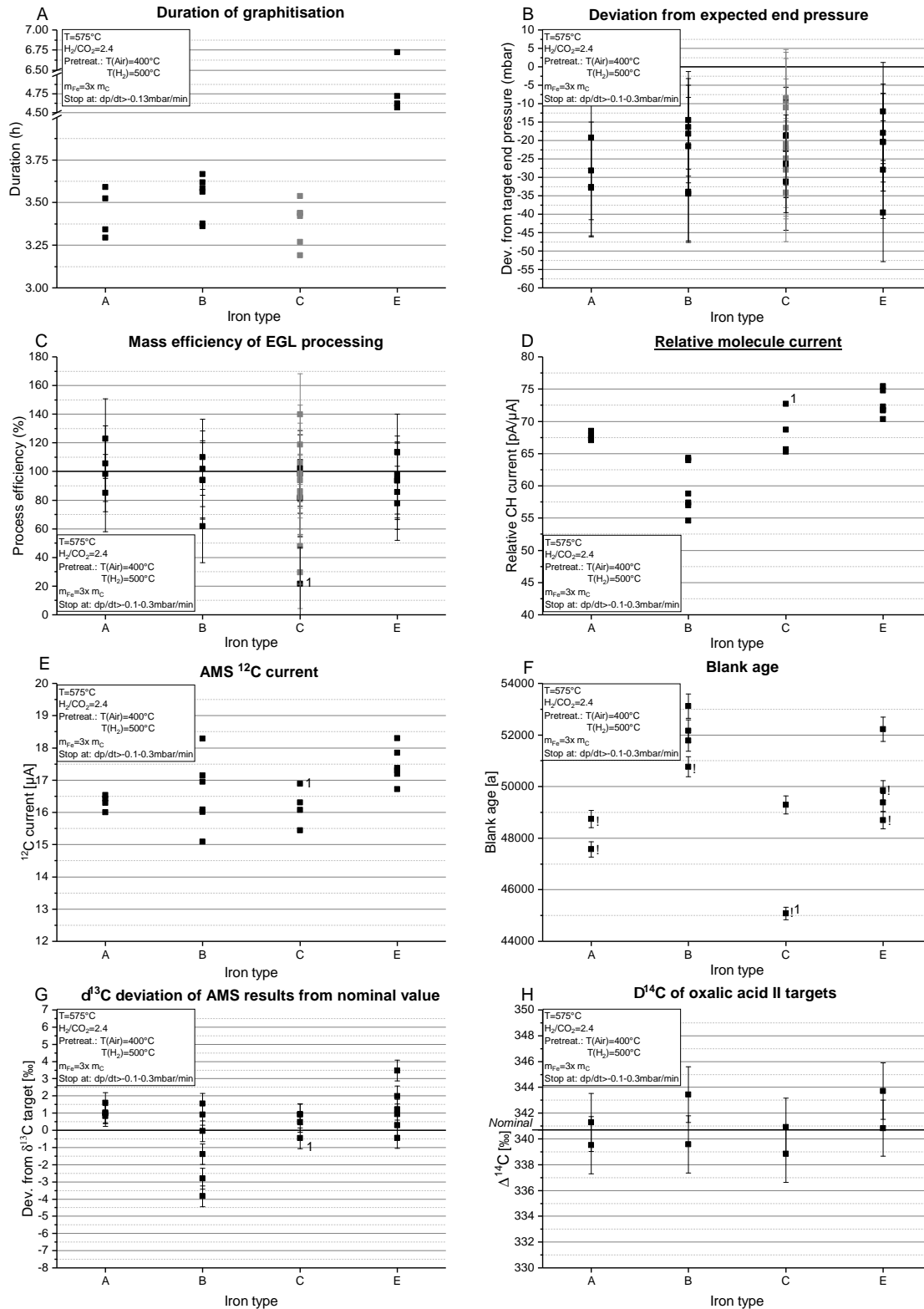
Iron type A has been used for graphitisation at the IUP  $^{14}\text{C}$  laboratory (see Chapter 2). Type C originates from the same batch, but is biweekly preheated in laboratory air at 200  $^{\circ}\text{C}$ . I tested this approach, since the graphitisation lab at the CEZ, preheats the catalyst prior to the regular catalyst pretreatment by default. Iron B and E are nominally equal but the batches showed significant differences in the graphitisation results (see below); furthermore iron E seemed to be much more coarse grained than its equivalent B. Due to its fine-grained structure, B tended to build catalyst chunks after pretreatment, which complicated further processing at the target press.

Figure 3.19 shows the results of the examination of the different iron types. In *Performance indicator specific results*, the details of the test outcomes are summarised, referring to the sub-figures in 3.19.

Following the performance indicators, which could be evaluated in short-term, I chose iron C for continuation of the series ( $P_{p,1}$ ) and following tests ( $P_{p,2}$  for the QC results, presented in Section 3.7). The clump-forming catalyst B was not chosen, because of its more time-consuming and error-prone handling after graphitisation. Catalyst E was withdrawn, due to the very long graphitisation time. C showed the fastest graphitisation (indicating favourable reaction conditions), while yielding similar performance in deviation from expected end pressure and efficiency as A. After final examination, however, A is the catalyst of choice. In absolute values, it shows similar mean values as C in all AMS performance indicators, but the standard deviations of A targets are considerably lower in molecule current and  $^{12}\text{C}$  current.

In summary, the choice of the catalyst had the most considerable impact on process performance indicators like graphitisation duration and ease of target pressing. In terms of yielding viable  $\Delta^{14}\text{C}$  results, all tested catalyst would be suitable.

## Examination of iron type



**Figure 3.19.:** Examination of iron type; applied parameter given in the resp. boxes. (■): Graphitised, but not AMS analysed, targets. (1): Possibly incompletely harvested and contaminated target. (!): Blank targets, that have been prepared before introducing of volume flushing and were possibly contaminated by a previously processed Oxalic Acid target. Errors in **B**, **C**, **F**, **G** and **H** are measurement errors as given in Sec. 3.5.1. **A**, **D** and **E** are measured very precisely compared to the scale.

### 3. Set-up of the AMS target Extraction and Graphitisation Line

#### Performance indicator specific results

- H:** In  $\Delta^{14}\text{C}$  no significant deviations from the nominal value for Oxalic Acid II are visible. The measurement values for type A and C are inside their respective uncertainties.
- G:** In the  $\delta^{13}$  deviation from the standard gases' nominal values, the means of all types, except C, are significantly different from zero. The standard deviations of the respective measurement values are  $\pm 0.3\text{‰}$  for A,  $\pm 2.1\text{‰}$  for B,  $\pm 0.7\text{‰}$  for C and  $\pm 1.4\text{‰}$  for iron E.
- E:** Type E is the only catalyst that induces a substantially higher ( $\approx +1\text{ }\mu\text{A}$ )  $^{12}\text{C}$  current in the AMS. A shows the lowest current scatter ( $\pm 0.2\text{ }\mu\text{A}$ ), followed by C and E with  $\pm 0.6\text{ }\mu\text{A}$  and B with  $\pm 1.1\text{ }\mu\text{A}$ .
- F:** All targets of type B show a blank age older than 50 000 a as well as the target of type E, which was not subject of possible contamination, suggesting these to be the least contaminated catalysts. For type A, no reliable conclusions can be drawn.
- D:** The mean relative molecule current of iron B is with  $(59 \pm 4)\text{ pA }\mu\text{A}^{-1}$  the lowest among all tested catalysts. The lowest standard deviation shows A with  $(67.7 \pm 0.6)\text{ pA }\mu\text{A}^{-1}$ .
- B, C:** In EGL mass efficiency  $\epsilon_{graph}$  and deviation from expected end pressure  $p_{end,meas}^{1000\text{ mbar}} - p_{end,exp}^{1000\text{ mbar}}$  no catalyst shows a significant deviation from the common means:  $\overline{\epsilon_{graph}} = (90 \pm 25)\%$  and  $\overline{p_{end,meas}^{1000\text{ mbar}} - p_{end,exp}^{1000\text{ mbar}}} = (-23 \pm 15)\text{ mbar}$ . The observed variance corresponds to the assigned measurement uncertainties.
- A:** Graphitisations catalysed with type E took considerably longer ( $(5.2 \pm 1.0)\text{ h}$ ) than the comparative tests. For type C, the fastest achievement of the target slope of  $0.13\text{ mbar min}^{-1}$  was observed ( $(3.4 \pm 0.1)\text{ h}$ ).

#### 3.5.3. Test of graphitisation duration

The influence of different reaction durations on the graphitisation result was tested. In preparation of these tests, I expected a strong dependency of EGL mass efficiency and AMS  $^{12}\text{C}$  current on the given time for reaction. Preparatory tests, conducted at lower temperatures ( $<530\text{ }^\circ\text{C}$ ), showed  $\epsilon_{graph} \approx 30\%$  and  $10\text{ }\mu\text{A} \lesssim I_{^{12}\text{C}} \lesssim 12\text{ }\mu\text{A}$  for durations  $<4\text{ h}$ . These values improved to  $80\%$  to  $100\%$  and  $14\text{ }\mu\text{A}$  to  $16\text{ }\mu\text{A}$  for very long reaction times ( $>10\text{ h}$ ).

In this test series, under more canonical reaction circumstances, I didn't observe a significant performance improvement with longer reaction times. The results of these tests are shown in the annex in Figure B.10. As pressure slope threshold value for further experiments  $-0.2\text{ mbar min}^{-1}$  was chosen for all following parameter

sets ( $P_f, P_{p,1}, P_{p,2}$ ). The related difference in end pressure to the end pressure after complete reaction of  $\approx 6$  mbar (see Figure 3.18) corresponds to 0.5 % to 1 % of the total pressure decrease during reaction.

#### 3.5.4. Test of catalyst pretreatment

The procedure of preheating the catalyst in oxidising and reducing atmospheres was expected to strongly influence the course of graphitisation at the EGL. Némec et al. (2010) showed, that preheating with  $H_2$  at  $400^\circ C$  lowered the reaction time by a factor of more than two at the AGE-1 graphitisation system. A prior oxidation is intended to transform the catalyst into a well-defined state and oxidise impurities on the surface to volatile oxides, hence increasing the target's blank age (see also Section 1.4.3.1).

In this series, I tested the effect of different oxidation and reduction temperatures on the graphitisation performance. Tested catalysts were iron types A and C. The oxidising atmosphere was 1000 mbar synthetic air in the EGL reactors, reacting for 5 min. Reduction was performed at 800 mbar  $H_2$  (see gas types in Table 3.3) for respectively 10 min. Figure 3.20 shows the reactor gas pressure during the course of pretreatment for different temperature combinations and reduction step repetition numbers.

During the oxidation step, an increasing pressure drop for higher air temperatures can be observed. At  $400^\circ C$  no pressure decrease or even a slight increase of 2 mbar to 5 mbar can be seen. A pressure decrease indicates occurring oxidation of the iron surface, due to loss of  $O_2$  molecules for production of iron oxides. Combustion of impurities, on the other hand, does not necessarily lead to a change in reactor pressure, since each carbon or sulphur oxidising  $O_2$  molecule is replaced by a  $CO_2$  or  $SO_2$  molecule. Produced  $H_2O$  is slowly removed from the reaction by the reactor's peltier water removal system.

At the first reduction step, a larger  $H_2$  loss is observed on catalysts, that have been more widely oxidised before and consequently require more  $H_2$  to reduce the iron oxides. Under the targets reduced after  $400^\circ$  oxidation (dashed lines in Figure 3.20) only small dependencies on  $H_2$  temperature are visible for  $400^\circ C$  and  $500^\circ C$ . Under the high temperature ( $600^\circ C$ )  $H_2$  atmosphere, the reaction induced water vapour partial pressure presumably didn't reach its condensation point near the peltier cooled steel surface, hence staying gaseous and balancing out the reactor pressure. Further reduction steps didn't show considerable changes in pressure, indicating almost complete iron oxide reduction in the first 10 min.

Using the known reactor volume and the ideal gas law, the  $H_2$  pressure loss of  $(40 \pm 5)$  mbar in  $500^\circ C$  after oxidation in  $500^\circ C$  corresponds to an amount of  $H_2$  of  $n_{H_2} = (11.2 \pm 1.4) \mu mol$ , which has reacted. During oxidation before, the catalyst was – regarding the pressure drop – oxidised by  $(2.0 \pm 0.3) \mu mol O_2$ . Assuming now, that the  $H_2$  completely reduced iron oxides in the catalyst, we can estimate the mass of volatilised oxygen, that was present in the catalyst prior to pretreatment, as  $m_{loss, O_2} = (0.11 \pm 0.02)$  mg. This value compares well to the  $(0.09 \pm 0.03)$  mg

### 3. Set-up of the AMS target Extraction and Graphitisation Line

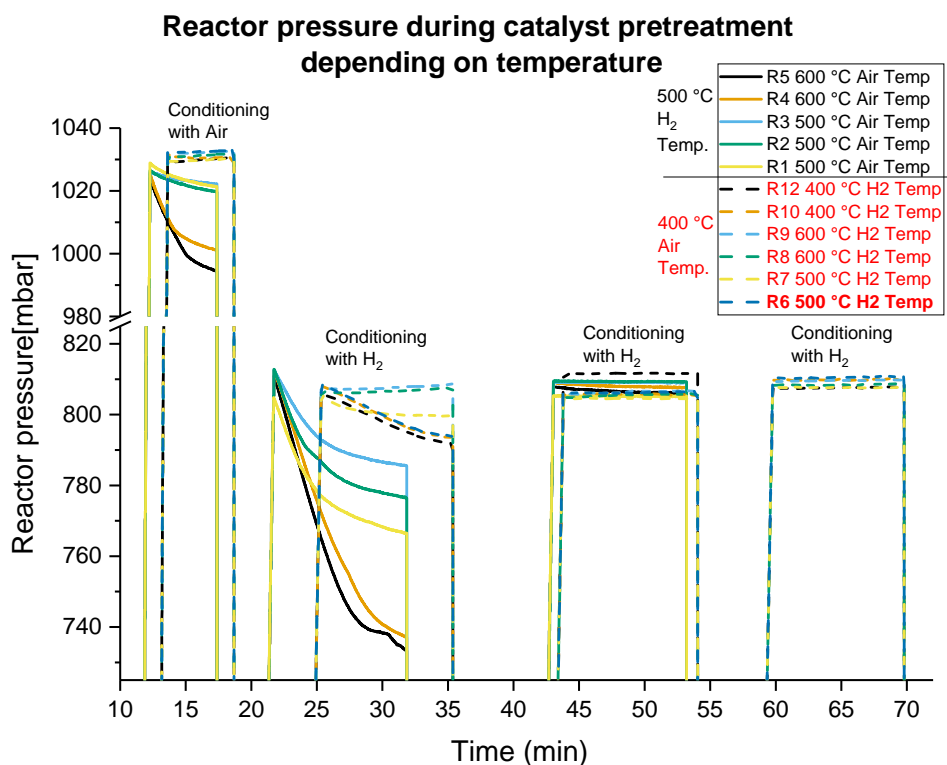


Figure 3.20.: Dependency of the pretreatment reactor pressure on the temperature of the oxidising (synt. air) and reducing (H<sub>2</sub>) agent. Pressure series taken with 4 mg iron powder (type A) in one session at different EGL reactors (see reactor numbers in the box). In bold (dark blue, dashed): Final conditioning parameter choice.

mass loss during pretreatment presented in Table 3.7, which was determined by catalyst weighting.

Figure 3.21 shows the results of the performance indicators for six different combinations of oxidation and reduction temperatures. In *Performance indicator specific results*, the details of the test outcomes are summarised, referring to the sub-figures in 3.21. The catalyst types A and C have been tested in this part of the series. I will refer to temperature combinations  $T(\text{air})$  and  $T(\text{H}_2)$  as  $[T(\text{air}) | T(\text{H}_2)]$ , in the following.

The pretreatment routine  $[500\text{ °C} | 600\text{ °C}]$  with three consecutive reduction steps was included into the preliminary graphitisation parameter list  $P_{p,1}$  for continuation of the parameter test series. It provides reliable surface oxidation (see Figure 3.20), without influencing target preparation due to catalyst sintering. Further tests have been performed (section 3.7) using set  $P_{p,2}$  with  $[500\text{ °C} | 500\text{ °C}]$ , which provided higher <sup>12</sup>C currents in this test series.

After final examination, I propose the routine  $[400\text{ °C} | 500\text{ °C}]$ , which overall provides stable results in all indicators, especially in AMS <sup>12</sup>C current and relative

# Examination of pretreatment

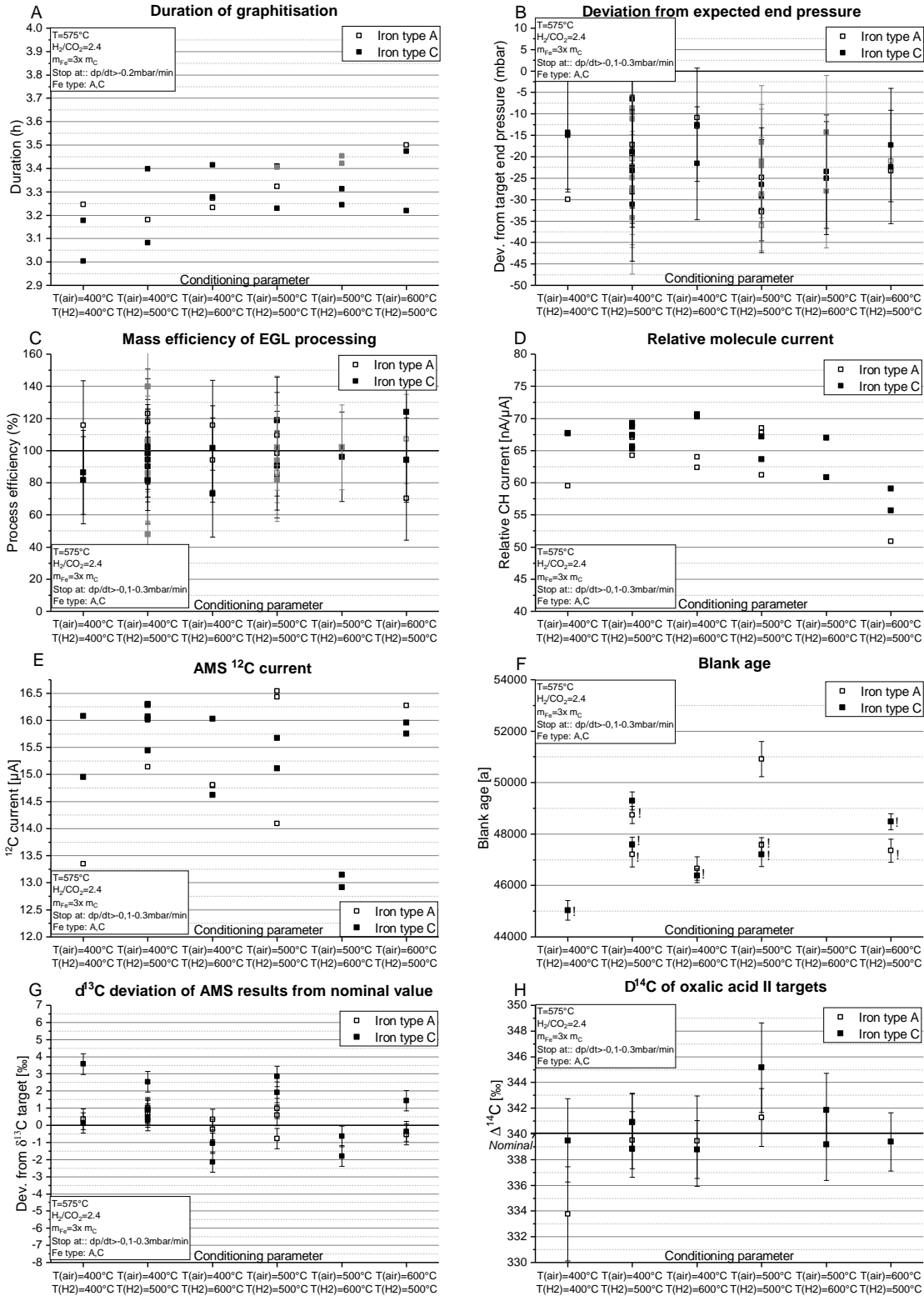


Figure 3.21.: Examination of catalyst pretreatment; applied parameter given in the resp. boxes. (■): Graphitised, but not AMS analysed, targets. (!): Blank targets, that have been prepared before introducing of volume flushing and were possibly contaminated by a previously processed Oxalic Acid target. Errors in B, C, F, G and H are measurement errors as given in Sec. 3.5.1. A, D and E are measured very precisely compared to the scale.

### 3. Set-up of the AMS target Extraction and Graphitisation Line

molecule current. The third reduction step should not be performed, to save processing time.

#### Performance indicator specific results

**H:** In  $\Delta^{14}\text{C}$ , the results for [400 °C | 500 °C], [400 °C | 600 °C] and [500 °C | 600 °C] show the most stable results, whereas the targets of [400 °C | 400 °C] show unusually high measurement uncertainties in their AMS results.

**G:** The standard deviations of  $\delta^{13}$  deviations from the standard gases' nominal values are for all combinations in the range of  $\pm 0.8\%$  to  $\pm 1.2\%$ . The targets for [400 °C | 400 °C] barely differ here.

**E:** All combinations except [500 °C | 600 °C] yield sufficient  $^{12}\text{C}$  currents in the AMS. Analysing the standard deviations, [500 °C | 600 °C] and [600 °C | 500 °C] scatter with  $\pm 0.2\ \mu\text{A}$  to  $\pm 0.3\ \mu\text{A}$ . [400 °C | 500 °C] and [400 °C | 600 °C] show standard deviations of  $\pm 0.6\ \mu\text{A}$ , the others are above this.

**F:** The blank target for [400 °C | 400 °C] lies at 45 000 a, which indicates an insufficient cleaning of impurities. The variance of the other combination's blank targets does not allow further interpretation.

**D:** The high-temperature oxidation in [600 °C | 500 °C] lead to a significantly lower mean relative molecule current of  $(55 \pm 4)\ \text{pA}\ \mu\text{A}^{-1}$ . The results of the other pretreatment routines are around  $(66 \pm 3)\ \text{pA}\ \mu\text{A}^{-1}$ .

**C:** On EGL mass efficiency  $\epsilon_{graph}$ , the conditioning parameters have no significant influence. The values derived from target weighting scatter around  $(96 \pm 20)\%$ .

**B:** In deviation from expected end pressure  $p_{end,meas}^{1000\ \text{mbar}} - p_{end,exp}^{1000\ \text{mbar}}$ , most pretreatment combinations fall within the common mean of  $(-22 \pm 7)\ \text{mbar}$ . The target mean of [400 °C | 600 °C] is situated one standard deviation closer to the expected end pressure:  $(-14 \pm 5)\ \text{mbar}$ .

**A:** In graphitisation duration, the data show a slight increase in duration with temperature from  $(3.1 \pm 0.1)\ \text{h}$  for [400 °C | 400 °C] to  $(3.4 \pm 0.2)\ \text{h}$  for [600 °C | 500 °C]. This effect points to an unfavourable transformation of the catalyst surface, e.g. surface downsizing, due to high temperatures. A similar conclusion, can be derived from the observation, that catalyst powder oxidised at 600 °C or more sinters to solid chunks of iron, that handicap further processing (esp. target pressing).

#### 3.5.5. Test of temperature and hydrogen amount variations

In this part of the test series, the influence of variations in graphitisation temperature and  $n_{\text{H}_2}/n_{\text{CO}_2}$  ratio has been examined. As sketched in Figure 3.15, I expected

### 3.5. Optimisation of the graphitisation parameters

for these parameters the most considerable impact on EGL performance indicators, since temperature as well as partial hydrogen pressure immediately change the chemical reaction conditions in the reactor (see equations in Section 1.4.3) and proofed their importance in preparatory tests of the EGL, the IUP  $^{14}\text{C}$  laboratory (Roos, 2013) and other labs (e.g. Němec et al., 2010; McNichol et al., 1992).

For this examination, 60 targets were prepared, which cover  $2 \leq n_{\text{H}_2}/n_{\text{CO}_2} \leq 2.8$  and  $565\text{ }^\circ\text{C} \leq T_{\text{graph}} \leq 620\text{ }^\circ\text{C}$ . Measurements have been performed at measurement clusters of 1 to 12 targets per parameter combination, with the aim to cover the examined parameter range uniformly. Promising parameter regions or those with high gradients in its performance indicators were examined more densely.

The adjustment of  $\frac{n_{\text{H}_2}}{n_{\text{CO}_2}}$  and  $T_{\text{graph}}$  in the EGL is subject to uncertainty: As shown in Section 3.5.1.7, the standard deviation of the  $\frac{n_{\text{H}_2}}{n_{\text{CO}_2}}$  of a single target was determined as  $\sigma\left(\frac{n_{\text{H}_2}}{n_{\text{CO}_2}}\right) = \pm 0.051$ . The distribution of temperature in the graphitisation reactor has been determined as well (see Figure 3.7). For the 9.5 cm reactor tubes used in this study, the temperature measurements showed a possible decrease in the graphitisation temperature inside the reaction zone of  $10\text{ }^\circ\text{C}$ . In the following we will use an uncertainty range of  $\sigma(T_{\text{graph}}) = -10\text{ }^\circ\text{C}$ . Figure 3.22 shows the results of the tests, illustrated as interpolated colormap between the means of the respective measurement clusters. In *Performance indicator specific results*, the details of the test outcomes are summarised, referring to the sub-figures in 3.22. Analogously to Section 3.5.4, I refer to parameter combinations  $n_{\text{H}_2}/n_{\text{CO}_2}$  and  $T_{\text{graph}}$  by  $[n_{\text{H}_2}/n_{\text{CO}_2} | T_{\text{graph}}]$ . In general, parameter sets were judged as promising, when situated near a local minimum, maximum or saddle point in the colormaps of the  $\Delta^{14}\text{C}$  and  $\delta^{13}\text{C}$  distribution, since the smallest gradient is expected there.

Investigation of the results leads to a final parameter combination  $P_f$  of  $[2.5 | -612.5\text{ }^\circ\text{C}]$ . Inside the range of the parameter errors, the range of the interpolated analysis results in  $\Delta^{14}\text{C}$  is below  $1\text{ }^\circ\text{‰}$ . The range in  $\delta^{13}\text{C}$  is  $2.2\text{ }^\circ\text{‰}$ , which are corrected for the largest part in  $\Delta^{14}\text{C}$ . Furthermore,  $P_f$  yields high  $^{12}\text{C}$  currents ( $18\text{ }\mu\text{A}$  with a range of  $2\text{ }\mu\text{A}$ ), medium low relative molecule currents ( $47\text{ pA }\mu\text{A}^{-1}$  with a range of  $9\text{ pA }\mu\text{A}^{-1}$ ) and deviations from the expected end pressure for complete Bosch reactions of less than  $20\text{ mbar}$  ( $2\%$  of the reaction start pressure). The resulting iron/graphite mixture could be further processed unproblematically at the CRL target press.

I also propose an alternative final parameter set  $P_{f,a}$  at  $[2.45 | 585\text{ }^\circ\text{C}]$ . In temperature,  $P_{f,a}$  is situated near the well established reaction conditions at CEZ,  $[2.5 | 580\text{ }^\circ\text{C}]$ , and the IUP  $^{14}\text{C}$  laboratory,  $[2.2 | 575\text{ }^\circ\text{C}]$ . The hydrogen to carbon dioxide ratio lies in between. In  $\delta^{13}\text{C}$ ,  $P_{f,a}$  lies in a zone of low variability ( $1.4\text{ }^\circ\text{‰}$ ), but the  $\Delta^{14}\text{C}$  range is with  $2\text{ }^\circ\text{‰}$  higher than at  $P_f$ . Moreover, the  $^{12}\text{C}$  current for  $P_f$  is lower than that of the mean over all measurements and the measured relative molecule currents near this parameter set were maximal. All together, the parameter range of  $P_{f,a}$  shows very stable  $\delta^{13}\text{C}$ , but is inferior to  $P_f$  in the majority of the important performance indicators.

## Examination of H<sub>2</sub>/CO<sub>2</sub> ratio and graph. temperature

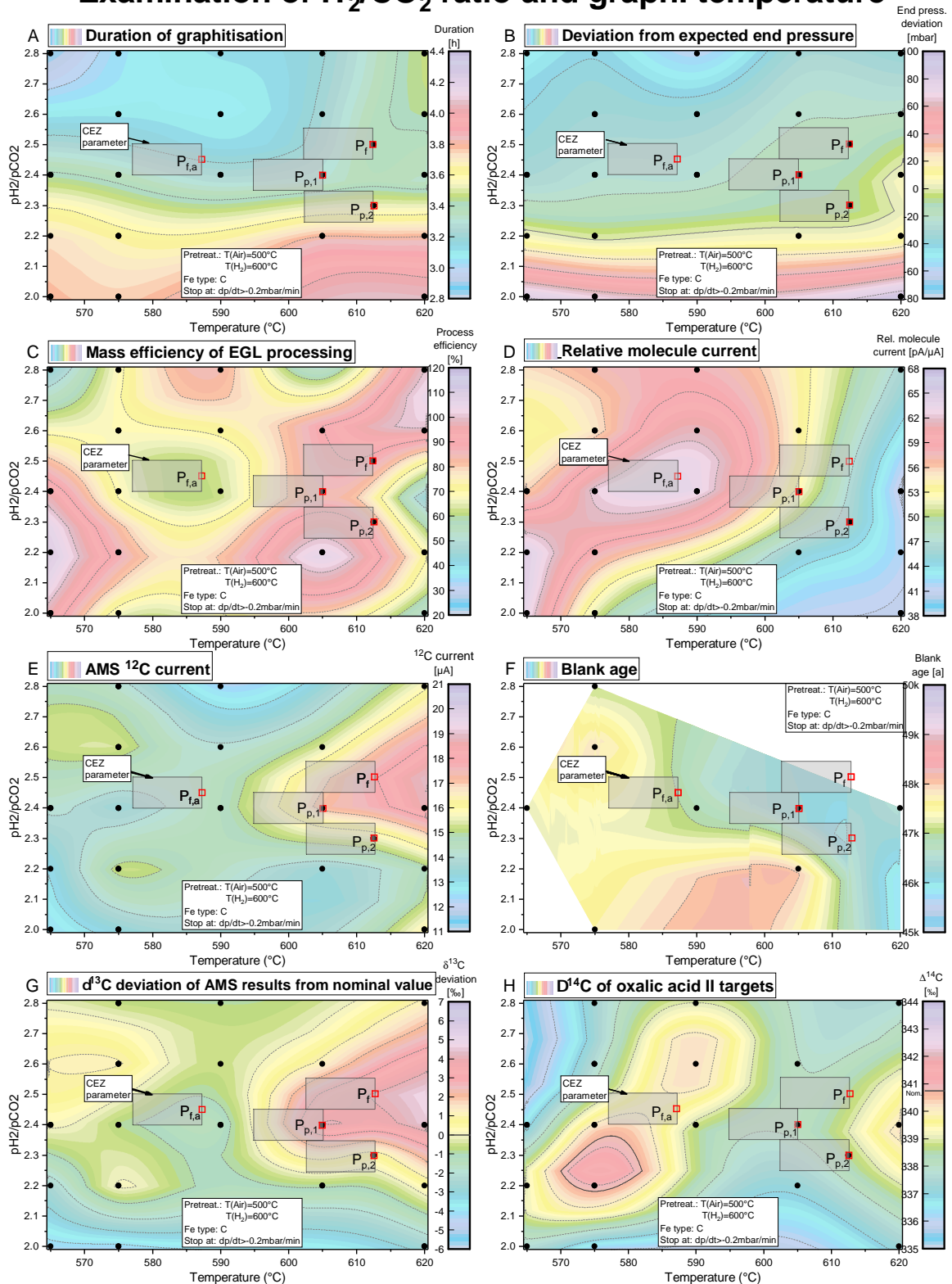


Figure 3.22.: Examination of H<sub>2</sub>/CO<sub>2</sub> ratio and graphitisation temperature; applied parameter given in the resp. boxes. (•): Cluster of 1 to 12 measurement values. (□): Final (P<sub>f</sub>), alternative final (P<sub>f,a</sub>) and preliminary (P<sub>p,1</sub>, P<sub>p,2</sub>) parameter sets with respective error range (grey box). Contour smoothing by Origin (Parameters: Point count factor: 15 000 to 20 000, smoothing parameter: 0.1). F: Only targets before implementation of the volume flushing.

### 3.5. Optimisation of the graphitisation parameters

In the preliminary parameter set  $P_{p,1}$ , [2.4 | 605 °C] was included for the continuation of the test series. The graphitisations here showed a satisfactory mass efficiency of 85 %, an end pressure deviation of 15 mbar and a duration of less than 3.4 h. The  $\Delta^{14}\text{C}$  are of similar stability as for  $P_f$ . After the test series, the set  $P_{p,2}$ , [2.3 | 612.5 °C], has been further tested in QC measurement series (section 3.7), which shows similar behaviour to  $P_{p,1}$ , but less dependency on temperature variations in  $^{12}\text{C}$  current and  $\delta^{13}\text{C}$ .

#### Performance indicator specific results

- H:** In  $\Delta^{14}\text{C}$ , 30 Oxalic Acid II targets have been analysed, overall yielding  $\Delta^{14}\text{C} = (338.4 \pm 2.5) \text{‰}$ . In general, the variability increases for lower temperatures and  $n_{\text{H}_2}/n_{\text{CO}_2}$  in the reactor. The absolute values are dependent on the standards, graphitised at CEZ with [2.5 | 580 °C].
- G:** Over all targets in this tests, I measured a mean  $\delta^{13}\text{C}$  deviation from the nominal target values of  $(0.07 \pm 2.60) \text{‰}$  for 46 targets. We see lighter results towards low  $n_{\text{H}_2}/n_{\text{CO}_2}$  (<2.5). The heavier isotopy around [2.4 | 600 °C to 620 °C] is presumably dependent on the high  $^{12}\text{C}$  currents in this region (see E).
- E:** The distribution of the  $^{12}\text{C}$  current is structurally similar to the  $\delta^{13}\text{C}$  distribution. This dependency is presumably connected to the known correlation between current and AMS  $\delta^{13}\text{C}$  and  $\Delta^{14}\text{C}$  measurement. During data evaluation, this effect is corrected by a linear function, fit to the standard target ratios (see Section 1.4.2.1). In this test series, all targets have been evaluated using CEZ standards, not covering the current range of the test series targets, leading to possible erroneous current correction.
- D:** The relative molecule current, indicating the relative strength of hydrocarbon production in graphitisation, shows a notable gradient to low molecule currents ( $40 \text{ pA } \mu\text{A}^{-1}$ ) towards higher temperatures and lower hydrogen amounts in the reactor. This finding is consistent to the expected chemical reactions (see Section 1.4.3):
- The methane formation via the equations (1.41) and (1.42) occurs exothermically, hence decreasing with temperature.
  - Lower hydrogen abundance in the reactor drags the reaction equilibrium to the left side of the respective equations, meaning an increased C and CO production.
- B:** The deviation from the expected end pressure in most part shows the expected behaviour from the theory. Similar to D, we see a strong dependency of methane (lower end pressure) or carbon monoxide (higher end pressure) production on the abundance of hydrogen in the reactor ( $\frac{n_{\text{H}_2}}{n_{\text{CO}_2}}$ ).

### 3. Set-up of the AMS target Extraction and Graphitisation Line

Above  $\frac{n_{\text{H}_2}}{n_{\text{CO}_2}} = 2.2$ , we observe as well an increase in end pressure as expected from the temperature dependency of the Boudouard-reaction (1.40). Below  $\frac{n_{\text{H}_2}}{n_{\text{CO}_2}} = 2.2$ , no temperature dependency can be observed, indicating a dominance of the hydrogen driven water gas reactions (1.37-1.39) over the temperature driven Boudouard-reaction. Equilibrium between pressure excess by CO and shortage by CH<sub>4</sub> is reached along  $\frac{n_{\text{H}_2}}{n_{\text{CO}_2}} = 2.2$  up to  $T_{\text{graph}} = 610$  °C.

- A:** In graphitisation duration, a notable prolongation for lower  $\frac{n_{\text{H}_2}}{n_{\text{CO}_2}}$  was observed. This is consistent with the expectations, since hydrogen drives the involved chemical reactions from the side of oxidised carbon educts to reduced carbon products (C, CH<sub>4</sub>). Furthermore, a slight increase of duration with temperature can be seen. A reason behind this might be a less efficient cold surface driven removal of H<sub>2</sub>O and thus slowed down carbon oxide reduction (1.37-1.39).
- C, F:** Considering the measurement uncertainties for mass efficiency ( $\approx \pm 27$  %) and typical sample scatter of blank targets of  $\pm 1200$  a no significant trends over temperature and hydrogen amount could be observed in the respective sub-figures.

#### 3.5.6. Test of catalyst amount

The influence of the ratio of iron catalyst to graphitised carbon has been examined, since in radiocarbon labs exists a wide variety of approaches for the amount of catalyst used. Used iron amounts and ratios are e.g.:

- 1.6 mg to 2.0 mg Fe for 0.5 mg to 1 mg C ( $1.6 \leq \frac{m_{\text{Fe}}}{m_{\text{C}}} \leq 4$ ) by Turnbull et al. (2015b)
- 3.2 mg Fe for 1 mg C ( $\frac{m_{\text{Fe}}}{m_{\text{C}}} = 3.2$ ) by Němec et al. (2010)
- 3 mg to 4 mg Fe for 0.4 mg to 1 mg C ( $3 \leq \frac{m_{\text{Fe}}}{m_{\text{C}}} \leq 10$ ) by Turnbull et al. (2010a)
- 4 mg to 5 mg Fe for 1 mg C ( $4 \leq \frac{m_{\text{Fe}}}{m_{\text{C}}} \leq 5$ ) by Santos et al. (2007)
- 5 mg Fe for 0.3 mg to 0.75 mg C ( $6.7 \leq \frac{m_{\text{Fe}}}{m_{\text{C}}} \leq 16.7$ ) by Fahrni et al. (2017)
- 5.5 mg Fe for 0.4 mg to 1 mg C ( $5.5 \leq \frac{m_{\text{Fe}}}{m_{\text{C}}} \leq 13.8$ ) by Turnbull et al. (2015b)

The optimal amount of catalyst is dependent on the AMS used for  $\Delta^{14}\text{C}$  analysis. For analysis at the MICADAS system (see Section 1.4.1), targets prepared at the IUP <sup>14</sup>C laboratory as well as at the graphitisation line at the CEZ, which is the main supplier for targets for the CEZ AMS, were graphitised under  $\frac{m_{\text{Fe}}}{m_{\text{C}}} \approx 3$ . Usually the iron amounts were ranging from 3 mg to 4 mg.

The EGL software is capable of estimating the carbon content of future targets, since meta-data like CO<sub>2</sub> concentration, flask pressure and sample container volume of incoming samples are transferred to the CRL database. For preparation

### 3.5. Optimisation of the graphitisation parameters

of the graphitisation reactors, the software displays the iron amount, which has to be dosed into reactor to yield a certain  $\frac{m_{\text{Fe}}}{m_{\text{C}}}$  in the resulting target. This feature facilitates to set up the  $\frac{m_{\text{Fe}}}{m_{\text{C}}}$ , leading to the most stable results, as default catalyst ratio for future targets.

In this test, 12 targets have been prepared, covering a range  $1.6 \leq \frac{m_{\text{Fe}}}{m_{\text{C}}} \leq 5.3$ . Calculation of  $\frac{m_{\text{Fe}}}{m_{\text{C}}}$  has been performed similarly to the efficiency calculation (3.12), using the carbon mass derived by the quantified CO<sub>2</sub> amount  $m_{\text{C},q}$  as carbon mass in the target:

$$\frac{m_{\text{Fe}}}{m_{\text{C}}} := \frac{m_{\text{Fe}}}{m_{\text{C},q}} = \frac{m_{\text{Fe}}}{n_{\text{CO}_2} Q_{14} M_{\text{C}}} \quad (3.18)$$

with pressure derived CO<sub>2</sub> amount  $n_{\text{CO}_2}$ , mole mass of carbon  $M_{\text{C}}$  and  $\Delta^{14}\text{C}$  quota of the whole gas amount  $Q_{14}$ . Losses in the catalyst amount due to handling in weight measurement are not taken into account here. Uncertainties in  $\frac{m_{\text{Fe}}}{m_{\text{C}}}$ , displayed in the following, are originating in weighting uncertainties and deviations in quantification.

Figure 3.23 shows the results of the tests. In *Performance indicator specific results*, the details of the test outcomes are summarised, referring to the sub-figures in 3.23. After examination of the test results, the well-established ratio  $\frac{m_{\text{Fe}}}{m_{\text{C}}} = 3.0 \pm 0.3$  was kept for EGL targets. In  $\delta^{13}\text{C}$  and AMS  $^{12}\text{C}$  current, I observed the strongest dependency of all conducted parameter tests on  $\frac{m_{\text{Fe}}}{m_{\text{C}}}$  (see Figure 3.23 E and F). In these performance indicators,  $\frac{m_{\text{Fe}}}{m_{\text{C}}} = 3$  yielded a robust high energy current around 17  $\mu\text{A}$ . Furthermore, the CRL targets fractionate at this point for the same extent as the CEZ standards ( $\delta^{13}\text{C}$  deviation around 0 ‰), which has also been prepared with  $\frac{m_{\text{Fe}}}{m_{\text{C}}} = 3$ . Furthermore, this test shows, that a fixed iron amount (e.g. 5 mg) for different sample sizes is not suitable to keep variations in fractionation and carbon current low for measurements with MICADAS.

#### Performance indicator specific results

- H:** In  $\Delta^{14}\text{C}$  no significant deviation of the 6 target results from their common mean ( $339.5 \pm 0.9$ ) ‰ can be observed. This indicates, that the considerable fractionation seen in  $\delta^{13}\text{C}$  (G) is mass dependent and could be corrected by sample normalisation.
- G:** This test yields a linear dependency of  $\delta^{13}\text{C}$  on  $\frac{m_{\text{Fe}}}{m_{\text{C}}}$  of  $(4.9 \pm 1.3)$  ‰  $\text{mg mg}^{-1}$ . All targets have been analysed in the same AMS magazine. Presumably, the absolute value of this slope is strongly dependent on AMS tuning. This result, however, shows, that the iron content in the target is the main driver of fractionation in the AMS, considering the tested parameter. Reasons behind this effect could be changes in the electric field near the target or in the sputtering behaviour.

# Examination of iron to carbon ratio

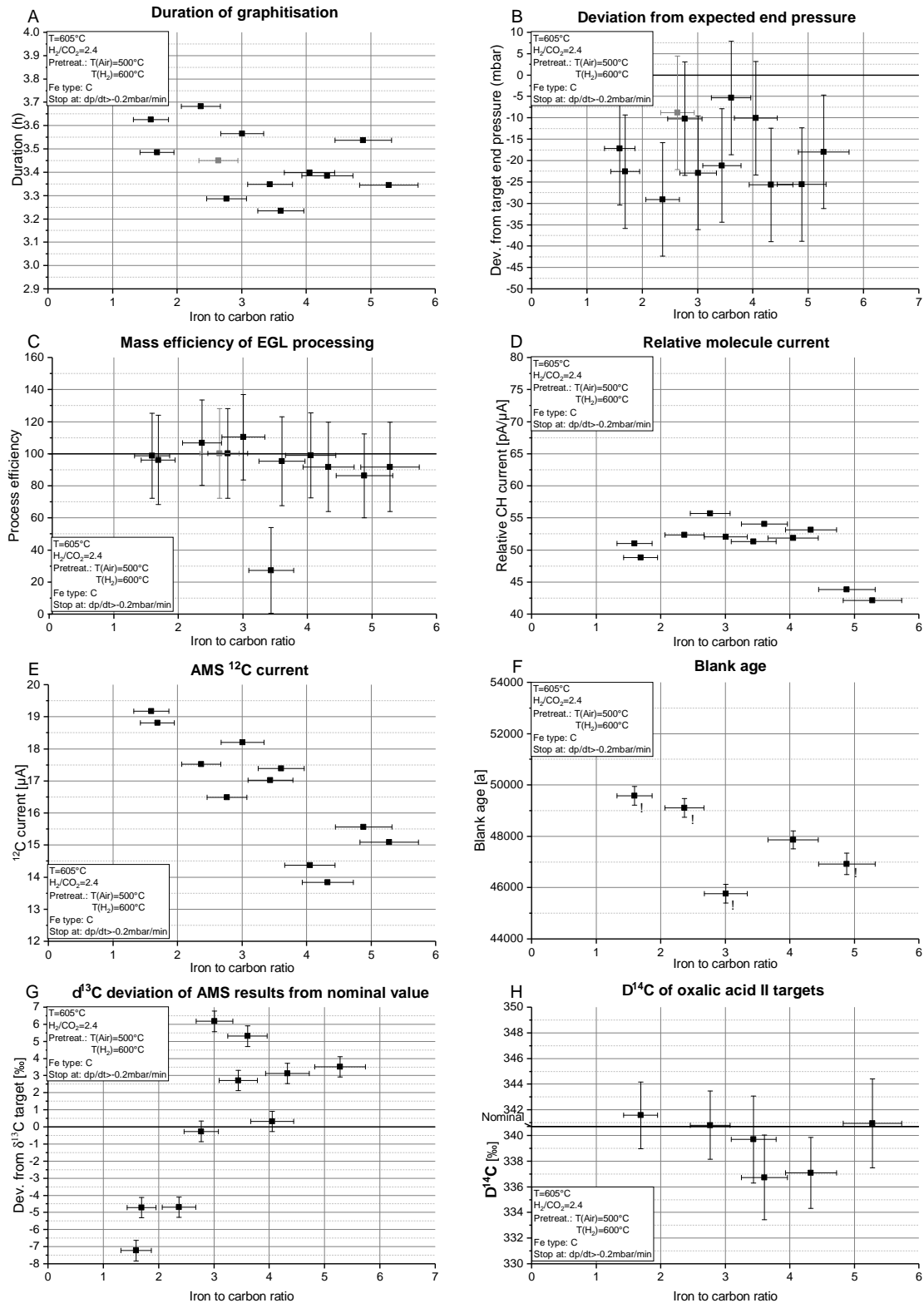


Figure 3.23.: Examination of iron to carbon ratio; applied parameter given in the resp. boxes. (■): Graphitised, but not AMS analysed, target. (!): Blank targets, that have been prepared before introducing of volume flushing and were possibly contaminated by a previously processed Oxalic Acid target. Errors in B, C, F, G and H are measurement errors as given in Sec. 3.5.1. A, D and E are measured very precisely compared to the scale. Errors in the iron to carbon ratio are deduced from uncertainties in weighting and  $\text{CO}_2$  quantification.

### 3.5. Optimisation of the graphitisation parameters

- E:** The  $^{12}\text{C}$  current decreases with a slope of  $(-1.3 \pm 0.3) \mu\text{A mg mg}^{-1}$  on higher  $\frac{m_{\text{Fe}}}{m_{\text{C}}}$ . The correlation between  $^{12}\text{C}$  current and  $\delta^{13}\text{C}$  in this test is reversed to the ones observed in experiments before: A burned through target usually drops heavily in current as well as in  $\delta^{13}\text{C}$ . This indicates different causes for both effects.
- F:** In blank age, a slight trend towards lower blank ages for higher iron contents can be seen. This might not be significant, but would be in accordance to the expectations, since blank contaminations considerably originate in catalyst impurities.
- A:** Graphitisations took  $(3.51 \pm 0.07)$  h for targets with  $\frac{m_{\text{Fe}}}{m_{\text{C}}} < 3$  and for  $\frac{m_{\text{Fe}}}{m_{\text{C}}} > 3$  ( $3.40 \pm 0.05$ ) h (errors of mean). A slightly faster reaction can originate in larger accessible catalyst surfaces.
- B, C, D:** In reaction end pressure, graphitisation efficiency and molecule currents, no dependency on  $\frac{m_{\text{Fe}}}{m_{\text{C}}}$  could be deduced by these test results.

#### 3.5.7. Overview of the parameter test results

As outlined in the beginning of this section, a number of graphitisation parameter sets  $P$  has been developed and tested in the course of the examination of the EGL: Starting from the parameters used at the IUP  $^{14}\text{C}$  laboratory  $P_{iup}$ , to the set of the first results of the EGL parameter test series  $P_{p,1}$ , leading to the medium-term preliminary parameter set  $P_{p,2}$ , whose results are discussed in Section 3.7. After final examination and AMS analysis of all corresponding targets, a final parameter set  $P_f$  could be proposed, complemented by an alternative final set  $P_{f,a}$ , which uses different graphitisation temperatures and  $\text{H}_2/\text{CO}_2$  ratios and showed higher stability in  $\delta^{13}\text{C}$  than  $P_f$  during the parameter test series. Table 3.9 lists the parameter sets mentioned here, which were the product of extensive test series.

**Table 3.9.:** Overview of the EGL parameter sets developed and tested in this work.

Set	Catalyst	Duration threshold	Catalyst pretreatment	Graph. temp.	Graph. $\frac{n_{\text{H}_2}}{n_{\text{CO}_2}}$	Catalyst ratio $\frac{m_{\text{Fe}}}{m_{\text{C}}}$
$P_{iup}$	A	$> -0.13 \text{ mbar min}^{-1}$	[400 °C   400 °C]	575 °C	2.4	3
$P_{p,1}$	C	$> -0.2 \text{ mbar min}^{-1}$	[500 °C   600 °C]	605 °C	2.4	3
$P_{p,2}$	C	$> -0.2 \text{ mbar min}^{-1}$	[500 °C   500 °C]	612.5 °C	2.3	3
$P_{f,a}$	A	$> -0.2 \text{ mbar min}^{-1}$	[400 °C   500 °C]	585 °C	2.45	3
$P_f$	A	$> -0.2 \text{ mbar min}^{-1}$	[400 °C   500 °C]	612.5 °C	2.5	3

### 3.6. Fractionation during preprocessing

Comparable to the situation in the graphitisation reactor, incomplete CO<sub>2</sub> extraction, expansion or transfer can lead to fractionation in the EGL target. To quantify these effects, the fractionation in the EGL, occurring at different preprocessing steps and for different target types (CO<sub>2</sub> from whole-air, Oxalic Acid I and II) has been examined in a comprehensive test series. *Extraction* (section 3.6.1), *Transfer to reactors* (section 3.6.2), *Sampling of standard gases* (section 3.6.3) and *Graphitisation* (section 3.6.4) have been tested in this order to take fractionation in a processing step into account, which might occur at the respective next test as well.

All  $\delta^{13}\text{C}$  measurements in this test series were conducted by storing the respective CO<sub>2</sub> samples in glass vials and determining the <sup>13</sup>C isotopy at the same MSP as for the tests in Section 2.1.1. The measurement uncertainty in  $\delta^{13}\text{C}$  is defined here as the error of the mean of 2 to 4 MSP measurements of every sample.

#### 3.6.1. Extraction

The dependency of  $\delta^{13}\text{C}$  on immersion depth  $d_i$  of the EGL cooling trap has been tested. As described in Section 3.2.2, the vertical position of the N<sub>2</sub>(l) dewar during CO<sub>2</sub> extraction can be adjusted. This test ought to determine the optimal CO<sub>2</sub>-extraction depth for air samples and target gases.

The experiment has been performed with 1000 ml<sub>n</sub>/min flow rate through the trap by default. The N<sub>2</sub>(l) level has been manually kept on the respective  $d_i$  with an uncertainty of  $\approx 2$  mm. The extracted CO<sub>2</sub> and H<sub>2</sub>O were then thawed and subsequently separated, by sublimating the trapped water in an acetone-dry ice mixture ( $-70$  °C to  $-80$  °C), replacing the N<sub>2</sub>(l). Water removal was performed to increase measurement precision of the MSP. The CO<sub>2</sub> was cryogenically transferred to a Duran glass break-seal on the CO<sub>2</sub> transfer position at reactor 1 (see Figure 3.6) and stored glass-sealed until MSP analysis.

Figure 3.24 shows the test results. The deviation of the results for  $d_i = 5$  cm to the nominal value is  $(0.008 \pm 0.010)$  ‰, hence agreeing within their uncertainties.  $d_i = 7$  cm lies with a deviation of  $(0.014 \pm 0.012)$  ‰ near the nominal value as well.  $d_i = 3$  cm shows with  $(-0.054 \pm 0.016)$  ‰ a significant depletion in  $\delta^{13}\text{C}$ . The reason behind this might be inverse kinetic fractionation due to incomplete extraction and therefore favoured draining of heavier carbon isotopes (see Mook, 2000). These results lead to a continuation of the fractionation tests on and recommendation of an extraction immersion depth of  $d_i = 5$  cm.

#### 3.6.2. Transfer to reactors

Methodologically analogous to the test of the immersion depth, fractionation in sample transfer to different reactors has been tested. Parallel, all four extraction

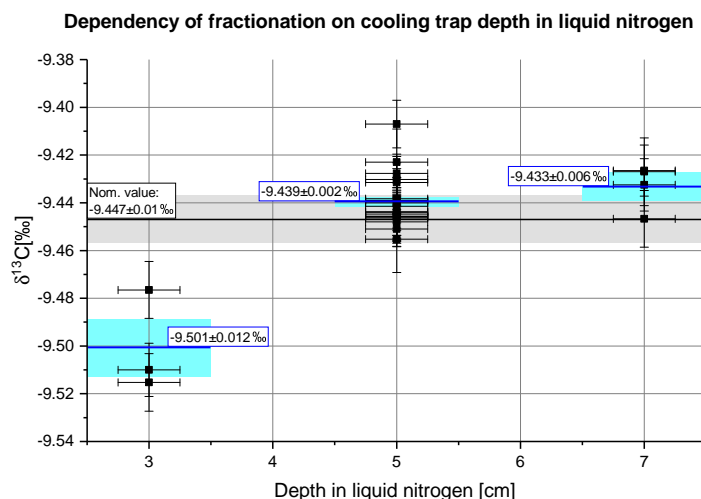


**Figure 3.24:**  $\delta^{13}\text{C}$  results dependent on immersion depth  $d_i$  of the EGL  $\text{CO}_2$  extraction of target gas high (see Figure 3.3). Blue lines are the mean of  $\delta^{13}\text{C}$  for each  $d_i$ . Teal zones indicate the error of these means ( $\sigma_{STD}(\delta^{13}\text{C})/\sqrt{N}$ ). Nominal value of the target gas derived from multiple MSP analyses, error (grey) is the error of the mean.

lines were examined. These experiments were performed, since – due to the geometry of the EGL – the  $\text{CO}_2$  transfer extends about 1 m more for samples moving to the reactors at the end of the line (e.g. 1 and 12), compared to reactors 6 to 7 in the middle (see Figure 3.8). The extraction lines were tested individually, since differences in the cooling trap geometry as well as in the extraction pump performance also could lead to differences in extraction efficiency and hence to sample fractionation.

Figure 3.25 shows the results of these tests. No significant dependency of sample fractionation on the extraction port nor on reactor number can be derived from these results. This means, all processing routes for the samples are equivalent and should produce compatible targets. The means of all tested parameters are in accordance with the nominal value within their respective uncertainties, except for the sample in reactor 2. The cause for this deviation is not known, but since for no other reactors any significant deviation from the mean is seen – especially for reactor 11, that is placed opposite to reactor 2 – I assume handling or manual processing errors to be responsible for that.

### 3.6.3. Sampling of standard gases

In this part of the test series, three issues were subject of investigation:

- The pure  $\text{CO}_2$  gases used in the EGL for quality control and standardisation in AMS measurements were tested for preset fractionation, i.e. deviations from the nominal values of the standard gases (oxalic acid I and II).

### 3. Set-up of the AMS target Extraction and Graphitisation Line

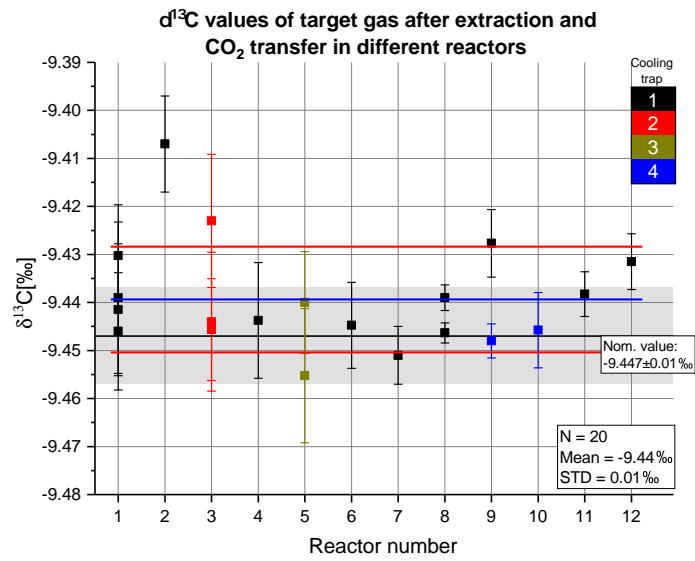


Figure 3.25.:  $\delta^{13}\text{C}$  results dependent on sample target reactor and extraction line. Immersion depth:  $d_i = 5$  cm. Blue line is the mean of  $\delta^{13}\text{C}$  for all reactors and traps. Red lines indicate the  $1\sigma$  range of the calculated standard deviation over all samples. Nominal value of the target gas derived from multiple MSP analyses; error (grey) is the error of the mean.

- The standard  $\text{CO}_2$  has been sampled and dosed through a 0.4 mm outer diameter capillary. Here, I tested for any fractionating effects ongoing during this process.
- In contrast to the previous tests (sections 3.6.1 and 3.6.2), the sample  $\text{CO}_2$  in this experiment went through the complete transfer and quantification process, which is performed by default by the EGL. This means, after  $\text{CO}_2$  dosing, the samples had been transferred to the quantification volume, aliquoted and further transferred to reactor 1.

$\delta^{13}\text{C}$  sampling and measurement was conducted in the same way as in Sections 3.6.1 and 3.6.2.

The results are plotted in Figure 3.26. The Oxalic Acid I samples show very small scatter and deviation from the nominal value:  $(0.003 \pm 0.005) \text{‰}$ . This suggests, that sampling through the capillary, two-stage  $\text{CO}_2$  transfer and aliquotation does not cause additional fractionation.

Considering this, the deviation of Oxalic Acid II of  $(-0.06 \pm 0.01) \text{‰}$  is presumably caused by differences in the isotopy of the used  $\text{CO}_2$  compared to the nominal value. Before being filled into the storage tank, the Oxalic Acid II standard material has to be combusted under controlled conditions, the used  $\text{CO}_2$  was analysed at least 10 times at the LLC laboratory, which includes several  $\text{CO}_2$  transfers, and

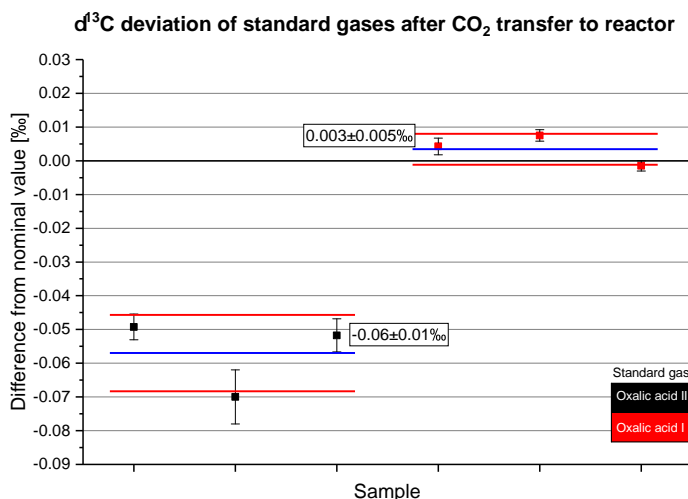


**Figure 3.26.**  $\delta^{13}\text{C}$  deviation from the nominal values for Oxalic Acid I and II standard gases, sampled from the built-in EGL standard gas supply tanks. Nom. values:  $-19.3\text{‰}$  for Oxalic Acid I and  $-17.8\text{‰}$  for Oxalic Acid II. Blue lines are the mean deviation, red lines indicate the  $1\sigma$  range of the measured standard deviation.

had to be transferred into the glass storage tank, which could lead to this small fractionation relative to the nominal value.

In summary, since no samples showed considerable deviations, the results indicate no occurring fractionation in standard gas sampling and transfer. The standard and QC  $\text{CO}_2$  in the EGL agrees well to the respective nominal values in  $\delta^{13}\text{C}$ .

### 3.6.4. Graphitisation

This section is about concluding the  $\delta^{13}\text{C}$  fractionation test series with a comprehensive experiment, which includes all preprocessing steps handled before (Sections 3.6.1-3.6.3) as well as graphitisation under the preliminary parameter set  $P_{p,2}$ , derived from the graphitisation parameter tests before. Graphite produced from Oxalic Acid II has been combusted in an EA (Elementar Inc., *Vario MicroCube*) yielding  $\text{CO}_2$  again, which has been stored in mini glass flasks with a volume of 4 ml (see Zipf, 2017) until analysis in MSP.

#### 3.6.4.1. $\delta^{13}\text{C}$ results

Figure 3.27 shows the  $\delta^{13}\text{C}$  isotope of the combusted graphite. The nominal value of Oxalic Acid II lies with  $(-17.76 \pm 0.09)\text{‰}$  within the error of the measurement mean. These results are in agreement with the findings without graphitisation of the standard samples (see Section 3.6.3) within the errors of the sample mean. The standard deviation increased by a factor of 20 to 40 from  $\pm 0.005\text{‰}$  to  $\pm 0.01\text{‰}$  to  $\pm 0.24\text{‰}$ . This indicates additional sources of uncertainties due to graphitisation

### 3. Set-up of the AMS target Extraction and Graphitisation Line

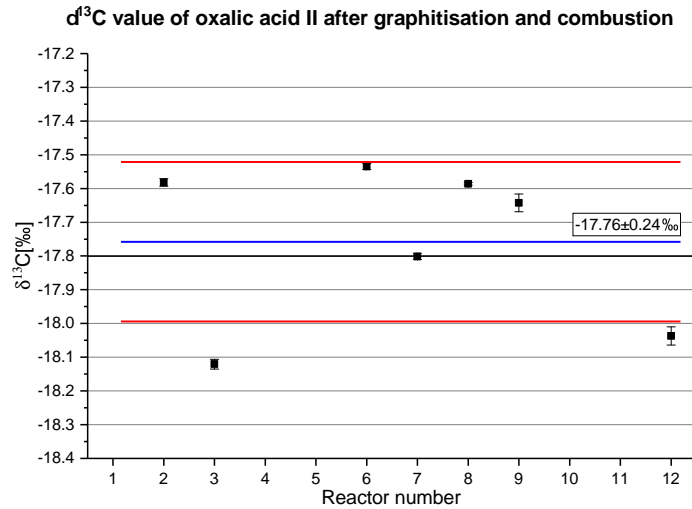


**Figure 3.27.:** Fractionation test including all EGL processing steps (sampling until graphitisation in different reactors and an additional combustion back to  $\text{CO}_2$ ) for Oxalic Acid II samples by usage of graphitisation parameter set  $P_{p,2}$ . Sample handling identical to the default processing procedure in the EGL. Graphite has been combusted in an EA at the CEZ, followed by subsequent  $\delta^{13}\text{C}$  measurement by MSP. The blue line is the measurement mean, red lines indicate the  $1\sigma$  standard deviation.

and target combustion, but no systematical offset after graphitisation can be observed, meaning that the EGL does not introduce a bias into the  $\delta^{13}\text{C}$  by sample fractionation. Furthermore, the scatter in  $\delta^{13}\text{C}$ , which was determined here, is much smaller than the typical  $\delta^{13}\text{C}$  target variability during AMS measurement of  $\approx 2$  ‰.

#### 3.6.4.2. Efficiency

The composition of 12 examined Oxalic Acid II targets was analysed by the EA in the course of combustion. This gives us an independent measure to quantify the efficiency of the EGL graphitisation besides catalyst and target weighting.

Table 3.10 shows the results of both approaches. For catalyst & target weighting,  $m_C$  and  $\epsilon_{graph}$  are calculated according to equations (3.11) and (3.12).  $m_{target}$  is the weighted target mass after graphitisation. In case of EA analysis,  $\frac{m_C}{m_{target}}$  is directly measured and displayed by the instrument. Preceding from this value,  $m_C$  is received by multiplication with  $m_{target}$ .  $\epsilon_{graph}$  is then again calculated by (3.12).

The results indicate a significant systematical deviation of both efficiency determination methods of  $(98 \pm 5)\%$  compared to  $(79 \pm 1)\%$ . This might suggest, that the catalyst handling loss has been overestimated for these samples or that parts of the graphite, which is finer than the catalyst powder, has been lost in prepara-

**Table 3.10.:** Comparison between graphitisation efficiency measures, derived from the default catalyst and target weighting at the CRL and elemental analysis (EA).  $\frac{m_c}{m_{target}}$  is the fraction of the whole target, which is carbon.  $\epsilon_{graph}$  expresses, which part of the expected carbon mass from CO<sub>2</sub> quantification is finally measured in the target. Uncertainties are the standard deviations of the measurements, errors of the means are given in brackets.

N	Catalyst & target weighting		EA analysis & target weighting	
	$\frac{m_c}{m_{target}}$ [%]	$\epsilon_{graph}$ [%]	$\frac{m_c}{m_{target}}$ [%]	$\epsilon_{graph}$ [%]
12	25.1 ± 1.4(±0.4)	98 ± 17(±5)	19.7 ± 0.9(±0.3)	79 ± 4(±1)

tion of EA analysis. It can be stated after this test, that the EGL graphitisation line operates with an efficiency of at least (79 ± 1)% for the graphitisation parameter set  $P_{p,2}$ . Since the final set  $P_f$  lies at the same level as  $P_{p,2}$  in end pressure deviation and mass efficiency, these results can presumably be transferred to the final procedure.

### 3.7. Establishing EGL quality control

In Section 2.2 was demonstrated, that performing long-term quality control measurements provides valuable data to assess target preparation and AMS analysis performance and to separate their uncertainties. In Sections 3.7.1 and 3.7.2 the mentioned measures have been continued for QC of the EGL. To allow, furthermore, an absolute statement about the EGL  $\Delta^{14}\text{C}$  scale, I present the results of a newly started Oxalic Acid I measurement series (section 3.7.3).

#### 3.7.1. Target gases

After completion of the EGL parameter test series (section 3.5) the target gas measurement series, presented in Section 2.2.1 for the IUP  $^{14}\text{C}$  laboratory, has been continued. Target gas processed at the EGL has been inserted into EGL CO<sub>2</sub> extraction directly from the respective pressurised aluminium cylinders.

8 targets were prepared at EGL from CO<sub>2</sub> extracted at the IUP  $^{14}\text{C}$  laboratory, which was stored in Duran glass break-seals. This enables to separately test the  $\Delta^{14}\text{C}$  stability of samples inserted as pure CO<sub>2</sub> into the EGL.

All target gas graphite targets have been prepared using the same graphitisation parameter sets as the concurrently used standard and blank targets. Each period of constant graphitisation parameters, which are analysed in the following, extends at least across two AMS magazines, to take across-magazine uncertainties into account (see Section 2.2.1.1).

Figure 3.28 shows the analysis results of the target targets for high (3.28A) resp. low (3.28B)  $\Delta^{14}\text{C}$ . The results show for both target gases standard deviations below 2 ‰ (1.7 ‰ and 1.9 ‰). The mean AMS measurement uncertainty lies for

### 3. Set-up of the AMS target Extraction and Graphitisation Line

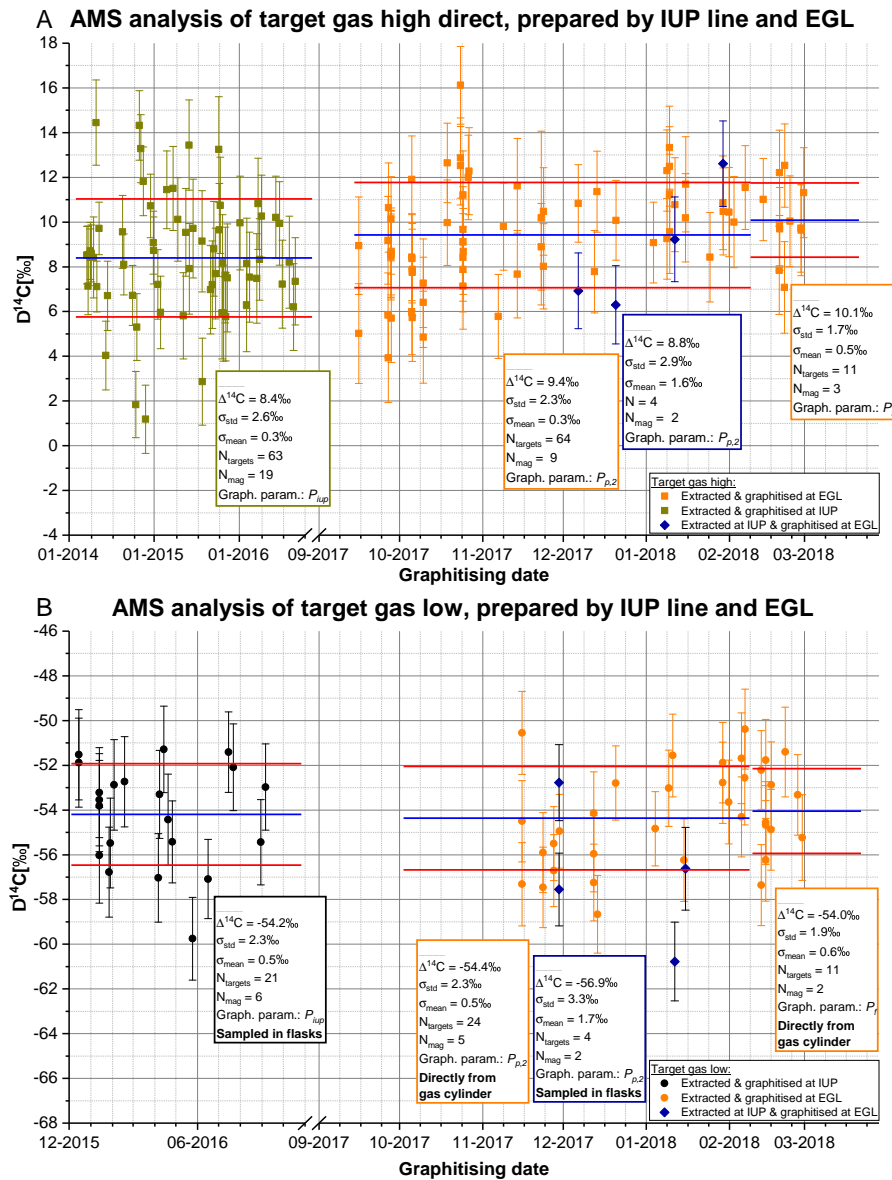


Figure 3.28:  $\Delta^{14}\text{C}$  analysis results of target gases prepared and graphitised at the IUP  $^{14}\text{C}$  laboratory and the EGL. Blue lines indicate the target mean over periods of the same graphitisation parameters. Red lines show the range of the empirical standard deviation. Informations in the boxes refer to targets indicated by the same colour in the respective periods. **A:** All targets'  $\text{CO}_2$  was extracted directly from the pressurised air storage cylinder. 4 targets (shown in dark blue) have been analysed, which were extracted at the IUP  $^{14}\text{C}$  lab and graphitised at EGL. **B:** IUP targets were sampled in 1 L and 2 L glass flasks prior to extraction. EGL targets'  $\text{CO}_2$  was extracted directly from the pressurised air storage cylinder. 4 targets have been analysed, which were extracted at the IUP  $^{14}\text{C}$  lab and graphitised at EGL.

both gases at 1.9 ‰, which means, that no additional uncertainties are introduced during target preparation using  $P_f$ .

The standard deviations for the targets prepared at IUP  $^{14}\text{C}$  laboratory ( $P_{iup}$ ) and EGL with  $P_{p,2}$  range from 2.3 ‰ to 2.6 ‰, hence showing no relevant differences. Analysis of the IUP aliquots, prepared by EGL, indicate an additional uncertainty of 1.8 ‰ to 2.4 ‰ to account for the higher standard deviation. Sources of errors, which are unaccounted for by the other EGL targets, could originate in the pure  $\text{CO}_2$  sample handling at EGL. This test, however, was performed with only 4 targets per target gas. 5 to 10 more existing IUP aliquots are ready to be analysed to confirm this finding in the future.

The mean level of  $\Delta^{14}\text{C}$  for target gas low stays constant over all results within the errors of the means. In target gas high, we see a significant tendency towards 1.7 ‰ heavier  $^{14}\text{C}$  isotopy with time. Figure 3.29 shows the course of the measured  $\delta^{13}\text{C}$  within the same timespan. We see an opposite trend in  $\delta^{13}\text{C}$  compared to

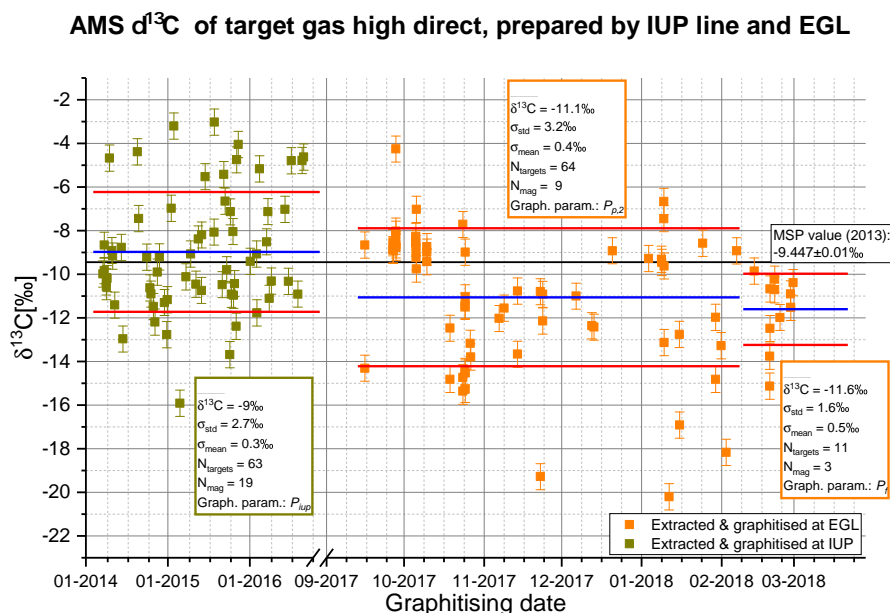


Figure 3.29.: AMS  $\delta^{13}\text{C}$  results for target gas high targets (see  $\Delta^{14}\text{C}$  in Figure 3.28A). Blue lines are the measurement means, red lines indicate the  $1\sigma$  standard deviation.

$\Delta^{14}\text{C}$  of  $-2.6$  ‰. The target gas high cylinder depleted at the end of this work: In March 2018, the remnant cylinder pressure amounted to 30 bar from 140 bar for the newly filled cylinder. These points might indicate a fractionation occurring in the target gas storage cylinder towards the end of its usage period, which can not be corrected for by normalisation of  $\Delta^{14}\text{C}$  results. The effect of observing drifts in

### 3. Set-up of the AMS target Extraction and Graphitisation Line

$\delta^{13}\text{C}$  in emptying pressurised air containers has been observed before at the IUP  $^{14}\text{C}$  laboratory<sup>6</sup>.

#### 3.7.2. LLC compatibility

The compatibility of the results of the two CRL  $^{14}\text{C}$  analysis systems has been examined. For this reason, the AMS-LLC compatibility test series, introduced in 2.2.2, has been continued at the EGL after completion of the parameter test series.

Figure 3.30 shows the results of these comparisons. The first finding, which can be deduced from this study, is a decrease in the scattering of the  $\Delta^{14}\text{C}$  deviations with introduction of the final graphitisation parameter set in March 2018 to 2.7 ‰ (3.30B), which corresponds to the expected uncertainty of the difference derived from the mean measurement uncertainties of the involved values. The scatter of deviation does presumably not originate in short-time deviations of the LLC analysis, since for all periods with two or more measured duplicate samples the standard deviation of the difference of the duplicate samples is larger or equal than the scattering in LLC-AMS difference.

This leads to the second important finding of this examination: Aliquots, which have been sampled and prepared at the CRL since November 2016, show a significant offset from the LLC  $\Delta^{14}\text{C}$  results of  $(2.6 \pm 0.7)$  ‰. For samples taken from January until October 2016, which are also prepared at the EGL, no such an offset can be observed. Together with the fact, that the deviations in the differences between duplicate aliquots are 2 ‰ larger than in the time of the IUP  $^{14}\text{C}$  laboratory, this might indicate issues regarding the CRL aliquotation device<sup>7</sup>. The bias of the duplicate sample difference, which is calculated as the difference between the first and the second taken aliquot, is with  $\Delta(\Delta^{14}\text{C}) = (-1.8 \pm 1.6)$  ‰ not significant. Another possible reason for the offset of LLC to AMS analysis could be a downshift in LLC measurement since beginning of 2017: A drop in  $\Delta^{14}\text{C}$  of the long-term LLC QC  $\text{CO}_2$  of  $(-2.5 \pm 0.6)$  ‰ was observed<sup>8</sup>. This matter is currently subject of further investigation.

Overall, these findings demonstrate the benefits achieved by performing long-term compatibility test series between the CRL labs. They yield not only additional information about AMS measurement precision of EGL-prepared pure  $\text{CO}_2$  samples, but also point out systematic problems in the analysis procedures of the involved laboratories.

#### 3.7.3. Oxalic Acid I as primary QC

As introduced in Section 1.2.3,  $\text{CO}_2$  from combusted Oxalic Acid I material was chosen to define the scale for  $\Delta^{14}\text{C}$  measurements. Reverting the normalisation

---

<sup>6</sup>Personal communication: Ingeborg Levin [April 2018]

<sup>7</sup>The effects of changes in the aliquotation process regarding incomplete  $\text{CO}_2$  transfer are currently subject of investigation.

<sup>8</sup>Personal communication: Samuel Hammer [March 2018]

### 3.7. Establishing EGL quality control

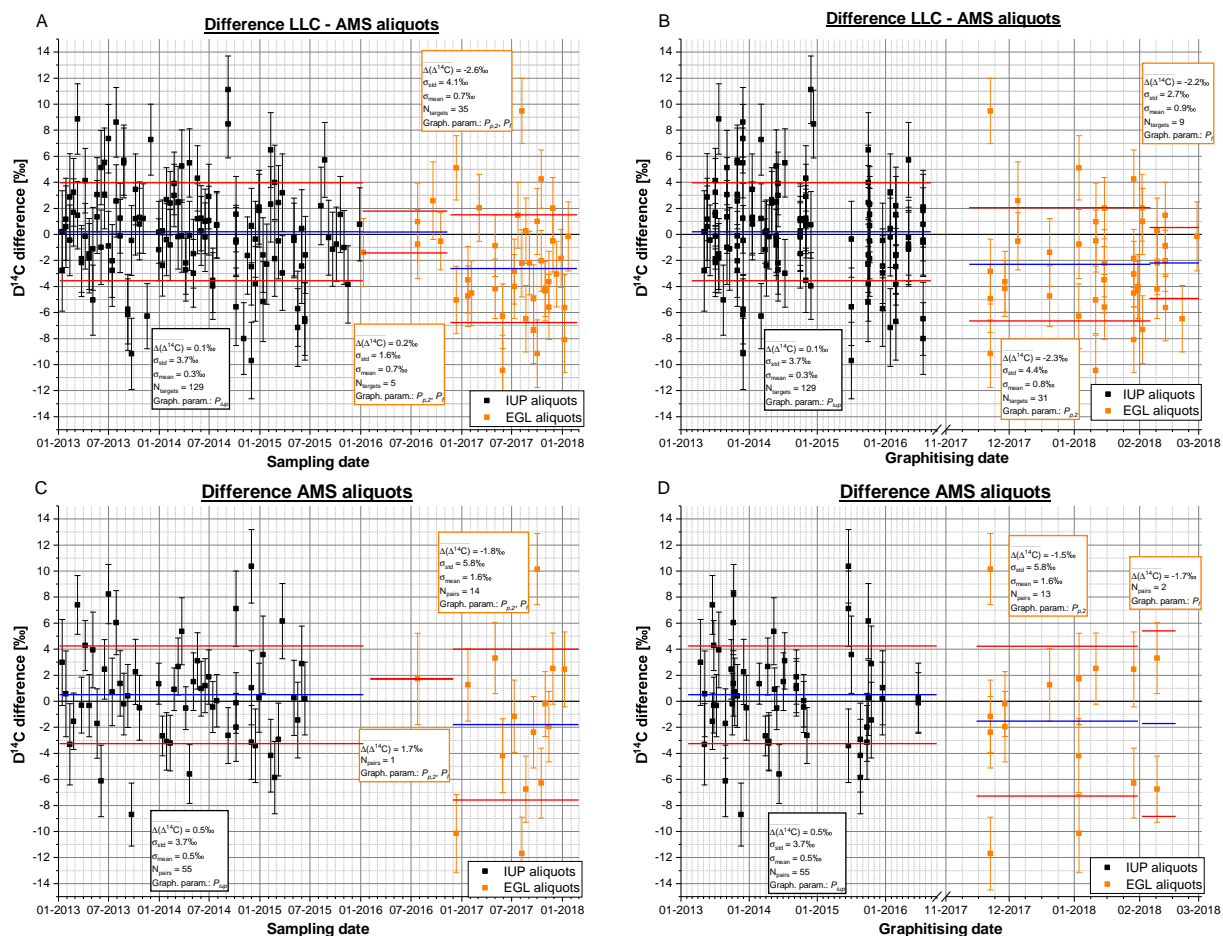


**Figure 3.30.:** Examination of the compatibility between LLC analysis of high-volume samples and AMS analysis of aliquots of the same samples prepared by IUP graphitisation (black points, see also Section 2.2.2) and EGL (orange). Blue lines are the measurement means, red lines indicate the  $1\sigma$  standard deviation. These lines also indicate the periods of time related to the results of the averaging periods presented in the boxes. Shown are the differences in  $\Delta^{14}\text{C}$  between LLC results and AMS aliquots dependent on sampling date of the NaOH sample (A) and graphitising date of the aliquot (B). The difference between the AMS aliquots of the respective same sample are also shown versus sampling date (C) and graphitisation date (D). Sampling date corresponds within a few days to LLC measurement and aliquot taking.

### 3. Set-up of the AMS target Extraction and Graphitisation Line

of the scale definition in equation (1.11) from  $-19\text{‰}$  to  $-25\text{‰}$  yields an nominal value of Oxalic Acid I, normalised to  $-25\text{‰}$ , of  $\Delta^{14}\text{C}_{\text{OxI}} = 39.8\text{‰}$ .

At this point, the foundation is laid for a long-term QC series, which classifies the  $\Delta^{14}\text{C}$  results of the EGL-prepared AMS measurements on an absolute scale. The recently filled pure  $\text{CO}_2$  Oxalic Acid I storage flask, inserted in the EGL, approximately supplies 1000 QC targets. For 1500 CRL samples per year and one primary QC target per AMS magazine, the Oxalic Acid I stock, stored in the EGL, supplies 15 a of QC operation.

Figure 3.31 shows the QC series for two different batches of Oxalic Acid I  $\text{CO}_2$  and the preliminary graphitisation parameter set  $P_{p,2}$  as well as the final set  $P_f$ . The standard deviation of the examined sample sets decreased from  $2.3\text{‰}$  to  $2\text{‰}$

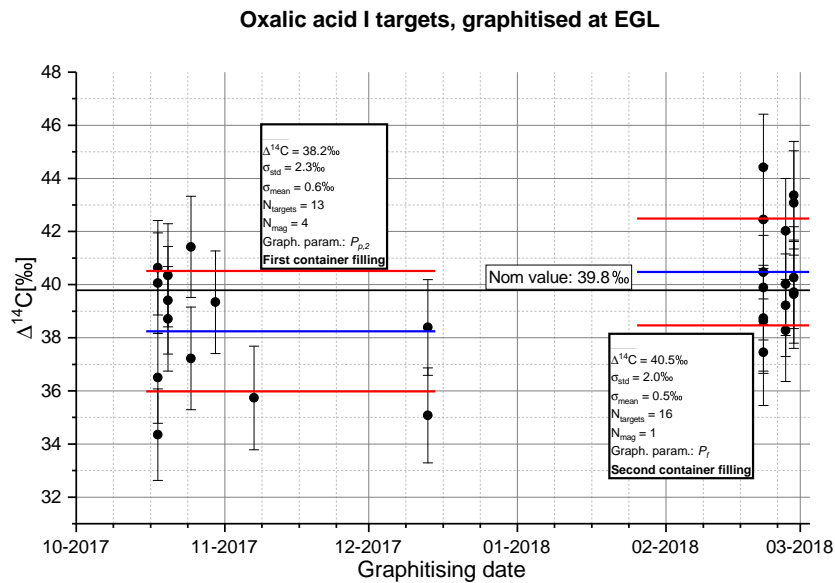


**Figure 3.31.:** Results of the primary QC test series with Oxalic Acid I targets, sampled by the internal pure  $\text{CO}_2$  sampling system of the EGL. Oxalic Acid I  $\text{CO}_2$  originating from two different combustion batches has been used in this work.

for the newly filled Oxalic Acid I storage, which is the source for the planned long-term QC. Therewith the empirical standard deviation is equal to the AMS measurement uncertainty, indicating that no additional errors are introduced by the target preparation at the EGL.

Furthermore, the mean  $\Delta^{14}\text{C}$  converges towards the nominal value, which lies within the  $2\sigma$  uncertainty of the targets prepared in 2018. This means, at the moment we can limit the offset to the canonical  $\Delta^{14}\text{C}$  scale for EGL targets to  $(0.7 \pm 0.5)\text{‰}$ . A continuation of this QC series will lead to a more precise determination of this offset value.

### 3.7.4. Overview of the first results of the EGL QC test series

After introduction of the parameter set  $P_{p,2}$  in July 2017, two long-term QC test series were started at the EGL for assessment of the repeatability of single sample measurements at the CEZ AMS (Section 3.7.1). These were performed using two different whole-air target gases, which were preprocessed in a similar way as whole-air flask samples and allow to determine the repeatability of sample measurements. During the first timespan (July 2017 to February 2018 with parameter set  $P_{p,2}$ ) substantial improvements of the processing protocol at the EGL were implemented; in particular should be mentioned the introduction of tube flushing (September 2017). From March 2018 on, after determination of the final process protocol and introduction of the final graphite parameters, the AMS results showed a standard deviation in  $\Delta^{14}\text{C}$  of  $\pm 1.7\text{‰}$  (Figure 3.28A) resp.  $\pm 1.9\text{‰}$  (Figure 3.28B), which correspond to the AMS measurement uncertainties. These results are comparable to other laboratories measuring  $\Delta^{14}\text{C}$  of air materials to high precision, as Graven et al. (2007) with long-term repeatabilities of  $\pm 1.7\text{‰}$  and (Lehman et al., 2013; Turnbull et al., 2015b), who report  $\pm 1.8\text{‰}$ . The EGL whole-air target gas measurement series, presented here, has been performed for only 2 months at the end of this work with 11 targets for each of the two target gases, which were distributed to 3 resp. 2 AMS magazines. A continuation of this series in the future will provide a reliable validation or falsification of these promising first results for the long-term repeatability for whole-air samples, which are processed at the EGL and analysed at the CEZ AMS. A similar result, regarding the variability in  $\Delta^{14}\text{C}$  results, was shown in the test series with Oxalic Acid I  $\text{CO}_2$  as primary QC material for  $\Delta^{14}\text{C}$  analysis (Section 3.7.3): The first results, using the final process protocol and graphite parameters, analysed in 1 AMS magazine showed a standard deviation of  $\pm 2\text{‰}$  and show no significant offset from the absolute  $\Delta^{14}\text{C}$  scale, defined by Oxalic Acid I.

The results for the LLC-AMS compatibility test series (Section 3.7.2) point out two main problems, which are under investigation right now (see *Summary & outlook*). Firstly, a bias of  $-2.3\text{‰}$  to  $-2.2\text{‰}$  between LLC and AMS measurements was observed for LLC aliquots prepared at the EGL, which corresponds to a drop in QC measurements performed at the LLC in 2017 of  $(-2.5 \pm 0.6)\text{‰}$ . Secondly, a large variability in the  $\Delta^{14}\text{C}$  differences of duplicate aliquots was observed, indicating problems in aliquotation of the large volume samples or in pure  $\text{CO}_2$  target insertion at the EGL. In summary, the compatibility of these two laboratories needs to be further addressed and does not reach that level of agreement shown in Section 2.2.2 for the IUP  $^{14}\text{C}$  laboratory or presented by Hammer et al. (2017) for a consensus value of AMS laboratories all over the world.



## 4. Development of new $^{14}\text{CO}_2$ sampling strategies

Chapter 3 described in detail the development and design of the facility, which serves to convert atmospheric air  $\text{CO}_2$  samples into graphite targets to allow estimation of the fossil  $\text{CO}_2$  component in the atmosphere by high-precision  $\Delta^{14}\text{C}$  measurements. This chapter is dedicated to developing new strategies and methods for  $^{14}\text{CO}_2$  sampling, which justify the still significant amount of time and resources for  $\Delta^{14}\text{C}$  measurements through valuable new information about the observed regions.

### 4.1. Set-up of time-triggered integrated $^{14}\text{CO}_2$ sampling in Heidelberg

Here, I present the methods and results of a newly built-up parallel integrated  $^{14}\text{CO}_2$  sampling system in Heidelberg (HEI). It samples time-triggered at night (19:00-7:00 UTC+1) and daytime (12:00-18:00 UTC+1). Parallel sampling is performed by two different  $^{14}\text{CO}_2$  sampling methods: On the one hand, a new approach of taking whole-air samples in flasks, which are integrated over a period of one week or more. These flask samples can then be analysed for trace gas concentrations and the  $\text{CO}_2$  be subsequently processed to graphite targets by the EGL and analysed for  $\Delta^{14}\text{C}$  by AMS. On the other hand and in addition to this, the traditional integrated  $\text{CO}_2$  absorption in  $\text{NaOH}$  solution and subsequent LLC analysis (see Levin et al., 1980) in Heidelberg has been extended to daytime and nighttime sampling parallelly to the flask sample collection.

$^{14}\text{CO}_2$  sampling in Heidelberg, which is situated in the moderately polluted Rhine valley area, has been performed since 1976 (Levin et al., 2003; Gamnitzer et al., 2006). The first 12 years of sampling were conducted the whole day, since 1988 only during the night to reduce influence of local sources (e.g. traffic emissions in the direct vicinity of the station).

#### 4.1.1. Objectives

Several objectives are behind the development of the new sampling strategy. Foremost, valuable new information about the  $\text{FFCO}_2$  emissions in the catchment area of HEI are expected by day- and nighttime sampling. As introduced in Section 1.5.1, we observe different regimes in the planetary boundary layer at different

#### 4. Development of new $^{14}\text{CO}_2$ sampling strategies

times of the day: At daytime, the FFCO<sub>2</sub> concentrations in the thermal convection driven mixed layer are less influenced by surface to atmosphere fluxes than at night. Additionally, model calculations performed in this work (sections 4.1.2 and 4.2) showed for the years 2005 and 2006, 53 % of the mean nocturnal FFCO<sub>2</sub> offset relative to a continental background originate from a radius of 30 km around HEI. The same region only contributes 36 % of the daytime FFCO<sub>2</sub> offset. Thus, we monitor a larger catchment area during daytime sampling, due to increased horizontal transport. The stable boundary layer at nighttime builds up from the remnants of the daytime mixed layer. For this reason, it is reasonable to see the mixed layer as background for the subsequent stable boundary layer. This approach was also taken by Vardag et al. (2015) and tested in this work for FFCO<sub>2</sub>.

The integrated flask sampling can be performed in a flexible interval. A more frequent period than the biweekly measurements of the traditional large volume sampling, e.g. weekly, enhances the temporal resolution of deduced regional fossil fuel offsets and lowers the impact of  $\Delta^{14}\text{C}$  measurement uncertainties on averaged results, due to a broader basis of measurement results.

An additional important reason for the introduction of daytime sampling in HEI are the requirements of current atmospheric modelling. As sketched in Section 1.1.1, night-time mixing ratios are not sufficiently well represented in global or regional atmospheric models. To enable the usage of our integrated  $^{14}\text{CO}_2$  data in current model systems it is inevitable to provide daytime data. At the same time, the long-term nighttime measurement series is continued and can be utilised, when the models are capable to use them in a quantitative way.

The last substantial reason to set-up the parallel sampling system is the possibility to backup missing points in the respective measurement series by the second sampling system. Simultaneous sampling of the same atmospheric parameters is performed with two different sampling lines and two fundamentally different measurement methods (AMS and LLC). This complements the AMS-LLC compatibility tests (sections 2.2.2 and 3.7.2), which compares equally sampled specimens for the two analysis methods.

##### 4.1.2. Catchment area

The catchment area of time-triggered integrated sampling in HEI has been evaluated. In this work, an evaluation set-up for STILT emission influence maps (footprints) was developed (more details about this set-up will be presented in Section 4.2.1.1). Figure 4.1 shows the results of this evaluation regarding daytime and nighttime sampling.

As mentioned above, the sensitivity of nighttime sampling for near emission sources is substantially higher than that of daytime sampling. The mean sensitivities for different distance ranges from HEI are listed in Table 4.1. The closest range includes the Mannheim metropolitan area (MA) with the BASF industrial complex and the large power plant Mannheim with more than 2 GW output power and more than  $7\text{ Mt a}^{-1}$  CO<sub>2</sub> emission (Umweltbundesamt, 2018). Here, the inte-

#### 4.1. Set-up of time-triggered integrated $^{14}\text{CO}_2$ sampling in Heidelberg

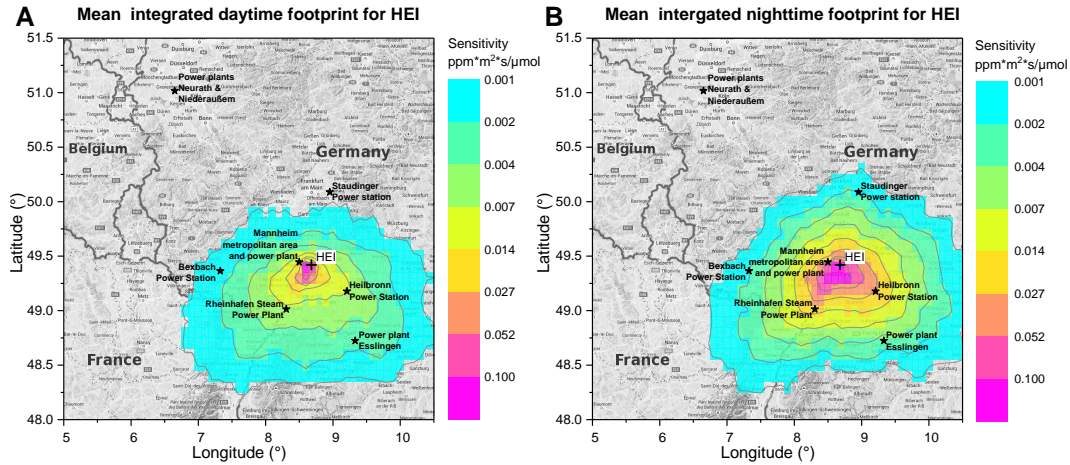


**Figure 4.1.:** Mean modelled sensitivity for trace gas fluxes from the surface to the atmosphere at HEI in integrated daytime (**A**) and nighttime samples (**B**) in 2005 and 2006. Averaged footprints obtained from one-hourly STILT footprints (see 4.2.1.1). The resolution is  $6'$ , which corresponds to  $7\text{ km} \times 11\text{ km}$  in HEI. Asterisks indicate the largest  $\text{CO}_2$  point emission sources in the vicinity of HEI. The colour scale is logarithmic.

**Table 4.1.:** Mean surface emission sensitivity of integrated day- and nighttime sampling for different distance ranges from HEI. For  $>100\text{ km}$ , no average sensitivity was calculated: Given is an upper threshold. Values derived from averaged STILT footprints.

Distance range from HEI	Mean sensitivity [ $\text{ppm m}^2 \text{ s } \mu\text{mol}^{-1}$ ] during	
	Daytime	Nighttime
$<30\text{ km}$	$1.3 \times 10^{-2}$	$4.8 \times 10^{-2}$
$30\text{ km to }100\text{ km}$	$2.1 \times 10^{-3}$	$4.3 \times 10^{-3}$
$>100\text{ km}$	$<1.8 \times 10^{-3}$	$<2.4 \times 10^{-3}$

grated nighttime sampling is 3.7 times more sensitive to  $\text{CO}_2$  fluxes. The second range up to  $100\text{ km}$  covers all major point source  $\text{CO}_2$  emitters, shown in Figure 4.1. In this range, the sensitivity differences flatten out to a factor of 2. The long-range sensitivity makes up a comparable background for both sampling methods, rapidly falling below  $1 \times 10^{-3} \text{ ppm m}^2 \text{ s } \mu\text{mol}^{-1}$  for both timeframes.

The results shown here refer to footprints integrated for more than two years. The sensitivity of the biweekly integrated samples depends on the weather conditions and season, but due to the long integration time they are structurally similar to the two-year averages shown in Figure 4.1. Since the night is not well represented in models for atmospheric mixing, the absolute values presented here might not be exact, but the principal behaviour of nighttime and daytime sensitivity is based on the physics of the boundary layer mixing.

#### 4. Development of new $^{14}\text{CO}_2$ sampling strategies

##### 4.1.3. Sampling set-up

Figure 4.2 shows the sampling set-up of the parallel time-triggered sampling. The ambient air, sampled by both systems, is transferred from the southwest edge of the institute's roof (30 m intake height) to the sampling room by a high throughput pump in less than 1 min.

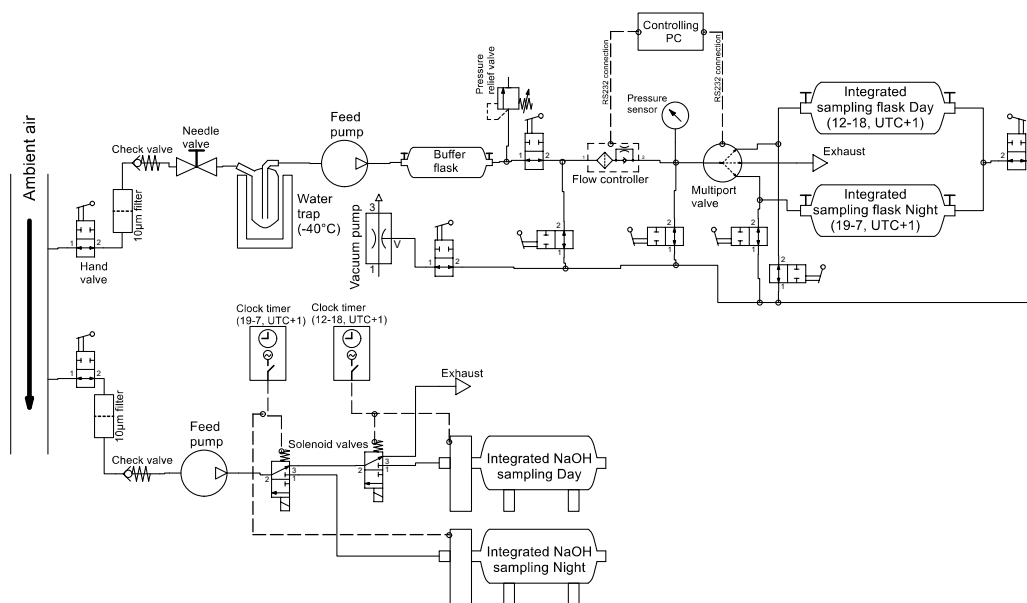


**Figure 4.2.:** Final set-up of the integrated sampling set-up in Heidelberg. Ambient air taken in by high volume flushing from the roof of the IUP (30 m) is sampled by a parallel  $\Delta^{14}\text{CO}_2$  sampling approach for daytime and nighttime. The existing integrated NaOH sampling (see Levin et al., 1980) was split up to time-triggered operation at two periods from only nighttime sampling.

For the integrated NaOH sampling, the ambient air is – after being filtered from dust particles – fed by a membrane pump into the respective Raschig tube device, built by the IUP workshop and described by Levin et al. (1980). Two clock timers toggle the power supply for the corresponding solenoid valves and the Raschig tube engine. Between 18:00-19:00 and 7:00-12:00 UTC+1, the valves are in electroless state, leading the air flow to an exhaust outlet. The air flow is set up for daytime sampling to  $200 \text{ l}_n \text{ h}^{-1}$  and for nighttime sampling to  $150 \text{ l}_n \text{ h}^{-1}$ .

In the flask sampling line, the filtered and cryogenically dried ( $-30^\circ\text{C}$ ) air is fed into the system by a membrane pump (KNF, *N 86 KT.18*). The flow through the high-flow region of the line is regulated by a needle valve to  $250 \text{ ml}_n \text{ min}^{-1}$ , since this flow rate proofed in preparatory tests to pass the membrane pump without being contaminated (esp. in  $\text{N}_2\text{O}$ ) by the pump. The pressure behind the pump is regulated to 2.3 bar by a pressure relief valve. Before sampling, the sampling flasks are evacuated to less than 1 mbar by a membrane vacuum pump (vacuubrand, *MV*

#### 4.1. Set-up of time-triggered integrated $^{14}\text{CO}_2$ sampling in Heidelberg

2 NT). The steady flow into the sampling flasks to perform temporally representative integrated sampling is performed by a low  $\Delta p$  flow controller (Bronkhorst, *Low  $\Delta p$ : F-200LV-002-ABD-11-E*) subsequent to a buffer volume (glass flask, 1 L). The buffer volume ensures non fluctuating high-pressure, which can be reliably regulated by the flow controller. Typically, the flow, which is lead into the sampling flasks or to exhaust by a multiport valve (VICI, *12G-1103V 15L*), is 1 ml<sub>n</sub>/min for nighttime sampling in standard ICOS 3L flasks and 0.79 ml<sub>n</sub>/min for daytime sampling in 1 L flasks. Setting up of flow rate and valve position is conducted by a connected controlling PC.

##### 4.1.4. Trace gases

Typically, air samples in flasks are taken as spot samples or short-time integrated samples ranging from about 1 h (e.g. Turnbull et al., 2012) to 1 d (Kuderer, 2016; Kneuer, 2017). The approach, tested in this work, relies on integration of the ambient air over a substantially longer timespan; time ranges from 3 d to 18 d have been tested. The combination of low flow ( $<1 \text{ ml}_n \text{ min}^{-1}$ ) and long sampling time makes this approach vulnerable to contamination by leakages and interaction with the sampling material like seal rings, pump membranes as well as steel and glass surfaces.

To examine the influence of these aspects, all flasks, sampled in the testing period from June 2015 until January 2018, were analysed for  $\text{CO}_2$ ,  $\text{CH}_4$ ,  $\text{N}_2\text{O}$ ,  $\text{CO}$  and  $\text{H}_2$  with the combined Heidelberg gas chromatographic (GC) system (see Hammer, 2008; Hammer and Levin, 2009). The trace gas concentrations were then compared to the respective mean concentrations over the sampling time in continuous trace gas measurements, performed by the same GC from the same intake line. The continuous mean was calculated by linearly interpolating valid GC measurement points and integrating the resulting piecewise linear function exactly over the time of sampling. A time shift of 18 min was added to the sampling time, which corresponds to the exchange time of the air in the volumes of the sampling system before the sampling flasks, i.e. the time difference between continuous measurement and arrival of the corresponding air parcel at the flask. An exact consideration of the sampling timings has significant impact on the comparison results, since the time-triggered sampling integrates over several shorter sampling periods, adding up the boundary effects.

Figure 4.3A shows the flask results, continuous measurements and its means. Displayed in red is sampling period 1, where in a slightly different set-up integrated samples over the whole day have been taken. In black (nighttime) and blue (daytime) the time-triggered results are shown (period 2), here as well as in the following sections. The ambient  $\text{CO}_2$  shows a range of 140 ppm with some higher exceptions. The mean  $\text{CO}_2$  concentrations range from 395 ppm to 465 ppm. The difference of mean nighttime (430 ppm) and daytime (418 ppm)  $\text{CO}_2$  is 12 ppm. In Section 4.1.6 will be shown, which part of this offset is  $\text{FFCO}_2$ .

#### 4. Development of new $^{14}\text{CO}_2$ sampling strategies

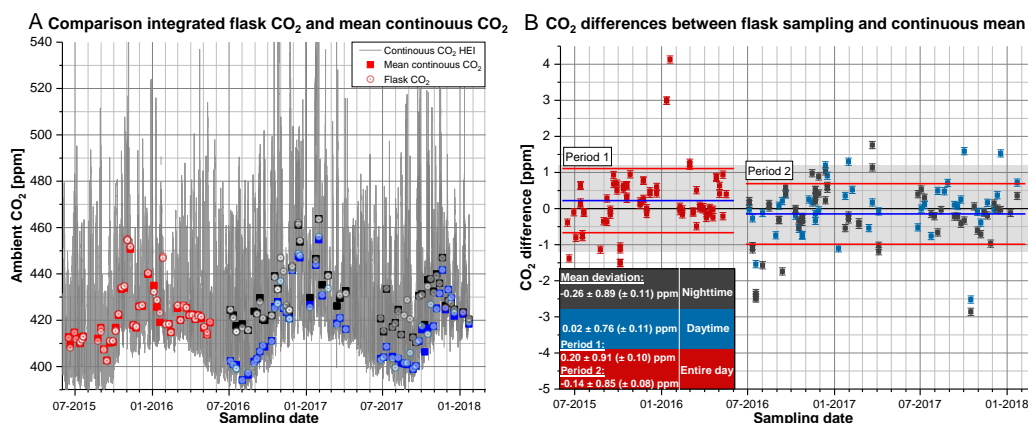


**Figure 4.3.:** Evaluation of the integrated flask sampling by comparison of the mean of continuous CO<sub>2</sub> measurements and flask results. **A:** CO<sub>2</sub> concentrations in ambient air, the mean of ambient air and integrated flasks. **B:** Concentration difference between flask and mean CO<sub>2</sub>:  $c_{flask} - c_{mean}$ . The grey zone indicates the concentration range outside of which contamination in pure FFCO<sub>2</sub> would have an effect of more than 2 ‰ on the  $\Delta^{14}\text{C}$  results.

Figure 4.3B shows the differences between flask CO<sub>2</sub> concentrations and continuous means. The mean difference in both periods lies within the  $2\sigma$  range of the error of the means at zero. The standard deviation of single differences lies at  $\pm 0.9$  ppm for both periods. Flasks have been flagged for this comparison, if the comparison could not be reliably performed due to large gaps ( $>5$  h) in the continuous data or problems with the GC system. The grey zone ( $\pm 1.2$  ppm) indicates the range, where sample contamination of pure FFCO<sub>2</sub> would cause an offset, smaller than the  $\Delta^{14}\text{C}$  measurement uncertainty according to (1.21). Samples outside this zone are considered as questionable in the following.

The comparison results for CH<sub>4</sub>, N<sub>2</sub>O, CO and H<sub>2</sub> are shown in Figure B.11. In methane, especially daytime flasks show an mean enrichment of  $(3.9 \pm 0.7)$  ppb. Nitrous oxide is slightly depleted in flasks ( $(-0.09 \pm 0.04)$  ppb), which has been observed before when conveying air with the feed pump used in this test setting. Hydrogen is slightly depleted in flasks, which is possibly caused by the high volatility of the small H<sub>2</sub> molecules and loss through small leakages. A flask offset in CO of 4 ppb to 5.3 ppb and the deviation in H<sub>2</sub> could also be caused by non-linearity effects in the GC measurement, since the range in continuous measurements is much larger than in the flasks.

In summary, we see a good agreement in the trace gas comparison. Especially, the scatter in CO<sub>2</sub> is less than 1 ppm, which is mainly driven by individual outliers. When no continuous trace gas measurement is available at the station, the flask samples provide reliable integrated trace gas concentrations. With parallel continuous measurements, a practicable tool is available to determine samples, which were taken non-optimally.

#### 4.1.5. $^{14}\text{CO}_2$ results

In Figure 4.4, the  $\Delta^{14}\text{C}$  results of almost 5 years of integrated NaOH sampling at day- and nighttime as well as long-term integrated flask sampling are presented. Graphite target preparation of flask samples, integrated over 3 d to 13 d without

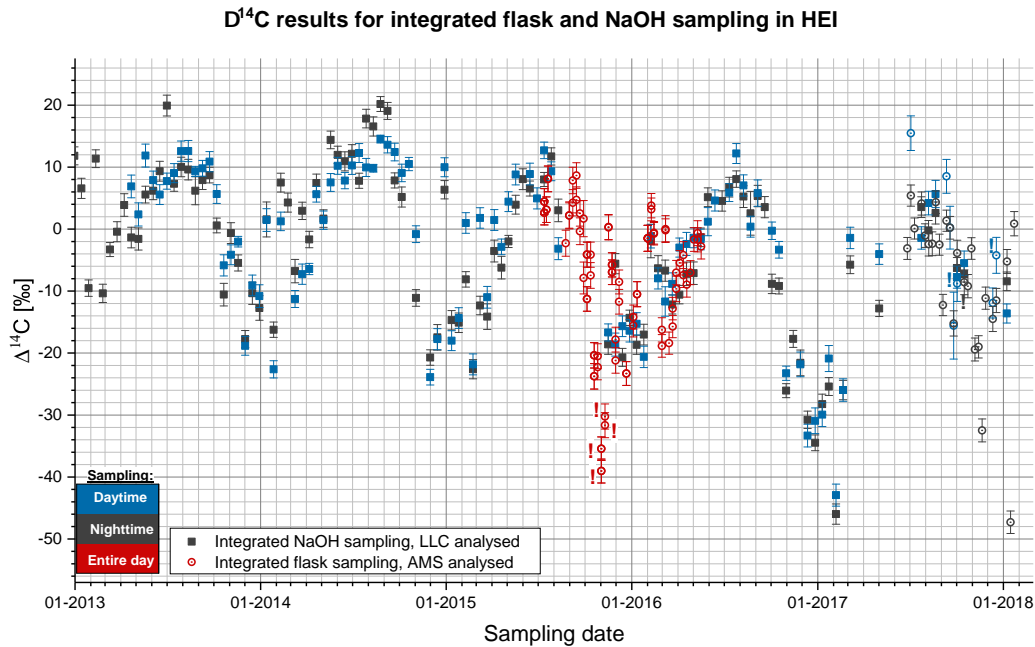


Figure 4.4.:  $\Delta^{14}\text{C}$  results for integrated sampling from 2013 to January 2018. Error bars indicate the measurement uncertainties of LLC or AMS analysis. In autumn 2015, unnoticed leakages in the NaOH sampling line lead to an interruption of the measurement series, compensated by integrated flask sampling. In summer 2017, the commissioning of the CRL caused a gap in LLC analysis. (!): Questionable flask results, which could not be examined in trace gas comparison or showed high deviations in  $\text{CO}_2$ .

time-triggering, has been performed at the IUP  $^{14}\text{C}$  laboratory. Night- and daytime triggered whole-air samples have been processed at the EGL with the graphitisation parameter set  $P_{p,2}$ . A long term measurement series of integrated daytime  $\Delta^{14}\text{C}$  has been established, providing Heidelberg  $^{14}\text{C}$  data at daytimes, which are well represented in current atmospheric models.

In general, a continuation of the long-term decrease in atmospheric  $\Delta^{14}\text{C}$  at HEI can be observed in all sampling and measurement methods. An examination of the differences between flask and NaOH sampling as well as AMS and LLC analysis are given in the following subsections.

#### 4. Development of new $^{14}\text{CO}_2$ sampling strategies

##### 4.1.5.1. Integrated flask sampling

The  $\Delta^{14}\text{C}$  results of the integrated flask samples have been compared to the measurements of the corresponding NaOH samples. For this measure two different averaging methods had to be used. For period 1, the mean of two weekly taken integrated flasks (collected over the entire day) is compared to a hypothetical whole-day NaOH sampling result.

The weighted mean of the respective daytime and nighttime samples is calculated following the interpolation sketched in Figure 4.5. During period 2 the two week means of the day- and nighttime flasks are directly compared to the respective NaOH samples.

Figure 4.6 shows the results of this comprehensive comparison of fundamentally different sampling and analysis methods. Where available, the evaluation versus the LLC analysis results was supplemented by AMS analysis of NaOH sample aliquots.

The results for period 1 show in their mean value with  $(-0.4 \pm 0.9) \text{‰}$  no significant offset from zero. The standard deviation is with  $\pm 2.6 \text{‰}$  slightly higher than the mean measurement uncertainty induced uncertainty of  $1.7 \text{‰}$ . The resulting additional error component of  $2 \text{‰}$  is composed of unaccounted errors in sample preparation for  $^{14}\text{C}$  analysis, not sufficient representation of the true diurnal  $\Delta^{14}\text{C}$  cycle by the simple model shown in Figure 4.5 and contaminations during the sampling.

The evaluation of period 2 also shows no significant offset from zero between both analysis techniques. However, the results, which only differ in the method of their NaOH  $^{14}\text{C}$  analysis vary by  $(2.4 \pm 1.8) \text{‰}$ . This is consistent with the systematical offset between LLC and AMS in 2017, shown in Section 3.7.2. The sample variability of  $\pm 4.3 \text{‰}$  over all results in period 2 is also well in line with the value of  $\pm 4.4 \text{‰}$  found in the AMS-LLC compatibility test series (Figure 3.30B). This means no additional error contributions by the integrated flask sampling technique can be observed. Only four sequent daytime integrated flasks, which were not flagged due to trace gas concentration deviations, were prepared to graphite targets and analysed by AMS. Due to this, no substantial statement about differences in  $\Delta^{14}\text{C}$  between day- and nighttime flask sampling can be made here. In general, daytime targets show an increased AMS analysis error ( $\approx 3 \text{‰}$ ), since they provide only one third of the standard  $\text{CO}_2$  amount for EGL, due to the smaller sample volume of 1 l, leading to an lower AMS counting rate.

In summary, these results show, that integrated low-flow  $^{14}\text{CO}_2$  sampling in whole-air flasks is possible without applying substantial additional variation and any significant offset to the results of the integrated NaOH sampling technique,

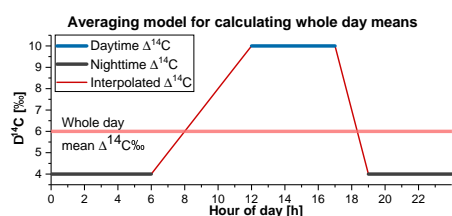
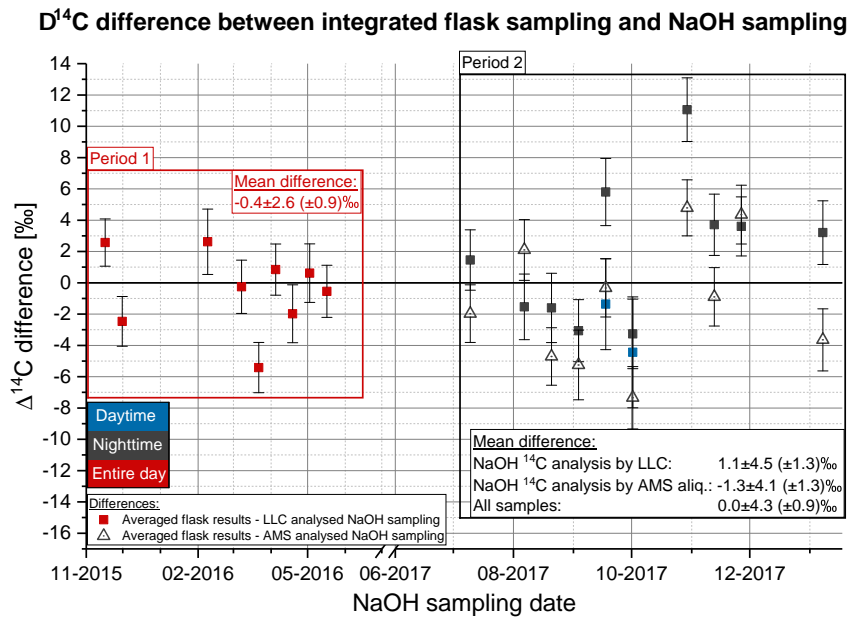


Figure 4.5.: Linear interpolation of day- and nighttime  $\Delta^{14}\text{C}$  to the whole day.

#### 4.1. Set-up of time-triggered integrated $^{14}\text{CO}_2$ sampling in Heidelberg



**Figure 4.6.:** Evaluation of the integrated flasks'  $\Delta^{14}\text{C}$  deviation versus integrated NaOH samples. Flask samples have been prepared for AMS at the IUP  $^{14}\text{C}$  lab (period 1) or with the EGL (period 2). Contributing NaOH results have been achieved by LLC analysis or EGL preparation and AMS analysis of the respective aliquots. Error bars are calculated by Gaussian error propagation of the measurement uncertainties in the related formulas for differences calculation. Displayed uncertainty values are standard deviations, listed in parentheses are errors of the mean.

proven over decades in Heidelberg. The integrated flask set-up allows to examine new sampling strategies for  $\Delta^{14}\text{C}$  monitoring and  $\text{FFCO}_2$  estimation. This could be a long-term measurement series in nocturnal  $\Delta^{14}\text{C}$  as started in this work or parallel day- and nighttime sampling to examine the differences in the respective  $\text{FFCO}_2$  offsets (compare Section 4.1.6 for the NaOH sampling results). New strategies for integrated  $^{14}\text{CO}_2$  sampling (see Section 4.2) can be realised on stations without continuous trace gas monitoring, since the flasks provide reliable integrated concentration information.

#### 4.1.6. Nighttime $\text{FFCO}_2$ offset in Heidelberg

Here, I present the nocturnal  $\text{FFCO}_2$  offset in HEI from 2013-2018 compared to the daytime level in the same period. As introduced in Section 1.3, the traditional approach in estimating regional  $\text{FFCO}_2$  offsets is to compare the  $^{14}\text{C}$  measurements at the polluted site (e.g. HEI) with a continental (e.g. Jungfrauoch – JFJ) or maritime (e.g. Mace Head – MHD) background site. The approach, presented here, follows the idea, sketched in 4.1.1 and utilised before by Vardag et al. (2015) and uses the  $\Delta^{14}\text{C}$  results of integrated daytime sampling as background to evaluate the night-

#### 4. Development of new $^{14}\text{CO}_2$ sampling strategies

time results for estimating nighttime FFCO<sub>2</sub> offsets. In Section 4.1.2 was shown that for distances from HEI >100 km the emission sensitivities according to STILT model runs for daytime and nighttime sampling are similar. For distances <100 km the mean sensitivity for daytime sampling amounts to  $3.1 \times 10^{-3} \text{ ppm m}^2 \text{ s } \mu\text{mol}^{-1}$  and for nighttime to  $8.2 \times 10^{-3} \text{ ppm m}^2 \text{ s } \mu\text{mol}^{-1}$ . It is evaluated, whether the sensitivity difference of  $5.1 \times 10^{-3} \text{ ppm m}^2 \text{ s } \mu\text{mol}^{-1}$  is reflected in the measurements. This method is only expected to yield reliable information about the nighttime catchment area of the HEI station for sampling times with distinctive nocturnal inversion. This means especially in winter no nocturnal FFCO<sub>2</sub> offset is expected.

Figure 4.7A shows the course of the nighttime versus daytime  $\Delta^{14}\text{C}$  results and the differences in mean CO<sub>2</sub> concentrations, which were calculated from continuously measured ambient CO<sub>2</sub> at the station. In the CO<sub>2</sub> differences an expected

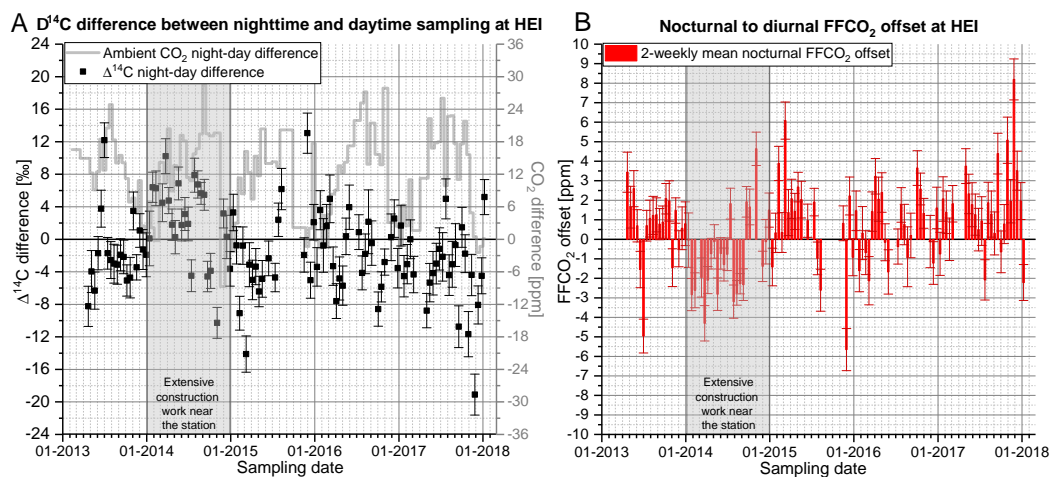


**Figure 4.7.:** FFCO<sub>2</sub> analysis of 5 a integral day- and nighttime sampling at HEI. This evaluation is performed with LLC analysis results of integrated NaOH samples. **A:**  $\Delta^{14}\text{C}$  and CO<sub>2</sub> concentration differences between night- and daytime samples. **B:** Nocturnal FFCO<sub>2</sub> offset in Heidelberg, calculated according to (1.19) using the measurement data shown in A and Figure 4.4. Errors of FFCO<sub>2</sub> were derived using (1.21) and originate as well as the uncertainties in the  $\Delta^{14}\text{C}$  differences in LLC measurement uncertainty.

seasonal cycle can be seen, which is dominated by biospheric activity: During the growing season, especially in summer, large-scale net uptake of CO<sub>2</sub> by photosynthesis depletes the atmospheric concentration on daytime and biospheric net fluxes increase the nighttime CO<sub>2</sub> concentration. The same plot shows the  $\Delta^{14}\text{C}$  differences between parallelly conducted nighttime and daytime integrated  $^{14}\text{CO}_2$  NaOH sampling, analysed by LLC. The absolute values were shown in Figure 4.4. In most years during the observed period, the majority of nighttime samples shows lower  $\Delta^{14}\text{C}$  than the parallel daytime sample, indicating a larger FFCO<sub>2</sub> component during night.

#### 4.1. Set-up of time-triggered integrated $^{14}\text{CO}_2$ sampling in Heidelberg

Figure 4.7B shows the biweekly integrated nocturnal FFCO<sub>2</sub> excess compared to the daytime sample as background, calculated according to (1.19). Most yearly mean nighttime FFCO<sub>2</sub> offsets range from 1 ppm to 1.5 ppm, without being distinguishable outside their error ranges. In 2014, however, the evaluation shows a higher FFCO<sub>2</sub> concentration during daytime. This is probably caused by extensive construction work, which was carried out to complete the Mathematikon building about 50 m from the sampling site on the roof of the IUP. The operation of construction machinery and extensive excavation caused presumably very local FFCO<sub>2</sub> concentration increases, which falsified the background provided by the daytime sampling. Therefore, further considerations were made by means of data from 2015-2017.

Table 4.2 lists the results of this study by seasons. As expected, the seasonality in the total FFCO<sub>2</sub> offset is different to what is seen in the traditional approach: E.g. Levin et al. (2011) show that the largest offset in HEI compared to JFJ is observed in January due to suppression of vertical mixing by long-lasting inversions in the Rhine valley. In this study relatively strong nighttime FFCO<sub>2</sub> offsets relative

**Table 4.2:** Ambient CO<sub>2</sub> and FFCO<sub>2</sub> excess of night versus day samples by seasons in the years 2015-2017. The fraction FFCO<sub>2</sub> in CO<sub>2</sub> surplus is the nighttime to daytime FFCO<sub>2</sub> offset divided by the total CO<sub>2</sub> excess. Uncertainties are the errors of the means calculated from offset variation within the respective seasons.

Season	Nighttime offset		Fraction FFCO <sub>2</sub> in
	CO <sub>2</sub> [ppm]	FFCO <sub>2</sub> [ppm]	CO <sub>2</sub> surplus [%]
Spring	12.6 ± 1.3	1.8 ± 0.5	14 ± 4
Summer	19.1 ± 1.4	0.3 ± 0.4	2 ± 2
Autumn	12.3 ± 2.4	1.6 ± 0.9	13 ± 8
Winter	3.3 ± 1.3	0.5 ± 0.4	15 ± 13

to daytime signals are seen in spring and autumn, while in winter and summer only insignificant FFCO<sub>2</sub> offsets can be observed. The fraction of FFCO<sub>2</sub> in the nocturnal CO<sub>2</sub> offset ranges from 13 % to 15 %, except for summer with a very small fossil part in the large, mainly biospheric, CO<sub>2</sub> offset. The fraction FFCO<sub>2</sub> in CO<sub>2</sub> surplus in winter could not reliably determined due to the small signal to noise ratio.

An explanation for these findings can likely be derived from two important influencing factors. On the one hand, FFCO<sub>2</sub> emissions are subject to variations on a seasonal and daily scale. This means in particular that in the night less emissions by domestic heating and traffic are expected to take place in the catchment area. The same is true for summertime, where less domestic heating occurs, especially in the city area of Heidelberg, which might explain the small offset in summer, where a distinct diurnal cycle of the atmospheric mixing should allow the usage of this method. On the other hand and presumably more important, the results obtained by this method are mainly not determined by the degree of vertical mixing in the PBL, but by the difference in the degree of vertical mixing between day and night.

#### 4. Development of new $^{14}\text{CO}_2$ sampling strategies

This means e.g., when the mixing in the PBL on a winter day is almost as weak as in the following night, the emitted nighttime FFCO<sub>2</sub> does not build up to a significant offset.

In summary, the method presented here with its first results provides additional information about the emissions in the catchment area by means of significant nighttime FFCO<sub>2</sub> offsets in spring and autumn. To retrieve quantitative statements, emission signals would need to be disentangled from atmospheric transport. This could be done by development of transport models, which represent the nocturnal atmosphere well enough, or by utilisation of the Radon-tracer method (Schmidt et al., 2003).

### 4.2. Modelling of trajectory-triggered integrated sampling

Here, a method is presented and investigated, which allows allocating measured FFCO<sub>2</sub> offsets to a certain source region by utilising a trajectory-triggered integrated sampling procedure. Figure 4.8 shows the principle of this sampling method for the example of the Heidelberg (HEI) sampling site.

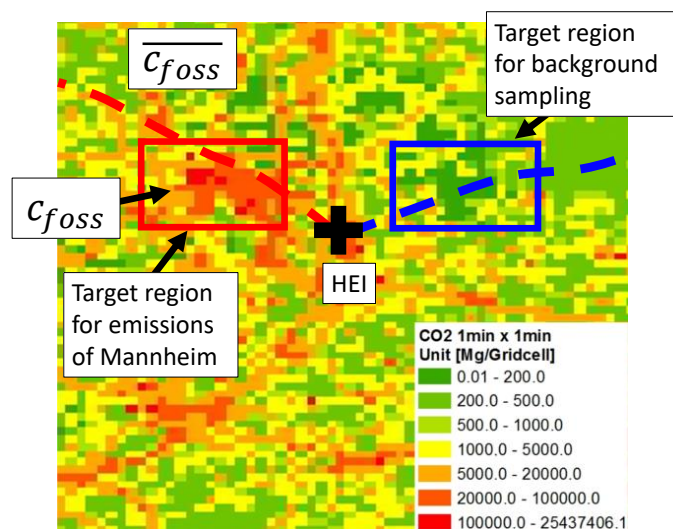


**Figure 4.8.** Principle of triggered FFCO<sub>2</sub> sampling, using the example of Heidelberg. Anthropogenic CO<sub>2</sub> emissions around HEI in 1' resolution are taken from Pregger et al. (2007). The red box indicates the region of interest (Mannheim metropolitan area), which contributes the FFCO<sub>2</sub> component  $c_{foss}$  to the concentration measured at the station. The blue box hems an area of low FFCO<sub>2</sub> emissions, used to estimate the background contribution  $\overline{c_{foss}}$ . Sampling at the station is triggered by trajectory forecasts (dashed lines).

The integrated  $^{14}\text{CO}_2$  sampling is triggered by air mass trajectory forecasts (see Section 4.2.1.2) passing a beforehand defined region of interest. This procedure

## 4.2. Modelling of trajectory-triggered integrated sampling

aims to enhance the sample's sensitivity for FFCO<sub>2</sub> emissions in the region of interest (ROI) compared to untriggered or time-triggered integrated sampling (see Section 4.1.2). In addition, a background FFCO<sub>2</sub> sampling is conducted. This background is supposed to be provided by a parallel integral sampling, triggered to a low-emission target region, which avoids direct contribution from the ROI.

The physical sampling method, e.g. long-term/low-flow integrated flask sampling (section 4.1.3), traditional NaOH sampling (Levin et al., 1980) or short-term integrated sampling (Kuderer, 2016; Kneuer, 2017), is not predefined by this methodology and can be chosen according to the conditions at the station. In this thesis, however, the sampling is virtually tested in a model environment, described in the following sections. For four ICOS stations (Gartow (GAT), Lindenberg (LIN), Hohenpeißenberg (HPB) and the pilot station Heidelberg (HEI)), the optimal station specific trajectory-triggered sampling routine has been investigated.

### 4.2.1. Model environment

To evaluate the real or simulated measurements of the integrated samples, the balance equations (1.16) and (1.17) have to be adapted to the sampling conditions for a targeted region:

$$c_{meas} = c_{bg} + c_{bio} + c_{foss} + \overline{c_{foss}} \quad (4.1)$$

$$c_{meas}(\Delta^{14}C_{meas} + 1000 \text{‰}) = c_{bg}(\Delta^{14}C_{bg} + 1000 \text{‰}) + c_{bio}(\Delta^{14}C_{bio} + 1000 \text{‰}), \quad (4.2)$$

where the fossil component from (1.16) and (1.17) is split up into one part  $c_{foss}$ , originating from the target region and  $\overline{c_{foss}}$  contributed by emitters in the catchment area, which are not in the target region (cf. Figure 4.8).  $c_{bg}$  is the contribution from the continental background and  $c_{bio}$  from the biosphere. The equations (4.1) and (4.2) describe the concentrations and isotopic balance in the sample, triggered for the ROI. To solve these equations for the contribution only from the target region ( $c_{foss}$ ), we need to make following assumptions:

1. Within the same sampling period,  $\overline{c_{foss}}$  of the ROI can be estimated by the whole FFCO<sub>2</sub> component of the background sampling.
2. Both samples share the same continental background CO<sub>2</sub> level  $c_{bg}$ .
3. The biospheric <sup>14</sup>C signature can be approximated by the  $\Delta^{14}C$  measurement of the background sample:  $\overline{\Delta^{14}C_{meas}} = \Delta^{14}C_{bio}$

In other words, the triggered sampling for the low-emission region provides a station specific background for the sample, triggered for the ROI, when these assumptions can be made. Especially near-field emissions in the direct vicinity of the station are removed from the equation, facilitating a separate monitoring

#### 4. Development of new $^{14}\text{CO}_2$ sampling strategies

of the FFCO<sub>2</sub> originating in emissions from the ROI. With these assumptions, an equation can be established, analogously to (1.19):

$$c_{foss} = c_{meas} \frac{\overline{\Delta^{14}\text{C}_{meas}} - \Delta^{14}\text{C}_{meas}}{\Delta^{14}\text{C}_{meas} + 1000 \text{‰}} \quad (4.3)$$

Assumption 2 can likely be made, since, even if the backgrounds of both samples would be better represented by different background domains, the differences are small. Levin and Kromer (2004) found a difference between the continental  $\Delta^{14}\text{C}$  background level at Jungfraujoch and the marine background at Mace Head of only 0.7 ‰. Assumption 3 is justified in the same way as shown in Section 1.3.1.

For the justification of assumption 1, a model environment for the stations mentioned above has been set up, in a way that only FFCO<sub>2</sub> emissions are present ( $c_{bg} = c_{bio} = 0$ ), to prove this concept without disturbances. An evaluation software has been developed to conduct the required calculations for the investigated time automatically, summarise the results and create visual representations of the results. In the following, I will give an short overview of the used model systems.

##### 4.2.1.1. Atmospheric transport

Simulation of the atmospheric FFCO<sub>2</sub> transport to the station locations has been conducted using STILT footprints. The operating principle of STILT footprint generation was explained in Section 1.5.3.2. Table 4.3 lists the characteristics of the emission sensitivity data used in this work. The set of STILT model sensitivity

**Table 4.3.:** Characteristics of the STILT footprint data used in this study. Timeframe indicates the years, for which the model has been run. Backward time is the time, which the meteorological fields were run backwards to create the emission sensitivity. Footprints were provided by Frank-Thomas Koch (*Max Planck Institute for Biogeochemistry, Jena, Germany*) and Felix Vogel (*Laboratoire des Sciences du Climat et de l'Environnement, Gif-sur-Yvette, France*).

Evaluated stations	Resolution		Timeframe	Spatial coverage	Backw. time
	Space	Time			
HEI	6' × 6'	1 h	2005-2006	40° × 40°	24 h
HPB, LIN, GAT	15' × 15'	3 h	2007	28° × 47°	300 h

results provides for each point in space and time, defined by the resolution, a linear mapping from the emission space to the observation, i.e. concentration, space. The sensitivity is given in units of concentration per emission rate density:  $\text{ppm} / \frac{\mu\text{mol}}{\text{m}^2 \text{s}} = \text{ppm m}^2 \text{s} \mu\text{mol}^{-1}$ .

#### 4.2.1.2. Trajectory calculation

The HYSPLIT trajectories (see Section 1.5.3.1) in a real-world sampling system are calculated using wind fields from weather forecast data. Kuderer (2016) used the forecasts provided by the Global Forecast System (GFS) with a spatial resolution of  $0.5^\circ \times 0.5^\circ$  and a temporal resolution of 3 h.

In the virtual sampling set-up presented here, trajectory analysis based on archived meteorological data is performed. For the years 2005-2007, covered by the used STILT footprints, the Global Data Assimilation System (GDAS) archive with  $1^\circ \times 1^\circ$  spatial resolution is utilised. This archive is the only globally operating, which provides hourly time resolution for HYSPLIT trajectory calculation before 2012. After this time, a resolution of  $0.25^\circ \times 0.25^\circ$  is provided. In the framework of this study, the evaluation software was used to calculate the respective simulated HYSPLIT trajectory forecast for the date of every utilised STILT footprint.

#### 4.2.1.3. A priori emission model

As described above, a model world with purely anthropogenic emissions has been set up. For this purpose three different GHG emission inventories have been used to simulate FFCO<sub>2</sub> emissions in the evaluated station's catchment areas

IER-5 covers the entirety of Europe in a spatial resolution of 5'. The decomposition of this inventory from the official UNFCCC Greenhouse gas inventory data 2004 has been sketched in Section 1.5.4.1 and by Pregger et al. (2007). Figure 4.9 gives an overview of the distribution of anthropogenic CO<sub>2</sub> emissions in Europe, given by the yearly total of IER-5. IER-1 has been decomposed in even more detail to 1' resolution, but is only available for the area of Germany. Both inventories differentiate between emission sources according to the Selected Nomenclature for Air Pollution (SNAP). For this study, the combined emissions of the SNAP sectors 1 to 9 have been used for the simulation of the trajectory-triggered sampling, assuming the emissions for the most part to be fossil. The modelled emissions are modulated on a daily, weekly and monthly basis, to represent e.g. the increased emissions by domestic heating in winter or rush-hour traffic on weekdays. This was taken into account in the calculations carried out in this study.

To perform a comparison with another set of emission inventory data, the Emissions Database for Global Atmospheric Research (EDGAR 4.2 EDGAR, 2011) was additionally used. EDGAR provides decomposed inventory data based on the energy balance statistics of the International Energy Agency (IEA). In this study, the CO<sub>2</sub> emission inventory excluding short term cycles (e.g. biomass burning) was used and assumed to be fossil for the most part.

#### 4.2.1.4. Contribution matrices and sample concentrations

The concentration contribution analysis performed in this study is based on generated contribution matrices. For each point in time, which was chosen by the

#### 4. Development of new $^{14}\text{CO}_2$ sampling strategies

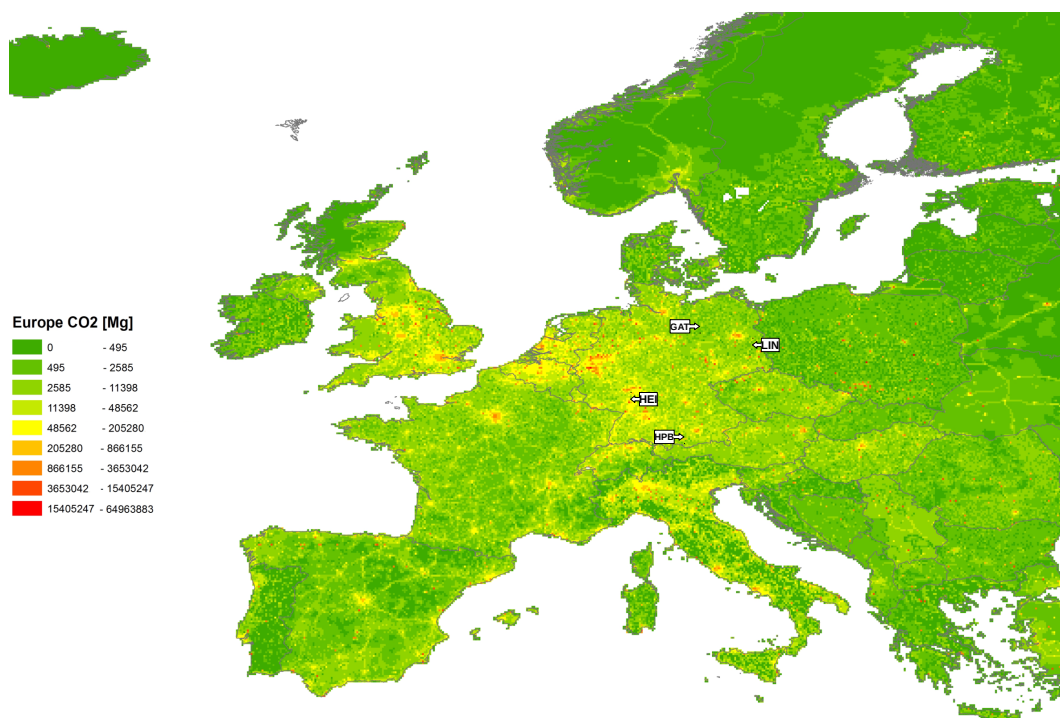


**Figure 4.9.:** Anthropogenic CO<sub>2</sub> emission inventory for Europe. Regional decomposition performed on the basis of the official UNFCCC Greenhouse Gas Inventory Data 2004 (excluding biomass burning, international bunkers, agriculture, land-use change and forestry). Emission units are Mg a<sup>-1</sup>, colour scale is logarithmic. Marked on the map are the ICOS stations Gartow (GAT), Lindenberg (LIN), Hohenpeißenberg (HPB) and pilot station Heidelberg (HEI), which have been investigated regarding triggered sampling in this work. Emission map in 5' resolution by Pregger et al. (2007).

respective trajectory triggering, a contribution matrix has been calculated from the data of the spatially gridded emission and transport models according to the scheme displayed in Figure 4.10.

For the simulation of integrated sampling, the contribution matrices, associated to the sampling times, have been averaged over the duration of sampling (e.g. one month). The sum of all entries of a mean contribution matrix indicates the total FFCO<sub>2</sub> concentration in the respective integrated sample. The share of a subregion (e.g. the Mannheim metropolitan area for sampling in HEI) is determined by the sum of the entries that are spatially assigned to this region. In the following sections, the contribution matrices are visualized as contribution maps with the units concentration contribution per angle surface: ppb (°)<sup>-2</sup>.

## 4.2. Modelling of trajectory-triggered integrated sampling

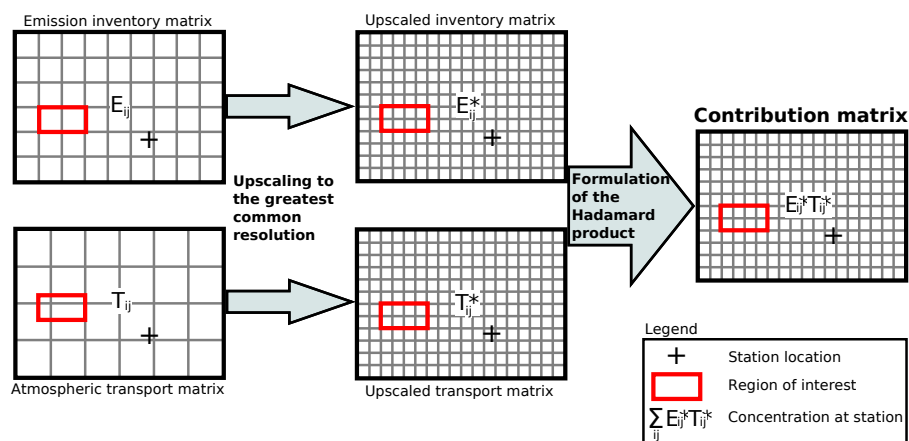


**Figure 4.10.:** Schematic diagram of the conducted convolution of the emission models (entries  $E_{ij}$ ) with the STILT transport models ( $T_{ij}$ ). The emission data were converted into a grid of emission rate densities ( $\mu\text{mol m}^{-2} \text{s}^{-1}$ ) taking into account the cell size and the value of the time resolution. For each time step studied, the emission and sensitivity grids in matrix form are upscaled (indicated by \*) to a common resolution. The new grid cells are loaded with the same values as the underlying cells in sensitivity and emission rate density. The Hadamard product of both upscaled matrices of the same dimensions yields the contribution matrix, which specifies the contribution  $E_{ij}^* \cdot T_{ij}^*$  of each grid cell to the measured concentration at the station.

### 4.2.2. Virtual FFCO<sub>2</sub> sampling at German ICOS stations

Here, the results of the virtual sampling at four different ICOS stations are presented. For every station, one or two metropolitan ROIs have been defined (Mannheim, Munich, Berlin or Hamburg) for enhancement of the FFCO<sub>2</sub> sampling. Regarding the background sampling, in principle three different triggering methods have been tested for each station:

- Triggering for a specific region with low FFCO<sub>2</sub> emissions. This background sample aims to reliably represent the near field FFCO<sub>2</sub> signal of the station. However the background signal windward of the ROI is not covered by the background sample. For this approach to work, the contribution pattern on the windward side of the region of interest must be approachable by the signal on the windward side of the background region. This strategy is sketched in Figure 4.8.
- Background sampling at all times when no triggered sampling takes place on the ROI. Hence, this covers the complement of the triggered sampling and an untriggered integrated sampling (see Figure 4.1) and yields a broad background, but is also sensitive to other emission hotspots in the station's catchment area.

#### 4. Development of new $^{14}\text{CO}_2$ sampling strategies

- Triggering by trajectories, which pass a wide-scale target area on the windward side of the ROI, but not the ROI itself. By this method, the true background of the hotspot sample is presumably represented in the most correct way. At the downside, these strict triggering criteria might only be met by a small number of trajectories during the sampling time, leading to a background sample integration over a short period of time.

##### 4.2.2.1. HEI–Heidelberg

First, it is shown what effects the new sampling strategy has on the characteristics of the monitored area of Mannheim. Figure 4.11C illustrates this in comparison to the taking of spot-samples of the ROI (4.11A and 4.11B). Both shown sensitivities of spot sampling are trajectory-triggered to the Mannheim area and show their highest sensitivity for this ROI. However, a fundamental problem of the spot sampling approach also becomes apparent: Every single spot sample has a very specific background, which is sampled together with the signal from the ROI. The exemplary sample shown in Figure 4.11A is influenced by two lignite-fired plants near Cologne, forming the largest FFCO<sub>2</sub> emission hotspot in Germany and potentially simulating an additional signal from the monitored area. A similar situation can be seen in Figure 4.11B in a westerly regime with unusually high surface emission sensitivity for sampling in HEI within 100 km of the station. A footprint between the two mentioned would not cover significant FFCO<sub>2</sub> emitters with substantial sensitivity.

In contrast, untriggered or time-triggered sampling (see the sensitivity plots in Figure 4.1) yields, due to the blending of the footprints, a reliable spatial coverage, which is subject to short-term fluctuations with respect to overall sensitivity in the catchment area, but not with respect to relative sensitivity to smaller regions. This behaviour, however, renders the sampling procedure unspecific to certain observation areas, which makes it difficult to assign a source area to the measured signals.

Trajectory-triggered integral sampling combines the advantages of the two methods described above, while mitigating the respective disadvantages, as shown in Figure 4.11C. The displayed footprint represents an average of 175 1-hourly triggered sampling occasions in May 2005. In comparison to the time-triggered sampling, the sensitivity of the integrated sample is shifted northwestwards, keeping only one of the five major FFCO<sub>2</sub> point sources inside the catchment area ( $> 0.001 \text{ ppm m}^2 \text{ s } \mu\text{mol}^{-1}$ ). Due to the averaging process, the variability of the target area's background is estimated to be reduced, proportional to the inverse square root of the number of sampling occasions.

For HEI, trajectory-triggering to a ROI, covering Mannheim, of  $13 \text{ km} \times 32 \text{ km}$  area lead to reliable sampling of the hot spot area (see Figure 4.12A). A FFCO<sub>2</sub> contribution map for triggering the background sampling to an area of similar size, situated in the rural Odenwald region northeast of HEI, is shown in Figure 4.12B.

## 4.2. Modelling of trajectory-triggered integrated sampling

### Comparison between spot and integrated sampling

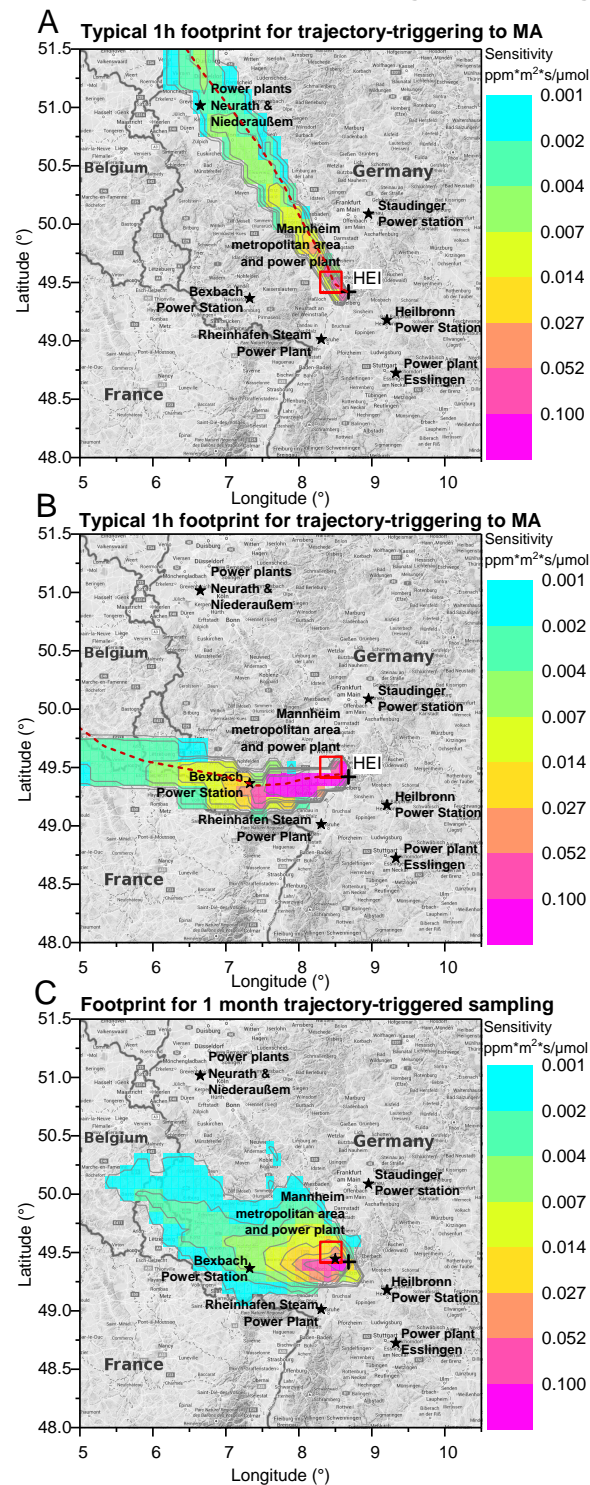


Figure 4.11.: Sensivities in HEI for two 1h spot samples, triggered for MA in May 2005 (A,B) and for one month trajectory-triggered integrated sampling in May 2005 (C). Trajectory forecast plotted as dashed red lines.

#### 4. Development of new $^{14}\text{CO}_2$ sampling strategies

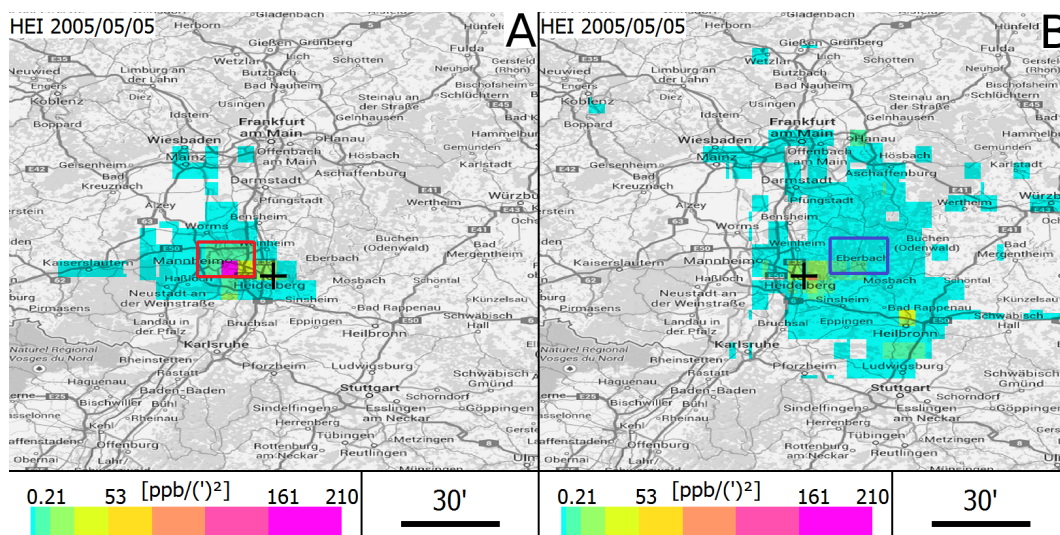


Figure 4.12.: FFCO<sub>2</sub> contribution maps for trajectory-triggered integrated sampling at HEI in May 2005. Triggering was performed for the metropolitan area of Mannheim/Ludwigshafen (red box in A). Background sampling was triggered to a region in the rural Odenwald area (blue box in B). Emission model: IER-5.

The emissions from the area marked by blue only contributes ( $0.3 \pm 0.1$ ) ppm to the FFCO<sub>2</sub> signals in the background samples in HEI. The background, retrieved by this strategy, represent well the near field contributions of the Heidelberg urban area, but is moderately influenced by the emissions of coal fired power plants in Heilbronn and Hanau.

Table 4.4 shows the averaged results of the sampling strategy for the three used emission models. The samples triggered for Mannheim show an FFCO<sub>2</sub> content of 8.4 ppm to 9.9 ppm, which has its origin in the ROI. This corresponds to a fraction of 56 % to 65 % on the total FFCO<sub>2</sub> signal. It was furthermore determined that for un-

Table 4.4.: Results of the contribution analysis for the trajectory-triggered sampling at HEI in 2005/2006. The contributions from the sources inside ( $c_{foss}$ ) and outside ( $\overline{c_{foss}}$ ) the ROI Mannheim as well as the estimation of  $\overline{c_{foss}}$  by background sampling to the Odenwald region are shown. Coverage shows the mean percentage of the sampling periods (1 month), where the respective samplings are triggered. Monthly means, which consist of less than 70 h sampling, were flagged. All uncertainties are errors of the means.

Emission inventory	Triggering for Mannheim			Triggering for background	
	$c_{foss}$ [ppm]	$\overline{c_{foss}}$ [ppm]	Coverage [%]	$\overline{c_{foss}}$ [ppm]	Coverage [%]
IER-5	$8.4 \pm 0.9$	$6.5 \pm 0.9$		$6.3 \pm 0.8$	
IER-1	$9.9 \pm 1.0$	$5.3 \pm 0.9$	$23 \pm 2$	$4.4 \pm 0.7$	$17 \pm 2$
EDGAR	$9.6 \pm 0.8$	$5.8 \pm 0.9$		$7.0 \pm 0.8$	

triggered sampling in the same timeframe the same ROI contributes ( $2.1 \pm 0.2$ ) ppm

## 4.2. Modelling of trajectory-triggered integrated sampling

to a total FFCO<sub>2</sub> signal of  $(10.7 \pm 1.1)$  ppm (IER-5). Therefore, the signal from this region can be increased by a factor 4 to 5, when following the sampling strategy, presented here.

The background signal, estimated by the parallel integrated background sampling, underestimates the true background for the ROI sample by 0.2 ppm to 0.9 ppm for the simulations using IER-5 and IER-1. The overestimating EDGAR-background is presumably falsified by a strong emission source, which is shown 1° eastward of HEI, but has no known counterpart in reality.<sup>1</sup> It is important to notice, that the reliability of the background estimation strongly depends on the temporal coverage of the integrated samples. This means, samples with less than 70 h integration times, i.e. 10 % coverage, show a higher variability and larger deviations in their respective backgrounds and were therefore discarded. Following this requirement, three quarter of the integration episodes can be utilised to estimate the FFCO<sub>2</sub> contribution of the ROI Mannheim.

Furthermore, complementary background sampling at all times, at which no triggered sampling to Mannheim took place, has been tested (see figures B.12 and B.13). This strategy yields a less reliable background in HEI. Strong contributions from other emitters in the Heidelberg catchment area as well as contributions from the Mannheim region itself lead to an overestimation of the FFCO<sub>2</sub> background signal by this strategy of  $(2.8 \pm 1.0)$  ppm (error of mean, emission model: IER-5).

The third background sampling strategy, triggering for a region windward of the ROI, lead to reliably estimated background results, but a very low coverage for the background sampling and can therefore not be recommended. Figures B.14 and B.15 show the contribution maps for this strategy.

### 4.2.2.2. HPB–Hohenpeißenberg

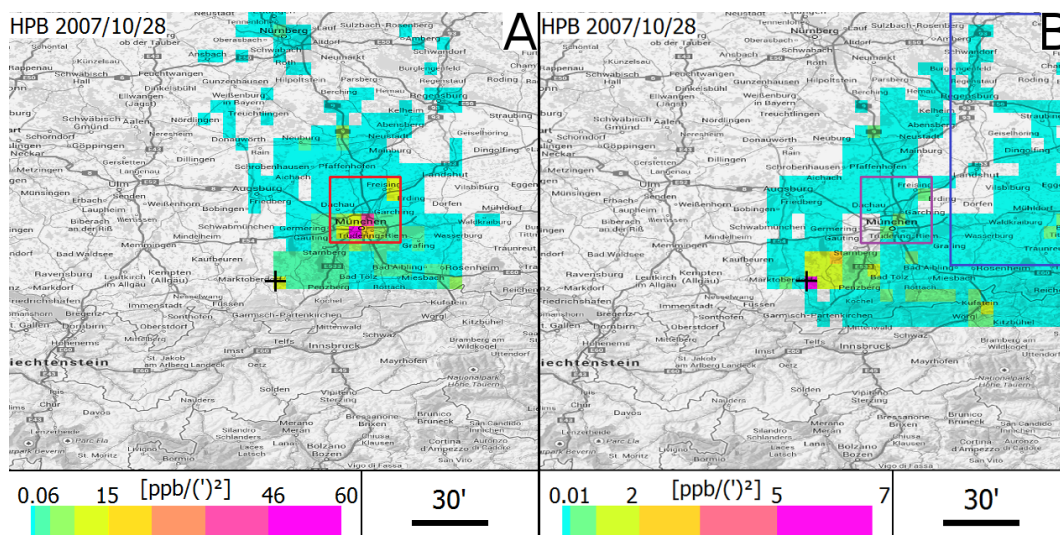
The HPB Meteorological Observatory is situated in the alpine uplands 80 km southwest of Munich. The station is a mountain observatory on top of the Hoher Peißenberg, 988 m above sea level. The model station, simulated here, samples 100 m above ground level. The largest FFCO<sub>2</sub> emission hotspot within a radius of 100 km is the Munich metropolitan area, which is here used as target ROI for the simulation of trajectory-triggered integrated sampling.

Figure 4.13A shows the contribution map for triggered sampling on the Munich area. The strongest spot contributions can be observed inside the ROI. Furthermore, contributions from the Nürnberg city area and from the direct vicinity of the station can be seen. Figure 4.13B shows the contribution map for one month of the chosen background sampling strategy for this station, which best estimates the background of the samples triggered for Munich. The contributions from the near-field of HPB and the interspace between HPB and Munich are well represented.

---

<sup>1</sup>In the new EDGAR release, this mistake has been corrected.

#### 4. Development of new $^{14}\text{CO}_2$ sampling strategies



**Figure 4.13.:** FFCO<sub>2</sub> contribution maps for trajectory-triggered integrated sampling at HPB in November 2007. Triggering was performed for the metropolitan area of Munich (red box in **A**). Background sampling was triggered to a region windward of Munich (blue box in **B**) and prevention of triggering for Munich (purple). Emission model: IER-5.

The contribution distribution of a tested alternative background sampling strategy is shown in B.16: Background sampling was performed at all times, at which no sampling for Munich took place. The background FFCO<sub>2</sub> retrieved by this method, however, underestimates the true ROI background by 0.5 ppm for the IER-5 emission inventory. This is possibly caused by a stronger sensitivity for the weaker sources eastward of HPB than westward. Though, the complementary sampling yields a long integration time for the background sampling and hence a better blending of the footprints.

Table 4.5 lists the mean results of monthly integrated simulated sampling in 2007. The FFCO<sub>2</sub> signals of the Munich region range from 1.9 ppm to 2.6 ppm for the different emission models. This corresponds to a share of the total FFCO<sub>2</sub> signal of 47% to 53%. In comparison to untriggered sampling, which yields a FFCO<sub>2</sub> contribution from Munich of  $(0.4 \pm 0.1)$  ppm out of a total of  $(2.6 \pm 0.3)$  ppm, the signal sampled at the station is increased by a factor of 6.5. In particular, this strategy lifts the sampled FFCO<sub>2</sub> offset over the current measurement uncertainty of 1.2 ppm due to 2‰  $\Delta^{14}\text{C}$  uncertainty.

For IER-5 and EDGAR, the background sample estimates the true background of the Munich-triggered sample well within the range of standard deviation. The relatively low values of the IER-1 test runs might be explained by the proximity of the station to the Austrian border, since only emissions inside Germany are represented by IER-1.

## 4.2. Modelling of trajectory-triggered integrated sampling

**Table 4.5:** Results of the contribution analysis for the trajectory-triggered sampling at HPB in 2007. The contributions from the sources inside ( $c_{f_{oss}}$ ) and outside ( $\overline{c_{f_{oss}}}$ ) the ROI Munich as well as the estimation of  $\overline{c_{f_{oss}}}$  by background sampling to a region windward of Munich are shown. For the test run with EDGAR, a different BG region was tested, extending further to the south. Coverage shows the mean percentage of the sampling periods (1 month), where the respective samplings are triggered. All uncertainties are errors of the means.

Emission inventory	Triggering for Munich			Triggering for background	
	$c_{f_{oss}}$ [ppm]	$\overline{c_{f_{oss}}}$ [ppm]	Coverage [%]	$\overline{c_{f_{oss}}}$ [ppm]	Coverage [%]
IER-5	$2.6 \pm 0.4$	$2.9 \pm 0.3$		$2.7 \pm 0.3$	
IER-1	$1.9 \pm 0.3$	$1.7 \pm 0.2$	$7 \pm 2$	$1.2 \pm 0.2$	$4 \pm 1$
EDGAR	$2.0 \pm 0.4$	$2.0 \pm 0.2$		$2.4 \pm 0.3$	$17 \pm 4$

The temporal coverage of Munich sampling is only 7%, but is fairly constant over the course of the year; no samples were discarded. In summary, at HPB the sampling strategy presented here is required to render the FFCO<sub>2</sub> offset of the Munich metropolitan area observable and provided reliable background signals for the result analysis over the course of one year.

### 4.2.2.3. LIN–Lindenberg

The Lindenberg Meteorological Observatory is situated in the suburban but still agricultural area 50 km southeast of Berlin. The area around the station has a flat topography; the simulated LIN station here samples in a height of 100 m above ground level.

Figure 4.14A shows an exemplaric contribution map for one month integrated sampling, triggered for the Berlin metropolitan area. The background sampling (4.14B) was triggered analogously to the procedure for HPB in Section 4.2.2.2. The result of another tested background sampling strategy is displayed in B.17: Sampling at all times, which are not trajectory-triggering for Berlin, provides a background FFCO<sub>2</sub> value, which compares well to the results of the previous mentioned strategy, but contains strong hotspot contributions from two lignite-fired power plants near Cottbus resp. Eisenhüttenstadt and was therefore not chosen.

It is noticeable, that the maximum contribution density of cells within the hotspot area only amounts to 10 ppb (°)<sup>-2</sup>. When this is compared to the contributions for triggered sampling at HPB at the same time in the year, the observed peak-contributions are lower by a factor of 6, even though HPB is 30 km more distant from its ROI. This might be partly explained by a wider distribution of emissions in the Berlin area, but also the mean FFCO<sub>2</sub> contributions  $c_{f_{oss}}$  from the whole ROI, which are listed in Table 4.6, range just from 1.1 ppm to 1.5 ppm. This means for LIN an increase of the Berlin-signal by a factor of about 2 from the case of

#### 4. Development of new $^{14}\text{CO}_2$ sampling strategies

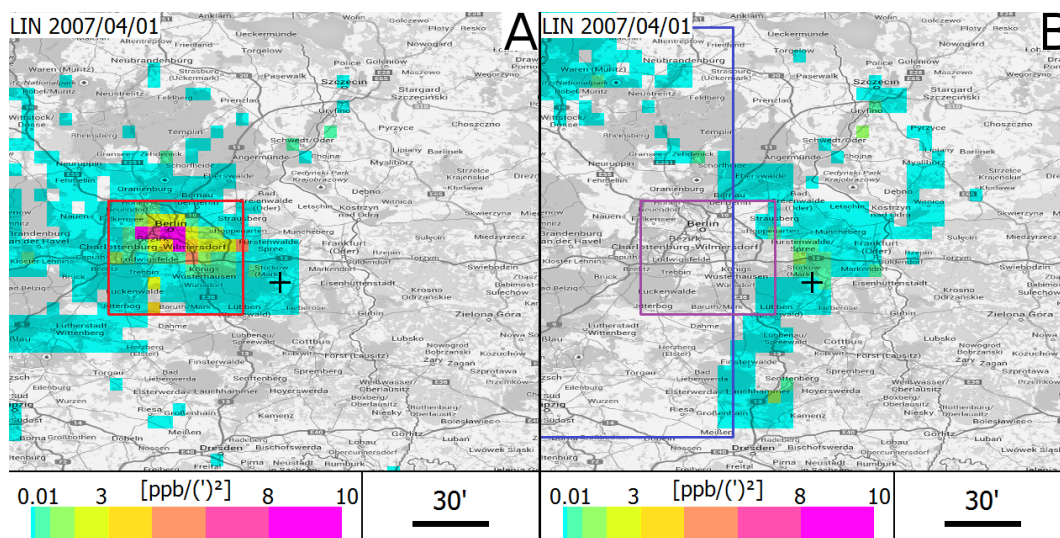


Figure 4.14.: FFCO<sub>2</sub> contribution maps for trajectory-triggered integrated sampling at LIN in April 2007. Triggering was performed for the metropolitan area of Berlin (red box in A). Background sampling was triggered to a region windward of Berlin (blue box in B) and prevention of triggering for Berlin (purple). Emission model: IER-5.

Table 4.6.: Results of the contribution analysis for the trajectory-triggered sampling at LIN in 2007. The contributions from the sources inside ( $c_{foss}$ ) and outside ( $\overline{c}_{foss}$ ) the ROI Berlin as well as the estimation of  $\overline{c}_{foss}$  by background sampling to a region windward of Berlin are shown. No test run with EDGAR was performed for this station. Coverage shows the mean percentage of the sampling periods (1 month), where the respective samplings are triggered. All uncertainties are errors of the means.

Emission inventory	Triggering for Berlin			Triggering for background	
	$c_{foss}$ [ppm]	$\overline{c}_{foss}$ [ppm]	Coverage [%]	$\overline{c}_{foss}$ [ppm]	Coverage [%]
IER-5	$1.5 \pm 0.2$	$2.0 \pm 0.3$	$53 \pm 4$	$2.7 \pm 0.4$	$10 \pm 1$
IER-1	$1.1 \pm 0.2$	$1.6 \pm 0.2$		$2.1 \pm 0.3$	

## 4.2. Modelling of trajectory-triggered integrated sampling

untriggered sampling ( $(0.80 \pm 0.02)$  ppm as part of a total FFCO<sub>2</sub> of  $(3.1 \pm 0.1)$  ppm, IER-5) could be achieved.

For both emission models tested here, the background sampling overestimates the true FFCO<sub>2</sub> background of the ROI-sampling by 0.5 ppm to 0.7 ppm. Considering the small signals received from the ROI monitoring, this is a severe drawback, since the error of the background amounts to about the half of the FFCO<sub>2</sub> offset monitored in Berlin.

In summary, the monitoring of Berlin from LIN is performed with a high temporal coverage, but the sensitivity of the averaged footprints for the metropolitan area is low. The reason for this could be that the north-south flow direction of the air masses only touches the ROI. So, even though it is located in relative vicinity, LIN is an unexpectedly unfavourable location to monitor FFCO<sub>2</sub> emissions from the Berlin metropolitan region by triggered <sup>14</sup>CO<sub>2</sub> sampling, following the model results elaborated in this work.

### 4.2.2.4. GAT-Gartow

The Gartow measurement tower is situated near the banks of the Elbe, about in the middle between Hamburg (linear distance 115 km) and Berlin (140 km). There is no significant FFCO<sub>2</sub> emission hotspot in the near-field of the station, which means it is expected to be able to take undisturbed integrated trajectory-triggered samples from the metropolitan regions of Hamburg and Berlin, provided that the respective footprints show sufficient sensitivity for these distant ROIs. Simulated sampling at GAT has been performed at a height of 100 m.

Figure 4.15 visualises the set of contribution matrices obtained by simulations for trajectory-triggered sampling for Berlin (**A**), Hamburg (**B**) and the background contribution (**C**), which is the complementary sampling time to the first mentioned ROIs. It becomes apparent, that the maximum contribution observed at GAT from the Berlin area exceeds the maximum value monitored at LIN by more than a factor of 2. The contribution peaks from the Hamburg ROI does not exceed 10 ppb (')<sup>-2</sup>.

These findings can also be found in the summary of the averaged results in Table 4.7. Sampling, triggered for Berlin, can only be performed in 6% of the time of each sampling period. Similar to the situation at HEI, a very short integration time of the ROI samples lead to high variability in the FFCO<sub>2</sub> contributions and to extreme results. Therefore, samples with less than 10 h integration time have been discarded. The triggered sampling provides a strong FFCO<sub>2</sub> signal of 2.8 ppm to 3.5 ppm from the Berlin ROI. The background sampling represents the true Berlin background well inside the uncertainty for IER-5 and inside the 2σ range for EDGAR.

Triggering for Hamburg gives a weak contribution of 0.8 ppm to 0.9 ppm FFCO<sub>2</sub> from the ROI, while overestimating the true background by 0.7 ppm to 1.1 ppm. This means, the error of the background estimation lies in the same range as the offset to be found.

#### 4. Development of new $^{14}\text{CO}_2$ sampling strategies

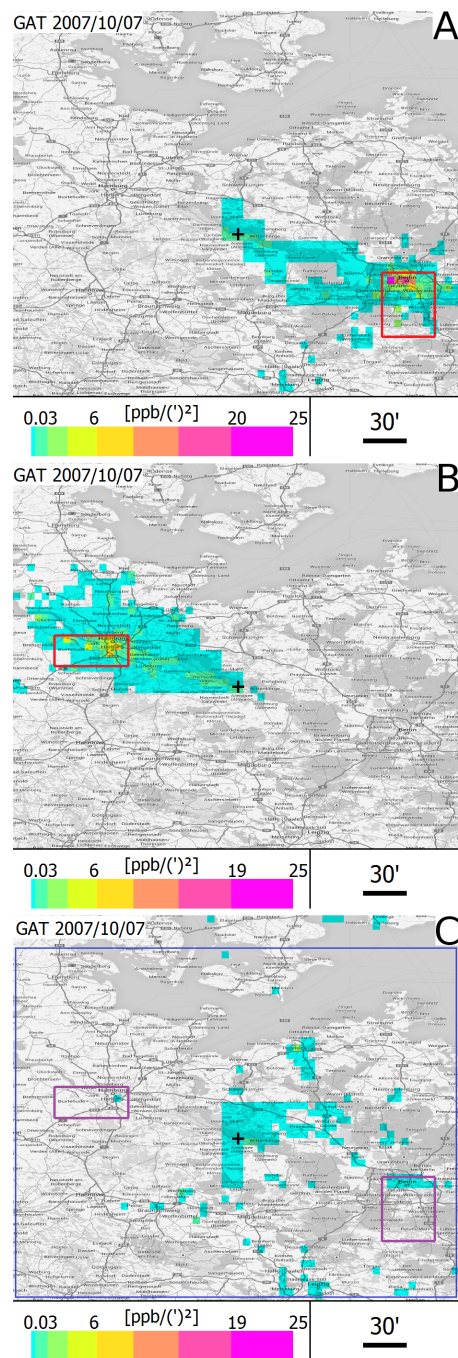


Figure 4.15.: FFCO<sub>2</sub> contribution maps for trajectory-triggered integrated sampling at GAT in October 2007. Triggering was performed for the metropolitan regions of Berlin (A) and Hamburg (B). Background sampling (C) was performed at complementary times as for the ROI sampling. Emission model: IER-5.

## 4.2. Modelling of trajectory-triggered integrated sampling

**Table 4.7:** Results of the contribution analysis for the trajectory-triggered sampling at GAT in 2007. The contributions from the sources inside ( $c_{foss}$ ) and outside ( $\overline{c_{foss}}$ ) of the ROIs Berlin and Hamburg as well as the estimation of  $\overline{c_{foss}}$  by background sampling to the complement to Hamburg and Berlin are shown. No test run with IER-1 was performed for this station. Coverage shows the mean percentage of the sampling periods (1 month), where the respective samplings are triggered. Monthly means, which consist of less than 10 h sampling, were flagged. Differences in the background values for Berlin and Hamburg are caused by differences in the flagging. All uncertainties are errors of the means.

Emission inventory	Triggering for Berlin			Triggering for background	
	$c_{foss}$ [ppm]	$\overline{c_{foss}}$ [ppm]	Coverage [%]	$\overline{c_{foss}}$ [ppm]	Coverage [%]
IER-5	$2.8 \pm 0.8$	$2.0 \pm 0.4$	$6 \pm 2$	$2.1 \pm 0.4$	$80 \pm 3$
EDGAR	$3.5 \pm 0.9$	$3.1 \pm 0.5$		$2.3 \pm 0.2$	
Triggering for Hamburg					
IER-5	$0.8 \pm 0.1$	$1.2 \pm 0.2$	$14 \pm 2$	$1.9 \pm 0.3$	$80 \pm 3$
EDGAR	$0.9 \pm 0.1$	$1.1 \pm 0.1$		$2.2 \pm 0.2$	

In summary, GAT is well suited to perform trajectory-triggered sampling for the Berlin metropolitan region. Despite the triple distance, the sampled FFCO<sub>2</sub> offset from this region is about twice as high as for the LIN station. Triggered sampling for Hamburg at GAT is not feasible for the current  $\Delta^{14}\text{C}$  measurement precision. In addition, a background sampling strategy specific to Hamburg would have to be worked out.

### 4.2.3. Emission inventory error reduction potential

Here, the effect of FFCO<sub>2</sub> signal increase by trajectory-triggering to a ROI, located on an area of high emissions, on future inverse modelling attempts, performed by means of these measurement data, will be illustrated. Following the principle way of proceeding, presented by Thompson et al. (2011) in a much more extensive approach, a minimalistic linear two-parameter inversion is set-up. The nomenclature is used here analogously to 1.5.2.

The state parameters, which describe the state of the system according to (1.44), are the FFCO<sub>2</sub> emissions from the resp. ROI ( $x_{roi}$ ) and the emissions from the remaining catchment area of the station ( $x_{\overline{roi}}$ ), forming the state vector  $\vec{x}$ , which is normalised to the a priori emission vector  $\vec{x}_a$ :

$$\vec{x} = \begin{pmatrix} x_{roi} \\ x_{\overline{roi}} \end{pmatrix} \quad (4.4)$$

$$\vec{x}_a = \begin{pmatrix} x_{roi,a} \\ x_{\overline{roi},a} \end{pmatrix} = \begin{pmatrix} 1 \\ 1 \end{pmatrix} \quad (4.5)$$

#### 4. Development of new $^{14}\text{CO}_2$ sampling strategies

The measurement vector  $\vec{y}$  is defined according to the sampling and analysis strategy described in 4.2.1 as the offset of the total FFCO<sub>2</sub> concentration in the sample triggered for the ROI to the total FFCO<sub>2</sub> concentration in the sample triggered for the background, which is used to estimate the background of the ROI-sample. For the calculations here, the model results averaged over one or two years as presented in the summarising tables in Section 4.2.2 are used as measurement results. This provides for every model run a measurement vector  $\vec{y}$  of the dimension 1 with an error covariance matrix  $S_e$  of dimension  $1 \times 1$ , which is approximated by the variance of the measurement results in the course of the modelled evaluation period plus the expected variance due to  $\Delta^{14}\text{C}$  measurement uncertainty.

The linear function  $F$ , which maps the emission to the observation space, can now be derived by the results of the forward runs separated into contributions from the ROI and non-ROI, which are given in Section 4.2.2.  $F$  has the dimension  $1 \times 2$ . As an example, for HEI and the emission model IER-5,  $F$  is formulated as

$$F = (8.4 \text{ ppm} \quad 0.2 \text{ ppm}) \quad (4.6)$$

The error covariance matrix  $S_a$  of the a priori state  $\vec{x}_a$  depends on the uncertainties of the emission inventories on a small ( $x_{roi}$ ) and much larger ( $x_{\overline{roi}}$ ) scale. In Section 1.5.4.2 some considerations to inventory uncertainties were presented. The choice of uncertainties is, however, for the most part in the hands of the examiner. Here, a conservative estimation was made with 10 % error of the large scale emissions and 30 % for the small-scale emissions from the ROI. No spatial correlation between these two regions was assumed, which is also a conservative approach since a larger number of independent state variables decreases the error reduction, which can be achieved by the inversion approach (Gerbig et al., 2006). With these estimations, the a priori covariance matrix can be formulated as

$$S_a = \begin{pmatrix} 0.09 & 0 \\ 0 & 0.01 \end{pmatrix} \quad (4.7)$$

The posterior error covariance matrix  $\hat{S}$ , which represents the uncertainties of the emission inventories after the inversion, can now be calculated according to (1.51). The error reduction for the individual elements of  $\vec{x}_a$  can be expressed as  $1 - \sigma_{posterior}/\sigma_{prior}$ , where the  $\sigma$  are the square roots of the diagonal entries of the corresponding covariance matrices (Gerbig et al., 2006). Table 4.8 shows the results of the described inversion approach. As expected, the largest error reduction can be seen for the samples with the highest signal-to-noise ratio. For all stations, but especially for HPB and GAT, almost no information about the high emission region of interest can be retrieved from the untriggered sampling, since the signals are covered up by the much larger total FFCO<sub>2</sub> signal and the observation error. Since the difference in trajectory-triggered ROI sampling and background sampling is the measurement value in this new approach, the background contribution is mathematically almost cancelled out in the linear mapping (depending

#### 4.2. Modelling of trajectory-triggered integrated sampling

**Table 4.8:** Estimated emission inventory (IER-5) error reduction in a hypothetical two-parameter inversion set-up for the four ICOS stations, investigated in this work. Observation error contains the dispersion of the forward model results as well as estimated measurement uncertainties for the required  $\Delta^{14}\text{C}$  analyses.

Station	ROI	Observation error [ppm]	ROI error reduction [%]	
			Triggered	Untriggered
HEI	Mannheim	1.6	55	8
HPB	Munich	0.5	31	2
LIN	Berlin	0.4	18	7
GAT	Berlin	1.1	22	0.2

on how well the background is estimated by the resp. sampling), as seen in (4.6). This means, the information content of the measurements is foremost used for estimation of the posterior state variable  $\hat{x}_{roi}$ . A comprehensive inversion approach in the future could use such measurement results to constrain more accurate small scale inventory data in regions of high FFCO<sub>2</sub> emissions.



## Summary & outlook

The main objective of this thesis was achieved by the successful commissioning of a newly developed AMS target Extraction and Graphitisation Line (EGL) in the Central Radiocarbon Laboratory of the European ICOS RI infrastructure. Extensive preparatory investigations at the IUP  $^{14}\text{C}$  laboratory, which has been in operation for many years, were carried out in advance to bring this project to a successful conclusion. The individual components that served as the basis for the new Extraction and Graphitisation Line were tested to show no significant fractionation and contamination effects. Furthermore, continuous quality control procedures were examined under the conditions of the IUP  $^{14}\text{C}$  laboratory over several years. Using a QC method, presented before by Turnbull et al. (2015b), it was demonstrated that most of the variation, which goes beyond the given AMS measurement error, has its origin in across magazine uncertainties, indicating that long-term variations in sample pre-treatment or AMS measurement are the cause and not scattering introduced by the graphitisation. The differences between AMS analysis at the CEZ in Mannheim and LLC results at the CRL were determined significantly within the WMO compatibility goal for the first time with  $(0.1 \pm 0.3) \%$ . In conclusion of the preparatory phase, an AMS magazine composition for the future CRL routine operation has been proposed to maintain the quality control level. It provides a set of AMS standards, which allows  $\Delta^{14}\text{C}$  measurement uncertainties below 2 ‰ even for small samples of 0.5 mg carbon. To further investigate the origin of the different uncertainty components it is currently planned to analyse a series of quality control samples by another AMS laboratory.

The design of the EGL was determined to achieve the highest possible degree of standardisation and purity of the respective  $^{14}\text{C}$  targets. Long-lasting sub-processes of the extraction and graphitisation process were parallelised. This reduced the process time of a low-water sample from registration of the sample flask at the EGL to the (automatic) start of graphitisation to below 15 min. Targets extracted from air containing substantial amounts of water vapour, however, lead to considerably longer processing time of 25 min or more. For this reason, first on-line air drying tests with a plug-in magnesium perchlorate water removal system have been successfully performed and will be further investigated in the near future. An EGL control software has been developed to guide the operator through the manual steps of target preprocessing. The software provides the required degree of automatisation that each target of the same type performs the same preprocessing steps. Furthermore, automatic process quality control was made possible by saving all relevant metadata (e.g. pressures, temperatures, sample volumes) to the CRL database and comparing them to beforehand known expected quantities.

The fractionation effects to which the targets are exposed during processing in EGL were measured. Here, all samples showed a fractionation in  $\delta^{13}\text{C}$  of less than 0.3 ‰; the means of the respective test series indicate no systematical EGL process fractionation with  $(0.04 \pm 0.09)$  ‰.

In an extensive series of tests, all relevant adjustable graphitising parameters were analysed for their influence on a number of performance indicators, including in particular the influence on the stability of  $\Delta^{14}\text{C}$  and  $\delta^{13}\text{C}$  AMS measurement results. The whole-air target gas test series, recommenced at the EGL with the final graphitisation parameter set, lead to a variation of 1.9 ‰ or less in the AMS results, hence fulfilling the goal of achieving a  $\Delta^{14}\text{C}$  reproducibility of less than 2 ‰ for air samples. Investigations of the absolute  $^{14}\text{C}$  scale, on which the EGL lies with the AMS measurements at the CEZ, by the first results of an Oxalic Acid I test series showed a systematic deviation from the canonical scale of  $(0.7 \pm 0.5)$  ‰ in the mean value. This is no significant deviation outside of  $2\sigma$  and will be determined more precisely by continuation of this series in the future.

The compatibility tests between traditional NaOH collected  $^{14}\text{CO}_2$  samples, which were analysed by the CRL-LLC, and EGL-processed aliquots of these samples lead to a systematic difference between LLC and AMS results of  $(-2.2 \pm 0.9)$  ‰. Comparisons of the  $\Delta^{14}\text{C}$  results of aliquots originating in the same high-volume samples showed a high variation in the differences of  $\pm 6$  ‰. These findings are probably caused by two different experimental issues. Currently a bias in LLC QC results for the year 2017 and the handling of sample aliquotation is under investigation.

The final part of this thesis was dedicated to the development of new sampling strategies and methods for future  $^{14}\text{CO}_2$  sampling. A new integrated low-flow sampling in glass flasks was tested over a period of three years. Deviations in trace gas concentrations of the integrated samples from continuous measurement results were evaluated and showed no considerable contaminations or problems in the uniformity of the sampling. Parallel daytime and nighttime  $^{14}\text{CO}_2$  sampling using the whole-air as well as the NaOH sampling approach has been established. FFCO<sub>2</sub> offsets of the nighttime samples using the respective daytime results as background were calculated. Significant FFCO<sub>2</sub> excess of 1.6 ppm to 1.8 ppm was observed in spring and autumn, while the nocturnal concentration in winter and summer is not enriched. To make further use of this information, it would be necessary to perform model calculations specific for this set up or to disentangle emission and transport signals, for example by the radon-tracer method.

A forward model system has been set up using STILT footprints and three different regionally disintegrated emission inventories. Herewith, virtual trajectory-triggered FFCO<sub>2</sub> sampling was performed at four different German ICOS stations. With this method the FFCO<sub>2</sub> signal of chosen emission hotspots located in the catchment area could be increased by a factor of 2 to 7 at the stations. At the same time, the strategy for collection a station specific background sample to estimate the background of the hotspot signal was developed and simulated for all four stations. Except for the Lindenberg station, this study showed an increase of the

measured hotspot FFCO<sub>2</sub> offsets to values, which can be resolved by current  $\Delta^{14}\text{C}$  measurement precision. An exemplaric two-parameter inversion approach performed by means of the forward results for the stations showed the potential, this method has for future model approaches and emission inventory error reduction and hence monitoring of the goals the European countries agreed on in form of the Nationally Determined Contributions of the Paris Agreement.



# Annex



## A. Detailed explanations

### A.1. Description of regulation electronic and hardware control

Here detailed lists and descriptions of the individual components of EGL electronics and useful information for the hardware control and communication protocols are given.

#### A.1.1. Control of heating elements

The heating wires for thawing of sublimated CO<sub>2</sub> (see sections 3.2.2.4 and 3.2.4) and the ovens for the graphitisation reactors (see section 3.2.6.4) are regulated quasi-independently from the controlling PC by a separate proportional-integral-derivative (PID) controller (Omron Electronics, *CelciuX*<sup>o</sup>). This approach has the advantage over direct temperature regulation by the PC, that in case of a shut-down or restart of the computer or a breakdown of the control software the temperature regulation remains in a defined state as long as the voltage supply for 24 V in the electric cabinet is maintained.

The control software sends the target temperature utilising the Modbus communication protocol in a RS485 communication interface (see Table A.1 for details); for software feedback, the current temperature can be read regularly.

The regulation signal (24 V) for each heater toggles a corresponding solid state relay switching the driving power supply.

##### A.1.1.1. Regulation sensors

The regulation sensors (Thermal elements type K, constructed at the IUP workshop) are placed as near at the elements to regulate as possible; i.e. on the tip of the reactor quartz glass tube and on top of the steel surface of the quantification and extraction volumes. The quantification volume and the corresponding sensor are sheathed by aluminium foil to accelerate temperature balancing between the steel surface and the thermal element. Connection of the sensors with the PID is conducted using IEC (International Electrotechnical Commission) 584 conform wiring. Used in-line screw terminal connections, however, introduce contact points to other metal types and possibly offset the measured thermal voltage.

Temperature comparison tests between a laboratory thermometer (Greisinger, *GTH 1160*, NiCr-Ni sensor) and the regulation sensors built-in the EGL provided

## A. Detailed explanations

Table A.1.: Details of the heater control electronics.

	Designation	Details
<b>Controlling device</b>	Omron Electronics, <i>CelciuX°</i> system	<ul style="list-style-type: none"> <li>•1x End unit: <i>EJ1C-EDUC-NFLK</i></li> <li>•5x Base module <i>EJ1N-TC4B-QQ</i></li> </ul>
<b>Sensor technology</b>	Thermal element type K	NiCr – Ni
<b>Comm. interface</b>	National Instruments, <i>PCI-8431/4</i> 4 Port, RS485/RS422 Serial Interface	Settings: <ul style="list-style-type: none"> <li>•Transceiver mode: 2-wire auto</li> <li>•Baud rate: 9600</li> <li>•Data bits: 8</li> <li>•Parity: None</li> <li>•Stop bits: 1</li> <li>•Flow control: None</li> </ul>
<b>Comm. protocol</b>	Modbus	Driver: <i>MODBUS Library for LabVIEW</i>
<b>Current control</b>	Omron electronics Solid state relay	<i>G3NA-D210B-UTU DC5-24</i> <ul style="list-style-type: none"> <li>•Control voltage: <math>V_{ctrl} = 4\text{ V to } 32\text{ V}</math></li> <li>•Load voltage: <math>V_{load} = 5\text{ V to } 200\text{ V}</math></li> <li>•Load current: <math>I_{load} = 10\text{ A}</math></li> </ul>

an offset in measured temperature  $\Delta T = T_{EGL} - T_{ref}$  of  $\Delta T = 2\text{ K}$  at laboratory temperature and  $\Delta T = 8\text{ K}$  at approximate graphitisation temperature  $\approx 600\text{ }^\circ\text{C}$ .

### A.1.2. Control of extraction pumps, elevators and reactor cooling

The pumps for  $\text{CO}_2$  extraction (section 3.2.2.2), the elevators for  $\text{N}_2(\text{l})$  dewars (sections 3.2.2.3 and 3.2.6.1) and the peltiers for water removal during graphitisation (section 3.2.6.3) are controlled directly by the controlling PC resp. the EGL control software via a digital I/O device (see Table A.2) for details. Half of the digital channels at the EGL are defined as inputs (signalling), the other half as outputs (steering).

In case of the extraction pumps, the 5 V TTL signal switches solid state relays for the 230 V<sub>eff</sub> power supply. The peltiers are regulated by an relay switching the corresponding 14.4 V power supply, meaning that the water removal of the 12 reactors can only be changed for all at once.

Every motor for elevator movement (horizontal and vertical) is driven by a relay board, specified for motor steering; the signal for rotational direction is transferred by respectively two 5 V TTL signals. That means motor movement is completely steered by the controlling PC, utilising a set of signalling switches.

#### A.1.2.1. Position signalling

Indication of the current elevator position is performed by mechanical switches. An elevator passing a defined position, therewith closes a 5 V circuit to the corre-

## A.1. Description of regulation electronic and hardware control

**Table A.2.:** Details of control electronics for extraction pumps, elevator motors and sensors and peltier elements.

	<b>Designation</b>	<b>Details</b>
<b>Controlling device</b>	National Instruments, <i>NI USB-6509</i> :	Inputs and outputs are distributed via
<b>Comm. interface</b>	96-Channel, 5 V/TTL/ CMOS Digital I/O	National instruments, <i>SCB-100A Shielded I/O Connector Block</i>
<b>Control interface</b>	USB	Driver: <i>NI-DAQmx 17.0</i>
<b>Current control</b>	Direct regulation by 5 V TTL	
	•Pumps:	4x Solid state relay: Kudom, <i>KSI240D80-L</i>
	•Motors:	7x Relay board: <i>robotikhardware.de</i> , <i>RN-VNH2 Dualmotor</i>
	•Peltiers:	Solid state relay: Kudom, <i>KSI480D10-LM</i>

sponding input channel, giving a digital signal, that is then processed by the EGL control software.

### A.1.3. Pressure sensors

The EGL utilises 26 pressure transmitters of three different types – depending on the respective requirement on the monitored volume (see Figure 3.8).

#### A.1.3.1. Piezoresistive pressure transmitters

Measurements in the low vacuum region in the EGL are conducted by linear, piezoresistive pressure transmitters (for details see Table A.3). For monitoring the graphitisation reaction a pressure range of 0 mbar to 3000 mbar was chosen. Measurement of the CO<sub>2</sub> extraction pressure, standard gas metering, CO<sub>2</sub> quantification and prevacuum monitoring (see section 3.2.7.2) are performed below atmospheric pressure; therefore a smaller range of 0 mbar to 1000 mbar was chosen – leading to a lower absolute measurement error (see section Sensor uncertainties).

The sensor technology builds upon the piezoresistive effect; that means the sensor's material resistance changes with applied pressure. The *PAA-9LD* uses a piezo element embedded in an silicone oil-filled stainless steel housing. Pressure changes on the steel diaphragm are transferred to the oil pressure inside. Figure A.1 shows the schematic structure of the pressure transmitter.

The pressure transmitter's stainless steel housing are installed into the EGL utilising welded-on solid steel mountings, constructed at the IUP workshop; vacuum sealing is conducted by Viton O-rings.

## A. Detailed explanations

**Table A.3.:** Details of piezoresistive pressure transmitters.  $P_i$  indicates the transmitters with a sensor index  $i$  used in this thesis, e.g. in Figure 3.8.

	Designation	Details
<b>Sensor</b>	Keller AG, PAA-9LD:	Pressure ranges (abs.):
	• Reactors:	$P_{10} - P_{21}$ : 0 mbar to 3000 mbar
	• Low vacuum sections:	$P_4 - P_9, P_{22}$ : 0 mbar to 1000 mbar
<b>Comm. interface</b>	National Instruments, NI USB-8452:	Driver: NI-845x 17.0
	I <sup>2</sup> C/SPI Interface device	
<b>Comm. protocol</b>	I <sup>2</sup> C	Driver: NI-845x 17.0

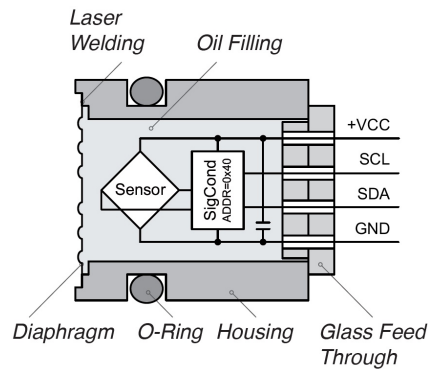


**Figure A.1.:** Scheme of the PAA-9LD pressure transmitter (Keller AG (2017)).

The pressure read out is performed using the I<sup>2</sup>C bus technology. All transmitters are connected parallel to the bus master (NI USB-8452), bearing a unique slave address, which – in case of sensor replacement – has to be assigned before starting operation.

A specific 4-wire connection for the sensors was designed and built by the IUP workshop; connecting four of the five connection pins of each sensors to the I<sup>2</sup>C interface: Electric ground (GND), 1.8 V to 3.6 V power supply (+VCC), I<sup>2</sup>C clock (SCL) and I<sup>2</sup>C data wires (SDA). A possible additional End of Conversion (EOC) signal is not used for the EGL (see Keller AG (2017) for more details).

During the first months of operation, it became apparent, that the I<sup>2</sup>C bus is sensitive to fluctuations in the power supply of the controlling PC, which powers the bus. To damp fluctuations induced by switching on or off large electrical loads (e.g. pumps) a mains filter (Ehmann 0463x0000) has been built in before the PC. That measure greatly reduced the need to reset the I<sup>2</sup>C bus during operation.

**Sensor uncertainties** Under operating conditions of the EGL the manufacturer (Keller AG (2017)) states a maximum accuracy of  $\pm 0.15\%$  FS (full scale) at room

## A.1. Description of regulation electronic and hardware control

temperature (Linearity best straight line, hysteresis, repeatability), with a typical long term stability of  $\pm 0.1\%$  FS.

In the EGL, slight irregularities in the installations of individual transmitters lead to larger deviations in pressure. At  $1 \times 10^{-1}$  mbar, I observed deviations up to  $-18$  mbar at  $P_{22}$ , which corresponds to  $1.8\%$  FS. Therefore, I designed a 2-point calibration method on the software side (section 3.4) to separately calibrate the measurement values of the individual sensors.

### A.1.3.2. Pirani pressure transmitters

Pressure measurements in the medium vacuum range ( $1 \times 10^{-3}$  mbar to 30 mbar) at the flask inlets of the EGL are performed by Pirani pressure transmitters (see Table A.4 for details). Here the absolute accuracy in pressure is less important than repeatability of measurements, since the main purpose of these transmitters is to perform reliable tests of pressure increase.

**Table A.4.:** Details of Pirani pressure transmitters. Pressure sensors  $P_0 - P_3$  are realised with this type.

	<b>Designation</b>	<b>Details</b>
<b>Sensor</b>	Thyracont, <i>VSP63MV</i> : Vacuum Transducer	Pressure range (abs.): $1 \times 10^{-4}$ mbar to 1000 mbar
<b>Controlling device</b>	National Instruments, <i>USB-6210</i> Multifunction I/O Device	Driver: <i>NI-DAQmx 17.0</i> Analog-to-digital converter
<b>Comm. interface</b>	USB	
<b>Control interface</b>	Analog input	Voltage range: 1.5 V to 8.5 V
<b>Control interface</b>		Digital precision: 16 bit

Read out of the pressure values is executed by measuring the Pirani voltage, that is logarithmically dependent on pressure, by a 16 bit analog-to-digital converter. Then, the pressure value is calculated on software side by

$$p[\text{mbar}] = 10^{U_{\text{Pirani}}[\text{V}] - 5.5} \quad (\text{A.1})$$

with  $p[\text{mbar}]$  as the pressure in mbar and  $U_{\text{Pirani}}[\text{V}]$  as the read out Pirani voltage in Volt.

**Sensor uncertainties** The accuracy of the *VSP63MV* is stated by the manufacturer (Thyracont (2016)) as

**20 mbar to 1000 mbar:**  $\pm 30\%$  from reading

**$2 \times 10^{-3}$  mbar to 20 mbar:**  $\pm 10\%$  from reading

**$< 2 \times 10^{-3}$  mbar:**  $<$  factor 2 from reading

### A. Detailed explanations

The repeatability, as deviation between measurements within a short period of time, is given as  $\pm 2\%$  in the  $2 \times 10^{-3}$  mbar to 20 mbar range.

The measurement principle of Pirani transmitters is based on the pressure dependent thermal diffusivity of gases, which differs for different gas types. The standard measurement is calibrated for dry air or  $N_2$ . When performing pressure measurements in other gases a specific correction factor has to be multiplied on the calculated pressure value. For  $CO_2$  a factor of 0.89 has to be applied.

An additional error is introduced by the step-width of the analog-to-digital conversion. The relative quantisation error for the 16 bit converter and a measurement range of  $-10\text{ V}$  to  $10\text{ V}$  is in the order of  $2^{-16} \cdot 20\text{ V} = 3 \times 10^{-4}$ . On the basis of (A.1) the resulting error in pressure can be expressed as

$$\sigma(p)[\text{mbar}] = p[\text{mbar}] \cdot \ln 10 \cdot \sigma(U_{\text{Pirani}})[\text{V}] = 7 \times 10^{-4} \cdot p[\text{mbar}] \quad (\text{A.2})$$

which is much smaller than the sensor uncertainty and can therefore be neglected.

#### A.1.3.3. Cold cathode pressure transmitter

In the high-vacuum region directly before the turbo vacuum pumps ( $P_{23}$  and  $P_{24}$ ) and at the central position in the EGL ( $P_{25}$ ), where transfer of pure  $CO_2$  to the reactors takes place, pressure measurements down to  $1 \times 10^{-7}$  mbar are required. The *MPT 200* Pirani/cold cathode transmitter, described in Table A.5 meets this requirement.

**Table A.5.:** Details of Pirani/cold cathode pressure transmitters. Pressure sensors  $P_{23} - P_{25}$  are realised with this type.

	Designation	Details
<b>Sensor</b>	Pfeiffer Vacuum, <i>MPT 200</i> : Digital Pirani/cold cathode- Transmitter	Pressure range (abs.): $5 \times 10^{-9}$ mbar to 1000 mbar
<b>Comm. interface</b>	National Instruments, <i>PCI-8431/4</i> 4 Port, RS485/RS422 Serial Interface	Settings: • Transceiver mode: 2-wire auto • Baud rate: 9600 • Data bits: 8 • Parity: None • Stop bits: 1 • Flow control: None
<b>Comm. Protocol</b>	Pfeiffer Vacuum-Protocol	Driver: <i>Pfeiffer Vacuum Digiline</i> <i>labVIEW driver</i>

The pressure transmitters are connected to a serial interface on the controlling PC and a 24 V power supply using a commercial available wiring.

## A.1. Description of regulation electronic and hardware control

**Sensor uncertainties** In Pfeiffer Vacuum (2016), the accuracy of the *MPT200* is specified by the manufacturer as

$1 \times 10^{-8}$  mbar to  $2 \times 10^{-3}$  mbar:  $\pm 25\%$

$2 \times 10^{-3}$  mbar to 10 mbar:  $\pm 10\%$

10 mbar to 100 mbar:  $\pm 30\%$

100 mbar to 1000 mbar:  $\pm 50\%$

Below  $1 \times 10^{-2}$  mbar the repeatability of the measurement results lies within  $\pm 7\%$ .

Analogous to the pure Pirani sensor described above, the values of the combined Pirani/cold cathode pressure transmitter needs to be corrected for gas types. Table A.6 lists these factors for the gases, its pressures are routinely measured by the EGL. The EGL control software assumes the gas type as dry air or  $N_2$  by de-

**Table A.6.:** Correction factors for different gas types, that are multiplied on the raw pressure result. The *MPT 200* switches between Pirani and cold cathode at  $1 \times 10^{-3}$  mbar to  $2 \times 10^{-3}$  mbar (see Pfeiffer Vacuum (2016)).

Gas	Correction factors	
	Pirani	Cold cathode
$N_2$ or dry air	1.00	1.00
$CO_2$	0.89	0.74
Ar	1.59	0.80
$H_2$	0.58	2.39

fault, hence introducing an additional systematic deviation from the true pressure depending on gas type as shown in the Table A.6.

### A.1.4. Pneumatic valve control

The high purity pneumatically steered PDVNs operating in the EGL (see section 3.2.7) are controlled individually by a set of solenoid valves (SMC Pneumatik, *SY100*). The solenoid valves in turn are directly operated by the EGL control software utilising a 64-port relay card (see Table A.7 for details) for toggling the 24 V opening voltage. The control pressure is set to 5 bar at the EGL.

Respectively 20 solenoid valves are grouped into a valve terminal. Connection of each valve terminal to the control interface is implemented via a D-Sub (26 pins) connection wire, that is split-up to single wire connection on the connector block.

### A.1.5. Air flow control

The Low  $\Delta p$  MFCs regulating the extraction flow (see section 3.2.2.2) are set and read-out by the EGL control software utilising a proprietary bus protocol of the

A. Detailed explanations

**Table A.7.:** Details of the pneumatic valve control. The 24 V outputs of the relay card directly switch the solenoid valves, which control the pressure on the pneumatic valves.

	<b>Designation</b>	<b>Details</b>
<b>Controlling devices</b>	60x SMC Pneumatik, <i>V110-D5NCZ-C4: SY100 Solenoid valve</i>	Pressure transmission by 5 mm PVC-compressed-air hose, valves normally closed
<b>Comm. interface</b>	PCI	
<b>Control interface</b>	National Instruments, <i>PCI-6512</i> 64-port Digital I/O Device	Driver: <i>NI-DAQmx 17.0</i> 24 V supply and output distribution via National instruments, <i>SCB-100A Shielded I/O Connector Block</i>

manufacturer. The MFCs are wired individually to respectively one RS232 interface using customised D-Sub (9-pin) wiring, providing communication linkage and 24 V power supply.

**Table A.8.:** Details of the flow controller electronics.

	<b>Designation</b>	<b>Details</b>
<b>Controlling device</b>	Flow controller: Bronkhorst, <i>Low <math>\Delta p</math>: F-201DV-ABD-88-V</i>	
<b>Comm. interface</b>	<i>Delock 87414</i> USB 2.0 to 4 port serial HUB	Settings: •Baud rate: 38400 •Data bits: 8 •Parity: None •Stop bits: 1 •Flow control: None
<b>Comm. protocol</b>	Bronkhorst-FLOW-BUS	Driver: <i>Bronkhorst-FLOW-BUS for LabVIEW</i>

The communication driver allows reading-out of current flow and passed gas volume during routine operation. Analogously flow set-point, gas type and a reset signal for the gas volume value can be transferred to the flow controller by the software.

### A.1.6. Controlling PC

The composition of the controlling PC was chosen regarding the requirements of the control elements described above. That means especially the availability of sufficient fast USB ports and two PCI expansion slots for the RS485 hub (see sections A.1.1 and A.1.3.3) and the solenoid valve steering relay card (section A.1.4). The essential properties of the computer system are listed in Table A.9.

Table A.9.: Details of the controlling PC of the EGL.

Function	Designation	Details
<b>Mainboard</b>	Asus, <i>M5A97</i>	ATX, Socket AM3+, AMD 970, USB 3.0, FireWire, Gigabit LAN Expansion slots: •2× PCIe x16 •2× PCI
<b>CPU</b>	AMD, <i>FX Series FX-8320</i>	•CPU-cores: 8 •Threads: 8 •Clock rate: 3.5 GHz •Thermal Design Power: 125 W
<b>Working memory</b>	Kingston, <i>ValueRAM</i>	2 × 4 GB DDR3 (1066 MHz to 2133 MHz)
<b>Graphic</b>	MSI, <i>Radeon HD 5450</i>	•1×DVI, 1×HDMI, 1×VGA •Engine clock: 650 MHz •Memory clock: 1066 MHz •DDR3 memory: 1 GB •passively cooled
<b>Hard drive</b>	•Samsung, <i>840 EVO</i> •WD, <i>Blue WD10EZEX</i>	120 GB SSD 1000 GB 3.5" hard disc
<b>DVD drive</b>	Samsung, <i>SH-224DB/BEBE SW</i>	Read/write DVD, CD

Furthermore, the processes of the EGL control software (section 3.4) are running parallelised to a high degree; the used programming language LabVIEW allows, to assign individual tasks to certain processor threads. The central processing unit (CPU) of the controlling PC is capable of handling 8 different threads at 8 physical CPU-cores simultaneously and is therefore suitable for the requirements of the control software.

#### A.1.6.1. User Interface

The user interface (UI) for the interaction with the controlling PC of the EGL consists of keyboard and mouse as well as two 24" monitors (Dell, *UltraSharp U2412M*) mounted on the side of the electric cabinet. Computer operation and sample handling at the EGL can be performed by the technician within a walking distance of less than three meters.

## A. Detailed explanations

### A.1.6.2. Sample scanning

Samples, which are registered at the CRL database, can be quickly inserted into the EGL processing chain by scanning the Unique Container Number (UCN) of the respective sample container (Flask or pure-CO<sub>2</sub> glass break-seal). Scanning is performed by a wireless linear barcode scanner (Honeywell, *Voyager 1202g*); since the EGL software is entirely linked to the CRL database, every scanned string is compared to known UCNs in the database, yielding the ID of the sample for further processing at the EGL. This approach minimises the administrative effort and the susceptibility to errors when handling several flasks during EGL processing, as the allocation of the samples' IDs to the flasks is performed automatically.

## B. Additional figures

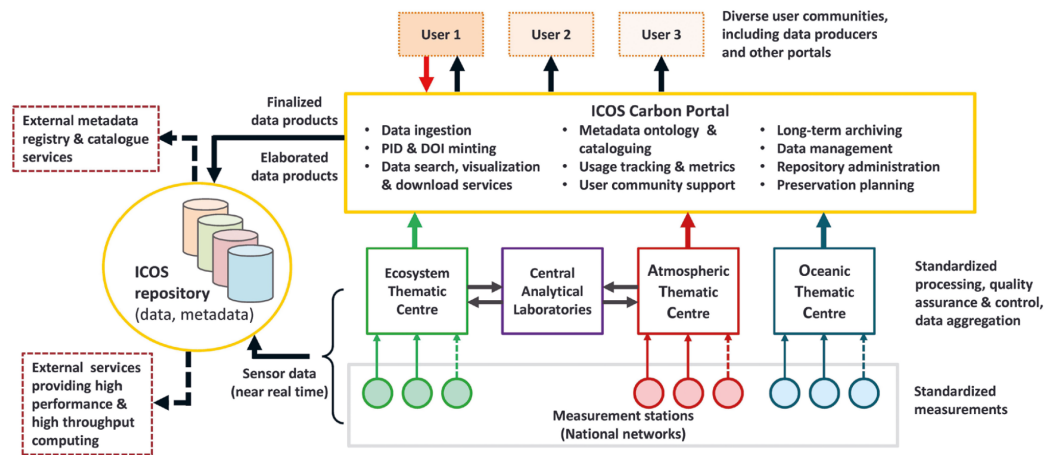


Figure B.1.: ICOS data cycle (ICOS RI, 2017b).

B. Additional figures

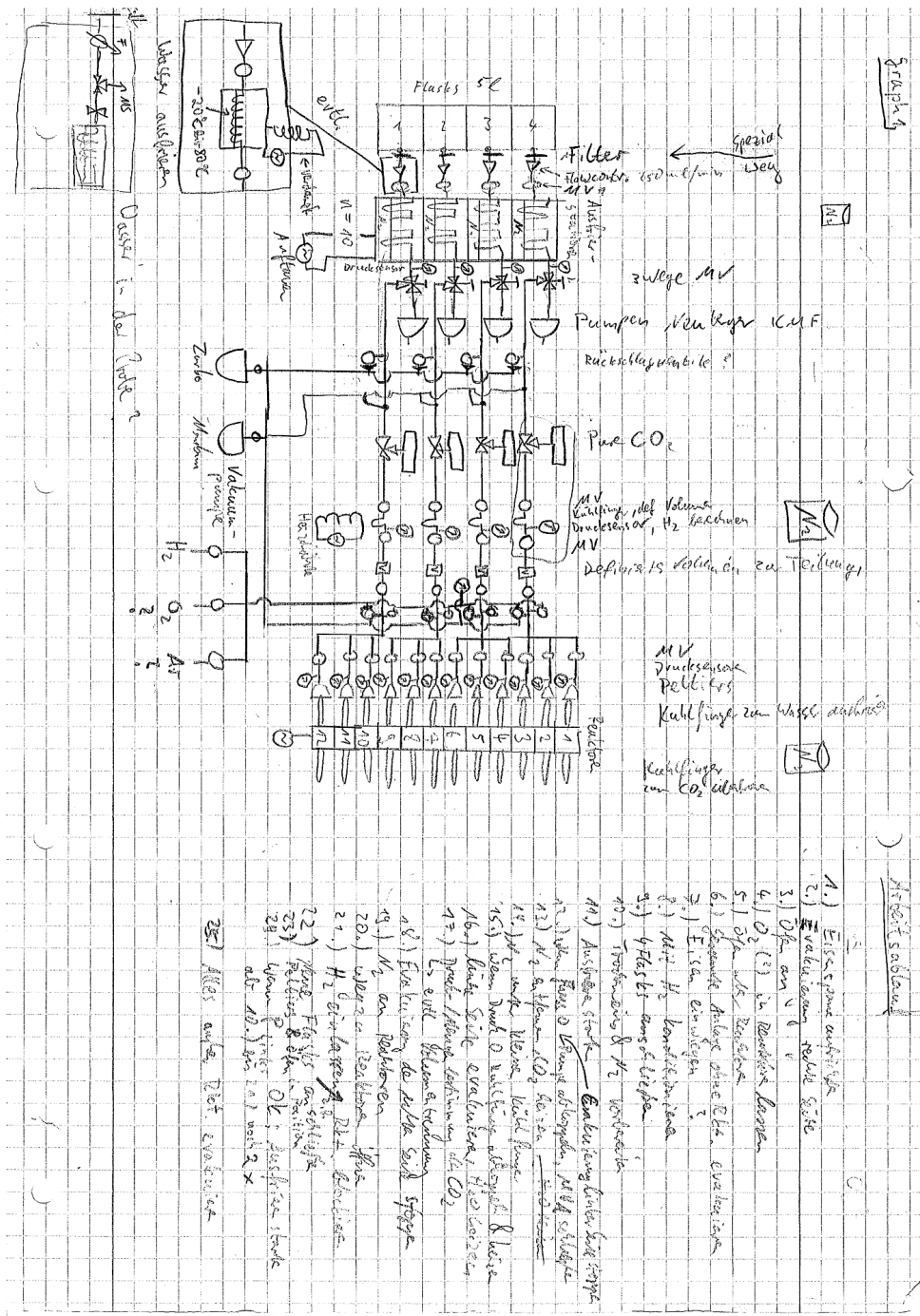


Figure B.2.: First sketch of the planned EGL in the beginning of this work.



Figure B.3.: Final set-up of the EGL in the CRL.

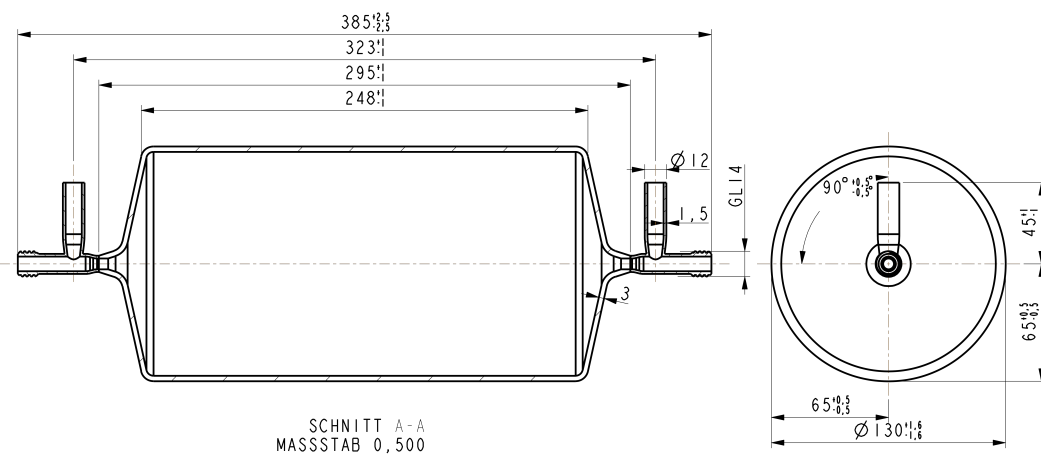


Figure B.4.: Technical drawing of ICOS 31 flask (created by Stephan Baum).

## B. Additional figures

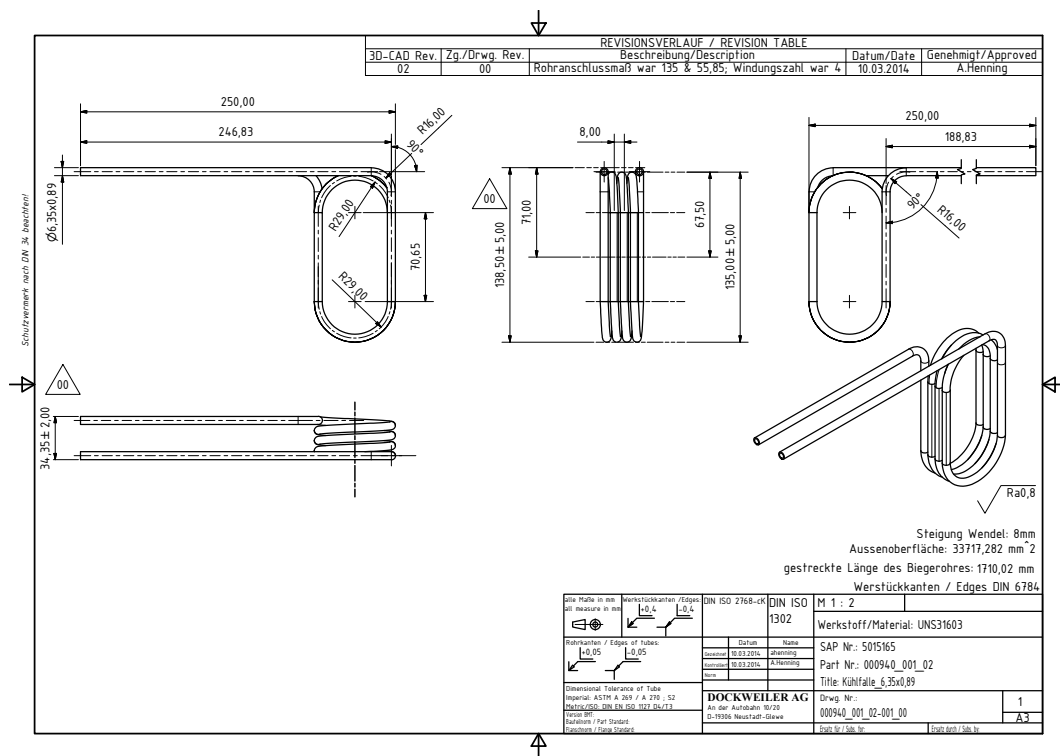


Figure B.5.: Technical drawing of EGL solid steel cooling trap (created by the technical support of Dockweiler AG)

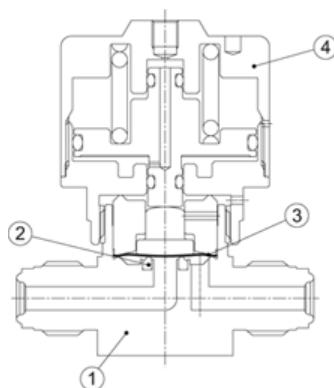


Figure B.6.: Technical drawing of the pneumatic valves in the EGL: 1: Body, stainless steel; 2: Seat, PCTFE; 3: Diaphragm, Ni-Co Alloy; 4: Handle, aluminium

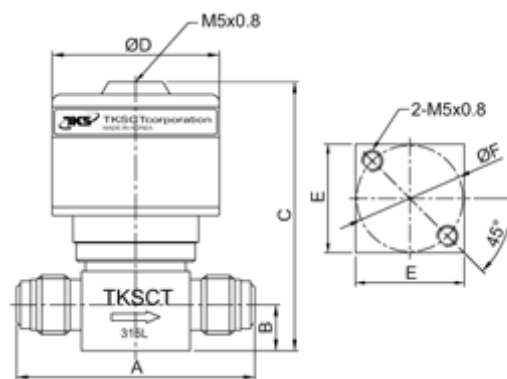


Figure B.7.: Dimensions of the pneumatic valves in the EGL: A: 57 mm; B: 11 mm; C: 61 mm; D: 40 mm; E: 26 mm; F: 25.4 mm

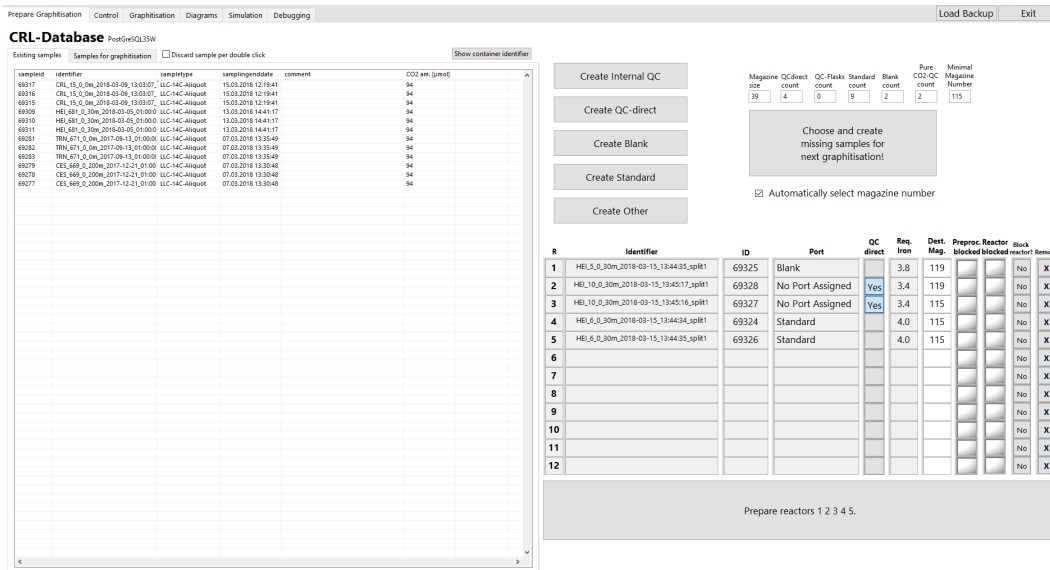


Figure B.8.: User interface for sample selection from DB in EGL control software.

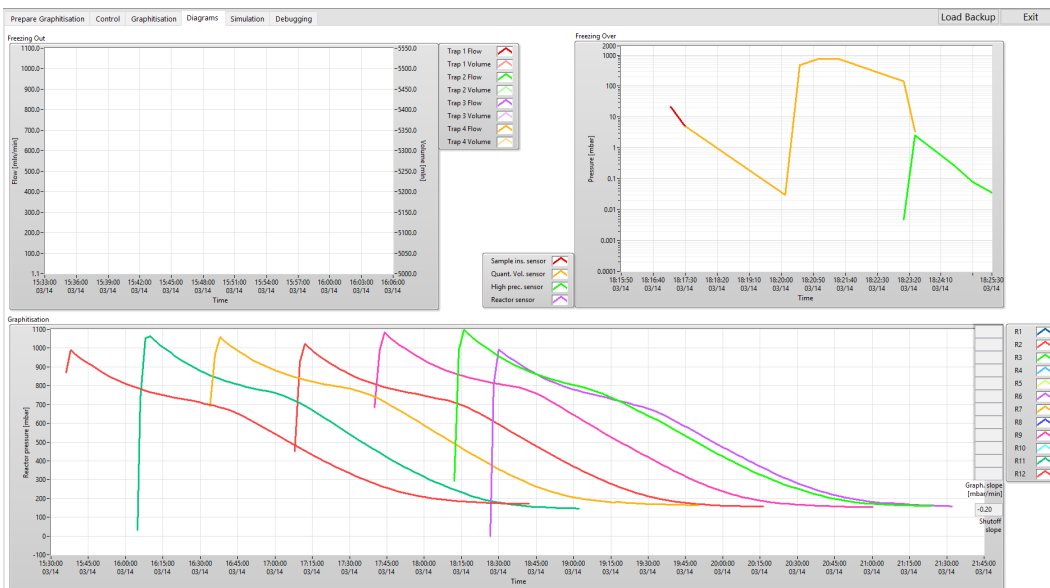


Figure B.9.: Interface for process monitoring in the EGL control software. Top left: Flow and volume monitoring for CO<sub>2</sub> extraction. Top right: Sample transfer pressure monitoring. Bottom: Graphitisation pressure and pressure slope monitoring.

## Examination of graphitisation duration

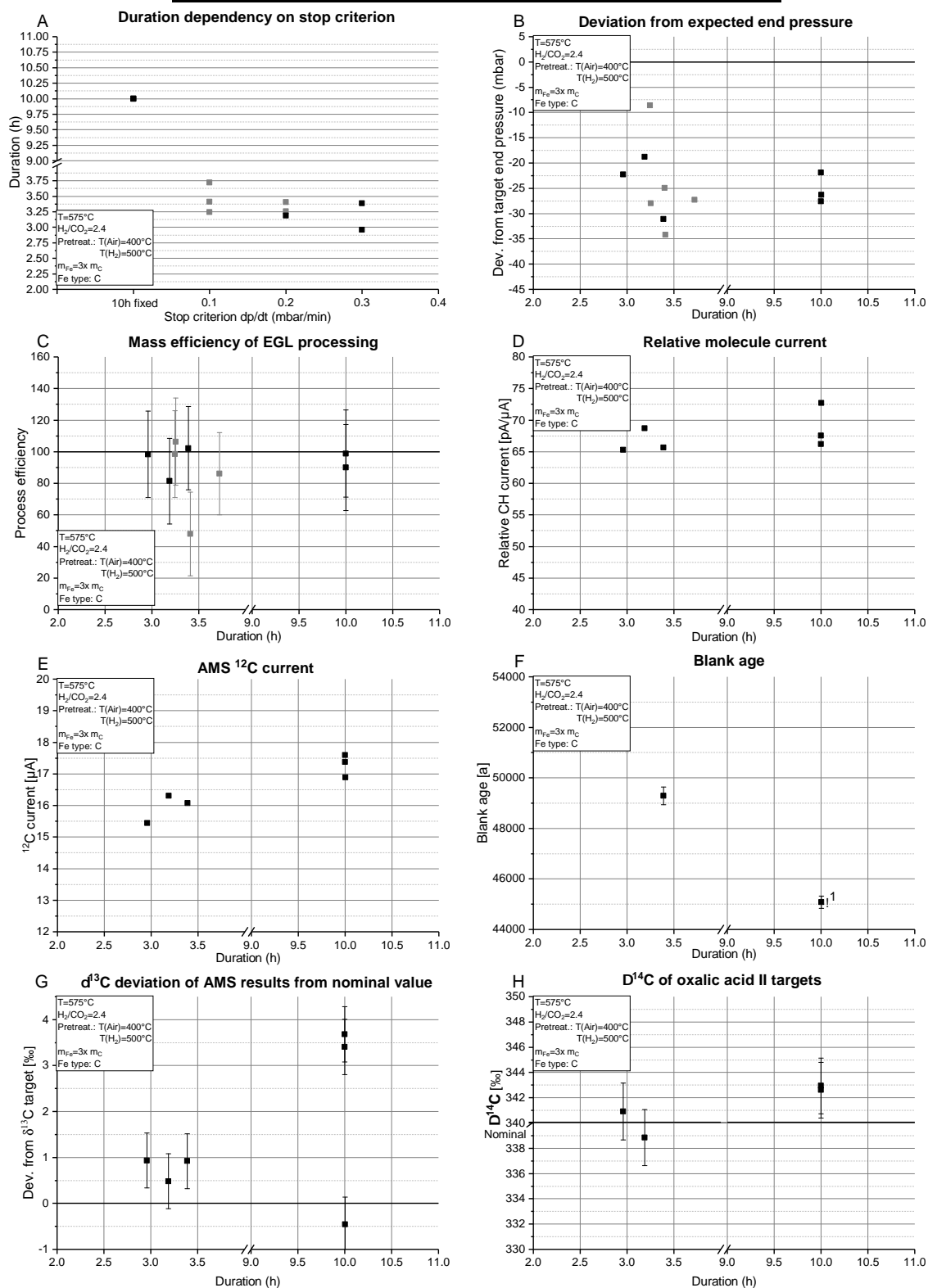


Figure B.10.: Examination of graphitisation duration; applied parameter given in the resp. boxes. (■): Graphitised, but not AMS analysed, targets. (□): Possibly incompletely harvested and contaminated targets. (!): Blank targets, that have been prepared before introducing of volume flushing and were possibly contaminated by a previously processed oxalic acid target. Errors in B, C, F, G and H are measurement errors as given in Sec. 3.5.1. A, D and E are measured very precisely compared to the scale.

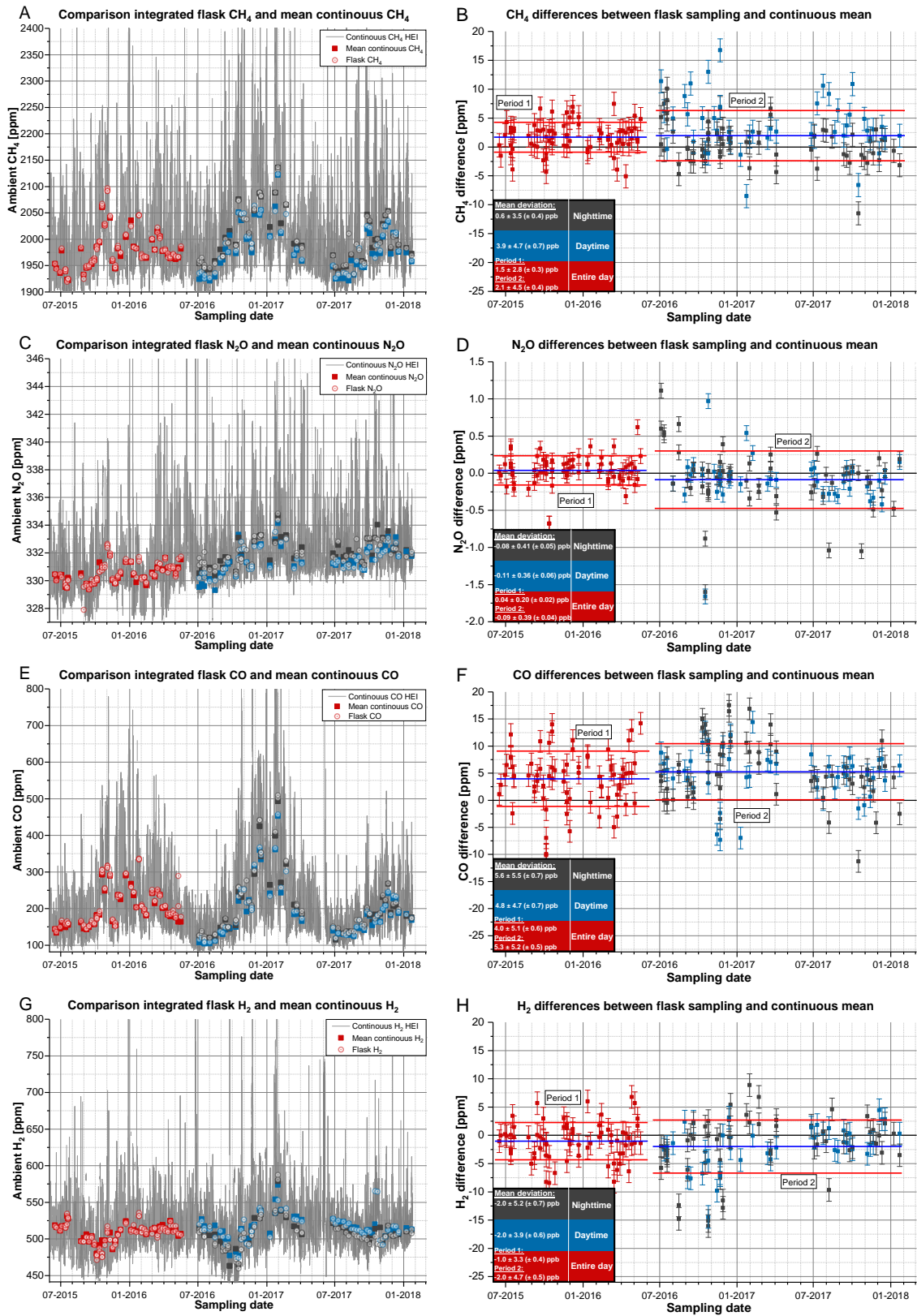


Figure B.11.: Evaluation of the flask sampling by comparison of the mean of continuous CH<sub>4</sub> (A,B), N<sub>2</sub>O (C,D), CO (E,F) and H<sub>2</sub> (G,H) measurements and flask results.

## B. Additional figures

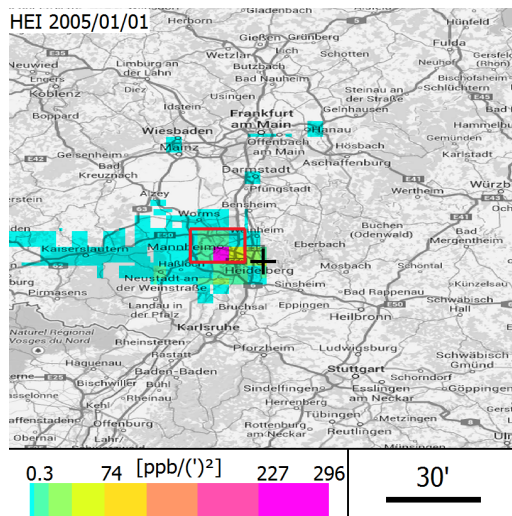


Figure B.12.: Contribution map for trajectory-triggered integrated sampling to Mannheim metropolitan area (red box) in January 2005. Emission model: IER-5.

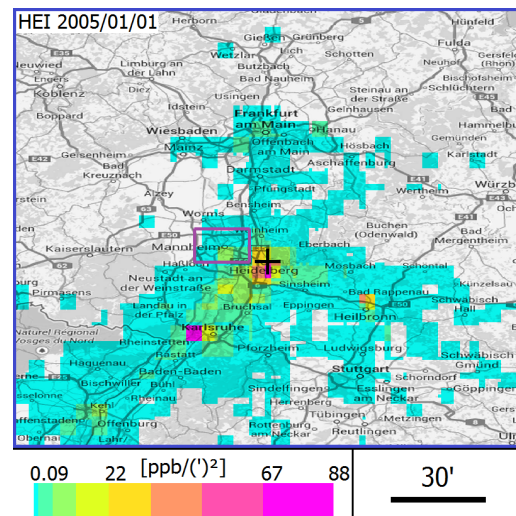


Figure B.13.: Contribution map for background sampling complementary to triggering for the Mannheim area in January 2005. Emission model: IER-5.

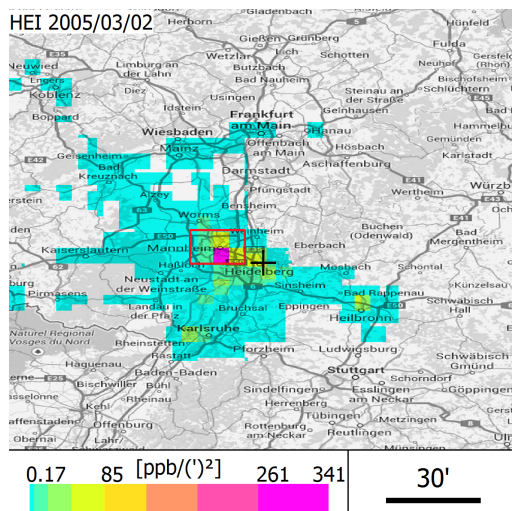


Figure B.14.: Contribution map for trajectory-triggered integrated sampling to Mannheim metropolitan area (red box) in March 2005. Emission model: IER-5.

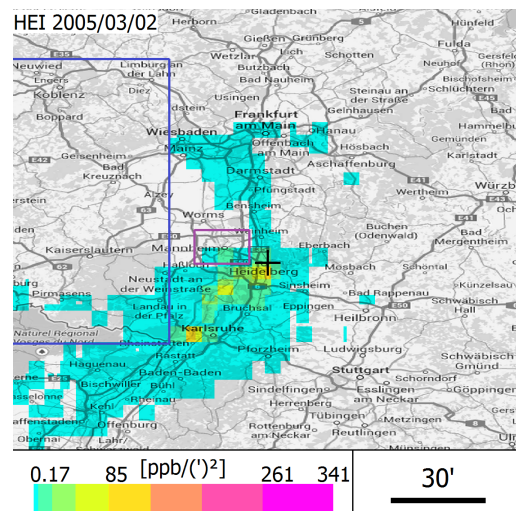


Figure B.15.: Contribution map for trajectory-triggered integrated sampling to a background region windward of Mannheim and prevention of triggering for Mannheim in March 2005. Emission model: IER-5.

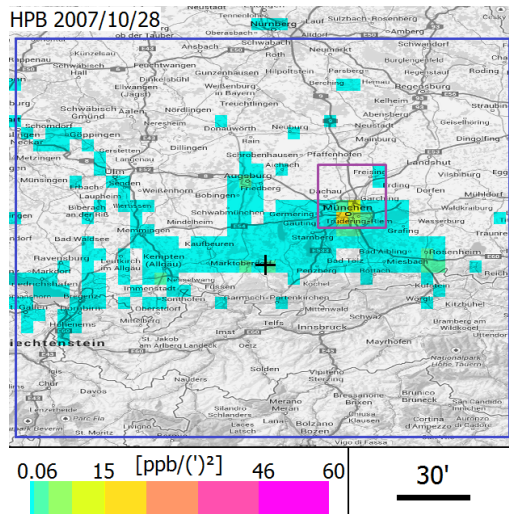


Figure B.16.: Contribution map for trajectory-triggered integrated sampling to the complementary contribution (blue) to Munich (purple) at HPB in November 2007. Emission model: IER-5.

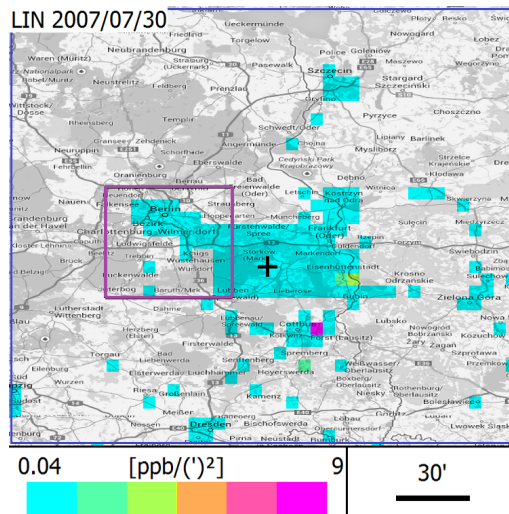


Figure B.17.: Contribution map for trajectory-triggered integrated sampling to the complementary contribution (blue) to Berlin (purple) at LIN in August 2007. Emission model: IER-5.



## C. Material lists

### C.1. Software

D&C Scheme Editor 5.0	Bosch Rexroth AG
Delphi XE3	Embarcadero Technologies
Dia	Steffen Macke
HYSPLIT for Windows	NOAA
JabRef 4.0	jabref.org
LabVIEW 2017	National Instruments
Libre Office	The Document Foundation
Maps	Google Maps
Microsoft Mathematics 4.0	Microsoft
Microsoft Office	Microsoft
MiKTeX 2.9	Christian Schenk
PGNP OLEDB Provider for PostgreSQL	Intellisoft LLC
TeXnicCenter 2.02	Tino Weinkauff and Sven Wiegand

### C.2. EGL parts

64-port relais card	National Instruments, PCI-6512
96-port digital IO	National Instruments, PCI-6509
Analog-digital converter	National Instruments, PCI-6210
Barcode scanner	Honeywell, Voyager 1202g
Extraction pumps	KNE, PM28170-938.50
Filter gaskets	Swagelok, SS-4-VCR-2-20M
Flow controlers	Bronkhorst, Low $\Delta p$ : F-201DV-ABD-88-V

*C. Material lists*

<b>Heating wire 0.75 m</b>	Thermocoax, SEA 10/75
<b>Heating wire 3 m</b>	Thermocoax, SEA 15/300
<b>I2C controller</b>	National Instruments, USB-8452
<b>Mains filter</b>	Ehmann 0463x0000
<b>Motor control board</b>	robotikhardware.de, RN-VNH2 Dualmotor
<b>Ovens</b>	Watlow, VC400J06A-0000R
<b>Peltier elements</b>	TRU components, TEC2-127-63-04
<b>Pirani/cold cathode pressure transm.</b>	Pfeiffer Vacuum, MPT 200
<b>Pirani pressure transmitter</b>	Thyracont, VSP63MV
<b>Pneumatic valves</b>	TK-FUJIKIN, S4PDVN-VM-C
<b>Pressure sensor</b>	Keller AG, PAA-9 LD
<b>Prevacuum pump</b>	vacuubrand, MD 1
<b>RS485 interface</b>	National Instruments, PCI-8431/4
<b>Target storage vial</b>	Rotilabo-storage vials, 2 ml
<b>Serial interface</b>	Delock, 87414
<b>Solenoid valves</b>	SMC Pneumatik, V110-D5NCZ-C4: SY100
<b>Temperature controller</b>	Omron Electronics, CelciuX°
<b>Tubing</b>	Dockweiler, TCC LZ1.4404 / 316L (S)
<b>Turbo vacuum pump</b>	Pfeiffer vacuum, HiCube

## List of Figures

1.	Emission scenarios and associated surface temperature models . . . .	10
2.	Emission progress to accomplish the 2-degree target . . . . .	10
3.	Schematic representation of the global carbon budget . . . . .	11
4.	Origin and reservoirs of $^{14}\text{C}$ . . . . .	11
5.	Development of atmospheric $^{14}\text{C}$ during the last 70 years . . . . .	12
1.1.	Current station network of ICOS RI . . . . .	15
1.2.	3L flask for whole air $^{14}\text{CO}_2$ sampling . . . . .	16
1.3.	Relation between variations in $^{13}\text{C}$ and $^{14}\text{C}$ . . . . .	21
1.4.	Schematic picture of the MICADAS . . . . .	27
1.5.	Baur-Glaessner diagrams for the reactions between iron, carbon and hydrogen compounds . . . . .	32
1.6.	Equilibria and temperature dependency of the water gas reaction . .	32
1.7.	Changes in total, $\text{CO}_2$ , $\text{CO}$ and $\text{CH}_4$ pressure during reaction . . . .	33
1.8.	The PBL in high pressure regions. . . . .	35
1.9.	Comparison between forward and backward time simulations . . . .	40
2.1.	Graphitisation line at IUP . . . . .	44
2.2.	AMS target gases during preparatory phase . . . . .	45
2.3.	Target gas high AMS result residuals . . . . .	47
2.4.	Target gas low AMS result residuals . . . . .	47
2.5.	Compatibility between IUP low-level counting and IUP AMS analysis from 2013-2016 . . . . .	50
2.6.	Chronological sequence of AMS measurements in different times after one common graphitising date for every sample type . . . . .	52
2.7.	Typical running-in effect of two blank measurements in the AMS . .	53
2.8.	Dependency of the AMS measurement uncertainty increase on the number of standard targets in the same magazine and the AMS $^{14}\text{C}$ counts of the targets . . . . .	55
3.1.	Basic scheme of the main technical components of the EGL and allocated features . . . . .	59
3.2.	Schematic figure of the EGL standard gases and pure- $\text{CO}_2$ -QC supply part . . . . .	61
3.3.	EGL cooling trap . . . . .	62
3.4.	Scheme of the EGL $\text{CO}_2$ quantification finger . . . . .	66
3.5.	Functional scheme of the EGL sections taking part in $\delta^{13}\text{C}$ aliquotation	69

List of Figures

3.6. Schematic representation of the EGL graphitisation reactor . . . . .	70
3.7. Temperature profiles in the reaction zone of the graphitisation reactor	73
3.8. Complete scheme of mechanical and electrical parts of the EGL in- teracting with the samples . . . . .	76
3.9. Pressure increase in EGL vacuum sections . . . . .	80
3.10. Schematic view of the interconnection regarding signalling and po- wer supply of the electrical components of the EGL . . . . .	83
3.11. Detailed view of the controlling PC, its periphery and directly con- nected devices . . . . .	84
3.12. Graphical representation of tubing, reactors, measurement devices, evacuation and valve control in EGL control software . . . . .	86
3.13. User interface of the EGL control software for automatic sample processing. . . . .	86
3.14. Simplified overview chart about the data flow and process arrange- ment in the EGL control software . . . . .	89
3.15. Scheme of the adjustable and measurable parameters for the EGL parameter test . . . . .	91
3.16. Dependency of $\Delta^{14}\text{C}$ results of target gas targets prepared at the IUP 14C laboratory on AMS $\delta^{13}\text{C}$ results . . . . .	93
3.17. $^{14}\text{C}$ age of blank targets during the course of parameter test series .	95
3.18. Reaction pressure and corresponding pressure slope at the end of the graphitisation . . . . .	99
3.19. Examination of iron type . . . . .	101
3.20. Dependency of the pretreatment reactor pressure on the tempera- ture of the oxidising (synt. air) and reducing ( $\text{H}_2$ ) agent . . . . .	104
3.21. Examination of catalyst pretreatment . . . . .	105
3.22. Examination of $\text{H}_2/\text{CO}_2$ ratio and graphitisation temperature . . . .	108
3.23. Examination of iron to carbon ratio . . . . .	112
3.24. $\delta^{13}\text{C}$ results dependent on immersion depth $d_i$ of the EGL $\text{CO}_2$ ex- traction . . . . .	115
3.25. $\delta^{13}\text{C}$ results dependent on target reactor and extraction line . . . . .	116
3.26. $\delta^{13}\text{C}$ deviation from the nominal values for Oxalic Acid I and II standard gases, sampled from the built-in EGL standard gas supply tanks . . . . .	117
3.27. Fractionation test including all EGL processing steps (sampling until graphitisation) for Oxalic Acid II samples . . . . .	118
3.28. $\Delta^{14}\text{C}$ analysis results of target gases prepared and graphitised at the IUP $^{14}\text{C}$ laboratory and the EGL . . . . .	120
3.29. AMS $\delta^{13}\text{C}$ results for target gas high targets . . . . .	121
3.30. Examination of the compatibility between LLC analysis of high- volume samples and AMS analysis of aliquots of the same samples .	123
3.31. Results of the primary QC test series with Oxalic Acid I targets . . .	124

4.1.	Mean modelled sensitivity for trace gas fluxes from the surface to the atmosphere at HEI . . . . .	129
4.2.	Final set-up of the integrated sampling set-up in Heidelberg . . . . .	130
4.3.	Evaluation of the integrated flask sampling by comparison of the mean of continuous CO <sub>2</sub> measurements and flask results . . . . .	132
4.4.	$\Delta^{14}\text{C}$ results for integrated sampling from 2013 to January 2018 . . . . .	133
4.5.	Interpolation of day- and nighttime $\Delta^{14}\text{C}$ results to the whole day . . . . .	134
4.6.	Evaluation of the integrated flasks' $\Delta^{14}\text{C}$ deviation versus integrated NaOH samples . . . . .	135
4.7.	FFCO <sub>2</sub> analysis of 5 a integral day- and nighttime sampling at HEI . . . . .	136
4.8.	Principle of triggered sampling, using the example of Heidelberg . . . . .	138
4.9.	Anthropogenic CO <sub>2</sub> emission inventory for Europe . . . . .	142
4.10.	Schematic diagram of the conducted convolution of the emission models with the STILT transport models . . . . .	143
4.11.	Emission sensitivities in HEI for two different 1 h spot samples and for one month trajectory-triggered integrated sampling . . . . .	145
4.12.	FFCO <sub>2</sub> contribution maps for trajectory-triggered integrated sampling at HEI in May 2005 . . . . .	146
4.13.	FFCO <sub>2</sub> contribution maps for trajectory-triggered integrated sampling at HPB in November 2007 . . . . .	148
4.14.	FFCO <sub>2</sub> contribution maps for trajectory-triggered integrated sampling at LIN in April 2007 . . . . .	150
4.15.	FFCO <sub>2</sub> contribution maps for trajectory-triggered integrated sampling at GAT in October 2007 . . . . .	152
A.1.	Scheme of the PAA-9LD pressure transmitter . . . . .	166
B.1.	ICOS data cycle . . . . .	173
B.2.	First sketch of the planned EGL in the beginning of this work . . . . .	174
B.3.	Final set-up of the EGL in the CRL . . . . .	175
B.4.	Technical drawing of ICOS 3l flask . . . . .	175
B.5.	Technical drawing of EGL solid steel cooling trap . . . . .	176
B.6.	Technical drawing of the pneumatic valves in the EGL . . . . .	176
B.7.	Dimensions of the pneumatic valves in the EGL . . . . .	176
B.8.	User interface for sample selection from DB in EGL control software . . . . .	177
B.9.	Interface for process monitoring in the EGL control software . . . . .	177
B.10.	Examination of graphitisation duration . . . . .	178
B.11.	Evaluation of the flask sampling by comparison of the mean of continuous trace gas measurements . . . . .	179
B.12.	Contribution map for trajectory-triggered integrated sampling to Mannheim metropolitan area . . . . .	180
B.13.	Contribution map for background sampling complementary to triggering for the Mannheim area . . . . .	180

*List of Figures*

B.14. Contribution map for trajectory-triggered integrated sampling to Mannheim metropolitan area . . . . .	180
B.15. Contribution map for trajectory-triggered integrated sampling to a background region windward of Mannheim and evasion of triggering for Mannheim . . . . .	180
B.16. Contribution map for trajectory-triggered integrated sampling to the complementary contribution to Munich from HPB . . . . .	181
B.17. Contribution map for trajectory-triggered integrated sampling to the complementary contribution to Berlin from LIN . . . . .	181

## List of Tables

2.1. Applied parameters for graphitisation reaction at IUP . . . . .	43
2.2. $\delta^{13}\text{C}$ fractionation at the IUP graphitisation line before and after graphitisation . . . . .	44
2.3. Results of the error analysis of target gas measurement series . . . . .	48
2.4. Characteristics of the measurement results of the AMS-LLC compatibility study . . . . .	50
2.5. Target press comparison of the CEZ press or the CRL press: $\Delta^{14}\text{C}$ results . . . . .	54
2.6. Planned composition of future magazines . . . . .	56
3.1. Steps of procedure for AMS sample preparation and measurement at the CRL . . . . .	58
3.2. Fractions of the total $\text{CO}_2$ amount for $\Delta^{14}\text{C}$ and $\delta^{13}\text{C}$ analysis . . . . .	68
3.3. Working gas and connection properties . . . . .	72
3.4. Comparison of different reaction tube dimensions . . . . .	74
3.5. Volumes and volume to quantification volume ratios for different EGL vacuum sections . . . . .	78
3.6. Pressure increase after evacuation, leakage rates and $\text{CO}_2$ contaminations in different EGL sections . . . . .	81
3.7. Catalyst mass loss during different processing steps . . . . .	96
3.8. Iron catalyst powders, that have been tested in this series . . . . .	100
3.9. Overview of the EGL parameter sets developed and tested in this work . . . . .	113
3.10. Comparison between graphitisation efficiency measures . . . . .	119
4.1. Mean surface emission sensitivity of integrated day- and nighttime sampling for different distance ranges from HEI . . . . .	129
4.2. Ambient $\text{CO}_2$ and $\text{FFCO}_2$ excess of night versus day samples by seasons . . . . .	137
4.3. Characteristics of the STILT footprint data used in this study . . . . .	140
4.4. Results of the contribution analysis for the trajectory-triggered sampling at HEI in 2005/2006 . . . . .	146
4.5. Results of the contribution analysis for the trajectory-triggered sampling at HPB in 2007 . . . . .	149
4.6. Results of the contribution analysis for the trajectory-triggered sampling at LIN in 2007 . . . . .	150

*List of Tables*

4.7. Results of the contribution analysis for the trajectory-triggered sampling at GAT in 2007 . . . . .	153
4.8. Estimated emission inventory (IER-5) error reduction in a hypothetical two-parameter inversion set-up for the four ICOS stations, investigated in this work . . . . .	155
A.1. Details of the heater control electronics . . . . .	164
A.2. Details of control electronics for extraction pumps, elevator motors and sensors and peltier elements . . . . .	165
A.3. Details of piezoresistive pressure transmitters . . . . .	166
A.4. Details of Pirani pressure transmitters . . . . .	167
A.5. Details of Pirani/cold cathode pressure transmitters . . . . .	168
A.6. Correction factors for different gas types . . . . .	169
A.7. Details of the pneumatic valve control . . . . .	170
A.8. Details of the flow controller electronics . . . . .	170
A.9. Details of the controlling PC of the EGL . . . . .	171

## List of abbreviations

N <sub>2</sub> (l)	Liquid nitrogen
AGE	Automated Graphitisation Equipment
AMS	Accelerator Mass Spectrometry
CAL	Central Analytical Laboratories
CEZ	Curt-Engelhorn-Zentrum für Archäometrie
CPU	Central Processing Unit
CRL	Central Radiocarbon Laboratory
DB	Database
EA	Elemental analyser
EGL	Extraction and Graphitisation Line
EPDM	Ethylene propylene diene monomer
FCL	Flask and Calibration Laboratory
FFCO <sub>2</sub>	Fossil fuel carbon dioxide
FS	Full scale
GAT	Gartow station
GC	Gas Chromatograph
GDAS	Global Data Assimilation System
GFS	Global Forecast System
GHG	Greenhouse Gas
HEI	Heidelberg station
HID	Human Interface Device
HPB	Hohenpeißenberg station
HYSPLIT	Hybrid Single Particle Lagrangian Transport
I/O	input/output
IAEA	International Atomic Energy Agency
ICOS	Integrated Carbon Observation System
IEA	International Energy Agency
IEC	International Electrotechnical Commission
INDC	Intended national determined contributions
IRIS	Infrared Isotope Spectrometry
IUP	Institut für Umweltphysik
LIN	Lindenberg station
LLC	Low Level Counting
MFC	Mass flow controller
MICADAS	Mini-Radiocarbon Dating System
MSP	Mass spectrometer
NDC	National determined contributions

*List of Tables*

NIST .....	National Institute of Standards and Technology
PBL .....	Planetary Boundary Layer
PCTFE .....	Polychlorotrifluoroethylene
pdf .....	probabilty density function
PDVN .....	Plastic Diaphragm Valve Nest
PID .....	proportional-integral-derivative
PTFE .....	Polytetrafluoroethylene
QC .....	Quality Control
RI .....	Research Infrastructure
RINGO .....	Readiness Of ICOS For Necessities Of Integrated Global Observations
ROI .....	Region Of Interest
SNAP .....	Selected Nomenclature for Air Pollution
STILT .....	Stochastic Time-Inverted Lagrangian Transport
TDP .....	Thermal Design Power
TEB .....	Total error band
TTL .....	Transistor-transistor logic
UCN .....	Unique Container Number
UI .....	User Interface
UNFCCC .....	United Nations Framework Convention on Climate Change
VPDB .....	Vienna Pee Dee Belemnite
WMO .....	World Meteorological Organization
WT .....	Wall thickness

## Bibliography

- F. Brown. The exchange of C<sup>14</sup> between elementary carbon and its oxides. *Trans. Faraday Soc.*, 48:1005–1014, 1952. doi:10.1039/TF9524801005.
- P. Ciais et al. Carbon and Other Biogeochemical Cycles. In T. Stocker, D. Qin, G.-K. Plattner, M. Tignor, S. Allen, J. Boschung, A. Nauels, Y. Xia, V. Bex, and P. Midgley, editors, *Climate Change 2013: The Physical Science Basis. Contribution of Working Group I to the Fifth Assessment Report of the Intergovernmental Panel on Climate Change*, book section 6, pages 465–570. Cambridge University Press, Cambridge, United Kingdom and New York, NY, USA, 2013. ISBN ISBN 978-1-107-66182-0. doi:10.1017/CBO9781107415324.015.
- L. A. Currie. Environmental radiocarbon measurements, 1978.
- D. Donahue, A. Jull, and L. Toolin. Radiocarbon measurements at the university of arizona AMS facility. *Nuclear Instruments and Methods in Physics Research Section B: Beam Interactions with Materials and Atoms*, 52(3-4):224–228, dec 1990. doi:10.1016/0168-583x(90)90410-v.
- R. R. Draxler. The accuracy of trajectories during anateX calculated using dynamic model analyses versus rawinsonde observations. *Journal of Applied Meteorology*, 30(10):1446–1467, 1991. doi:10.1175/1520-0450(1991)030<1446:TAOTDA>2.0.CO;2.
- R. R. Draxler and G. H. Hess. An overview of the HYSPLIT\_4 modelling system for trajectories, dispersion and deposition. *Australian Meteorological Magazine*, 1998.
- EDGAR. European Commission, Joint Research Centre (JRC)/Netherlands Environmental Assessment Agency (PBL). Emission Database for Global Atmospheric Research (EDGAR), release version 4.2. <http://edgar.jrc.ec.europa.eu>, 2011.
- S. Fahrni, J. Southon, G. Santos, S. Palstra, H. Meijer, and X. Xu. Reassessment of the c-13/c-12 and c-14/c-12 isotopic fractionation ratio and its impact on high-precision radiocarbon dating. *Geochimica et Cosmochimica Acta*, 213:330–345, 9 2017. ISSN 0016-7037. doi:10.1016/j.gca.2017.05.038.
- U. Gamnitzer, U. Karstens, B. Kromer, R. E. M. Neubert, H. A. J. Meijer, H. Schroeder, and I. Levin. Carbon monoxide: A quantitative tracer for fossil fuel CO<sub>2</sub>? *Journal of Geophysical Research*, 111(D22), nov 2006. doi:10.1029/2005jd006966.

## Bibliography

- 18th WMO/IAEA Meeting on Carbon Dioxide, Other Greenhouse Gases and Related Tracers Measurement Techniques (GGMT-2015), number 229 in 18, Sept. 2015. GAW.
- C. Gerbig, J. C. Lin, J. W. Munger, and S. C. Wofsy. What can tracer observations in the continental boundary layer tell us about surface-atmosphere fluxes? *Atmospheric Chemistry and Physics*, 6(2):539–554, Feb. 2006. doi:10.5194/acp-6-539-2006.
- H. D. Graven. Impact of fossil fuel emissions on atmospheric radiocarbon and various applications of radiocarbon over this century. *Proceedings of the National Academy of Sciences*, 112(31):9542–9545, jul 2015. doi:10.1073/pnas.1504467112.
- H. D. Graven, T. P. Guilderson, and R. F. Keeling. Methods for high-precision  $^{14}\text{C}$  AMS measurement of atmospheric  $\text{CO}_2$  at llnl. *Radiocarbon*, 49(2):349–356, 2007. doi:10.1017/S0033822200042284.
- H. D. Graven, B. B. Stephens, T. P. Guilderson, T. Campos, D. S. Schimel, J. E. Campell, and R. F. Keeling. Vertical profiles of biospheric and fossil fuel-derived  $\text{CO}_2$  and fossil fuel  $\text{CO}_2$  :  $\text{CO}$  ratios from airborne measurements of  $\Delta^{14}\text{C}$ ,  $\text{CO}_2$  and  $\text{CO}$  above colorado, usa. *Tellus B*, 61(3):536–546, 2009. ISSN 1600-0889. doi:10.1111/j.1600-0889.2009.00421.x.
- H. W. Gudenau, D. Senk, S. Wang, K. de Melo Martins, and C. Stephany. Research in the reduction of iron ore agglomerates including coal and c-containing dust. *ISIJ International*, 45(4):603–608, 2005. doi:10.2355/isijinternational.45.603.
- K. R. Gurney, Y.-H. Chen, T. Maki, S. R. Kawa, A. Andrews, and Z. Zhu. Sensitivity of atmospheric  $\text{CO}_2$  inversions to seasonal and interannual variations in fossil fuel emissions. *Journal of Geophysical Research*, 110(D10), 2005. doi:10.1029/2004jd005373.
- S. Hammer. *Quantification of the Regional  $\text{H}_2$  Sources and Sinks Inferred from Atmospheric Trace Gas Variability*. PhD thesis, Heidelberg University, 2008.
- S. Hammer and I. Levin. Seasonal variation of the molecular hydrogen uptake by soils inferred from continuous atmospheric observations in heidelberg, southwest germany. *Tellus B: Chemical and Physical Meteorology*, 61(3):556–565, jan 2009. doi:10.1111/j.1600-0889.2009.00417.x.
- S. Hammer, R. Friedrich, B. Kromer, A. Cherkinsky, S. J. Lehman, H. A. J. Meijer, T. Nakamura, V. Palonen, R. W. Reimer, A. M. Smith, and et al. Compatibility of atmospheric  $^{14}\text{CO}_2$  measurements: Comparing the heidelberg low-level counting facility to international accelerator mass spectrometry (AMS) laboratories. *Radiocarbon*, 59(3):875–883, 2017. doi:10.1017/RDC.2016.62.
- M. Hellström, A. Vermeulen, O. Mirzov, S. Sabbatini, D. Vitale, D. Papale, J. Tarniewicz, L. Hazan, L. Rivier, S. D. Jones, B. Pfeil, and T. Johannesen. Near real time data processing in ICOS RI. *OpenAIRE*, pages –, 2016. doi:10.5281/zenodo.204817.

- ICOS RI. Technical and scientific description of ICOS research infrastructure (ICOS RI). [https://www.icos-ri.eu/documents/ICOS ERIC Public](https://www.icos-ri.eu/documents/ICOS%20ERIC%20Public_03%202014), 03 2014.
- ICOS RI. ICOS-CAL website. <https://www.icos-cal.eu>, Nov. 2017a.
- ICOS RI. ICOS-RI website. <https://www.icos-ri.eu/>, Nov. 2017b.
- K. Juhlich. CO<sub>2</sub> emission factors for fossil fuels. Technical report, Umweltbundesamt, 2016.
- Keller AG. *Piezoresistive OEM pressure transmitters Series 4 LD...9 LD*. Keller AG, 2017. URL [http://www.keller-druck.com/picts/pdf/engl/41d\\_91d\\_e.pdf](http://www.keller-druck.com/picts/pdf/engl/41d_91d_e.pdf).
- A. Kent and J. G. Williams, editors. *Applications of Artificial Intelligence to Agriculture and Natural Resource Management to Transaction Machine Architectures*. Encyclopedia of Computer Science and Technology. CRC Press, 1991. ISBN 0824722752.
- T. Kneuer. Trajektoriengestützte Luftprobensammlung. Heidelberg university, Heidelberg University, 2017.
- B. Kromer and K. O. Münnich. CO<sub>2</sub> gas proportional counting in radiocarbon dating - review and perspective. In *Radiocarbon After Four Decades*, pages 184–197. Springer New York, 1992. doi:10.1007/978-1-4757-4249-7\_13.
- B. Kromer, S. Lindauer, H.-A. Synal, and L. Wacker. MAMS – a new AMS facility at the curt-engelhorn-centre for achaeometry, mannheim, germany. *Nuclear Instruments and Methods in Physics Research Section B: Beam Interactions with Materials and Atoms*, 294:11–13, jan 2013. doi:10.1016/j.nimb.2012.01.015.
- M. Kuderer. Influence of nuclear power plants to the radiocarbon budget in heidelberg and trajectory-based sampling. Master’s thesis, Heidelberg University, 2016.
- M. Kuderer, S. Hammer, and I. Levin. The influence of <sup>14</sup>CO<sub>2</sub> releases from regional nuclear facilities at the heidelberg <sup>14</sup>CO<sub>2</sub> sampling site (1986-2014). *Atmospheric Chemistry and Physics Discussions*, pages 1–16, feb 2018. doi:10.5194/acp-2018-84.
- R. L. Langenfelds, M. V. van der Schoot, R. J. Francey, L. P. Steele, M. Schmidt, and H. Mukai. Modification of air standard composition by diffusive and surface processes. *Journal of Geophysical Research: Atmospheres*, 110(D13), 2005. ISSN 2156-2202. doi:10.1029/2004JD005482. D13307.
- O. Laurent. ICOS atmospheric station specifications. Technical report, ICOS ATC, 2016.

## Bibliography

- C. Le Quéré, R. M. Andrew, P. Friedlingstein, S. Sitch, J. Pongratz, A. C. Manning, J. I. Korsbakken, G. P. Peters, J. G. Canadell, R. B. Jackson, T. A. Boden, P. P. Tans, O. D. Andrews, V. K. Arora, D. C. E. Bakker, L. Barbero, M. Becker, R. A. Betts, L. Bopp, F. Chevallier, L. P. Chini, P. Ciais, C. E. Cosca, J. Cross, K. Currie, T. Gasser, I. Harris, J. Hauck, V. Haverd, R. A. Houghton, C. W. Hunt, G. Hurtt, T. Ilyina, A. K. Jain, E. Kato, M. Kautz, R. F. Keeling, K. K. Golde-wijk, A. Körtzinger, P. Landschützer, N. Lefèvre, A. Lenton, S. Lienert, I. Lima, D. Lombardozzi, N. Metzl, F. Millero, P. M. S. Monteiro, D. R. Munro, J. E. M. S. Nabel, S. ichiro Nakaoka, Y. Nojiri, X. A. Padín, A. Peregón, B. Pfeil, D. Pierrot, B. Poulter, G. Rehder, J. Reimer, C. Rödenbeck, J. Schwinger, R. Séférian, I. Skjelvan, B. D. Stocker, H. Tian, B. Tilbrook, I. T. van der Laan-Luijkx, G. R. van der Werf, S. van Heuven, N. Viovy, N. Vuichard, A. P. Walker, A. J. Watson, A. J. Wiltshire, S. Zaehle, and D. Zhu. Global carbon budget 2017. *Earth System Science Data Discussions*, pages 1–79, nov 2017. doi:10.5194/essd-2017-123.
- C. Le Quéré et al. Global carbon budget 2016. *Earth System Science Data*, 8(2): 605–649, 2016. doi:10.5194/essd-8-605-2016.
- S. J. Lehman, J. B. Miller, C. Wolak, J. Southon, P. P. Tans, S. A. Montzka, C. Sweeney, A. Andrews, B. LaFranchi, T. P. Guilderson, and J. C. Turnbull. Allocation of terrestrial carbon sources using  $^{14}\text{CO}_2$ : Methods, measurement and modeling. *Radiocarbon*, 55(03):1484–1495, 2013. doi:10.1017/s0033822200048414.
- I. Levin and V. Hesshaimer. Radiocarbon – a unique tracer of global carbon cycle dynamics. *Radiocarbon*, 42(01):69–80, 2000. doi:10.1017/s0033822200053066.
- I. Levin and B. Kromer. The tropospheric  $^{14}\text{CO}_2$  level in mid-latitudes of the northern hemisphere (1959–2003). *Radiocarbon*, 46(03):1261–1272, 2004. doi:10.1017/s0033822200033130.
- I. Levin and C. Rödenbeck. Can the envisaged reductions of fossil fuel  $\text{CO}_2$  emissions be detected by atmospheric observations? *Naturwissenschaften*, 95(3):203–208, 2008. ISSN 0028-1042. doi:10.1007/s00114-007-0313-4.
- I. Levin, K. O. Münnich, and W. Weiss. The effect of anthropogenic  $\text{CO}_2$  and  $^{14}\text{C}$  sources on the distribution of  $^{14}\text{C}$  in the atmosphere. *Radiocarbon*, 22(02): 379–391, 1980. doi:10.1017/s003382220000967x.
- I. Levin, J. Schuchard, B. Kromer, and K. O. Münnich. The continental european suess effect. *Radiocarbon*, 31(03):431–440, 1989. doi:10.1017/s0033822200012017.
- I. Levin, B. Kromer, M. Schmidt, and H. Sartorius. A novel approach for independent budgeting of fossil fuel  $\text{CO}_2$  over Europe by  $^{14}\text{CO}_2$  observations. *Geophysical Research Letters*, 30(23):n/a–n/a, 2003. ISSN 1944-8007. doi:10.1029/2003GL018477. 2194.

- I. Levin, S. Hammer, B. Kromer, and F. Meinhardt. Radiocarbon observations in atmospheric CO<sub>2</sub>: Determining fossil fuel CO<sub>2</sub> over Europe using Jungfrauoch observations as background. *Science of The Total Environment*, 391(2?3):211 – 216, 2008. ISSN 0048-9697. doi:10.1016/j.scitotenv.2007.10.019. Research at Jungfrauoch – Contributions to the International conference in celebration of the 75th anniversary of the High Altitude Research Station Jungfrauoch at Interlaken, Switzerland (11-13 September, 2006).
- I. Levin, S. Hammer, E. Eichelmann, and F. R. Vogel. Verification of greenhouse gas emission reductions: the prospect of atmospheric monitoring in polluted areas. *Philosophical Transactions of the Royal Society A: Mathematical, Physical and Engineering Sciences*, 369(1943):1906–1924, 2011. doi:10.1098/rsta.2010.0249.
- I. Levin et al. Observations and modelling of the global distribution and long-term trend of atmospheric <sup>14</sup>CO<sub>2</sub>. *Tellus*, 62B:26–46, 2010. doi:10.1111/j.1600-0889.2009.00446.x.
- W. F. Libby. Atmospheric helium three and radiocarbon from cosmic radiation. *Physical Review*, 69(11-12):671–672, jun 1946. doi:10.1103/physrev.69.671.2.
- W. F. Libby, E. C. Anderson, and J. R. Arnold. Age determination by radiocarbon content: World-wide assay of natural radiocarbon. *Science*, 109(2827):227–228, mar 1949. doi:10.1126/science.109.2827.227.
- J. C. Lin, C. Gerbig, S. C. Wofsy, A. E. Andrews, B. C. Daube, K. J. Davis, and C. A. Grainger. A near-field tool for simulating the upstream influence of atmospheric observations: The Stochastic Time-Inverted Lagrangian Transport (STILT) model. *Journal of Geophysical Research: Atmospheres*, 108(D16):n/a–n/a, 2003. ISSN 2156-2202. doi:10.1029/2002JD003161. 4493.
- A. P. McNichol, A. R. Gagnon, G. A. Jones, and E. A. Osborne. Illumination of a black box: Analysis of gas composition during graphite target preparation. *Radiocarbon*, 34(3):321–329, 1992. doi:10.1017/S0033822200050785.
- W. G. Mook. *Environmental isotopes in the hydrological cycle – Introduction*. Number 39 in Technical Documents in Hydrology. UNESCO, Paris, 2000.
- W. G. Mook and J. van der Plicht. Reporting <sup>14</sup>C activities and concentrations. *Radiocarbon*, 41(03):227–239, 1999. doi:10.1017/s0033822200057106.
- H. A. Mooney, P. M. Vitousek, and P. A. Matson. Exchange of Materials Between Terrestrial Ecosystems and the Atmosphere. *Science*, 238(4829):926–932, 1987. doi:10.1126/science.238.4829.926.
- T. Naegler. *Simulating bomb radiocarbon: implications for the global carbon cycle*. PhD thesis, Heidelberg University, 2005.

## Bibliography

- M. Němec, L. Wacker, and H. Gaggeler. Optimization of the Graphitization Process at AGE-1. *Radiocarbon*, 52(3), 2010. ISSN 0033-8222. doi:10.1017/s0033822200046464.
- P. Peylin, S. Houweling, M. C. Krol, U. Karstens, C. Rödenbeck, C. Geels, A. Vermeulen, B. Badawy, C. Aulagnier, T. Pregger, F. Delage, G. Pieterse, P. Ciais, and M. Heimann. Importance of fossil fuel emission uncertainties over Europe for CO<sub>2</sub> modeling: model intercomparison. *Atmospheric Chemistry and Physics*, 11(13):6607–6622, jul 2011. doi:10.5194/acp-11-6607-2011.
- Pfeiffer Vacuum. *MPT 200 - Digitaler Pirani/Kaltkathoden-Transmitter*. Pfeiffer Vacuum, 2016.
- T. Pregger, Y. Scholz, and R. Friedrich. Documentation of the Anthropogenic GHG Emission Data for Europe Provided in the Frame of CarboEurope GHG and CarboEurope IP. Technical report, Universität Stuttgart, 2007.
- proQuarz. proQuarz website. <http://proquarz.de/>, Nov. 2017.
- C. D. Rodgers. *Inverse methods for atmospheric sounding - Theory and Practice*. World Scientific, 2000. doi:10.1142/3171.
- M. Roos. Optimierung des Graphitisierungsprozesses zur Probenvorbereitung von <sup>14</sup>C-Messungen mittels AMS. Bachelor's thesis, Heidelberg University, 2013.
- G. Santos, M. Mazon, J. Southon, S. Rifai, and R. Moore. Evaluation of iron and cobalt powders as catalysts for <sup>14</sup>C-AMS target preparation. *Nuclear Instruments and Methods in Physics Research Section B: Beam Interactions with Materials and Atoms*, 259(1):308–315, jun 2007. doi:10.1016/j.nimb.2007.01.220.
- M. Schmidt, R. Graul, H. Sartorius, and I. Levin. The schauinsland CO<sub>2</sub> record: 30 years of continental observations and their implications for the variability of the European CO<sub>2</sub> budget. *Journal of Geophysical Research*, 108(D19), 2003. doi:10.1029/2002jd003085.
- A. M. Smith, V. V. Petrenko, Q. Hua, J. Southon, and G. Brailsford. The effect of N<sub>2</sub>O, catalyst, and means of water vapor removal on the graphitization of small CO<sub>2</sub> samples. *Radiocarbon*, 49(2):245–254, 2007. doi:10.1017/S003382220004217X.
- K. Stenström, G. Skog, E. Georgiadou, J. Genberg, and A. Johansson. A guide to radiocarbon units and calculations. Technical report, Lund University, Nuclear Physics, 2011.
- M. Strogies and P. Gniffke. Submission under the United Nations Framework Convention on Climate Change and the Kyoto protocol 2017 – National Inventory Report for the German greenhouse gas inventory 1990-2015. Technical report, Umweltbundesamt, 2017.

- M. Stuiver and H. A. Polach. Discussion reporting of  $^{14}\text{C}$  data. *Radiocarbon*, 19(3): 355–363, 1977. doi:10.1017/s0033822200003672.
- M. Stuiver and P. Quay. Atmospheric  $^{14}\text{C}$  changes resulting from fossil fuel  $\text{CO}_2$  release and cosmic ray flux variability. *Earth and Planetary Science Letters*, 53(3): 349–362, may 1981. doi:10.1016/0012-821x(81)90040-6.
- M. Stuiver and S. W. Robinson. University of Washington geosecs north Atlantic carbon-14 results. *Earth and Planetary Science Letters*, 23(1):87–90, aug 1974. doi:10.1016/0012-821x(74)90034-x.
- R. B. Stull. *Introduction to Boundary Layer Meteorology*. Springer Netherlands, 2012. URL [http://www.ebook.de/de/product/25442280/roland\\_b\\_stull\\_introduction\\_to\\_boundary\\_layer\\_meteorology.html](http://www.ebook.de/de/product/25442280/roland_b_stull_introduction_to_boundary_layer_meteorology.html).
- H. E. Suess. Radiocarbon concentration in modern wood. *Science*, 122:415–417, 1955. doi:10.1126/science.122.3166.415-a.
- M. Suter, R. Balzer, G. Bonani, and W. Wölfli. A fast beam pulsing system for isotope ratio measurements. *Nuclear Instruments and Methods in Physics Research Section B: Beam Interactions with Materials and Atoms*, 5(2):242–246, nov 1984. doi:10.1016/0168-583x(84)90519-6.
- H.-A. Synal, M. Döbeli, S. Jacob, M. Stocker, and M. Suter. Radiocarbon AMS towards its low-energy limits. *Nuclear Instruments and Methods in Physics Research Section B: Beam Interactions with Materials and Atoms*, 223-224:339–345, aug 2004. doi:10.1016/j.nimb.2004.04.067.
- H.-A. Synal, M. Stocker, and M. Suter. Micadas: A new compact radiocarbon AMS system. *Nuclear Instruments and Methods in Physics Research Section B: Beam Interactions with Materials and Atoms*, 259(1):7 – 13, 2007. ISSN 0168-583X. doi:<https://doi.org/10.1016/j.nimb.2007.01.138>. Accelerator Mass Spectrometry.
- A. Tarantola. *Inverse Problem Theory and Methods for Model Parameter Estimation*. siam, 2005. doi:10.1137/1.9780898717921.
- R. L. Thompson, C. Gerbig, and C. Rödenbeck. A Bayesian inversion estimate of  $\text{N}_2\text{O}$  emissions for western and central Europe and the assessment of aggregation errors. *Atmospheric Chemistry and Physics*, 11(7):3443–3458, 2011. doi:10.5194/acp-11-3443-2011.
- Thyracont. *VSP63MV - Vacuum Transducer Operating Instructions*. Thyracont, 2016.
- K. Trusilova, C. Rödenbeck, C. Gerbig, and M. Heimann. Technical note: A new coupled system for global-to-regional downscaling of  $\text{CO}_2$  concentration estimation. *Atmospheric Chemistry and Physics*, 10(7):3205–3213, apr 2010. doi:10.5194/acp-10-3205-2010.

## Bibliography

- J. Turnbull, S. Lehman, S. Morgan, and C. Wolak. A New Automated Extraction System for  $^{14}\text{C}$  Measurement for Atmospheric  $\text{CO}_2$ . *Radiocarbon*, 52(3), 2010a. ISSN 0033-8222. doi:10.1017/s0033822200046348.
- J. Turnbull, C. Prior, and Graphitization Workshop Participants. Report on the 20th international radiocarbon conference graphitization workshop. *Radiocarbon*, 52 (2-3):1230–1235, 2010b. doi:10.1017/s0033822200046312.
- J. Turnbull, D. Guenther, A. Karion, C. Sweeney, E. Anderson, A. Andrews, J. Kofler, N. Miles, T. Newberger, S. Richardson, and P. Tans. An integrated flask sample collection system for greenhouse gas measurements. *Atmospheric Measurement Techniques*, 5(9):2321–2327, sep 2012. doi:10.5194/amt-5-2321-2012.
- J. C. Turnbull, S. J. Lehman, J. B. Miller, R. J. Sparks, J. R. Southon, and P. P. Tans. A new high precision  $^{14}\text{CO}_2$  time series for north american continental air. *Journal of Geophysical Research: Atmospheres*, 112(D11):n/a–n/a, 2007. ISSN 2156-2202. doi:10.1029/2006JD008184. D11310.
- J. C. Turnbull, C. Sweeney, A. Karion, T. Newberger, S. J. Lehman, P. P. Tans, K. J. Davis, T. Lauvaux, N. L. Miles, S. J. Richardson, M. O. Cambaliza, P. B. Shepson, K. Gurney, R. Patarasuk, and I. Razlivanov. Toward quantification and source sector identification of fossil fuel  $\text{CO}_2$  emissions from an urban area: Results from the INFLUX experiment. *Journal of Geophysical Research: Atmospheres*, 120 (1):292–312, jan 2015a. doi:10.1002/2014jd022555.
- J. C. Turnbull, A. Zondervan, J. Kaiser, M. Norris, J. Dahl, T. Baisden, and S. Lehman. High-precision atmospheric  $^{14}\text{CO}_2$  measurement at the rafter radiocarbon laboratory. *Radiocarbon*, 2015b. doi:10.2458/azu\_rc.57.18390.
- Umweltbundesamt. Emission register of the german federal environment agency. <https://www.thru.de>, Mar. 2018.
- UNFCCC. Paris agreement. 12 2015. URL [http://unfccc.int/paris\\_agreement/items/9485.php](http://unfccc.int/paris_agreement/items/9485.php).
- I. Unkel. *AMS-14C-Analysen zur Rekonstruktion der Landschafts- und Kulturgeschichte in der Region Palpa (S-Peru)*. PhD thesis, Heidelberg University, 2006.
- S. N. Vardag, C. Gerbig, G. Janssens-Maenhout, and I. Levin. Estimation of continuous anthropogenic  $\text{CO}_2$ : model-based evaluation of  $\text{CO}_2$ ,  $\text{CO}$ ,  $\delta^{13}\text{c}(\text{CO}_2)$  and  $\Delta^{14}\text{c}(\text{CO}_2)$  tracer methods. *Atmospheric Chemistry and Physics*, 15(22):12705–12729, 2015. doi:10.5194/acp-15-12705-2015.
- S. N. Vardag, S. Hammer, and I. Levin. Evaluation of 4 years of continuous  $\delta^{13}\text{C}$  data using a moving keeling plot method. *Biogeosciences*, 13(14):4237–4251, jul 2016. doi:10.5194/bg-13-4237-2016.

- L. Wacker, G. Bonani, M. Friedrich, I. Hajdas, B. Kromer, M. Němec, M. Ruff, M. Suter, H.-A. Synal, and C. Vockenhuber. MICADAS: Routine and high-precision radiocarbon dating. *Radiocarbon*, 52(02):252–262, 2010a. doi:10.1017/s0033822200045288.
- L. Wacker, M. Christl, and H.-A. Synal. Bats: A new tool for ams data reduction. *Nuclear Instruments and Methods in Physics Research Section B: Beam Interactions with Materials and Atoms*, 268(7):976 – 979, 2010b. ISSN 0168-583X. doi:https://doi.org/10.1016/j.nimb.2009.10.078. Proceedings of the Eleventh International Conference on Accelerator Mass Spectrometry.
- L. Wacker, M. Němec, and J. Bourquin. A revolutionary graphitisation system: Fully automated, compact and simple. *Nuclear Instruments and Methods in Physics Research Section B: Beam Interactions with Materials and Atoms*, 268(7):931 – 934, 2010c. ISSN 0168-583X. doi:https://doi.org/10.1016/j.nimb.2009.10.067. Proceedings of the Eleventh International Conference on Accelerator Mass Spectrometry.
- R. Wang, S. Tao, P. Ciais, H. Z. Shen, Y. Huang, H. Chen, G. F. Shen, B. Wang, W. Li, Y. Y. Zhang, Y. Lu, D. Zhu, Y. C. Chen, X. P. Liu, W. T. Wang, X. L. Wang, W. X. Liu, B. G. Li, and S. L. Piao. High-resolution mapping of combustion processes and implications for CO<sub>2</sub> emissions. *Atmospheric Chemistry and Physics*, 13(10): 5189–5203, may 2013. doi:10.5194/acp-13-5189-2013.
- P. Zannetti, editor. *Computer Techniques in Environmental Studies*, chapter Receptor-oriented Lagrangian-Eulerian model of mesoscale air pollution dispersion, pages 57–68. WIT Press, Billerica, 1990.
- L. Zipf. Further development of a  $\delta^{13}\text{C}$ -spectrometer for small sample analysis. Master's thesis, Universität Heidelberg, 2017.



## Credits

Zuerst möchte ich Ingeborg Levin ganz herzlich für die Betreuung über die Zeit meiner Doktorarbeit danken und für all das, was ich von ihr gelernt habe, nicht nur für die Arbeit sondern auch darüber hinaus für das ganze Leben.

Bernd Jähne danke ich dafür, dass er sich die Zeit genommen hat, diese Arbeit zu begutachten.

Sam Hammer danke ich dafür, dass er immer als kompetenter Ansprechpartner für alle Arten von Problemen zur Verfügung stand und mich bei der Formulierung dieses Schriftwerks so engagiert unterstützt hat. Das gemeinsame Planen der Anlage und von neuen Experimenten und die Diskussionen darüber haben nicht nur meine Arbeit sondern auch mich persönlich weitergebracht.

Ronny Friedrich und Bernd Kromer, den Meistern des MICADAS in Mannheim, danke ich für das sorgfältige Messen und manchmal Verbrennen unserer Graphitproben und für zahlreiche Diskussionen über das Wesen der  $\delta^{13}\text{C}$  Normalisierung und vieles mehr.

Ohne all die Leute, die in unseren Laboren so eine gute Arbeit machen hätte ein Großteil der Graphittargets nie das Licht der Welt erblickt: Sabine und Eva halten das Radiokarbonlabor am Laufen und hatten auf so viele praktische Fragen eine Antwort. Manuel, Menno, Chris, Lennard und Fabian haben viele Proben genommen und Targets prozessiert und mir mit ihren Hinweisen ermöglicht viele Funktionen der Anlagen zu verbessern. Michael sorgt dafür, dass die kontinuierlichen Spurengasmessungen im IUP am Laufen bleiben, und übernahm die  $\delta^{13}\text{C}$  Messungen am Massenspektrometer.

Den aktuellen und früheren Mitgliedern der Kohlenstoffgruppe danke ich für das angenehme Arbeitsklima. Ich durfte viele verschiedene Arbeitsgebiete kennenlernen, über die wir in unseren Gruppensitzungen nachdenken und ausführlich diskutieren konnten.

Meinem IUP-Büro und meinen anderen Freunden, danke ich für die Zeit, die wir in den Pausen von der Arbeit miteinander verbracht haben, ob in einer Grillhütte, beim Bierbrauen, im Koprulu-Sektor, Lorakis oder Norditalien (Flandern).

Meinen Eltern danke ich dafür, dass sie es ermöglicht haben, dass ich Physik studieren konnte und mich so manches Mal aufgebaut und mir mit Rat und Tat zur Seite standen, wenn es nicht so gut lief.

Köszönöm Rita, hogy segített nekem a stresszes idő alatt. Várom, hogy megvalósítsuk terveinket, és megnézzük Rick & Mortyt (az ágyban). Szeretlek és a kis családunk!